

Dottorato di Ricerca in Ingegneria Geotecnica

XXII Ciclo

Consorzio tra:

*Università degli Studi di Napoli, Seconda Università di Napoli, Università di
Napoli “Parthenope”, Università di Salerno, Università del Sannio*

Coordinatore:

prof. ing. Carlo Viggiani

Tesi per il conseguimento del titolo

***Seismic soil-structure interaction for
pile supported systems***

novembre 2009

Candidato:

ing. Raffaele Di Laora

Relatore:

prof. ing. Alessandro Mandolini

Correlatore:

prof. ing. George Mylonakis

Index

Introduction	5
1 Basic of dynamics	7
1.1 Single Degree Of Freedom systems	7
1.1.1 General equation	7
1.1.2 Undamped free vibration	8
1.1.3 Damped free vibration	9
1.1.4 Damped forced vibration: response to periodic loading	10
1.1.5 Damped forced vibration: response to generic loading	13
1.1.6 Response spectra	13
1.2 Multiple Degree Of Freedom systems	14
1.2.1 General equation	14
1.2.2 Combination of modal contributions	16
1.3 Numerical evaluation of dynamic response: Newmark method	17
1.3.1 Basic procedure	17
1.3.2 Stability and computational error	18
1.4 Continuous systems	20
1.4.1 Frequency domain analysis	20
1.4.2 One-dimensional ground response	21
2 Basic of finite elements	24
2.1 Overview	24
2.2 Element discretisation	25
2.3 Displacement approximation	25
2.4 Element equations	28
2.5 Numerical integration	31
2.6 Global equations and evaluation of stresses and strains	31
3 Kinematic interaction	32
3.1 Literature review	33
3.1.1 Modification of motion parameters	34
3.1.2 Bending moments	40
3.2 Numerical analyses	58

3.2.1	Introduction	58
3.2.2	Overview of the analyses	61
3.2.3	Kinematic interaction analyses for piles embedded in homogeneous deposits	64
3.2.3.1	Effect of modes of vibration	64
3.2.3.2	Group effects	66
3.2.3.3	Displacements and rotational component for pile groups	71
3.2.4	Kinematic interaction analyses for piles embedded in 2-layers deposits	75
3.2.5	Curvature and acceleration ratios vs. frequency	76
3.2.6	Parametric studies	79
3.2.6.1	Effect of the depth of the interface	81
3.2.6.2	Effect of the stiffness contrast	84
3.2.6.3	Effect of the stiffness ratio	84
3.2.6.4	Effect of diameter and length	88
3.2.6.5	Simplified evaluation of interface and head bending moments	89
3.2.6.5.1	Interface bending moments	89
3.2.6.5.2	Head bending moments	94
3.2.6.6	Considerations about piles in multi-layer deposits	98
3.2.6.7	Some considerations about transmissibility	100
3.2.7	Alteration of the signal at the base of a structure due to the presence of piles	102
3.2.7.1	Parameters ruling the “filtering effect” for a two-layers deposit	103
3.2.7.2	Response spectra	109
4	Inertial interaction	112
4.1	Literature review	112
4.1.1	Dynamic impedance for a single pile	112
4.1.2	Dynamic impedance for a pile group	115
4.1.3	The role of SSI	124
4.2	Kinematic vs. inertial interaction	129
4.2.1	Relative importance of kinematic vs. inertial interaction	129
4.2.1.1	Parametric study	131
4.2.2	Phase lag between kinematic and inertial interaction	138
4.2.2.1	Theoretical considerations	138
4.2.2.2	Numerical analyses	141
4.2.2.3	Combination of kinematic and inertial maxima at pile cap	146
	Concluding remarks	147
	References	148

Acknowledgements

Few hours from the deadline, at the end of this work, I have to thank the persons which, during the Doctorate, gave me any significant contribution.

The first person I want to thank is the coordinator of the school, prof. Carlo Viggiani; our relation didn't start in the best way, but I hope that now he is happy of my work.

Naturally a person I have to thank is my supervisor, prof. Alessandro Mandolini. I have to thank him not only for his great contribution in increasing my knowledge, but, above all, for all he taught me in terms of human relations; thanks to him, now I am a better person.

A particular thank to all the professors who gave me lessons: I never attended a boring course. Particular mention to Vincenzo Minutolo, professor of solid mechanics, who sustained me during my approach to numerical analyses; from him, I learned that one has to be very careful with them.

A special thank to my colleagues. They are really friends. Fantastic friends.

Thanks to prof. George Mylonakis, who gave me hospitality in Patras, and taught me a lot.

Moreover, there are persons who contributed from an affective point of view.

In primis I must thank my family, because I am happier and happier of myself. I have also to thank my parents because they allowed me to attend a Doctorate school.

I have to thank my girlfriend, Elisabetta. I never said it, but her contribution was fundamental, because she encouraged me also in the (fortunately few) darkest moments. I have also to thank her because she taught me a lot in a lot of fields.

A special thank to anyone shared with me positive and negative moments; in any way, each of these persons influenced my character.

Finally, thanks to myself for the obstinacy in doing my work as well as possible, and thanks to everyone trust and will trust in me.

Introduction

Civil engineering structures involve structural elements with direct contact with ground. When the external actions, such as earthquakes, act on these systems, neither the structural displacements nor the ground displacements, are independent of each other. The process in which the response of the soil influences the motion of the structure and the motion of the structure influences the response of the soil is termed as soil-structure interaction (SSI).

Damage occurred in recent earthquakes, have highlighted that the seismic behaviour of a structure is highly influenced not only by the response of the superstructure (considered as fixed based), but also by the response of the foundation and the ground as well.

Hence, some modern seismic design codes impose that the effect of SSI must be taken into account, even if only in particular situations (depending on the particular Code).

The complex 3-component interaction (soil-foundation-structure) may be analysed (in the hypothesis of linear elasticity) with reference to two separate interaction, reflecting distinct physic phenomena. The first one is the modification of the input motion at the base of the structure due to the different stiffness of the foundation with respect to the soil, referred to as kinematic interaction; the structure vibrates (because of its inertia) in dependence also of the soil-foundation system, and the latter experiences additional deformations (inertial interaction).

The thesis deal with seismic SSI problems for pile supported structures with particular reference to the design aspects in the light of the recent Italian Codes and Eurocodes.

In fact, despite the state of the art in SSI analyses has evolved steadily over the last decades, the state of practice for engineering characterization of SSI effects for routine structures has not undergone recent similar advancement.

For this reason, aim of the thesis is:

- to better understand the mathematical and physical meaning of kinematic interaction;
- to provide simplified formulas for evaluating its effects in terms of bending moments (interface and pile head);to find simply rules to estimate the importance of “filtering effect” exerted by piles on foundation input motion;
- to investigate the relative importance of kinematic vs. inertial interaction;
- to provide a criterion to combine inertial and kinematic maximum effects.

The thesis is divided in 4 chapters; the first one describes the fundamental instruments to analyze the dynamics of discrete and continuous systems; chapter 2 deals with the base principles of Finite Element Method, necessary to better understand the analyses that have been carried out.

Chapter 3 concentrates on kinematic interaction. Starting from the main previous works on the topic, principal results which have been obtained are described, proposing simplified formulations to evaluate the effect of kinematic interaction in terms of bending moments at the interface (in two-layers deposits) and at pile top (when restrained against rotation). The chapter deals also with the modification of the seismic signal at the base of a structure exerted by piles which act as a filter. Some simple rules to understand when it is possible to neglect the filtering effect (and when an interaction analysis should be performed) are furnished.

Chapter 4 examines inertial interaction and its relation with kinematic interaction.

In simple hypotheses it is shown the trend of the ratio inertial/kinematic bending moment at pile cap, discussing about the Code statements on the topic.

Moreover the phase lag between the two interactions is studied, furnishing a simple method to estimate it a priori, in order to establish how to combine inertial and kinematic effects at pile cap.

1 Basic of dynamics

1.1 SINGLE DEGREE OF FREEDOM SYSTEMS

1.1.1 General equation

The simplest model used to predict and quantify the response of any structure under dynamic loading is a single degree of freedom system, in which a rigid mass, M , is connected in parallel to a spring of stiffness K and a dashpot of viscous damping coefficient C , and subjected to some external load, $F(t)$, as shown in Figure 1.1a.

Applying this dynamic load, the tendency for motion is resisted by the inertia of the mass and by forces that develop in the dashpot and spring.

The external load, $F(t)$, acting in the positive x -direction is then opposed by three forces that act in the negative x -direction: the internal force, f_I , the viscous damping force f_D and the elastic spring force f_S (Figure 1.1b).

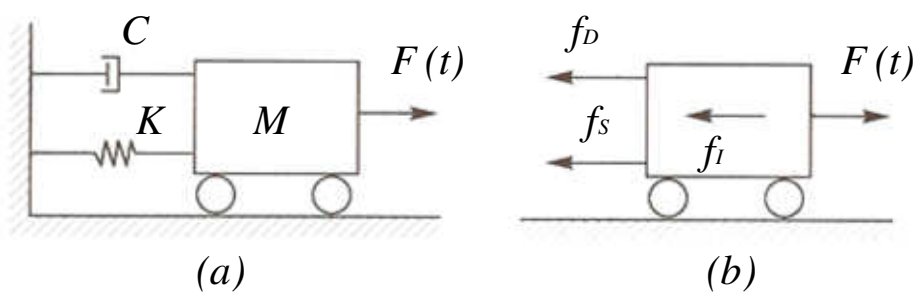


Figure 1.1: SDOF system (adapted from Kramer, 1996).

The equation of motion can be expressed in terms of dynamic equilibrium of these forces:

$$f_I(t) + f_D(t) + f_S(t) = F(t) \quad (1.1)$$

in which, in linear hypotheses:

- $f_i(t)$ is the inertia force, equal to $M\ddot{u}(t)$
- $f_d(t)$ is the force exerted by the viscous damper (which opposes to the motion dissipating energy), equal to $C\dot{u}(t)$
- $f_s(t)$ is the elastic spring force, equal to $Ku(t)$

For earthquake engineering problems, dynamic loading generally results from vibration of the supports of a system, then the equation of motion can be written as:

$$M \cdot \ddot{U}(t) + C \cdot \dot{u}(t) + K \cdot u(t) = 0 \quad (1.2)$$

where $\ddot{U}(t)$ is the total acceleration of the mass, sum of the relative acceleration $\ddot{u}(t)$, and the base acceleration $\ddot{u}_b(t)$. Rearranging,

$$M \cdot \ddot{u}(t) + C \cdot \dot{u}(t) + K \cdot u(t) = -M \cdot \ddot{s}(t) \quad (1.3)$$

1.1.2 Undamped free vibrations

A SDOF system undergoes free vibrations when it oscillates without being acted upon by any external loads. When damping is not present the equation of motion (for undamped free vibration) reduces to:

$$M \cdot \ddot{u}(t) + K \cdot u(t) = 0 \quad (1.4)$$

The solution of the differential equation (with initial conditions $u(0) = u_0$ and $\dot{u}(0) = \dot{u}_0$) is:

$$u(t) = u_0 \cos \omega_0 t + \frac{\dot{u}_0}{\omega_0} \sin \omega_0 t \quad (1.5)$$

where:

$$\omega_0 = \sqrt{\frac{K}{M}} \quad , \quad T_0 = \frac{2\pi}{\omega_0} \quad (1.6)$$

T_0 is the natural period of vibration of the structure. Equation (1.5) can also be written as:

$$u(t) = A \sin(\omega_0 t + \Phi) \quad (1.7)$$

where the Amplitude and Phase angle are given by:

$$A = \sqrt{u_0^2 + \left(\frac{\dot{u}_0}{\omega_0} \right)^2} \quad (1.8)$$

$$\Phi = \tan^{-1} \frac{u_0 \omega_0}{\dot{u}_0} \quad (1.9)$$

The solution to the equation of motion of an undamped system indicates that the response of the system depends on its initial displacement and velocity (Figure 1.2). Note that the amplitude remains constant with time. Because no energy is lost in an undamped system, it will continue to oscillate forever. Obviously, truly undamped systems do not exist in the real world.

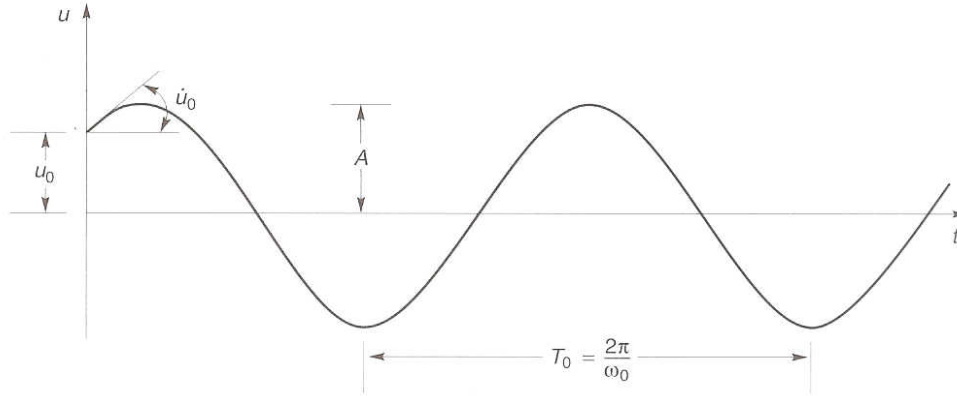


Figure 1.2: Undamped free vibration of a SDOF system (Kramer, 1996).

1.1.3 Damped free vibrations

In real structures, energy may be lost as a result of friction, heat generation, air resistance, and so on. Hence, the amplitude of motion decreases with time. The equation of motion for damped free vibrations is:

$$M \cdot \ddot{u}(t) + C \cdot \dot{u}(t) + K \cdot u(t) = 0 \quad (1.10)$$

Or, rearranging,

$$\ddot{u}(t) + 2\omega_0 \xi \cdot \dot{u}(t) + \omega_0^2 \cdot u(t) = 0 \quad (1.11)$$

where

$$\xi = \frac{C}{2\omega_0 M} = \frac{C}{C_0} \quad (1.12)$$

C_0 is called *critical damping coefficient* and ξ is called, therefore, *damping ratio*.

The solution of the differential equation depends on the value of damping ratio. When $\xi > 1$ the system is *overdamped*, when $\xi = 1$ the system is *critically damped*, while when $\xi < 1$ the system is *underdamped*. In the latter case, that covers civil engineering problems, the solution is:

$$u(t) = e^{-\xi\omega_0 t} \left(u_0 \cos \omega_d t + \frac{\dot{u}_0 + \xi\omega_0 u_0}{\omega_d} \sin \omega_d t \right) \quad (1.13)$$

where:

$$\omega_d = \omega_0 \sqrt{1 - \xi^2} \quad (1.14)$$

is the *damped natural circular frequency* of the structure (Figure 1.3).

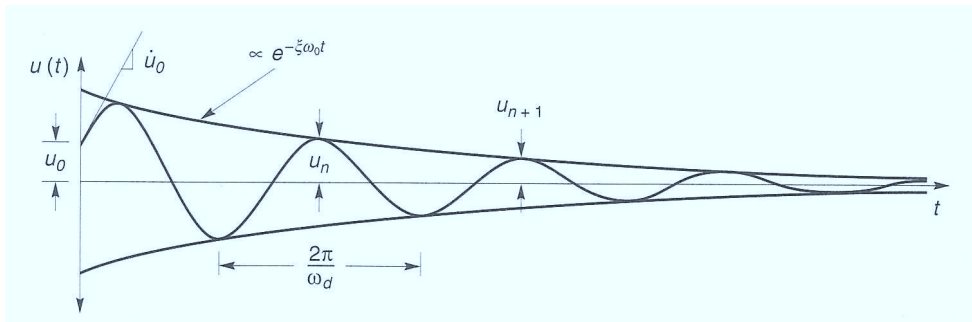


Figure 1.3: Damped free vibration of a SDOF system (Kramer, 1996).

3.2.2 Damped forced vibrations: response to periodic loading

When a SDOF system is excited by a force, the response is governed not only by structural characteristics, but also by force ones. Calling $F(t)$ the periodic loading, the dynamic equilibrium of the system is written as:

$$M \cdot \ddot{u}(t) + C \cdot \dot{u}(t) + K \cdot u(t) = F(t) \quad (1.15)$$

with

$$F(t) = F_0 \sin \bar{\omega} t \quad (1.16)$$

In this case the solution is the sum of a *complementary solution* (for the homogeneous case in which the right side of the equation is 0) and the *particular solution*.

The complementary solution is Equation (1.13), while it can be shown that the particular solution is

$$u_p(t) = \frac{F_0 \cos(\bar{\omega}t - \vartheta)}{K\sqrt{(1-R^2)^2 + (2\xi R)^2}} \quad (1.17)$$

where R is the *tuning ratio* of the system, given by $R = \frac{\bar{\omega}}{\omega_0}$ and ϑ is the phase angle, expressed by the relation

$$\tan \vartheta = \frac{2\xi R}{1-R^2} \quad (1.18)$$

Then,

$$u(t) = e^{-\xi\omega_0 t} \left(u_0 \cos \omega_d t + \frac{\dot{u}_0 + \xi\omega_0 x_0}{\omega_s} \sin \omega_d t \right) + \frac{F_0 \cos(\bar{\omega}t - \vartheta)}{K\sqrt{(1-R^2)^2 + (2\xi R)^2}} \quad (1.19)$$

Note that the complementary solution decays with time, and then describes a transient response (Figure 1.4).

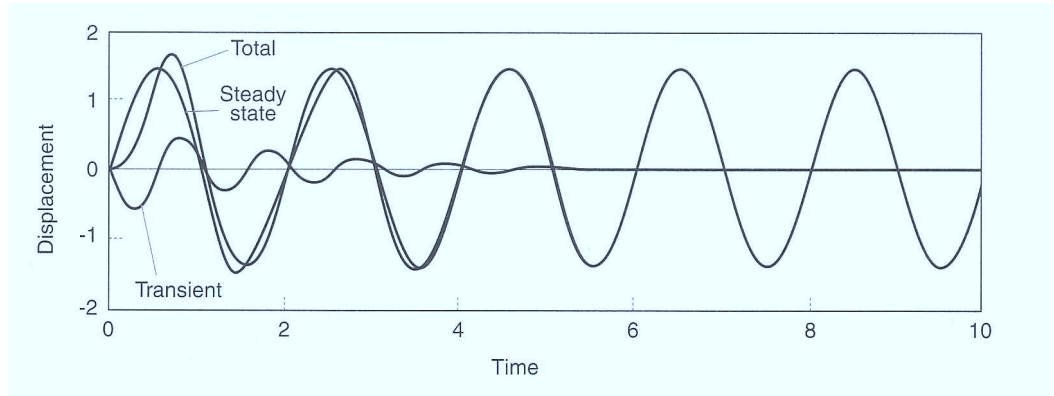


Figure 1.4: Damped forced vibration of a SDOF system (Kramer, 1996).

After this transient response dies out, only the particular solution remains, describing the steady-state response, that is:

$$u(t) = \frac{F_0 \cos(\bar{\omega}t - \vartheta)}{K\sqrt{(1-R^2)^2 + (2\xi R)^2}} \quad (1.20)$$

It can be observed that F_0/K is the displacement the system would have if loaded statically. Then the term

$$M = \frac{1}{\sqrt{(1-R^2)^2 + (2\xi R)^2}} \quad (1.21)$$

represents a *dynamic magnification factor*.

The response can be written as:

$$u(t) = u_{static} \cdot M \cdot \cos(\bar{\omega}t - \vartheta) \quad (1.22)$$

M can be graphed in function of R and ξ :

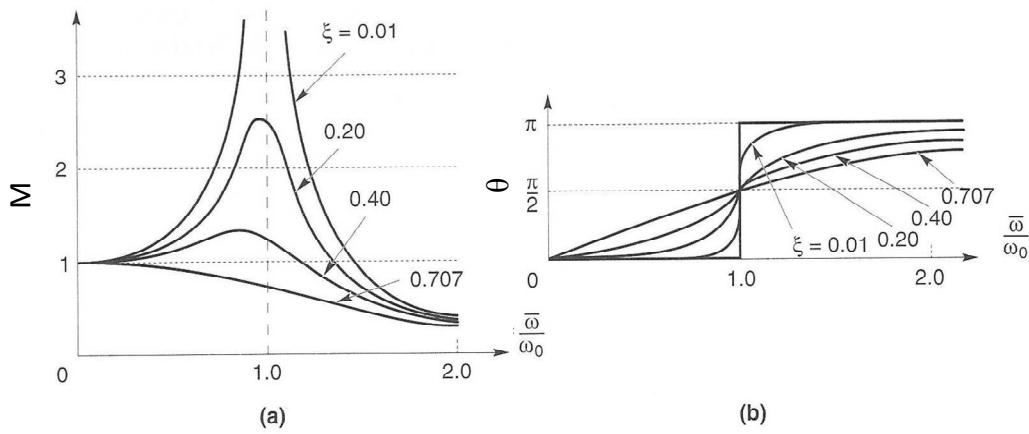


Figure 1.5: Magnification factor and phase angle (adapted from Kramer, 1996).

For $R=1$ there is the *resonance* condition. For zero damping, the dynamic response of the system is infinite.

The parameter ϑ represents the phase lag between the displacement and the force; it is graphed in Figure 1.5b.

For $\bar{\omega} < \omega$ the structure is rigid, or there is a low excitation frequency. Then, the response is practically “static” and the displacement is in-phase with the force. Hence, the elastic reaction equilibrates quite totally every time.

When $\bar{\omega} \cong \omega$ the mass has a phase lag of 90° with respect to F , and the static force is much larger than the force.

When $\bar{\omega} > \omega$ the mass is in opposition with the force and the inertial force equilibrates quite totally the force.

1.1.5 Damped forced vibrations: response to generic loading

A general loading can be thought of as a train of load pulses, each of infinitesimal duration. Through this approach, it is possible to show that:

$$u(t) = -\frac{I}{\omega_d} \int_0^t \ddot{s}(\tau) \cdot e^{-\xi\omega_0(t-\tau)} \sin[\omega_d(t-\tau)] d\tau \quad (1.23)$$

This equation is known as *Duhamel's integral*.

Its application, however, is constrained to linear systems. Later on it will be shown a general method to integrate the equation of motion.

1.1.6 Response spectra

For earthquake-resistant design, the entire time-history of response is not needed. Instead, design may be based only on maximum value of response of a structure to a particular base motion.

The response spectrum describes the maximum response of a SDOF system to a particular input motion as a function of the natural period and damping ratio of the SDOF system. The response may be expressed in terms of acceleration, velocity, or displacement (Figure 1.6).

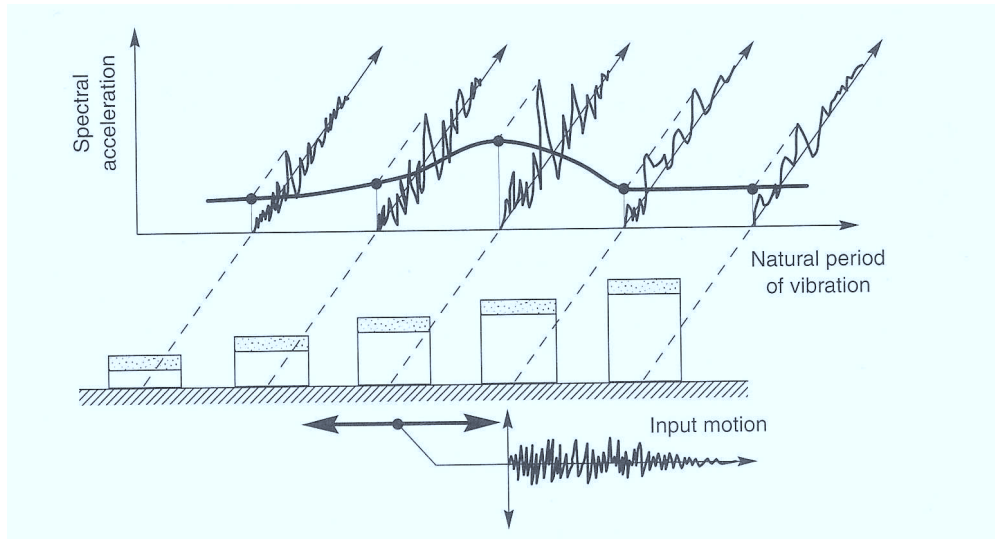


Figure 1.6: Magnification factor and phase angle (Kramer, 1996).

The application of the Duhamel integral to a linear SDOF system produces:

$$S_D = |u(t)|_{max} = \left| \frac{I}{\omega_d} \int_0^t \ddot{s}(\tau) \cdot e^{-\xi \omega_0 (t-\tau)} \sin[\omega_d (t-\tau)] d\tau \right|_{max} \quad (1.24)$$

Velocity and acceleration time histories are proportional (by a factor of ω and ω^2) to displacement one, except for a phase shift (due to the damping). Because the phase shift have not a significant influence on the maximum response values,

$$S_V = |\dot{u}|_{max} \approx \omega_0 S_D = PSV \quad (1.25)$$

$$S_A = |\ddot{u}|_{max} \approx \omega_0^2 S_D = PSA \quad (1.26)$$

PSV and PSA are referred as *pseudospectral velocity* and *pseudospectral acceleration*.

1.2 MULTIPLE DEGREE OF FREEDOM SYSTEMS

1.2.1 General equations

In evaluating the response of a multiple degree of freedom system, the equilibrium must be ensured simultaneously.

Considering an idealised two-story structure with two degrees of freedom (horizontal displacement of the two masses), the equilibrium of the undamped system is expressed as:

$$[M]\{\ddot{u}(t)\} + [K]\{u(t)\} = -[M]\{\ddot{s}(t)\} \quad (1.27)$$

in which $[M]$ is a diagonal matrix containing the masses, while $[K]$, that is full, contains the stiffnesses. For undamped free vibrations,

$$[M]\{\ddot{u}(t)\} + [K]\{u(t)\} = \{0\} \quad (1.28)$$

Assuming that the vector of unknown displacement can be expressed as a vector $\{a\}$, that rules deformed shape, multiplied by a function $\varphi(t)$ that rules its amplitude, the system of equations can be expressed as:

$$([K] - \lambda [M])\{a\} = \{0\} \quad (1.29)$$

A nontrivial solution can be obtained only if

$$\det([K] - \lambda[M]) = 0 \quad (1.30)$$

Equation 1.30 is the *frequency equation* (or *characteristic equation*) of the system, which for a system of N degrees of freedom, gives a polynomial of N th degree in ω^2 . The N roots of the frequency equation represent the frequencies at which the undamped system can oscillate without external force; these frequencies are called *natural circular frequencies* of the system.

Each frequency ω_i is associated with a *mode of vibration* of the system, that is the eigenvector associated with the eigenfrequency ω^2 . The period corresponding to the smallest frequency is called *fundamental period* of the structure (Figure 1.7).

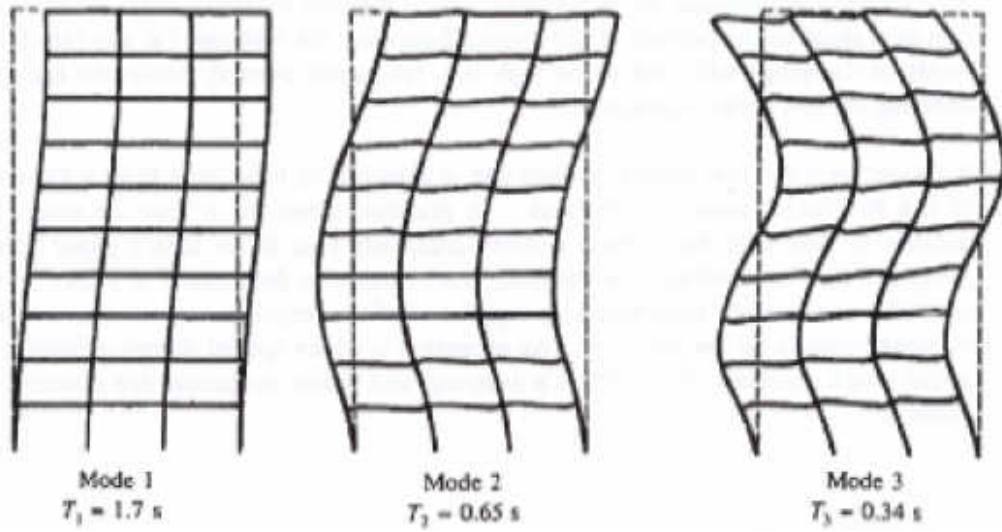


Figure 1.7: First 3 modes of vibration of a MDOF system.

The modes are called “*natural*” because it can be shown that if the system oscillates starting from a *natural mode of vibration*, only the amplitude of motion changes while the deformed shape remains.

For linear structures with certain types of damping, the response in each mode of vibration can be determined independently of the response in other modes.

The independent modal responses can be combined to give the total response. This procedure is called *mode superposition method*.

It can be shown that the equation of motion for the n th mode of vibration can be written as:

$$M_n \ddot{y}_n + C_n \dot{y}_n + K_n y_n = F_n(t) \quad (1.31)$$

where:

$$\begin{aligned} M_n &= \{a_n\}^T [M] \{a_n\} \\ C_n &= \{a_n\}^T [C] \{a_n\} \\ K_n &= \{a_n\}^T [K] \{a_n\} \end{aligned} \quad (1.32)$$

The equation (1.31) is based on the assumption that the damping matrix is orthogonal with respect to the eigenvectors (a diagonal matrix satisfy this condition). For the case of base shaking, the equation of motion can be expressed as:

$$\ddot{y}_n + 2\xi_n \omega_n \dot{y}_n + \omega_n^2 y_n = -\frac{L_n}{M_n} \ddot{s}(t) \quad (1.33)$$

where

$$L_n = \sum_{j=1}^N M_j a_{jn} \quad (1.34)$$

ξ_n is the damping ratio relative and $-L_n / M_n$ is called participation factor of the n^{th} mode. Then the total displacement is obtained by superposition of the modal contributions:

$$\{u(t)\} = \sum_{j=1}^N \{a_j\} y_j(t) \quad (1.35)$$

1.2.2 Combination of modal contributes

It's important to notice that, if each modal contribute is evaluates with reference to its maximum effect through response spectra, it is not possible to sum all contributes relative to different significant modes, as maxima do not occur at the same time step.

A general rule is to obtain the maximum effect in a section Ω as square root of the sum of squares of single modal contributes:

$$E(\Omega) = \sqrt{E_1^2(\Omega) + E_1^2(\Omega) + \dots + E_n^2(\Omega)} \quad (1.36)$$

This rule can be applied only if different modes have not a too close frequency ($\omega_i < 0.9\omega_{i+1}$), otherwise different techniques may be used (for instance CQC).

1.3 NUMERICAL EVALUATION OF DYNAMIC RESPONSE: NEWMARK METHOD

1.3.1 Basic procedure

In 1959, N. M. Newmark developed a family of time-stepping methods based on the following equations:

$$u_{i+1} = u_i + \Delta t \dot{u}_i + \frac{\Delta t^2}{2} \left[(1-2\beta) \ddot{u}_i + 2\beta \ddot{u}_{i+1} \right] \quad (1.37)$$

$$\dot{u}_{i+1} = \dot{u}_i + \Delta t \left[(1-\gamma) \ddot{u}_i + 2\gamma \ddot{u}_{i+1} \right] \quad (1.38)$$

The parameters β and γ define the variation of acceleration over a time step and determine the stability and accuracy characteristics of the method.

Newmark method can be applied in different ways, for example with the following procedure:

- Calculation of predictors of displacement and velocity at step $i+1$ (note that only quantities at step i are required):

$$\tilde{u}_{i+1} = u_i + \Delta t \dot{u}_i + \frac{\Delta t^2}{2} (1-2\beta) \ddot{u}_i \quad (1.39)$$

$$\tilde{\dot{u}}_{i+1} = \dot{u}_i + \Delta t (1-\gamma) \ddot{u}_i \quad (1.40)$$

- Calculation of “exact” acceleration at step $n+1$:

$$\ddot{u}_{i+1} = \left(M + \gamma \Delta t C + \beta \Delta t^2 K \right)^{-1} \left(F_{i+1} - C \tilde{\dot{u}}_{i+1} - K \tilde{u}_{i+1} \right) \quad (1.41)$$

- Upgrading of predictors to obtain “exact” values of displacement and velocity at step $i+1$:

$$u_{i+1} = \tilde{u}_{i+1} + \beta \Delta t^2 \ddot{u}_{i+1} \quad (1.42)$$

$$\dot{u}_{i+1} = \tilde{\dot{u}}_{i+1} + \gamma \Delta t \ddot{u}_{i+1} \quad (1.43)$$

The formula used to obtain the acceleration at step $n+1$ results in an implicit or explicit scheme:

$$\begin{aligned}\beta = 0 &\Rightarrow \ddot{x}_{n+1} = (M + \gamma \Delta t C)^{-1} (F_{n+1} - \dots) & (\text{explicit}) \\ \beta \neq 0 &\Rightarrow \ddot{x}_{n+1} = (M + \gamma \Delta t C + \beta \Delta t^2 K)^{-1} (F_{n+1} - \dots) & (\text{implicit})\end{aligned}\tag{1.44}$$

1.3.2 Stability and computational error

Newmark's method is stable if:

$$\frac{\Delta t}{T_n} \leq \frac{1}{\pi\sqrt{2}} \frac{1}{\sqrt{\gamma - 2\beta}}\tag{1.45}$$

where T_n is the period of the structure.

Numerical procedures that lead to bounded solutions if the time step is shorter than some stability limit are called conditionally stable procedures. Procedures that lead bounded solutions regardless of the time-step length are called unconditionally stable procedures. The average acceleration method (it can be shown that it corresponds to Newmark parameters set to $\gamma = 1/2$ $\beta = 1/4$) is unconditionally stable. The linear acceleration method ($\gamma = 1/2$ $\beta = 1/6$) is stable if $\Delta t/T_n < 0.551$. The stability criteria are not restrictive (i.e., they do not dictate the choice of time step) in the analysis of SDOF systems because $\Delta t/T_n$ must be considerably smaller than the stability limit to ensure adequate accuracy in the numerical results.

Stability of the numerical method is important, however, in the analysis of MDOF systems, where it is often necessary to use unconditionally stable methods.

About the computational error, it is inherent in any numerical solution of the equation of motion.

Considering the free vibration problem

$$M\ddot{u} + Ku = 0\tag{1.45}$$

it is solved by four numerical methods. The numerical results obtained using $\Delta t/T_n = 0.1$ are compared with the theoretical solution in Figure 1.8. This comparison shows that some numerical methods may predict that the displacement amplitude decays with time, although the system is undamped, and that the natural period is elongated or shortened.

Figure 1.9 shows the amplitude decay AD and period elongation PE in the four numerical methods as a function of $\Delta t/T_n$. Three of the methods predict no decay of displacement amplitude. Wilson's method contains decay of amplitude, however, implying that this method introduces numerical damping in the system. For $\Delta t/T_n$ less than its stability limit, the linear acceleration method gives the least period elongation. This property, combined with no amplitude decay, make this method the most suitable method (of the presented ones) for SDOF systems, but, as already said, not for MDOF systems because of stability.

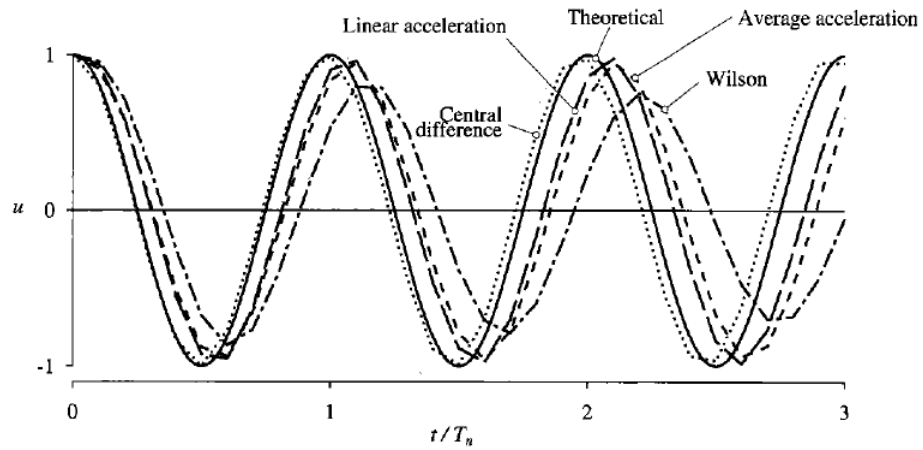


Figure 1.8: Free vibration solution by 4 numerical methods ($\Delta t/T_n=0.1$) and the theoretical solution (Chopra, 1995).

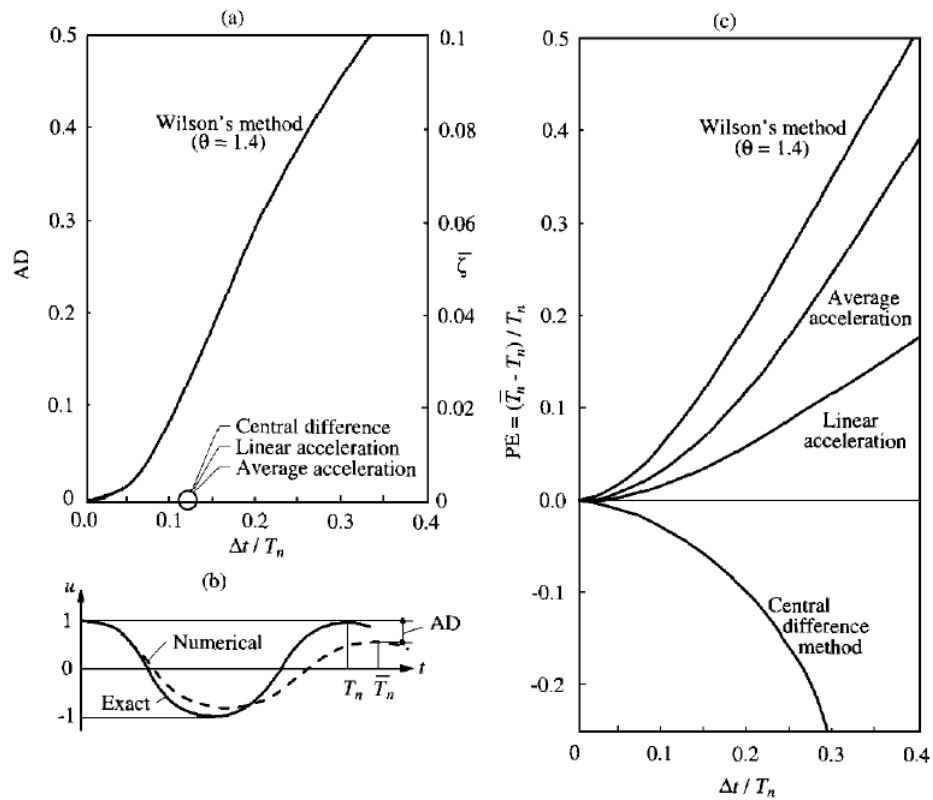


Figure 1.9: (a) Amplitude decay versus $\Delta t/T_n$; (b) definition of AD and PE; (c) Period elongation versus $\Delta t/T_n$ (Chopra, 1995).

1.4 CONTINUOUS SYSTEMS

1.4.1 Frequency domain analysis

It appears appropriate to introduce the basic procedure of a frequency domain analysis to better understand the content of the thesis.

A signal $X(t)$, defined in the time domain, whose duration is T_0 (for example a seismic record), even if extremely irregular can be made periodic (with period T_0) repeating it indefinitely in the time.

This allows to decompose it in *Fourier series*, that's to say the sum of an infinite number of harmonic functions of variable frequency (the smallest one is $f_0 = 1/T_0$):

$$X(t) = A_0 + \sum_{n=1}^{\infty} A_n \sin(2\pi n f_0 t + \varphi_n) \quad (1.46)$$

where A_0 is the mean value of the signal, A_n and φ_n are the amplitude and phase of the harmonic whose frequency is $f_n = n f_0$.

Amplitude and phase of each harmonic define a complex variable $X(f)$ and represent the *Fourier transform* of $X(t)$ from time to frequency domain.

The complex function $X(f)$ can be expressed as:

$$X(f) = \int_{-\infty}^{+\infty} X(t) e^{-j2\pi f t} dt \quad (1.47)$$

whose real part (R) and imaginary part (I) can be combined to give the amplitude and the phase of the different harmonics:

$$A(f) = \sqrt{R^2(f) + I^2(f)} \quad \varphi(f) = \tan^{-1} \left[\frac{I(f)}{R(f)} \right] \quad (1.48)$$

To come back in the time domain, it can be used the *inverse Fourier transform*:

$$X(t) = \int_{-\infty}^{+\infty} X(f) e^{j2\pi f t} df \quad (1.49)$$

To solve the above integrals, some numerical techniques are used operating on discrete signals, through algorithms called *FFT* (*Fast Fourier Transform*) and *IFFT* (*Inverse Fast Fourier Transform*).

1.4.2 One-dimensional ground response analysis

The analysis of continuous system is carried out here with reference to soil dynamics, considering the case of an uniform and damped soil layer (of height H) on rigid rock in one-dimensional conditions.

The dynamic equilibrium can be written as:

$$\rho \frac{\partial^2 u}{\partial t^2} = G \frac{\partial^2 u}{\partial z^2} + \eta \frac{\partial^3 u}{\partial t \partial z^2} \quad (1.50)$$

where ρ is the soil density and η is the viscosity coefficient for a *Kelvin-Voigt model*.

Applying the definition of damping coefficient this model, it can be shown that for an harmonic excitation:

$$\xi = \frac{\eta \omega}{2G} \quad (1.51)$$

Imposing the solution in the form $u(z, t) = p(z)e^{i\omega t}$, the equilibrium equation is written as:

$$(G + i\omega\eta) \frac{\partial^2 p}{\partial z^2} + \rho \omega^2 p = 0 \quad (1.52)$$

Introducing the *complex shear modulus* G^* , the *complex wavenumber* k^* and the *complex shear wave velocity* V_s^* :

$$G^* = G + j\omega\eta = G(1 + 2jD) \quad (1.53)$$

$$k^* = \frac{\omega}{V_s^*} = \frac{\omega}{\sqrt{\frac{G^*}{\rho}}} \quad (1.54)$$

it would be simple to show that the solution of the differential equation (1.50) is:

$$p(z) = Ae^{ik^*z} + Be^{-ik^*z} \quad (1.55)$$

and then the horizontal displacement is:

$$u(z, t) = Ae^{i(k^*z + \omega t)} + Be^{-i(k^*z - \omega t)} \quad (1.56)$$

The constants A and B represent the amplitudes of waves travelling in the $-z$ and $+z$ directions. At free-field surface ($z=0$) the shear stress (and then the shear strain) must be zero, that is:

$$\frac{\partial u(0,t)}{\partial z} = 0 \quad (1.57)$$

Substituting (1.56) in (1.57) gives $A=B$. Then the displacement can be expressed as:

$$u(z,t) = 2A \frac{e^{ik^*z} + e^{-ik^*z}}{2} e^{i\omega t} = 2A \cos(k^*z) e^{i\omega t} \quad (1.58)$$

Which describes a *standing wave* of amplitude $2A \cos(kz)$. The standing wave is produced by the *constructive interference* of the upward and downward travelling waves and has a fixed shape with respect to depth (Figure 1.10).

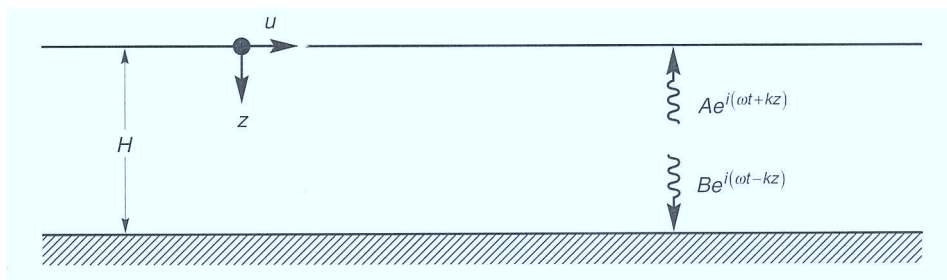


Figure 1.10: Linear elastic soil deposit of thickness H underlain by rigid bedrock. (Kramer, 1996).

Equation (1.58) can be used to define a *transfer function* which describes the ratio of displacement amplitudes at any two points in the soil layer.

Choosing as points the top and the bottom (bedrock) of the soil, the transfer function is written as:

$$H(\omega) = \frac{1}{\cos[k^*(1-i\xi)H]} = \frac{1}{\cos(k^*H - i\xi k^*H)} \quad (1.59)$$

The *amplification function* (from bedrock to surface), defined as the amplitude of the relative transfer function, is:

$$A(\omega) = \frac{1}{\sqrt{\cos^2(k^*H) + \sinh^2(\xi k^*H)}} \approx \frac{1}{\sqrt{\cos^2(k^*H) + (\xi k^*H)^2}} \quad (1.60)$$

As $|\ddot{u}| = \omega |\dot{u}| = \omega^2 u$, $A(\omega)$ is also the acceleration (and velocity) amplification function.

The frequencies that correspond to the local maxima are the *natural frequencies* of the soil deposit. The variation of the amplification factor with frequency is shown for different levels of damping in Figure 1.11. The n th natural frequency of the deposit is given by:

$$\omega_n \approx \frac{V_s}{H} (2n-1) \pi / 2 \quad (1.61)$$

while the maximum values are:

$$A_{\max,n} \approx \frac{2}{(2n-1)\pi\xi} \quad (1.62)$$

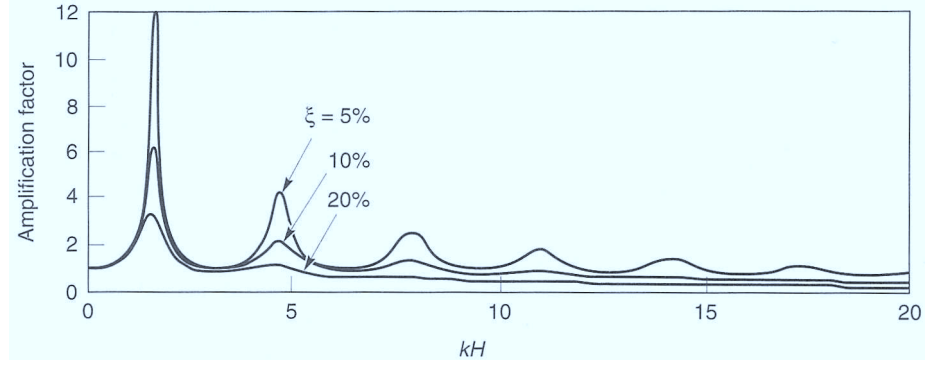


Figure 1.11: Influence of frequency on steady-state response of damped, linear elastic deposit on rigid rock (Kramer, 1996).

2 Basic of finite elements

2.1 OVERVIEW

The finite element method has a wide range of engineering applications. This chapter presents only a basic outline of the method, restricted to linear elastic two dimensional plane strain conditions (for simplicity). Only continuum elements are considered and attention is focussed on the 'displacement based' finite element approach.

The finite element method involves the following steps (Potts and Zdravkovic, 1995).

Element discretisation: this is the process of modelling the geometry of the problem under investigation by an assemblage of small regions, termed finite elements. These elements have nodes defined on the element boundaries, or within the element.

Primary variable approximation: a primary variable must be selected (e.g. displacements, stresses etc.) and rules as to how it should vary over a finite element established. This variation is expressed in terms of nodal values. In geotechnical and structural engineering it is usual to adopt displacements as the primary variable.

Element equations: use of an appropriate variational principle (e.g. Minimum potential energy) to derive element equations:

$$[K_E]\{\Delta d_E\} = \{\Delta R_E\} \quad (2.1)$$

where $[K_E]$ is the element stiffness matrix, $\{\Delta d_E\}$ is the vector of incremental element nodal displacements and $\{\Delta R_E\}$ is the vector of incremental element nodal forces. Global equations

Combine element equations to form global equations:

$$[K_G]\{\Delta d_G\} = \{\Delta R_G\} \quad (2.2)$$

where $[K_G]$ is the global stiffness matrix, $\{\Delta d_G\}$ is the vector of all incremental nodal displacements and $\{\Delta R_G\}$ is the vector of all incremental nodal forces.

Boundary conditions: Formulate boundary conditions and modify global equations.

Loadings: forces affect $\{\Delta R_G\}$, while displacements affect $\{\Delta d_G\}$.

Solve the global equations: The global Equations (2.2) are in the form of a large number of simultaneous equations. These are solved to obtain the displacements $\{\Delta d_G\}$ at all the nodes. From these nodal displacements secondary quantities, such as stresses and strains, are evaluated.

2.2 ELEMENT DISCRETISATION

The geometry of problem under investigation must be defined. Of course, simplifications and approximations may be necessary during this process. This geometry is then replaced by an equivalent element mesh which is composed of small regions called finite elements. Their geometry is specified in terms of the coordinates of keypoints on the element called nodes.

For elements with straight sides these nodes are usually located at the element corners. If the elements have curved sides then additional nodes, usually at the midpoint of each side, must be introduced.

In order to refer to the complete finite element mesh, the elements and nodes must be numbered in systematic manner. To describe the location of an element in the mesh, an element connectivity list has used. This list contains the node numbers in the element, usually in an anticlockwise order. When constructing the finite element mesh the geometry of the problem must be approximated as accurately as possible. For linear material behaviour the procedure is relatively straightforward and only the zones where unknowns vary rapidly need special attention. In order to obtain accurate solutions, these zones require a refined mesh of smaller elements; a mesh of regular shaped elements will give the best results and elements with widely distorted geometries or long thin elements should be avoided.

2.3 DISPLACEMENT APPROXIMATION

In the displacement based finite element method the primary unknown quantity is the displacement field which varies over the problem domain. Stresses and strains are treated as secondary quantities which can be found from the displacement field once it has been determined. In two dimensional plane strain situations, for example, the displacement field is characterised by the two global displacements u and v , in the x and y coordinate directions respectively.

The main approximation in the finite element method is to assume a particular form for the way these displacement components vary over the domain under investigation. Clearly, this assumed variation must satisfy the conditions of compatibility. Over each element the displacement components are assumed to have a simple polynomial form, where the order of the polynomial depends on the number of nodes in the element. The displacement components are then expressed in terms of their values at the nodes. For example, consider the displacement equations for the three element noded triangular element shown in Figure 2.1:

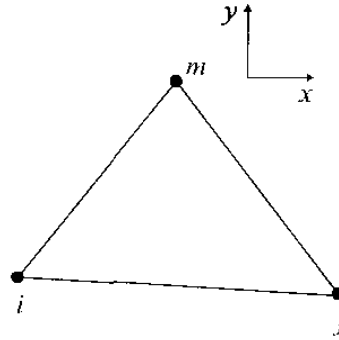


Figure 2.1: 3-node element (Potts and Zdravkovic, 1995)

$$\begin{aligned} u &= a_1 + a_2x + a_3y \\ v &= b_1 + b_2x + b_3y \end{aligned} \quad (2.3)$$

The six constants $a_1, a_2, a_3, b_1, b_2, b_3$ can be expressed in terms of the nodal displacements by substituting the nodal coordinates into the above equations, and then solving the two sets of three simultaneous equations which arise:

$$\begin{aligned} u_i &= a_1 + a_2x_i + a_3y_i \\ u_j &= a_1 + a_2x_j + a_3y_j \\ u_m &= a_1 + a_2x_m + a_3y_m \\ v_i &= b_1 + b_2x_i + b_3y_i \\ v_j &= b_1 + b_2x_j + b_3y_j \\ v_m &= b_1 + b_2x_m + b_3y_m \end{aligned} \quad (2.4)$$

The above simultaneous equations are solved for $a_1, a_2, a_3, b_1, b_2, b_3$ in terms of the nodal displacements to give:

$$\begin{Bmatrix} u \\ v \end{Bmatrix} = [N] \begin{Bmatrix} u \\ v \end{Bmatrix}_{nodes} \quad (2.5)$$

where the matrix $[N]$ is known as the matrix of shape functions. The displacement components u and v are now expressed in terms of their values at the nodes.

The accuracy of a finite element analysis depends on the size of the elements and the nature of the displacement approximation. For the accuracy to increase as the elements become smaller, the displacement approximation must satisfy the following compatibility conditions.

- Continuity of the displacement field. In order to avoid gaps or overlaps occurring when the domain is loaded, the displacement components must vary continuously within each element and across each element side. This can be achieved by ensuring that the displacements on an element side depend only on the displacements of the nodes situated on that side;

- The displacement approximation should be able to represent rigid body movement. Examples of such movements are translations and rotations. Such displacements do not induce strains in an element.

- The displacement approximation should be able to represent constant strain rates.

The simple polynomial approximation presented above satisfies these compatibility conditions.

The essential feature of the element-wise approximation is that the variation of the unknown displacements within an element is expressed as a simple function of the displacements at the nodes. The problem of determining the displacement field throughout the finite element mesh is, therefore, reduced to determining the displacement components at a finite number of nodes. These nodal displacements are referred to as the unknown degrees of freedom. For two dimensional plane strain problems there are two degrees of freedom at each node: the u and v displacements.

The *global element* is derived from a *parent element* which element has the same number of nodes, but is defined with respect to a natural coordinate system. Figure 2.2 shows the configuration of the parent element.

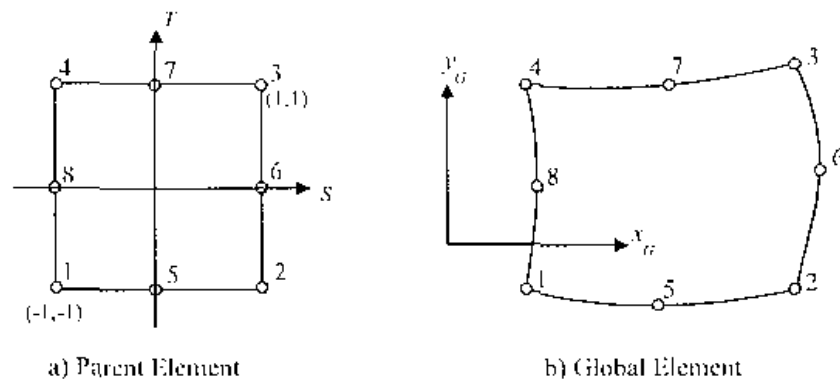


Figure 2.2: Isoparametric element (Potts and Zdravkovic, 1995)

The natural coordinates S, T for this element satisfy the conditions $-1 < S < 1, -1 < T < 1$.

The basic procedure in the isoparametric finite element formulation is to express the element displacements and element geometry in terms of interpolation functions using the natural coordinate system. The term isoparametric arises from the fact that the parametric description used to describe the variation of the unknown displacements within an element is exactly the same as that used to map the geometry of the element from the *global axes* to the *natural axes*.

For the element shown in Figure 2.2 the global coordinates of a point in the element can be expressed by coordinate interpolations of the form:

$$x = \sum_{i=1}^8 N_i x_i \quad ; \quad y = \sum_{i=1}^8 N_i y_i \quad (2.6)$$

where x_i and y_i are the global coordinates of the eight nodes in the element, and N_i are called interpolation functions. For isoparametric elements the interpolation functions are expressed in terms of the natural coordinates S and T which vary from -1 to +1. To construct the interpolation functions for the eight noded isoparametric element, the following properties are used.

Firstly, there is one interpolation function corresponding to each node in the element and each function is quadratic in the natural coordinates S and T .

Secondly, the interpolation function N_1 , is equal to 1 at node 1 ($S = -1, T = -1$) and is equal to zero at the other seven nodes; a similar relation holds for the other interpolation functions. Using these properties it can be shown that the interpolation functions take the form:

$$\begin{aligned} N_5 &= \frac{1}{2}(1-S^2)(1-T) & N_1 &= \frac{1}{4}(1-S)(1-T) - \frac{1}{2}N_5 - \frac{1}{2}N_8 \\ N_6 &= \frac{1}{2}(1+S)(1-T^2) & N_2 &= \frac{1}{4}(1+S)(1-T) - \frac{1}{2}N_5 - \frac{1}{2}N_6 \\ N_7 &= \frac{1}{2}(1-S^2)(1+T) & N_3 &= \frac{1}{4}(1+S)(1+T) - \frac{1}{2}N_6 - \frac{1}{2}N_7 \\ N_8 &= \frac{1}{2}(1-S)(1-T^2) & N_4 &= \frac{1}{4}(1-S)(1+T) - \frac{1}{2}N_7 - \frac{1}{2}N_8 \end{aligned} \quad (2.7)$$

Since the element is isoparametric, the displacements within the element are interpolated in the same way as the geometry. Consequently, the displacements within the 8 noded isoparametric element are also assumed to be quadratic in S and T .

The main advantage of the isoparametric formulation is that the element equations need only be evaluated in the parent element coordinate system. Thus, for each element in the mesh the stiffness matrix integrals can be evaluated by a standard procedure. The integrations need only be performed over a square, with S and T varying between -1 and +1.

For all types of finite elements the best results are obtained if the elements have reasonable shapes. Wildly distorted elements may lead to different forms of inaccuracy.

2.4 ELEMENT EQUATIONS

Element equations are those that govern the deformational behaviour of each element. They essentially combine the compatibility, equilibrium and constitutive conditions.

Displacements: As noted above, the chosen displacements are assumed to be given by:

$$\{\Delta d\} = \begin{Bmatrix} \Delta u \\ \Delta v \end{Bmatrix} = [N] \begin{Bmatrix} \Delta u \\ \Delta v \end{Bmatrix}_n = [N] \{\Delta d\}_n \quad (2.8)$$

Strains: The strains corresponding to these displacements are:

$$\begin{aligned}\Delta\epsilon_x &= -\frac{\partial(\Delta u)}{\partial x} ; \Delta\epsilon_y = -\frac{\partial(\Delta v)}{\partial y} ; \Delta\gamma_{xy} = -\frac{\partial(\Delta u)}{\partial y} - \frac{\partial(\Delta v)}{\partial x} \\ \Delta\epsilon_z &= \Delta\gamma_{xz} = \Delta\gamma_{yz} = 0 ; \{\Delta\epsilon\}^T = \{\Delta\epsilon_x \Delta\epsilon_y \Delta\gamma_{xy} \Delta\epsilon_z\}^T\end{aligned}\quad (2.9)$$

Combining the two above equations:

$$\begin{Bmatrix} \Delta\epsilon_x \\ \Delta\epsilon_y \\ \Delta\gamma_{xy} \\ \Delta\epsilon_z \end{Bmatrix} = - \begin{bmatrix} \frac{\partial N_1}{\partial x} & 0 & \frac{\partial N_2}{\partial x} & 0 & \dots & \dots & \frac{\partial N_n}{\partial x} & 0 \\ 0 & \frac{\partial N_1}{\partial y} & 0 & \frac{\partial N_2}{\partial y} & \dots & \dots & 0 & \frac{\partial N_n}{\partial y} \\ \frac{\partial N_1}{\partial y} & \frac{\partial N_1}{\partial x} & \frac{\partial N_2}{\partial y} & \frac{\partial N_2}{\partial x} & \dots & \dots & \frac{\partial N_n}{\partial y} & \frac{\partial N_n}{\partial x} \\ 0 & 0 & 0 & 0 & \dots & \dots & 0 & 0 \end{bmatrix} \begin{Bmatrix} \Delta u_1 \\ \Delta v_1 \\ \Delta u_2 \\ \Delta v_2 \\ \dots \\ \dots \\ \Delta u_n \\ \Delta v_n \end{Bmatrix}\quad (2.10)$$

That's to say:

$$\{\Delta\epsilon\} = [B]\{\Delta d\}_n \quad (2.11)$$

where the matrix $[B]$ contains only derivatives of the shape functions N_i while $\{\Delta d\}_n$ contains the list of nodal displacements for a single element.

Using isoparametric elements N_i , depend only on the natural coordinates S and T . Consequently, the global derivatives in Equation (2.10) cannot be determined directly. However, using the chain rule which relates the x, y derivatives to the S, T derivatives gives

$$\left\{ \frac{\partial N_i}{\partial S} \quad \frac{\partial N_i}{\partial T} \right\}^T = [J] \left\{ \frac{\partial N_i}{\partial x} \quad \frac{\partial N_i}{\partial y} \right\}^T \quad (2.12)$$

$$[J] = \begin{bmatrix} \frac{\partial x}{\partial S} & \frac{\partial y}{\partial S} \\ \frac{\partial x}{\partial T} & \frac{\partial y}{\partial T} \end{bmatrix} \quad (2.13)$$

Constitutive model: it can be written as:

$$\{\Delta\sigma\} = [D]\{\Delta\varepsilon\} \quad (2.14)$$

where $[D]$ is the elastic constitutive matrix.

To determine the element equations, the principle of minimum potential energy is invoked. It states that:

$$\delta\Delta E = \delta\Delta W - \delta\Delta L = 0 \quad (2.15)$$

Its application (omitted), leads to:

$$\sum_{i=1}^N [K_E]_i (\{\Delta d\}_n)_i = \sum_{i=1}^N \{\Delta R_E\} \quad (2.16)$$

where

$$[K_E] = \int_{Vol} [B]^T [D][B] dVol \text{ is the element stiffness matrix, and}$$

$$\{\Delta R_E\} = \int_{Vol} [N]^T \{\Delta F\} dVol + \int_{Srf} [N]^T \{\Delta T\} dSrf \text{ accounts for body and surface loads}$$

Thus the problem is reduced to determining and summing the separate element equilibrium equations:

$$[K_E]\{\Delta d\}_n = \{\Delta R_E\} \quad (2.17)$$

The element stiffness matrix for isoparametric elements is evaluated using the natural coordinate system. The isoparametric coordinate transformation gives:

$$dVol = t dx dy = t |J| dS dT \quad (2.18)$$

where for plane strain problems the thickness t is unity and the element stiffness matrix becomes:

$$[K_E] = \int_{-1}^1 \int_{-1}^1 [B]^T [D][B] |J| dS dT \quad (2.19)$$

The explicit evaluation of Equation (2.19) cannot usually be performed, except for very special element shapes. It is therefore convenient to use a numerical integration procedure.

2.5 NUMERICAL INTEGRATION

To evaluate the element stiffness matrix and right hand side vector, integrations must be performed.

Essentially, the integral of a function is replaced by a weighted sum of the function evaluated at a number of *integration points* x_i (sampling points), each of these combined with a specific weight W_i .

$$\int_{-1}^1 f(x)dx = \sum_{i=1}^N f(x_i)W_i \quad (2.20)$$

The values of the weights, W_i , and the location of the integration points, depend on the nature of the integration scheme being used. The number of integration points determines the integration order. The higher order of integration gives the more accurate integration process. Unfortunately, the number of function evaluations also depends on the integration order, so the cost of an analysis will increase when a higher order integration is employed.

The most common numerical integration scheme is Gaussian integration and the integration points are often referred to as *Gauss points*. For Gaussian integration the optimum integration order depends on the type of element being used and on its shape. Experience has shown that for the 8 noded isoparametric element either a 2x2 or a 3x3 order should be used. 2x2 and 3x3 integration orders are often referred to as *reduced* and *full* integration, respectively.

2.6 GLOBAL EQUATIONS AND EVALUATION OF STRESSES AND STRAINS

Once one has assembled the global stiffness matrix, the global equations are:

$$[K_G]\{\Delta d\}_{nG} = \{\Delta R_G\} \quad (2.21)$$

From the displacements, it is possible to obtain strains, and then stresses.

3 Kinematic interaction

The equations of motion of a complete soil-foundation-structure system can be expressed in the form (Kramer, 1996):

$$[M]\{\ddot{u}\} + [K^*]\{u\} = -[M]\{\ddot{u}_b(t)\} \quad (3.1)$$

where $[M]$ is the *mass matrix*, and

$$[K^*] = [K] + i\omega[C] \quad (3.2)$$

is the *complex stiffness matrix*; $\{\ddot{u}_b(t)\}$ is the vector containing motion at the nodal points of the base.

To introduce what has to be intended as kinematic interaction (and consequently inertial interaction), it is helpful to consider two extreme cases.

In the first case, it is assumed that only soil has mass, while the foundation and the superstructure (in the following named as structure) have stiffness but no mass. Under these assumptions, the equations of motion become:

$$[M_{soil}]\{\ddot{u}_{KI}\} + [K^*]\{u_{KI}\} = -[M_{soil}]\{\ddot{u}_b(t)\} \quad (3.3)$$

where $[M_{soil}]$ is the soil mass matrix (being the structure massless) and $\{\ddot{u}_{KI}\}$ is the *foundation input motion*. Once solved eq. (3.3), the motion experienced by the foundation in absence of a structural mass are available. Such motion represent the *kinematic interaction* between different elements. In must be noted that the term $[K^*]$ is the complex stiffness of the whole system (soil and structure); it follows that the structure influences anyhow kinematic interaction by its stiffness.

The second case is that in which the structure (superstructure and foundation) and the soil have both mass and stiffness. If the superstructure is excited by a foundation input motion, inertial forces due to its mass rise up (*inertial interaction*). Such inertial forces could vary if the soil-foundation system, as it is, is not rigid. In other terms, the deformation of the superstructure is different from the case in which it has a fixed base. Assuming that the soil has no mass, the equations of motion become:

$$[M]\{\ddot{u}_{II}\} + [K^*]\{u_{II}\} = -[M_{structure}]\{\ddot{u}_{KI}(t) + \ddot{u}_b(t)\} \quad (3.4)$$

where $[M_{structure}]$ is the mass matrix (superstructure and foundation). The right side of the above equation represents the inertial loading only on the structure-foundation system; it follows that inertial loading depends also on kinematic interaction through $\{\ddot{u}_{KI}(t)\}$.

By assuming linear elastic behaviour for all the components (soil, foundation, superstructure), it is possible to consider superposition method, that means to add eqs. (3.3) and (3.4):

$$\begin{aligned} [M_{soil}]\{\ddot{u}_{KI}\} + [M]\{\ddot{u}_{II}\} + [K^*](\{u_{KI}\} + \{u_{II}\}) = \\ = -([M_{soil}] + [M_{structure}])\{\ddot{u}_b\} - [M_{structure}]\{\ddot{u}_{KI}\} \end{aligned} \quad (3.5)$$

Since $\{u_{KI}\} + \{u_{II}\} = \{u\}$ and $[M_{soil}] + [M_{structure}] = [M]$, the original eq. (3.1) comes out.

It must be also noted is also possible to consider the mass of the foundation in kinematic interaction instead of inertial one; in any case, their sum gives the original equations of motion.

From all above it can be concluded that is possible to separate kinematic interaction from inertial interaction only if the hypotheses of linear elastic behaviour of the components is valid¹, meaning that the effects of kinematic and inertial interaction coming from separate analysis carried out under different hypotheses cannot be added.

3.1 LITERATURE REVIEW

Pile damage due to earthquakes has been observed in numerous post-earthquake investigations (Ross et al., 1969; Margason, 1975; CNEL-ENEL, 1976; Okamoto, 1983; Nishizawa et al., 1984; EEFIT, 1986). Mizuno (1987) reported 28 cases involving seismic failures of piles in Japan. More recently, pile damage was observed in the Loma Prieta earthquake (1989) and particularly in the Kobe earthquake (1995). Identified or suspected causes of failure in the above cases include:

- large pile movements due to liquefaction and subsequent lateral soil spreading
- excessive bending and shear forces transmitted to the piles from the superstructure
- bending due to vibratory deformations induced by the passage of seismic waves through the soil.

Support for the third scenario comes from the fact that damage has often been observed too deep to have been caused by loading coming from the pile top, in soils that could not possibly have suffered a severe loss of strength (e.g. liquefaction).

¹ For pile foundations, it is necessary to invoke also that the structural elements connecting pile head is rigid in order to possibly refer to the only inertial load resultant, so that the superstructure doesn't exert any influence on kinematic interaction.

Analytical and field evidence (Dobry & O'Rourke, 1983; Mizuno, 1987; Tazoh et al., 1987) have associated this type of damage with the presence of strong discontinuities in strength and, especially, stiffness in the soil profile. The most likely cause is the relatively large curvatures imposed to the piles by the surrounding soil, as it deforms while excited by propagating seismic waves. The reason is that soil shear strain is discontinuous across interfaces because of the different shear moduli between the layers, and thereby the associated soil curvature (the derivative of strain) is infinite. Accordingly, this type of distress is called kinematic, to distinguish it from the inertial distress due to head loading deriving from the inertia forces caused by structure vibrations.

About the *kinematic interaction*, a lot of efforts come from literature; a brief excursus of main contributions is therefore presented below.

3.1.1 *Modification of motion parameters*

In one-dimensional free-field conditions, a vertically incident S wave induces only horizontal displacements. A cylindrical pile diffracts the incident and reflected vertical waves, thereby modifying the free wave field. As a consequence, the horizontal displacement of pile cap is different from the surface free-field motion and, in addition, the pile top experiences a *rotation*.

Gazetas (1984) introduced the displacement and rotation *kinematic interaction factors*, defined as:

$$I_u = \frac{|u_p|}{u_{ff}} \quad \text{and} \quad I_\phi = \frac{|\phi_p|d}{2u_{ff}} \quad (3.5)$$

where u_p and ϕ_p are the displacement and the rotation of pile cap, while u_{ff} is the free-field displacement. Moreover, he defined the displacement and rotation *kinematic amplification factors* as:

$$A_u = \frac{|u_p|}{u_g} \quad \text{and} \quad A_\phi = \frac{|\phi_p|d}{2u_g} \quad (3.6)$$

where u_g is the displacement of the rigid bedrock. All these displacements and rotations are amplitudes of harmonic motions. In absence of kinematic interaction, $I_u = 1, I_\phi = A_\phi = 0$.

Because of the presence of damping the various displacements and rotations are not in-phase with the excitation; the four factors are complex functions of frequency (so completely defined by amplitude and phase), even if the study is carried out only with reference to amplitudes. In his study, Gazetas (1984) considered 3 different subsoil models: model A, in which Young modulus $E(z)$ is proportional to depth; in model B $E(z)$ is proportional to square root of z and in model C $E(z)$ is constant.

In Figure 3.1 the effect of stiffness ratio E_p/E_s (with E_p pile Young modulus and E_s Young modulus of soil at depth $z=d$) is showed.

It can be noticed that:

- the first frequency of vibration (in correspondence of the peak of the amplitude) is not influenced by the presence of the pile;
- up to a frequency of about $1.50 f_1$ even very stiff piles follow the ground motion;
- at high frequencies even flexible piles are not able to follow the ground motion;
- a rotational component of motion developed at pile cap.

Similarities and differences for different soil profiles can be in Figure 3.2. The curves highlight that:

- the second resonance occurs at f_2 , the second natural shear frequency of the respective unperturbed stratum; f_2 gets closer to f_1 as the degree of soil inhomogeneity increases;
- the peak rotation at $f=f_1$ increases for increasing the soil inhomogeneity, while the two resonant peaks of horizontal displacement and the second resonant peak of rotation are less sensitive to differences in the soil profile;
- the filtering effect exerted by the pile is stronger as the degree of soil inhomogeneity increases; at the same time, the rotational component of motion increases for inhomogeneous deposits.

Figure 3.3 portrays the effect of slenderness ratio on the kinematic response. It can be noticed that:

- there is an evident effect of L/d on the rotation of pile cap at all frequencies. It has also influence on displacements, but the difference become appreciable only at frequency greater than $1.50 f_1$, when the shorter piles produce stronger filtering effects;
- at frequencies which are lower than f_1 the rotation amplitudes are higher for shorter piles.

Gazetas (1984) reported a well documented case history presented by Ohta et al. The vibration of an 11-storey building supported on piles was recorded during seven earthquakes. It can be seen, in Figure 3.4, that near-distant events, rich in high frequencies, result in a greater pile-soil-structure interaction, in agreement with the results of the parametric study described above.

Figure 3.5 plots the ratio $\ddot{U}_p / \ddot{U}_{ff}$ of the Fourier Amplitude spectra of the pile cap and free-field (surface) acceleration records; also plotted in the Figure is an approximate theoretical curve. Again is possible to notice the greater influence of interaction as higher are the frequencies of excitation.

The same results were obtained also by Fan et al.; the general shape of the function I_u is idealized in Figure 3.6, in which on the x-axis is reported the dimensionless frequency $a_0 = \omega d / V_s$, with $\omega = 2\pi f$. Three regions are distinguishable.

At low frequencies ($a_0 < a_{01}$) I_u is about equal to 1; this means that pile cap follows the free-field motion associated with high wavelengths. At medium frequencies, I_u decreases drastically increasing the frequency, because the pile, with its stiffness, becomes unable to follow the wavy field of the soil. At high frequencies, I_u becomes very small, fluctuating around values of 0.2-0.4. Values of a_{01} and a_{02} depend on the soil profile, restraint condition at pile cap, relative pile-soil stiffness and pile group layout; typical values of a_{01} are, for example, 0.05 for heterogeneous and 0.20-0.30 for homogeneous profiles.

In agreement with these results are those obtained by Kaynia and Kausel (1991); they pointed out that heterogeneous media have a strong influence on filtering effect for both single piles and pile groups. In Figure 3.7 and 3.8 is shown the trend of I_u ; the stiffness ratio for inhomogeneous profile refers to the pile toe.

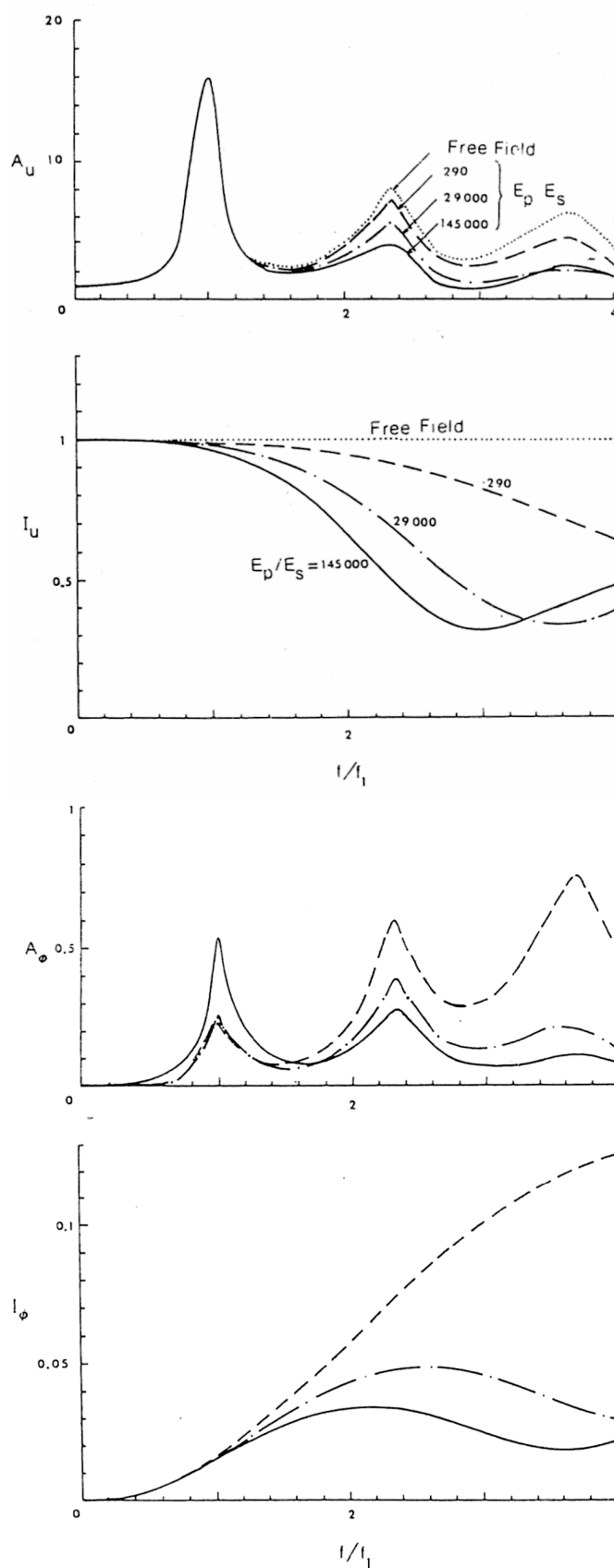


Figure 3.1: Influence of E_p/E_s ($L/d=40$; soil model A; $\beta_s=0.05$, $v_s=0.40$, $\rho_p/\rho_s=1.60$) (Gazetas, 1984)

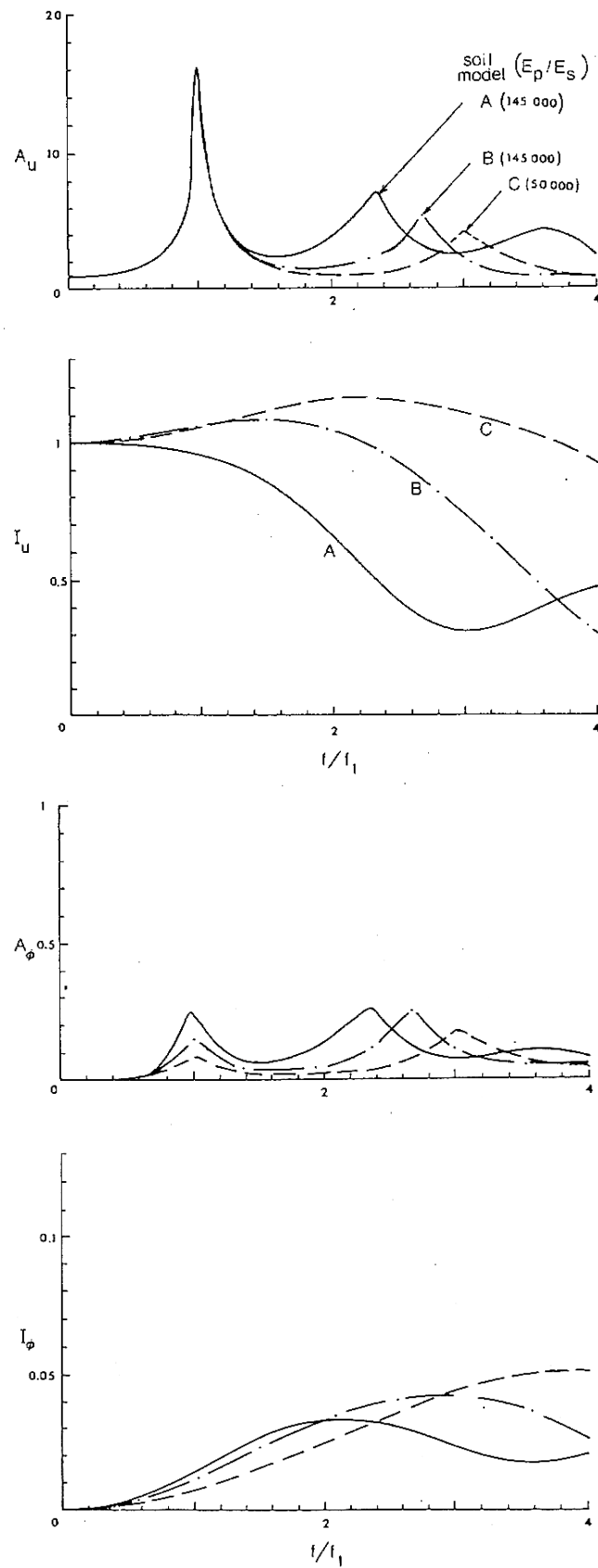


Figure 3.2: Influence of the soil profile ($L/d=40$; $\beta_s=0.05$, $v_s=0.40$, $\rho_p/\rho_s=1.60$) (Gazetas, 1984)

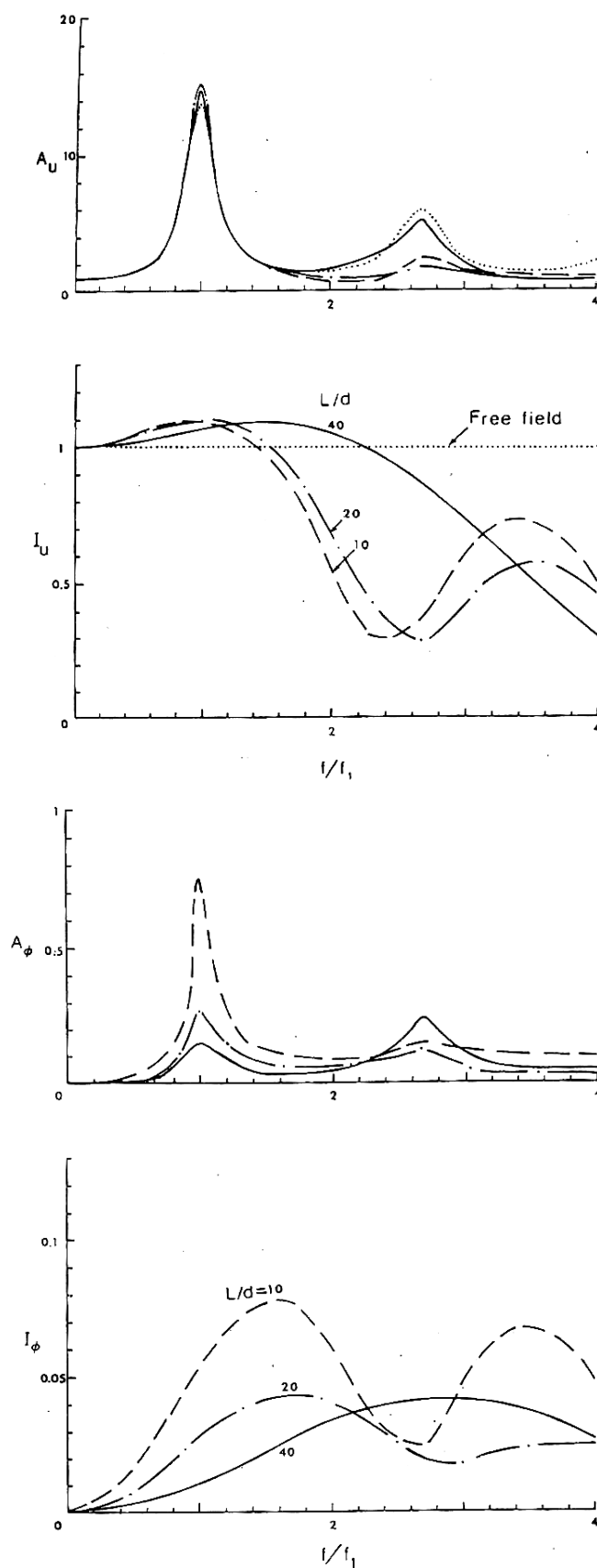


Figure 3.3: Influence of L/d ($E_p/E_s = 145000$; soil model B; $\beta_s=0.05$, $v_s=0.40$, $\rho_p/\rho_s=1.60$) (Gazetas, 1984)

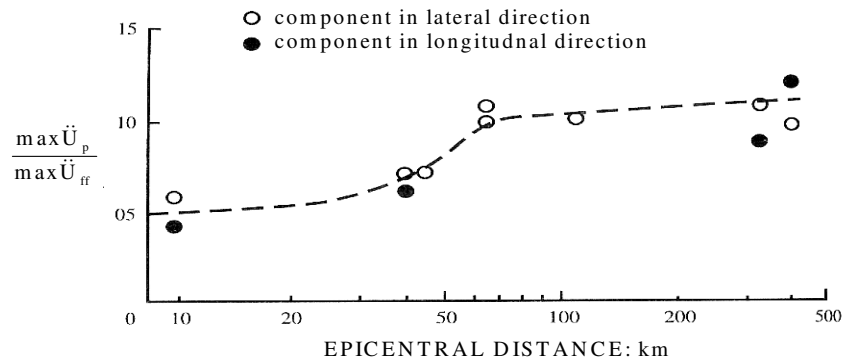


Figure 3.4: Case history: variation with epicentral distance of the ratio of the two maximum accelerations (Gazetas, 1984)

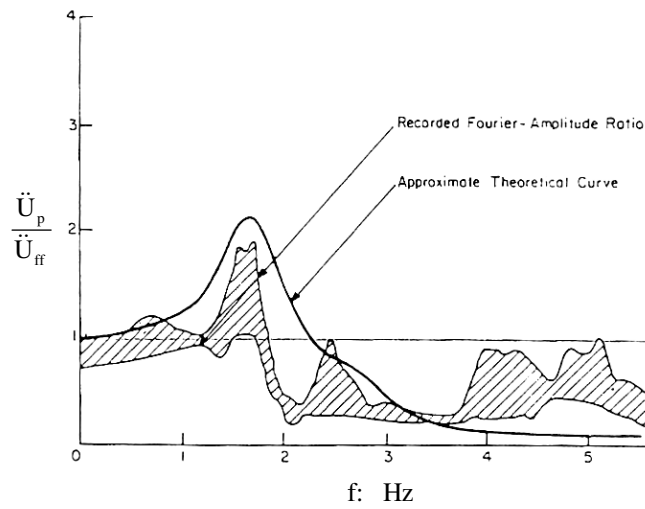


Figure 3.5: Comparison of predicted and recorded ratio of Fourier Amplitude spectra. (adapted from Gazetas, 1984)

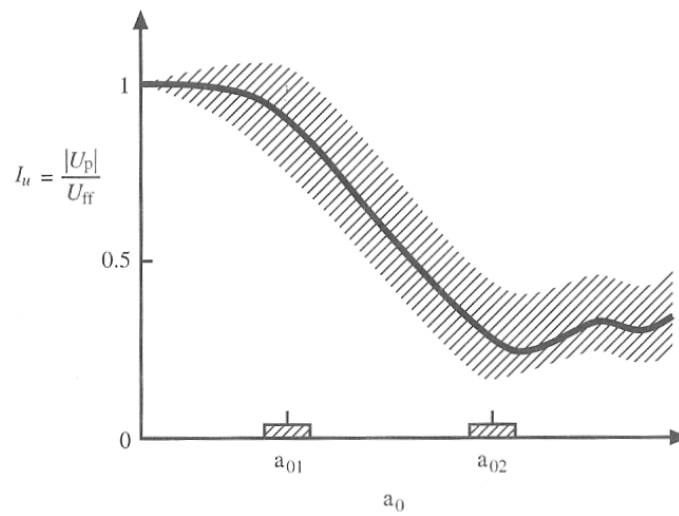


Figure 3.6: idealized trend of the factor I_u (Fan et al., 1991)

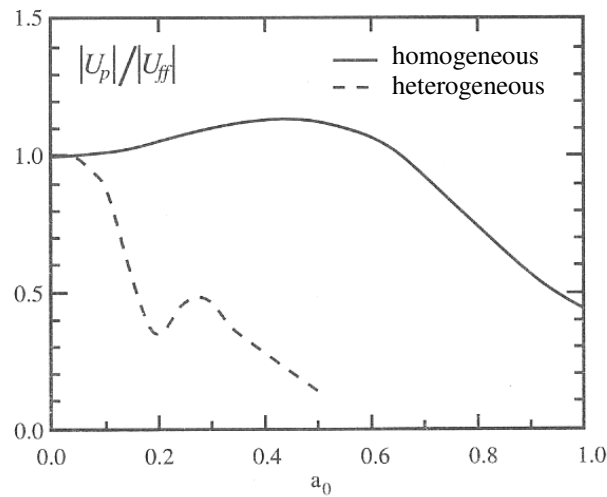


Figure 3.7: Trend of the factor I_u for a single pile ($E_p/E_s=100$, $L/d=20$, $\beta_s=0.05$, $v_s=0.4$, $\rho_s/\rho_p=0.7$) (adapted from Kaynia and Kausel., 1991)

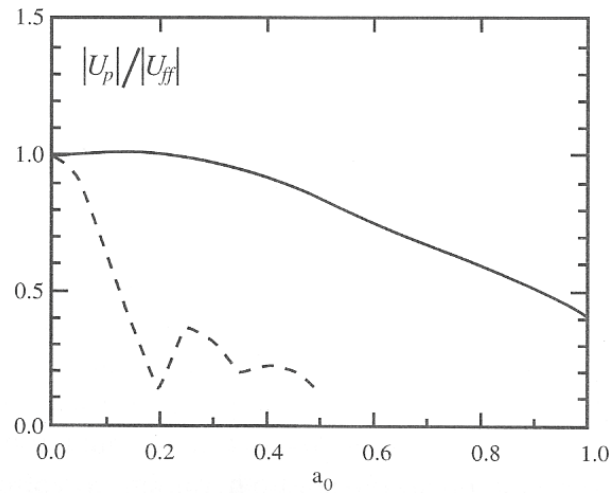


Figure 3.8: Trend of the factor I_u for a 3x3 pile group ($E_p/E_s=100$, $L/d=20$, $\beta_s=0.05$, $v_s=0.4$, $\rho_s/\rho_p=0.7$) (from Kaynia and Kausel., 1991)

Referring to a two-layers soil deposit, in which the first layer is soft and thin ($h_a/d < 5$, $V_a/V_b < 1/3$), the trend of I_u changes drastically. Gazetas et al. (1992) showed that in this cases, the function I_u becomes fluctuating and, at certain frequencies, the displacement of pile cap is greater than the free-field motion at ground surface. Figures 3.9, 3.10 and 3.11 show these trends.

3.1.2 Bending moments

The alteration of the seismic motion at surface is not the only consequence of kinematic interaction.

The transit of seismic waves through soil during earthquakes may cause significant strains to develop. If embedded piles are present, curvature will be imposed to the piles by vibrating soil, which will generate bending moments.

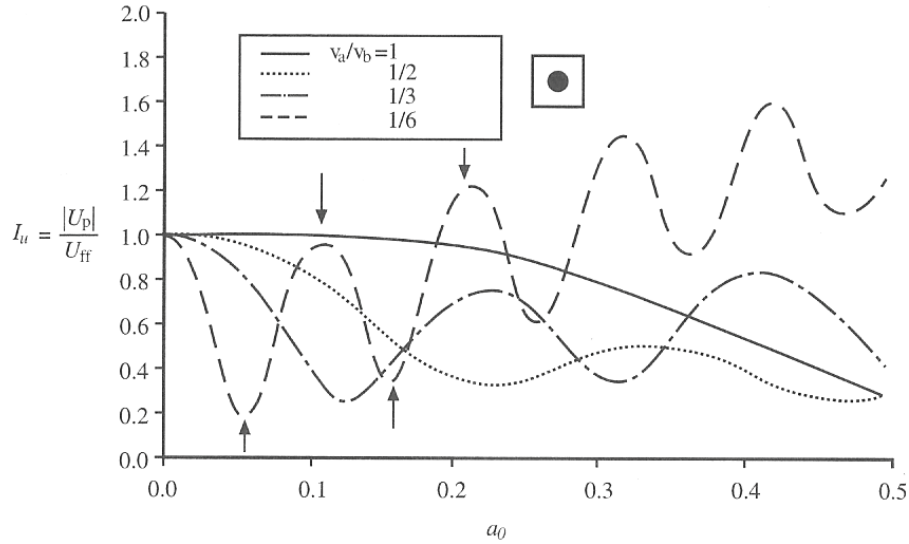


Figure 3.9: Trend of the factor I_u for a single pile with its cap restrained against rotation ($h_a=5d$, $E_p/E_s=1000$, $L/d=20$, $\beta_s=0.05$, $v_s=0.4$, $\rho_s/\rho_p=0.7$) (Gazetas et al., 1992)

These moments will develop even in the absence of a superstructure; as discussed above, they are commonly referred to as “kinematic”, in order to be distinguished from moments generated by loads imposed at pile head by the superstructure (“inertial” moments). This conceptual decomposition is important in piling engineering, since inertial moments vanish within few diameters, so only kinematic response may be important at larger depth.

The problem has been studied, among the others, by Margason (1975), Dobry & O’Rourke (1983), Mineiro (1990), Kavvadas & Gazetas (1993), Nikolaou et al. (1995), Nikolaou & Gazetas (1997), Mylonakis (1999), Mylonakis (2001).

Modeling a pile as a flexural beam, the bending moment can be computed from the formula:

$$M = E_p I_p (1/R) \quad (3.7)$$

where:

$M = M(z,t)$ = pile bending moment

I_p = pile cross-sectional moment of inertia

$(1/R)$ = earthquake-induced pile curvature

z = depth from soil surface

t = time.

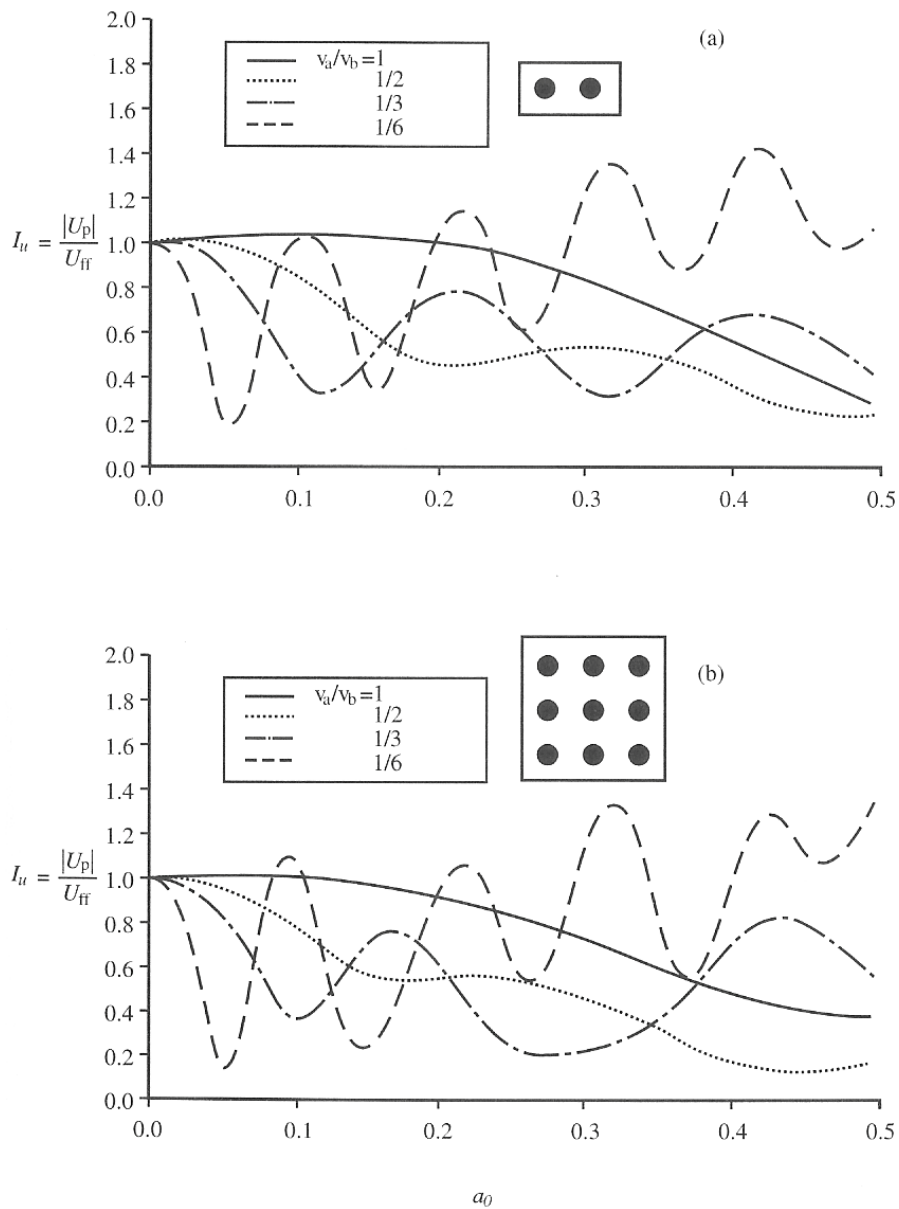


Figure 3.10: Trend of the factor I_u for pile groups: (a) 1x2; (b) 3x3 ($h_a=5d$, $E_p/E_s=1000$, $L/d=20$, $\beta_s=0.05$, $v_s=0.4$, $\rho_s/\rho_p=0.7$) (Gazetas et al., 1992)

Of course the key problem for computing M lies in the determination of the pile curvature ($1/R$) induced by earthquake. Several techniques have been proposed, hence a brief review of some of these methods is presented below.

Margason (1975) and Margason & Holloway (1977) assume that:

- a long pile follows the motion of the free-field soil
- the deflected shape of the pile can be approximated with a circular arc

Based on this assumption, the maximum curvature along an end-bearing pile in a homogeneous soil layer over rigid bedrock is:

$$(1/R) = nu_s / L^2 \quad (3.8)$$

where u_s denotes the maximum soil displacement at the soil surface and L the pile length; n is a dimensionless constant. For a pile with both ends fixed against rotation, $n=6$, while for a pile with one fixed end, $n=2$. Based on analytical studies of soil response to vertically-propagating shear waves, Margason & Holloway (1977) argue that during severe earthquakes peak soil curvatures are not likely to exceed 0.02 m^{-1} (if liquefaction does not occur).

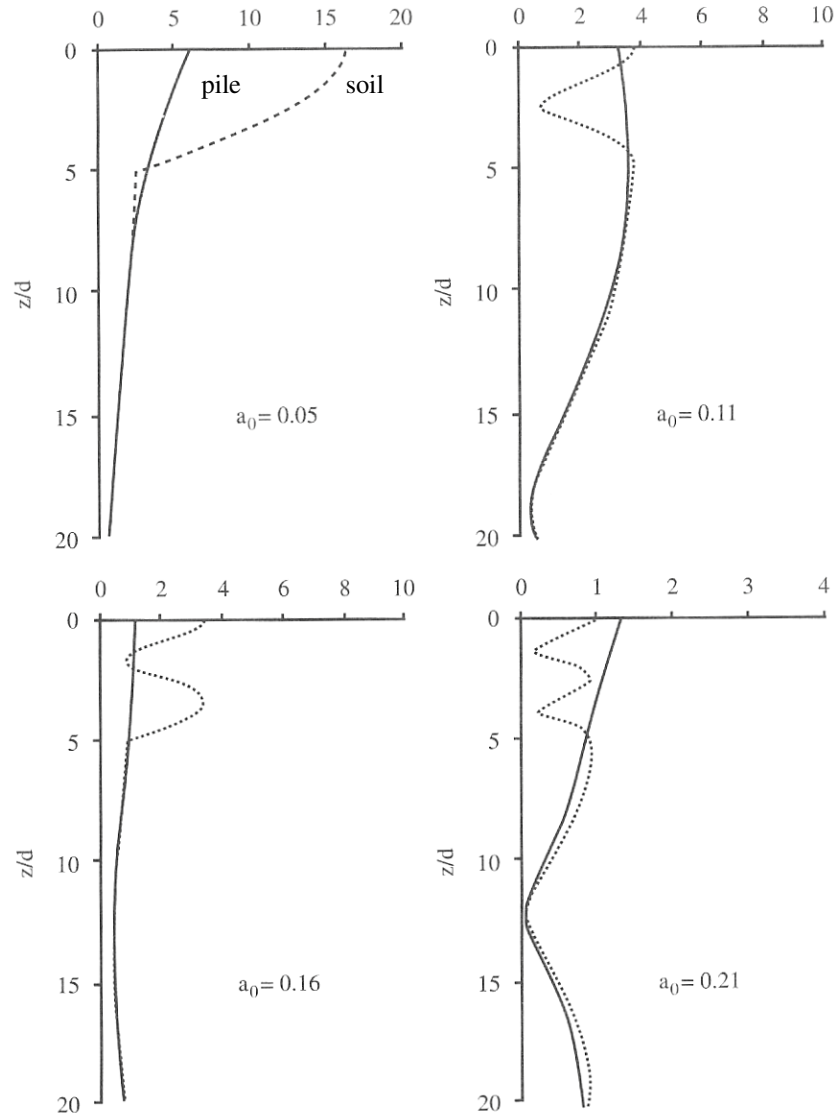


Figure 3.11: Trend of the displacement of soil and pile with depth, for 4 values of frequency ($h_a=5d$, $E_p/E_s=1000$, $L/d=20$, $\beta_s=0.05$, $v_s=0.4$, $\rho_s/\rho_p=0.7$) (Gazetas et al., 1992)

This early method suffers from some drawbacks and its use in practical applications appears to be limited. The most important drawbacks are:

- pile-soil interaction is neglected. Thereby, important parameters regulating this phenomenon such as pile-soil relative stiffness, excitation frequency and radiation damping are not incorporated;
- the method is inapplicable to soil layer interfaces since there soil curvature becomes infinite (it will be discussed in detail below);
- the circular arc used to derive Equation 3.8 in the hypothesis that the pile has one end fixed against rotation ($n=2$) implies pure bending, so the influence of shearing on pile response is neglected;
- arbitrary upper bounds for peak soil curvatures are assumed.

A modified formulation is proposed in the NEHRP-97 recommendations. According to this approach, the pile follows exactly the free-field soil motion. Under the common assumption of seismic excitation consisting exclusively of vertically-propagating shear waves, the equation governing 1-D wave propagation is:

$$\frac{\partial^2 u}{\partial t^2} = V_s^2 \frac{\partial^2 u}{\partial z^2} \quad (3.9)$$

and then the soil curvature may be expressed as:

$$(1/R) = \frac{a_{ff}}{V_s^2} \quad (3.10)$$

where:

a_{ff} = free-field soil acceleration

V_s = velocity of shear waves in the soil

The limitations of this method are practically the same as those of the Margason's approach. For instance, since free-field acceleration typically decreases with depth, eq. 3.10 will typically predict a maximum curvature at the pile head. While this may be true for piles whose head is restrained against rotation (fixed-head piles), it would obviously be false for piles that are free to rotate at the top (free-head piles).

Additional problems are at interfaces between soil layers, as mentioned above. Kinematic pile bending tends to be amplified in the vicinity of interfaces between stiff and soft soil layers, since soil shear strain is discontinuous across interfaces because of the different soil shear moduli and, thereby, the associated soil curvature (the derivative of strain) is *infinite* (see Figure 3.12).

With reference to interfaces, eq. 3.10 is inapplicable or unreliable because:

- $u(z)$ is not differentiable at the interface
- applying eq 3.6 slightly above or below the interface will underestimate the actual pile curvature. The latter effect was demonstrated by Kavvadas and Gazetas (1993) who showed that pile-soil interaction should not be neglected in such analyses.

To account for pile-soil interaction, Winkler models in which the pile is connected to the soil through continuously-distributed springs and dashpots (Flores-Berrones & Whitman, 1982; Kavvadas & Gazetas, 1993) may be used.

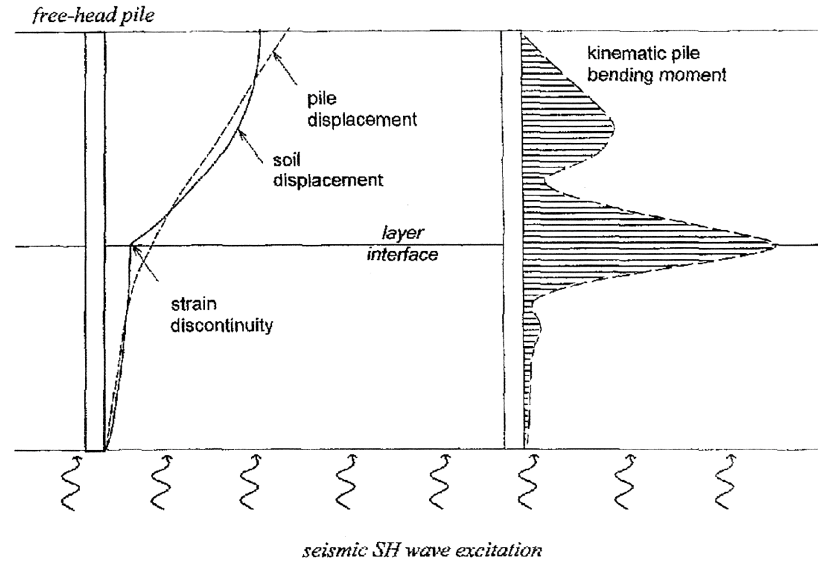


Figure 3.12: Kinematic bending of a free-head pile in a two-layer soil profile subjected to vertically-propagating seismic SH waves (Mylonakis., 2001)

In these techniques, springs represent soil stiffness while dashpots represent damping due to radiation (geometric) and hysteretic energy dissipation in the medium (material). The motion in the soil (calculated without interaction, that's to say in the free-field conditions) is the support excitation of the pile-soil system. In the case of long fixed head piles in homogeneous soil, pile curvature can be obtained in closed form:

$$(1/R) = \Gamma \frac{a_{ff}}{V_s^2} \quad (3.11)$$

which differs from the eq. 3.10 in the presence of the dimensionless factor Γ which accounts for pile-soil interaction. In the harmonic case, Γ can be determined analytically as (Flores-Berrones & Whitman, 1982; Nikolaou et al., 1995):

$$\Gamma \cong \left[1 + \frac{4E_p I_p \left(\frac{\omega}{V_s} \right)^4}{k} \right]^{-1} \quad (3.12)$$

in which ω is the cyclic vibrational frequency ($=2\pi f$) and k the modulus of the Winkler springs (modulus of subgrade reaction). It may be shown that Γ is always smaller than 1 and decreases monotonically with increasing frequency, and, as a first approximation, Γ values between 1 and 0.7 can be adopted (Makris & Gazetas 1992; Nikolaou et al. 1995).

Mineiro (1990) proposed an approximate technique for computing kinematic bending moments at pile cap. The assumptions are:

- the pile is end bearing
- the pile head follows the motion of the free-field soil

- an identical pile whose head is unrestrained against displacement and rotation would experience a head rotation which is equal to average soil shear strain (u_s/L), with u_s the free-field soil displacement at the surface and L the pile length
- the pile is modeled as beam on Winkler foundation

Based on these assumptions, to achieve zero rotation atop a fixed-head pile, the following “fixing curvature” has to be applied at the pile top

$$(1/R) = \lambda \frac{u_s}{L} \quad (3.13)$$

where λ denotes the well-known Winkler parameter (Poulos & Davis, 1980):

$$\lambda = \left(\frac{k}{4E_p I_p} \right)^{\frac{1}{4}} \quad (3.14)$$

Drawbacks of the method are prevalently:

- soil-pile interaction is accounted for only indirectly
- the maximum bending moment occurs always at the pile head
- the method is not applicable to free-head piles
- the curvature decreases monotonically with increasing pile length

Accordingly, it is expected that the method will underestimate curvatures in long piles.

From analytical studies by Flores-Berrones & Whitman (1982), Barghouthi (1984), and Makris & Gazetas (1992), the deflected shape $u_p(z)$ of a long fixed-head pile in an homogeneous halfspace, excited by vertically propagating harmonic S waves, is given by:

$$u_p(z) = \Gamma u_{ff}(z) \quad (3.15)$$

where Γ is the dimensionless response factor:

$$\Gamma = \frac{k + i\omega c_d}{E_p I_p (q^4 + 4\lambda^4)} \quad (3.16)$$

in which $k + i\omega c_d$ denotes the so-called dynamic impedance of the Winkler bed, $q = \omega/V_s$ is the wavenumber of the harmonic SH waves in the soil; λ is given by equation 3.14, but with the spring constant k replaced by the complex dynamic impedance.

Differentiating equation 3.15 twice with respect to depth, z , the ratio of the peak pile and soil curvatures is obtained as:

$$\frac{(1/R)_p}{(1/R)_s} = \Gamma \quad (3.17)$$

For a free-head pile, the corresponding solution gives (Mylonakis, 1999):

$$\frac{(1/R)_p}{(1/R)_s} = \Gamma \max \left[e^{-\lambda z} (\cos \lambda z + \sin \lambda z) - \cos qz \right] \quad (3.18)$$

Equations 3.17 and 3.18 are plotted in Figure 3.13.

It can be noted that at low frequencies pile and soil curvatures are approximately equal, which implies that the pile follows the free-field soil motion. With increasing frequency, however, the curvature ratio decreases monotonically with frequency, and tends to zero as a_0 tends to infinity. This can be interpreted as a progressively increasing destructive interference of the high-frequency (short-wavelength) seismic waves exciting the pile. The trend is stronger with large pile-soil stiffness contrasts. It is also observed that the curvature ratio is always smaller than 1; an except for $a_0 \rightarrow 0$ where the ratio is 1.04.

For a fixed-head pile of finite length in a homogeneous layer of thickness h over a rigid base, the curvature ratio is given by the expression (Mylonakis, 1999):

$$\frac{(1/R)_p}{(1/R)_s} = \Gamma \left[1 + \left(\frac{q}{\lambda} \right)^2 \frac{\cos qh (\sinh \lambda h \cos \lambda h - \cosh \lambda h \sin \lambda h) + (q/\lambda) \cosh \lambda h \cos \lambda h \sin \lambda h}{\sinh 2\lambda h + \sin 2\lambda h} \right] \quad (3.19)$$

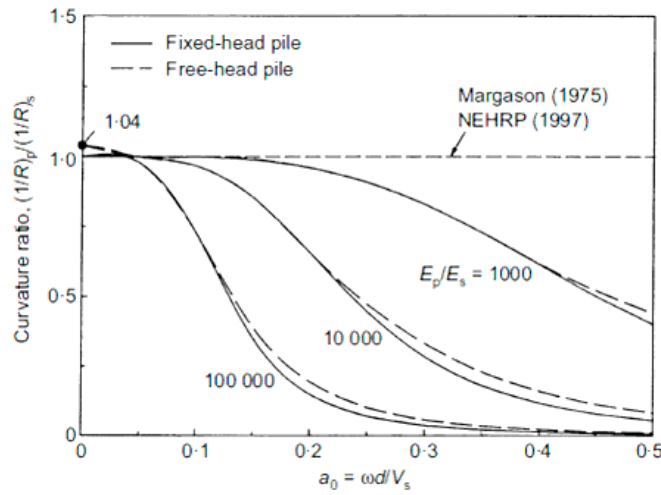


Figure 3.13: Ratio of peak pile and soil curvature for an infinitely long pile in homogeneous halfspace ($\beta_s=0$, $v_s=0.4$, $\rho_s/\rho_p=0.7$) (Mylonakis, 1999)

The above expression corresponds to stress-free conditions at the pile toe (floating-toe pile). For a pile with its toe socketed in the bedrock such that the bending moment at the toe is zero (hinged-toe pile), the corresponding expression is:

$$\frac{(1/R)_p}{(1/R)_s} = \Gamma \left\{ 1 - 2 \frac{\cos qh [\cosh \lambda h \cos \lambda h + 2 \sinh \lambda h (\lambda/q)^2 [(1/\Gamma) - 1] \sin \lambda h]}{\cosh 2\lambda h + \cos 2\lambda h} \right\} \quad (3.20)$$

Expressions 3.19 and 3.20 are plotted in Figure 3.14.

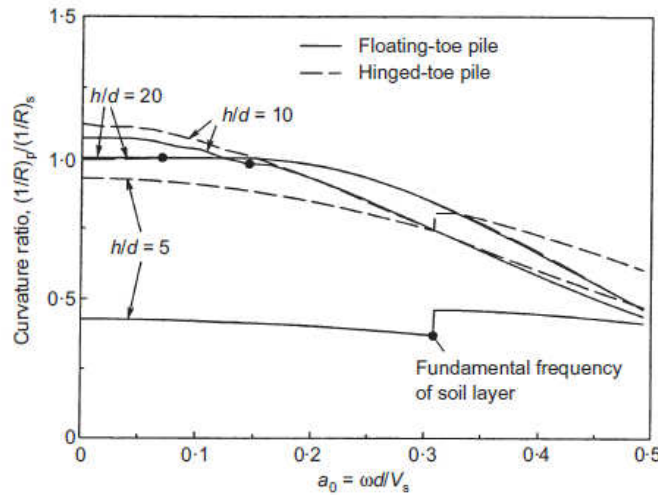


Figure 3.14: Ratio of peak pile and soil curvature for a fixed-head pile in homogeneous soil layer over rigid rock for various layer thicknesses ($E_p/E_s=1000$, $\beta_s=0.05$, $v_s=0.4$, $\rho_s/\rho_p=0.7$) (Mylonakis, 1999)

Note that, with increasing pile length, the second term in the right-hand side of the previous two equations converges to 1, and both expressions duly reduce to equation 3.17.

Contrary to the trends incited by the Margason/NEHRP equations, no clear relation between curvature ratio and pile diameter can be drawn from the graph. The jump observed at the fundamental natural period of the layer is associated with the sudden appearance of radiation damping in the medium at that frequency.

The above formulations have been developed for homogeneous soil conditions. As already mentioned kinematic bending moments tend to be amplified in the vicinity of interfaces, and may induce damage to the pile even at locations deep below the ground surface.

Some analytical methods have been developed to quantify its importance. Recently developed methods are discussed below.

A simple model has been developed by Dobry and O'Rourke (1983) for computing kinematic bending moments in a pile at an interface separating two soil layers, based on the following assumptions:

- the soil in each layer is homogeneous, isotropic, and linearly elastic
- both layers are thick enough so boundary effects outside the layers do not influence the response at the interface
- the pile is long, vertical, and linearly elastic
- perfect contact exists between pile and soil
- the soil is subjected to a uniform static stress field, τ , which generates constant shear strain within each layer
- displacements are small

Based on these assumptions and modeling the pile as a Beam on Winkler foundation (BWF), Dobry and O'Rourke (1983) presented an explicit solution for the pile bending moment at the interface:

$$M = 1,86(E_p \cdot I_p)^{3/4} (G_1)^{1/4} \gamma_1 \cdot F \quad (3.21)$$

where G_1 = soil shear modulus in layer 1, γ_1 = (uniform) soil shear strain in layer 1; $F = F(G_2/G_1)$ is a dimensionless function of the ratio of the shear moduli in the two layers:

$$F = \frac{(1 - c^{-4})(1 + c^3)}{(1 + c)(c^{-1} + 1 + c + c^2)} \quad (3.22)$$

where:

$$c = \left(\frac{G_2}{G_1} \right)^{1/4} \quad (3.23)$$

The Winkler spring coefficients (the ratios between the soil reactions per unit pile length and the horizontal displacements) used by Dobry and O'Rourke were $k_1 = 3G_1$ and $k_2 = 3G_2$.

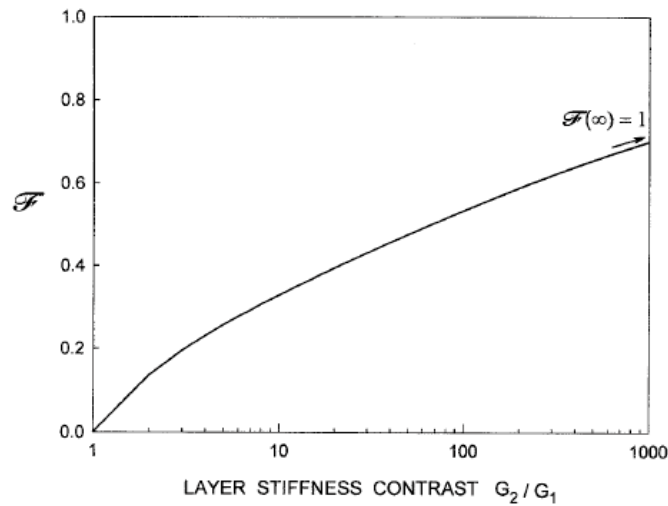


Figure 3.15: Trend of the dimensionless function of Dobry & O'Rourke (Mylonakis, 2001)

The function F (illustrated in Figure 3.15) attains values between 0 and 1 and tends to increase with increasing stiffness contrast between the layers. In the extreme case of an infinitely stiff second layer, c tends to infinity and F converges to 1. In a homogenous profile c is equal to 1 and F is 0; it is unrealistic, since kinematic bending develops even in homogeneous soil.

Contrary to the simplistic NEHRP method the Dobry & O'Rourke model incorporates the interaction between pile and soil, and thus overcomes the problem of singular soil curvature at the interface. Nevertheless, the dynamic nature of excitation and the effect of finite soil thickness are not incorporated.

Mylonakis (1999) suggested to use a deformation-related quantity (for example bending strain) to quantify kinematic pile bending. The maximum bending strain at the outer fiber of the pile cross-section has several advantages over bending moment:

- it is dimensionless
- it is experimentally measurable
- it can be used to quantify damage

- ultimate bending strains do not vary significantly among common structural materials

With reference to the Dobry-O'Rourke model, eq. 3.21 can be expressed in terms of bending strain as:

$$\varepsilon_p = 2\lambda_l r \gamma_l F \quad (3.24)$$

with λ_l expressed by eq. 3.14 with $k=k_l$. For a cylindrical pile of diameter d , eq. (3.21) simplifies to:

$$\varepsilon_p = 1.5 \left(\frac{k_l}{E_p} \right)^{\frac{1}{4}} \gamma_l F \quad (3.25)$$

The advantage of using bending strain instead of bending moment becomes evident by comparing eqs. 3.21 and 3.25. Eq. 3.25 involves only three parameters (instead of four in eq. 3.21). Moreover, the last formula helps clarifying the role of pile size on kinematic pile bending; in fact, it clearly indicates that pile bending strain is independent of pile diameter and, accordingly, reducing the size of a pile offers no improvement in seismic performance.

The expression (3.25) can be rewritten as:

$$\left(\frac{\varepsilon_p}{\gamma_l} \right) = 1.5 \left(\frac{k_l}{E_p} \right)^{\frac{1}{4}} F \quad (3.26)$$

The term on the left-side of this equation may be interpreted as a “strain transmissibility” function relating peak pile bending strain and soil shear strain at the interface (see Mylonakis, 2001). Eq. 3.26 has an advantage: since both γ_l and ε_p exhibit a similar sensitivity to frequency (recall the undulations with frequency of transfer functions of free-field soil response, by taking their ratio the effect of soil amplification is suppressed, and hence eq. 3.26 expresses exclusively pile-soil interaction effects.

Nikolaou and Gazetas (1997) and Nikolaou et al. (2001) performed a parametric study, based on the Beam on Dynamic Winkler Foundation model (Figure 3.16a), referring to harmonic steady-state bending strains in a pile in a two-layer soil deposit subjected to vertically propagating seismic shear waves (see Figure 3.16b). The analyzed cases are shown in Figure 3.17, both for free-head and fixed-head piles; in total 32 cases were analyzed by the authors.

They found a closed-form expression for computing approximately the maximum steady-state bending moment at the interface between the two layers (see Nikolaou et al., 1995). The expression is based on a “characteristic” shear stress τ_c , which is proportional to the actual shear stress that is likely to develop at the interface, as a function of the free-field acceleration at the soil surface, a_s :

$$\tau_c \approx a_s \rho_l h_l \quad (3.27)$$

The fitted formula is:

$$M_{max}(\omega) = 0.042 \tau_c d^3 \left(\frac{L}{d} \right)^{0.3} \left(\frac{E_p}{E_l} \right)^{0.65} \left(\frac{V_2}{V_l} \right)^{0.5} \quad (3.28)$$

The above equation indicates that bending moments tend to increase with increasing pile diameter, pile soil stiffness contrast, and layer stiffness contrast. Under transient seismic excitation, the authors showed that the above trends are still valid, but with one exception: the peak values of the transient bending moments are smaller than the steady-state amplitudes, by a factor of about 3 to 5. They proposed that a reduction factor η has to be applied to the $M_{max}(\omega)$, the maximum steady-state pile bending moment, in the frequency domain, to derive the actual maximum value in the time domain:

$$M_{max}(t) = M_{max}(\omega) \cdot \eta \quad (3.29)$$

Factor η is a function of the number of excitation cycles, N_c , and of the ratio of the predominant period of the excitation to the fundamental natural period of the soil T_p/T_l (Figure 3.18). For preliminary design purposes, η values between 0.2 to 0.3 are recommended.

Mylonakis (2001) proposed an improved model for kinematic pile bending. The model, shown in Figure 3.19, consists of a vertical pile embedded in a two-layer soil deposit which is subjected to vertically-propagating seismic SH waves. As with the earlier Dobry and O'Rourke (1983) model, both layers are assumed to be thick², with the soil material in each layer being homogeneous and linear, and the pile being long and linearly elastic.

With reference to the earlier model, the new model offers the following improvements:

- the seismic excitation is dynamic (as opposed to pseudostatic) having the form of a harmonic horizontal displacement imposed at the base of the profile (Figure 3.19(a))
- both radiation and material damping in the soil are explicitly accounted for by using a bed of pertinent radiation dashpots attached in parallel to the Winkler springs (Figure 3.19(b)) and by replacing the static shear modulus of the soil with a complex dynamic shear modulus $G^* = G(1 + 2i\beta)$
- the geometric characteristics of the profile (i.e., the layer thicknesses) and the inertia of the soil are incorporated through the properties of the seismic waves propagating vertically within the layers.

Using this model, peak pile bending strain at the interface can be put in a form analogous to eq. 3.25:

$$\varepsilon_p = 2\lambda_l r \gamma_l F \quad (3.30)$$

with the new function F given by:

² It is important to clarify that the assumption of "thick" soil layers does not imply an unbounded (i.e., infinitely deep) soil. Indeed, if the soil layers have thickness greater than the so-called "active pile length", which is, typically, equal to about 10 to 15 pile diameters (Poulos and Davis, 1980; Randolph, 1981; Pender, 1993), the pile in each soil layer can be treated as a semi-infinite beam with essentially no error. This assumption is adopted for layer 2 that has a finite thickness.

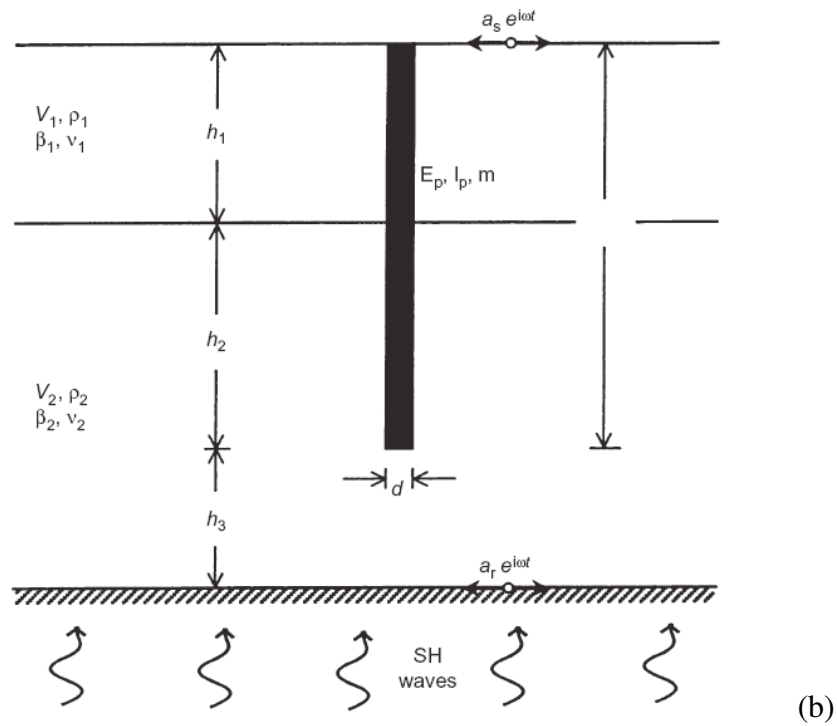
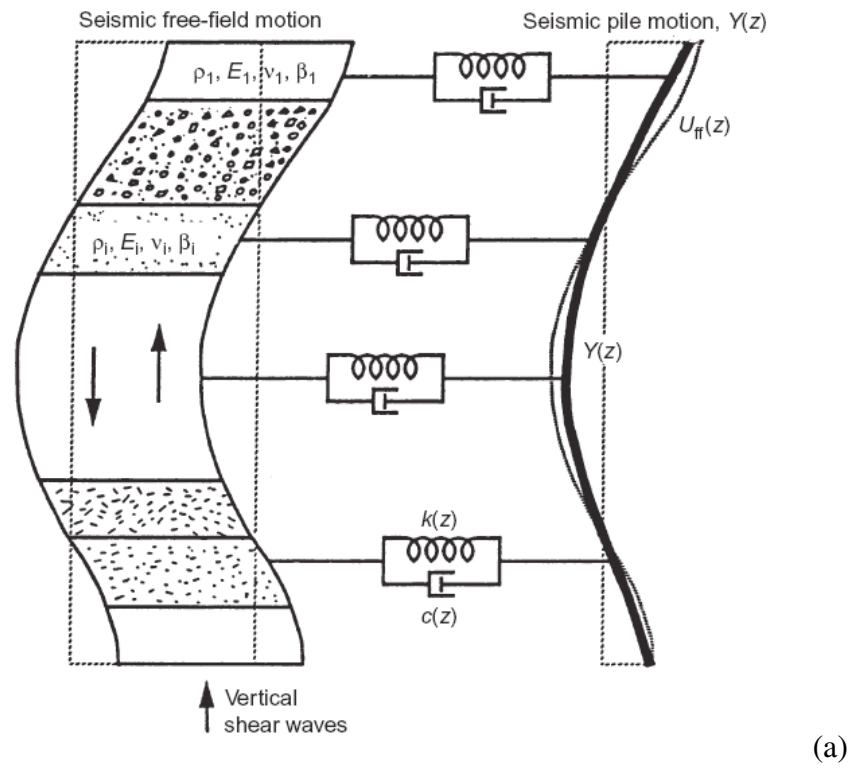


Figure 3.16: (a) The Beam on Dynamic Winkler Foundation model; (b) The system used in the parameter study: a single pile embedded in a two-layer profile on rigid bedrock, excited by harmonic SH seismic waves (Nikolaou et al., 2001)

Group	Case	L/d	E_p/E_1	h_1/L	V_1/V_2	ρ_1/ρ_2
A	1	20	1000	2/3	1	1
	2				0.5	0.8
	3				0.25	0.7
	4				0.1	0.6
B	1	20	5000	1/2	1	1
	2				0.5	0.8
	3				0.25	0.7
	4				0.1	0.6
C	1	40	5000	1/2	1	1
	2				0.5	0.8
	3				0.25	0.7
	4				0.1	0.6
D	1	20	10 000	1/2	1	1
	2				0.5	0.8
	3				0.25	0.7
	4				0.1	0.6

Figure 3.17: Parameter cases for maximum harmonic steady-state kinematic bending strains. In all cases $\beta_1 = \beta_2 = 0.10$, $v_1 = v_2 = 0.4$, $h_3/L = 1$ (Nikolaou et al., 2001)

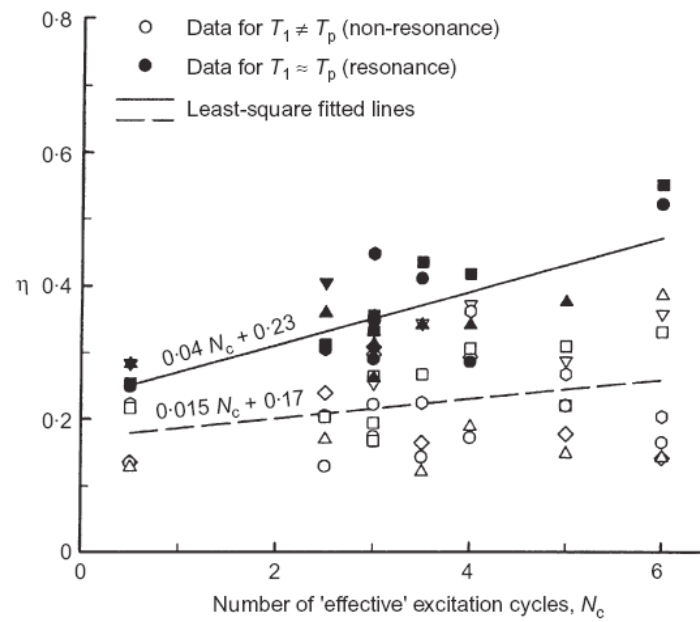


Figure 3.18: Proposed design curves for the frequency-to-time reduction factor η as a function of the number of 'effective' excitation cycles and resonance conditions (Nikolaou et al., 2001)

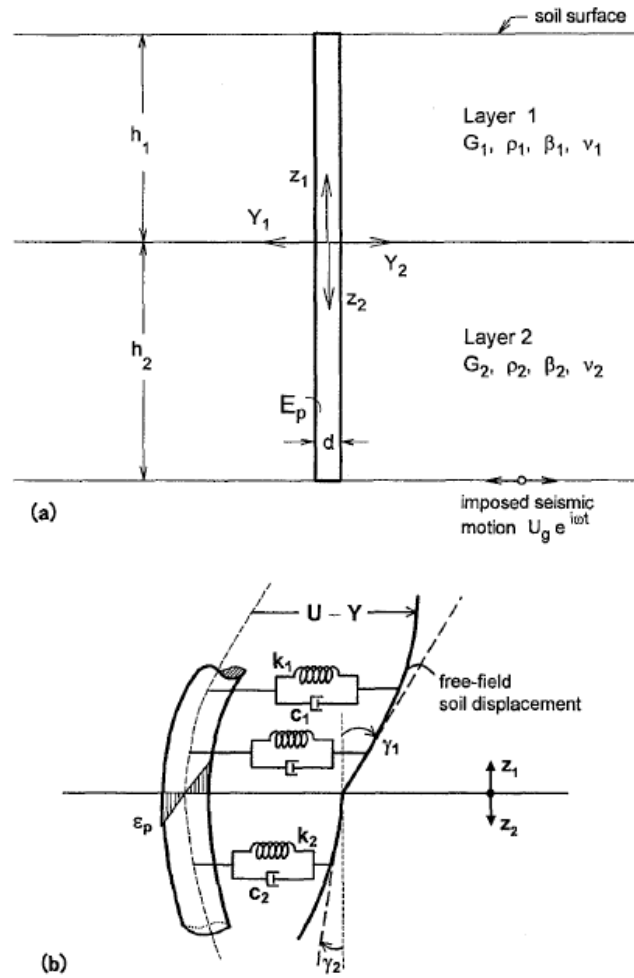


Figure 3.19: Pile-soil configuration (Mylonakis, 2001)

$$F = \frac{\lambda_1 \lambda_2 (S_1 + S_2) - [\lambda_2 (S_3 + S_4) + \lambda_1 S_5] \cotg(h_1 q_1)}{2 \lambda_1 q_1 (\lambda_1 + \lambda_2) (\lambda_1^2 + \lambda_2^2)} \quad (3.31)$$

in which S_1, S_2, S_3, S_4, S_5 are given by:

$$S_1 = 2(\Gamma_1 q_1 - \Gamma_2 q_2 I_R) (\lambda_1^2 - \lambda_1 \lambda_2 + \lambda_2^2) \quad (3.32a)$$

$$S_2 = -\Gamma_1 q_1^3 + \Gamma_2 q_2^3 I_R \quad (3.32b)$$

$$S_3 = 2(\Gamma_1 - \Gamma_2) \lambda_1^2 \lambda_2 (\lambda_1 - \lambda_2) \quad (3.32c)$$

$$S_4 = \Gamma_1 q_1^2 (2 \lambda_1^2 - \lambda_1 \lambda_2 + \lambda_2^2) \quad (3.32d)$$

$$S_5 = \Gamma_2 q_2^2 (\lambda_1^2 - \lambda_1 \lambda_2 + 2\lambda_2^2) \quad (3.32e)$$

In the above equations, λ_1 and λ_2 are complex quantities obtained using the impedances proposed by Kavvadas and Gazetas (1993); q_1 and q_2 are complex wavenumbers pertaining to the characteristics of the SH waves in the free-field soil

$$q_1 = \frac{\omega}{V_{s1}^*} \quad \text{and} \quad q_2 = \frac{\omega}{V_{s2}^*} \quad (3.33)$$

where V_{s1}^* and V_{s2}^* are the corresponding complex shear wave velocities for the two layers; Γ_1 and Γ_2 are dimensionless factors given by

$$\Gamma_1 = \frac{4\lambda_1^4}{q_1^4 + 4\lambda_1^4} \quad \text{and} \quad \Gamma_2 = \frac{4\lambda_2^4}{q_2^4 + 4\lambda_2^4} \quad (3.34)$$

whose magnitudes range between 1 (for $\omega=0$) and 0 (for $\omega \rightarrow \infty$). Finally, I_R reflects the impedance contrast between the two soil layers

$$I_R = \frac{\rho_1 V_{s1}^*}{\rho_2 V_{s2}^*} \quad (3.35)$$

It is noted that the thickness of the second layer does not appear explicitly in the above equations, but its influence is incorporated in the value of the interface shear strain γ_1 .

In the special case of a pile embedded in a homogeneous soil layer, the transmissibility is equal to:

$$\left(\frac{\varepsilon_p}{\gamma_1} \right) = \Gamma \frac{\omega d}{2V_s^*} \quad (3.36)$$

while the corresponding function of Margason's model is:

$$\left(\frac{\varepsilon_p}{\gamma_1} \right) = \frac{\omega d}{2V_s} \quad (3.37)$$

In relatively soft and deep profiles the fundamental natural frequency of the soil is usually quite small ($a_0 < 0.15$). At such low frequencies, Γ is approximately equal to 1 and eq. 3.36 duly reduces to eq. 3.37. These equations are plotted in Figure 3.20 in terms of the dimensionless frequency factor a_0 .

With reference to Eq. 3.36, the author states that at very low excitation frequencies both pile and soil tend to move as rigid bodies, leading to zero strain transfer to the pile; on the other hand, at very high oscillation frequencies the pile resists the input motion (mainly by its inertia) without bending, which, again, leads to zero strain transmission to the pile.

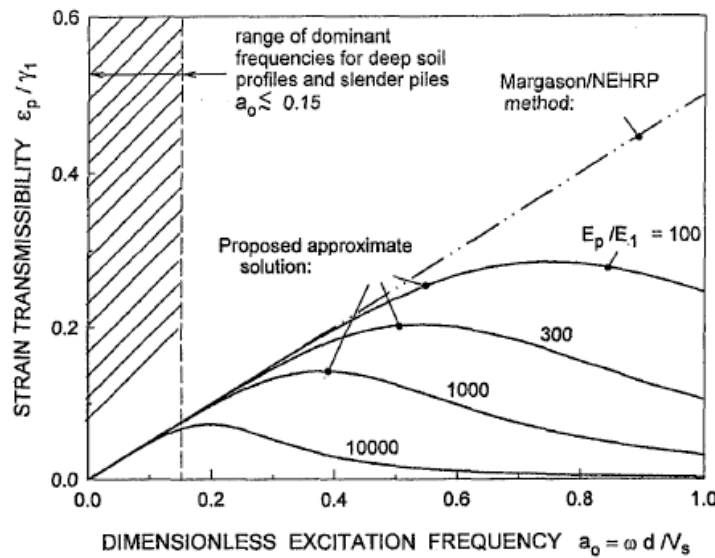


Figure 3.20: Strain transmissibility for a pile embedded in a homogeneous soil layer ($\beta_s=0$, $v_s=0.4$, $\rho_s/\rho_p=0.7$) (Mylonakis, 2001)

In the intermediate frequency range, pile bending strain may be of comparable magnitude to that generated at a sharp interface, especially with "soft" piles. In contrast, Margason's solution predicts strain transmissibility increasing proportionally with frequency, which always overestimates pile bending.

Regarding the effect of pile diameter, the Author also says that it is clear that pile bending strain may increase or decrease with increasing d .

With reference to an interface separating two soil layers, letting $\omega \rightarrow 0$ (low-frequency approximation), assuming that the soil material in the two layers has approximately the same mass density, the strain transmissibility becomes:

$$\left(\frac{\epsilon_p}{\gamma_1}\right) = \frac{(c^2 - c + 1) \left\{ \left[3 \left(\frac{k_l}{E_p} \right)^{1/4} \left(\frac{h_l}{d} \right) - 1 \right] c(c-1) - 1 \right\}}{2c^4 \left(\frac{h_l}{d} \right)} \quad (3.38)$$

This equation is plotted in Figure 3.21 as function of layer stiffness contrast, pile-soil stiffness and embedment ratio.

The effect of frequency on strain transmissibility (which has been neglected in eq. 3.38) is illustrated in Figure 3.22, expressed in terms of the ratio:

$$\Phi = \frac{(\epsilon_p / \gamma_1)}{(\epsilon_p / \gamma_1)_{\omega=0}} \quad (3.39)$$

It may be seen that Φ increases with increasing frequency and may exceed the value of 2 especially for stiff piles and deep interfaces.

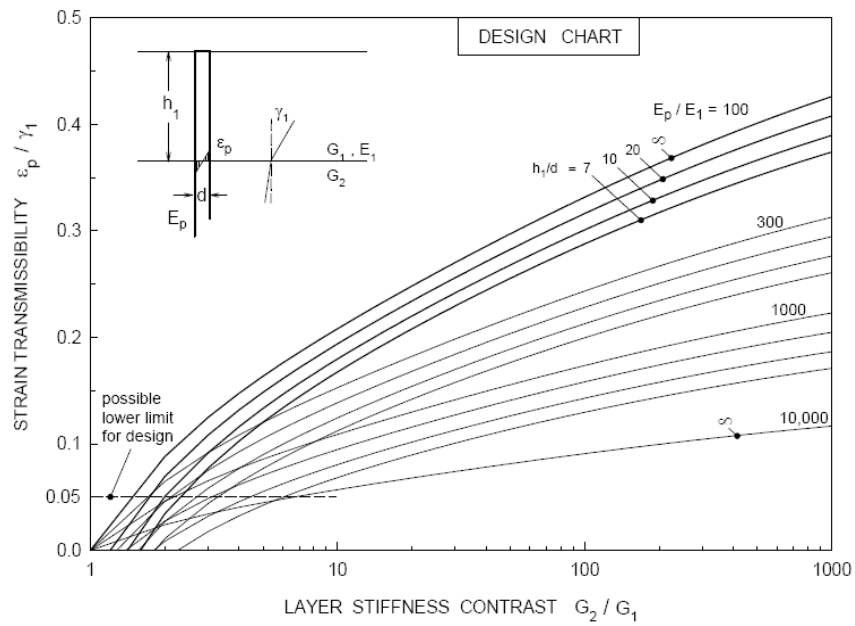


Figure 3.21: Strain transmissibility at low excitation frequency (Mylonakis, 2001)

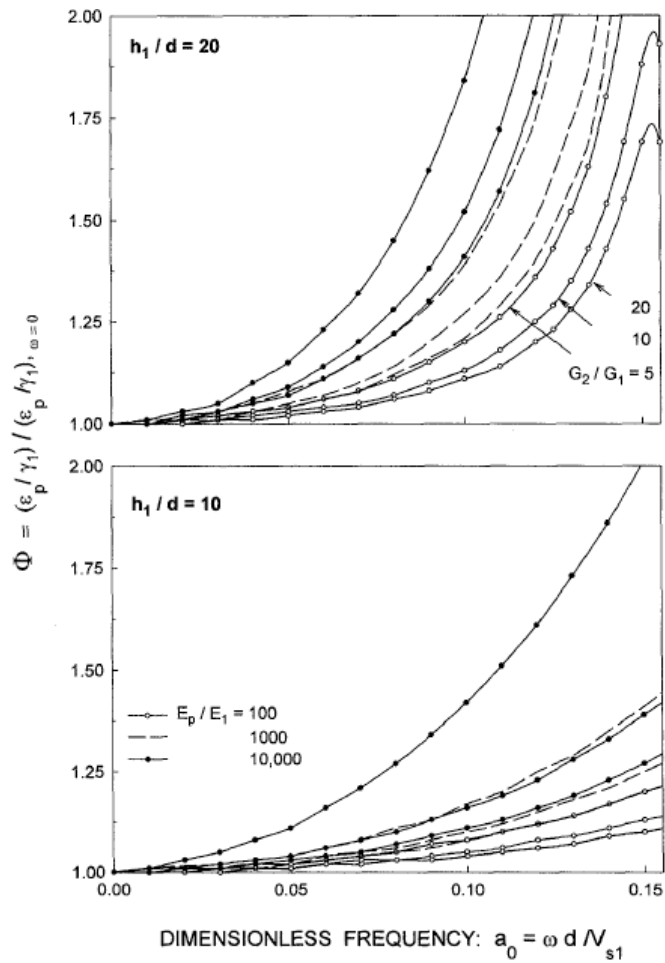


Figure 3.22: Variation with frequency of strain transmissibility (Mylonakis, 2001)

3.2 NUMERICAL ANALYSES

3.2.1 Introduction

The main results available in literature clearly help to identify the most important parameters governing the kinematic interaction.

Nevertheless, it seems that these studies did not cover exhaustively some aspects like, for instance:

- the role played by different parameters on kinematic bending moments for varying interface depth,
- in which cases is possible to carry out a structural analysis assuming free-field accelerations as foundation input motion, hence avoiding complex soil-structure interaction analysis

Moreover, a limited number of numerical analysis were carried out to derive the simplified formulas.

For all these reasons, it was decided to carry out a broad parametric study by means of a 3D FEM numerical analysis. To this aim, a commercial computer code (ANSYS v.10) was selected, largely used in several fields of Engineering being able to provide solutions for different problems (statics, dynamics, heat flow, fluid flow, electromagnetic, etc.).

As shown before, dynamic structural analysis are carried out by solving the equations of motion (eq. 3.1). Depending on the way in which the applied forces are represented, different type of analysis can be identified (Figure 3.23):

- modal analysis
- transient analysis
- harmonic analysis

A modal analysis is used to determine the vibration characteristics of a structure in terms of natural frequencies and mode shapes. The right hand side of the equation 3.1 is considered to be zero. A modal analysis can also be taken as a basis for other more detailed dynamic analyses like transient analysis, harmonic analysis or even spectrum analysis based on the modal superposition technique. It is important to point out that the modal analysis is a linear analysis; prestress effects may be considered if the case.

A transient analysis is used to determine a single time history response of a structure when subjected to a general system of forces varying with time. On the right hand side of equation 3.1 any load vector may be specified. This type of analysis yields the displacement, strain, stress and force time history response of a structure to any combination of transient or harmonic loads.

To obtain a solution for the equation 3.1, a time integration has to be performed. In literature, several time integration algorithms are discussed in detail (see also Chapter 1). They can be broadly classified into implicit and explicit methods. Considering the stability of these two types of integration methods it has to be noted that implicit methods are usually unconditionally stable, meaning that different time step sizes can be arbitrarily chosen without any limitations originating from the method itself.

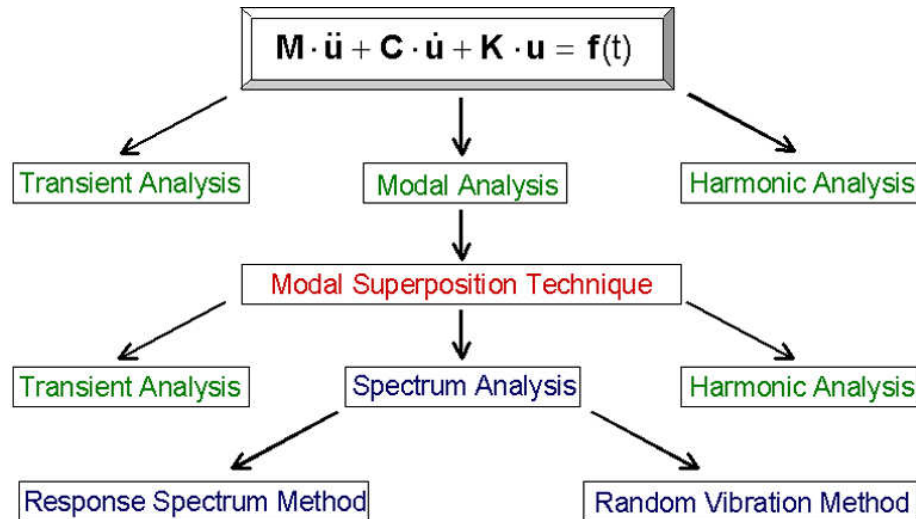


Figure 3.23: Classification of problems in structural dynamics

Explicit methods on the other hand are only stable if the time step size is smaller than a critical one which typically depends on the largest natural frequency of the structure. Due to the small time step necessary for stability reasons explicit methods are typically used for short-duration transient problems in structural dynamics.

Any sustained cyclic load will produce a sustained cyclic response in a structure which is often called a harmonic response. The harmonic response analysis solves the equation of motion (3.1) for linear structures undergoing steady-state vibrations. All loads and displacements vary with a sinusoidal law having the same known frequency although not necessarily in phase.

To solve a dynamic structural analysis, it is possible to use different solution options, precisely:

- Full method
- Reduced method
- Modal superposition method

The Full Method does not reduce the dimension of the considered problem since original matrices are used to compute the solution. As a consequence it is simple to use, all kinds of nonlinearities may be specified, automatic time stepping is available, all kinds of loads may be specified, masses are not assumed to be concentrated at the nodes and finally all results are computed in a single calculation. The main disadvantage of the Full Method is the fact that the required solution time will increase with the size of the considered model.

The Reduced Method originates from earlier years. Because of the reduced system matrices which are used to solve the transient problem, this method has an advantage when compared with the Full Method with respect to the required solution time. However, the user has to specify master degrees of freedom which represent the dynamic behaviour as good as possible. The only nonlinearity which can be specified is node-to-node contact via a gap condition. However, automatic time stepping is not possible. Consequently, this method is not very popular any more since all its disadvantages do not really compensate the advantage of lower costs in solution time.

The Modal Superposition Method usually reduces the dimension of the original problem as well since the transient analysis is finally performed in the modal subspace which has the dimension of the number of mode shapes used for the superposition. The main advantage is again the reduction of solution time. It turns out that this method is actually the most efficient one compared with the other two. The accuracy just depends on the number of mode shapes used for the modal superposition.

Wang and Nelson (2002) showed a comparison between Full Method and Modal Superposition Method. Each force vector in Figure 3.24 represents a load impulse of 1000 N acting during the time interval of $0 \text{ s} < t < 0.001 \text{ s}$. The time range of interest is considered to be $0 \text{ s} < t < 0.1 \text{ s}$. A constant time step size of $\Delta t = 0.0001 \text{ s}$ was chosen, and so 1000 time steps are performed altogether.

The comparison has been made looking to their performance in terms of CPU-Time; working in the modal subspace, the authors assumed the first ten mode shapes to be enough for an accurate representation of the dynamic response.

The following diagram in Figure 3.25 shows the transient response of the structure measured at Node A in the global y-direction (see Figure 3.24). Because of the transient load excitation, the structure resonates in its first damped natural frequency of 139.46 Hz.

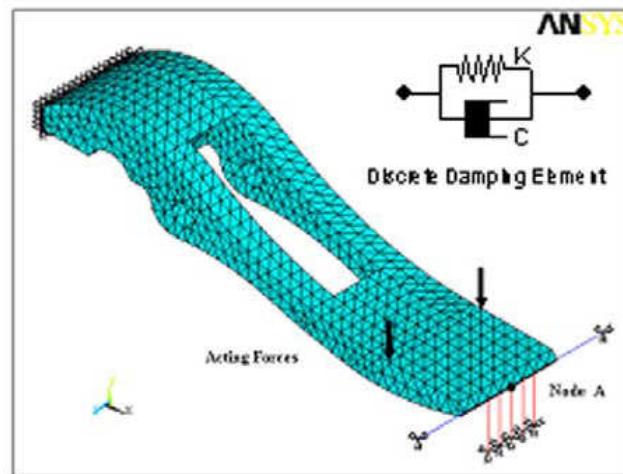


Figure 3.24: System with discrete damping elements (from Wang and Nelson, 2002)

Since the numerical results do not show any significantly differences by using the two methods, in Figure 3.25 are presented the results obtained by the Full Method.

The required CPU-Time was 3541050 s for the Full Method and 68740 s for the Modal Superposition Method (with a factor of 52). For this reason, the numerical analyses reported below were carried out by using Modal Superposition Method.

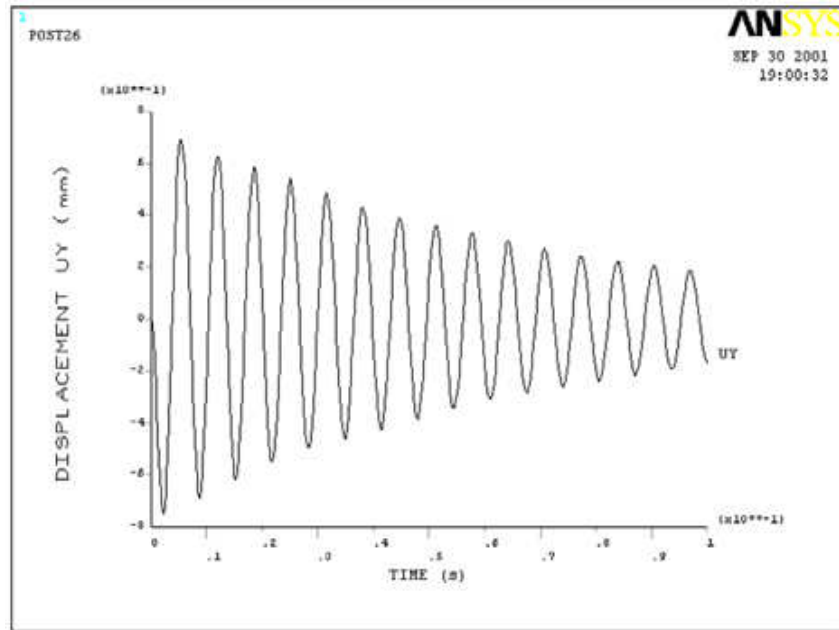


Figure 3.25: Displacements (mm) of node A in y-direction (from Wang and Nelson, 2002)

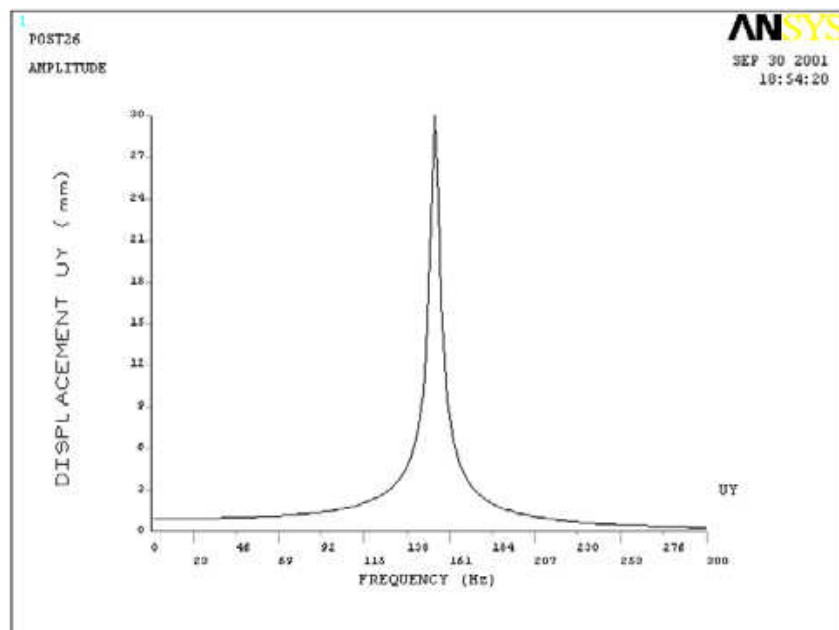


Figure 3.26: Displacements (mm) of node A in y-direction (from Wang and Nelson, 2002)

3.2.2 Overview of the analyses

A 3x3 pile group in different subsoil conditions have been analyzed with a constant thickness of 30 m. All the piles are 20 m length and 0.6 m diameter, spaced by 1.8 m (3·d) and connected to a raft 1 m thick.

Raft, piles and soil are modelled as linear elastic materials; for each of them, values for density, Young modulus and Poisson coefficient have been defined.

Among the different options given by ANSYS v.10 in terms of damping, a constant damping ratio ζ has been chosen.

The boundary conditions have been chosen in order to simulate at free-field the 1-D conditions.

On lateral boundaries, the vertical displacement (along Z-axis) are restrained.

At the base, the nodes are fully restrained, in order to simulate a rigid bedrock.

The size of the numerical model have been established comparing the results at boundaries with the local seismic response motion, ensuring that it is large enough to let the waves scattered by piles to damp down on.

Due to the presence of a symmetry plane (parallel to XZ), where only the displacement along Y-axis are restrained, and to the presence of an antisymmetry plane (parallel to YZ), on which the displacement along Z-axis are restrained, a total number of 12605 nodes and 10980 elements have been used (Figure 3.27).

All the elements are 8-node isoparametric bricks (see Figure 3.28) with extra shape functions; hence, the displacement u is given by:

$$\begin{aligned}
 u = \frac{1}{8} [& u_I (1-s)(1-t)(1-r) + u_J (1+s)(1-t)(1-r) + \\
 & + u_K (1+s)(1+t)(1-r) + u_L (1-s)(1+t)(1-r) + \\
 & u_M (1-s)(1-t)(1+r) + u_N (1+s)(1-t)(1+r) + \\
 & + u_O (1+s)(1+t)(1+r) + u_P (1-s)(1+t)(1+r)] + \\
 & + u_1 (1-s^2) + u_2 (1-t^2) + u_3 (1-r^2)
 \end{aligned} \tag{3.40}$$

where u_1, u_2, u_3 are nodeless displacement of the extra shape function.

All the analyses have been carried out by a modal analysis in the following way:

- a) a certain number of modes were extracted in order to adequately describe the response of the model by superposition of their contributes
- b) in the frequency domain, a unit acceleration (complex value with imaginary part equal to 0 and real part equal to 1) was applied at bedrock in order to get the steady-state response in terms of the various parameters of interest (displacement, stress, etc.).

Each output parameter (for example, displacement at surface) can be treated as transfer complex function (from bedrock acceleration to surface displacement): multiplying the latter by the Fourier transform of a given acceleration time history the Fourier spectrum of the parameter is obtained, and through an Inverse Fourier Transform its time history is then derived.

The check of the numerical procedure implemented was made by comparing the FE results with those coming from free-field seismic 1D analysis as obtained by EERA (Bardet et al., 2000), a program working in the frequency domain.

The input signal is TOLMEZZO, from Italian Database (Scasserra et al., 2006), scaled to 1 m/s^2 , applied along the x -axis (long direction); its acceleration time history and Fourier spectrum are shown in Figure 3.29.

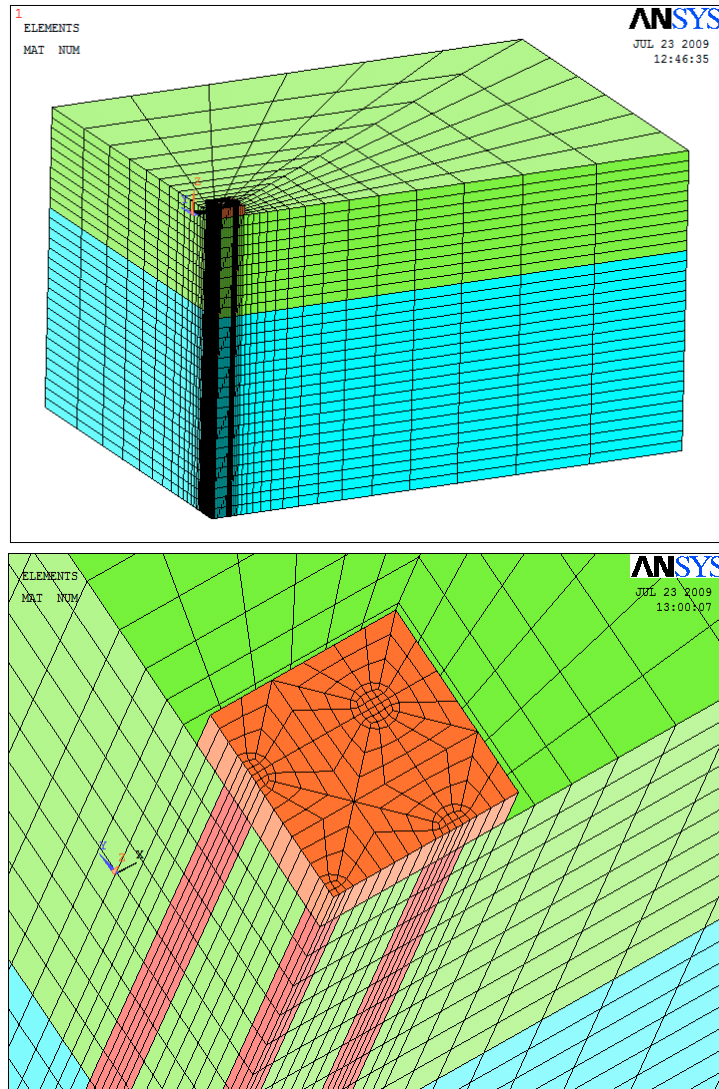


Figure 3.27: FE model

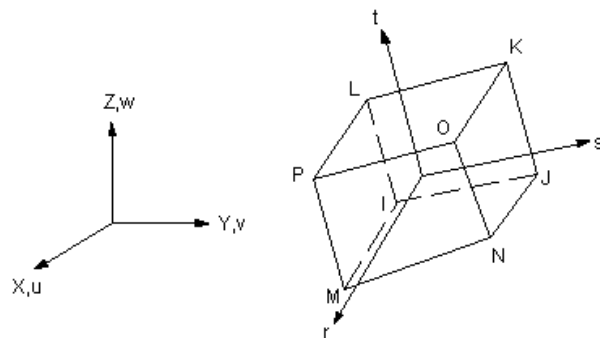


Figure 3.28: 3-D solid 8-node brick

The comparisons are reported in Figure 3.30, 3.31 and 3.32; as it can be seen, the agreement is very good.

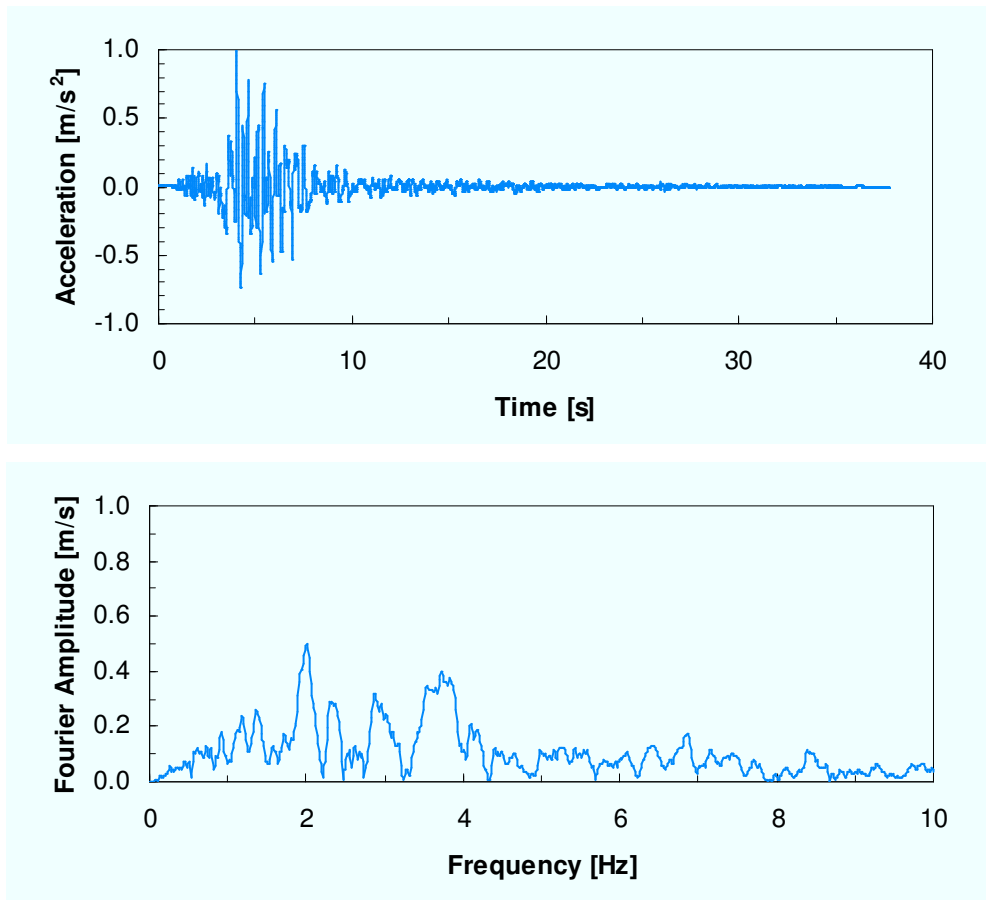


Figure 3.29: TOLMEZZO signal: acceleration time history and Fourier spectrum

3.2.3 Kinematic interaction analyses for piles embedded in homogeneous deposits

3.2.3.1 Effect of modes of vibration

In Table 3.1 and Figure 3.33 the first three modes of vibration of a system of a pile group embedded in an homogeneous soil is shown. It may be seen that the presence of the piles does not modify the frequency of vibration; in fact, for an homogeneous layer on rigid bedrock the first three frequencies are:

$$\omega_1 = \frac{V_s}{4H} \quad ; \quad \omega_2 = 3 \frac{V_s}{4H} \quad ; \quad \omega_3 = 5 \frac{V_s}{4H} \quad (3.41)$$

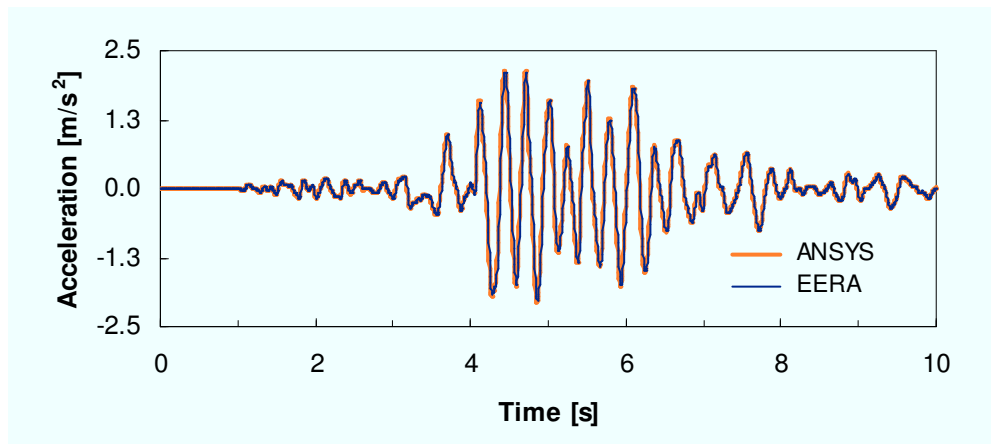


Figure 3.30: Comparison with EERA in terms of acceleration time history at ground surface ($V_s=400 \text{ m/s}$)

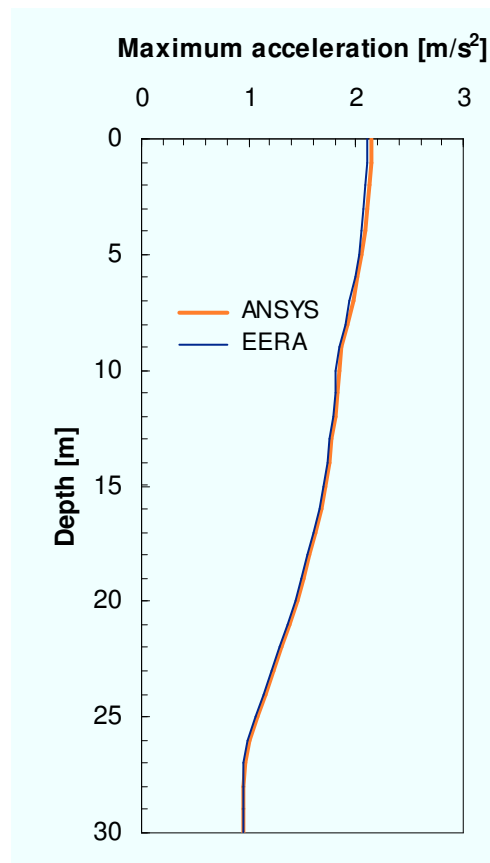


Figure 3.31: Comparison with EERA in terms of maximum accelerations profile ($V_s=400 \text{ m/s}$)

On the contrary, the piles modify the stress and strain field only up to a certain distance. The deformed shape and the contours show that the displacements are zero at one depth (bedrock) for the first mode, respectively at two and three different values of depth for the second and third mode, as it is well known from the seismic local response theory.

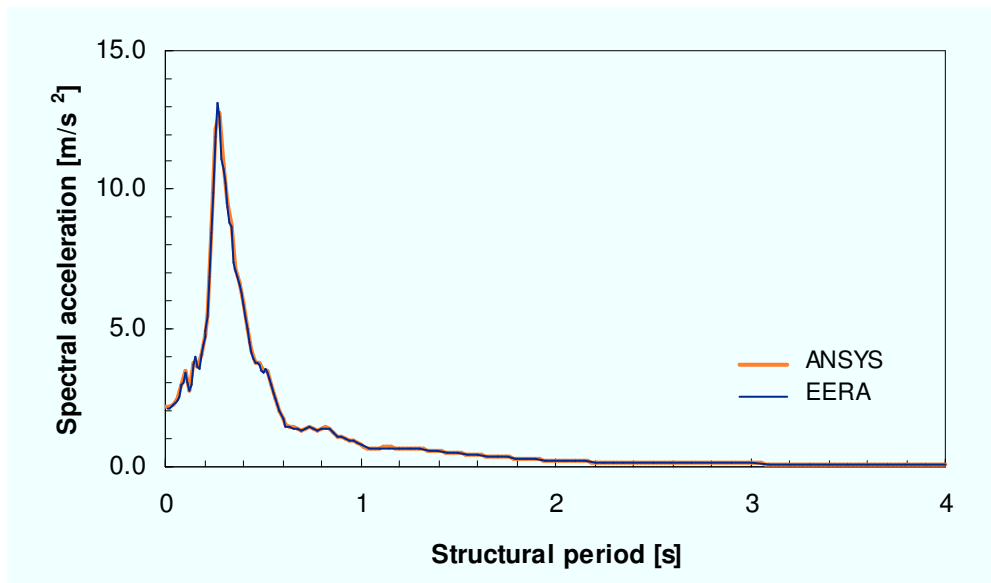


Figure 3.32: Comparison with EERA in terms of spectral accelerations ($V_s=400$ m/s, $D=5\%$)

Both the participation factor and the effective mass decrease increasing the natural mode of vibration (Table 3.1). The former is negative for mode n. 2, meaning that its contribution is opposite to that of the modes n. 1 and 3.

To verify the effect of the modes of vibration on the response, several analyses considering a different number of modes have been carried out.

In Figure 3.34 is reported the bending moment at pile cap and at a depth of 10 m as function of the number of modes³. As it can be seen, starting from 1000 mode of vibration (that means taking into account frequencies up to 8.65 Hz, 10 times the first natural frequency), the response is quite stable. The first mode alone seems not able to describe adequately the phenomenon.

3.2.3.2 Group effects

To investigate the role of the soil stiffness in group effects, several analyses have been performed. In Figure 3.35 the results relative to the case $V_s=100$ m/s is shown, in terms of maximum bending moments with depth.

No group effects are evident among piles in terms of bending moments; nevertheless some differences exist respect to single pile. In Figure 3.36 it may be seen that in the superficial layers single pile experiences a larger bending moment, even if at pile head it is very similar to the case of the group.

³ these modes are not the natural modes of vibration of the uniform stratum on rigid bedrock, but the modes extracted by the FE model (its number of modes is equal to its degrees of freedom).

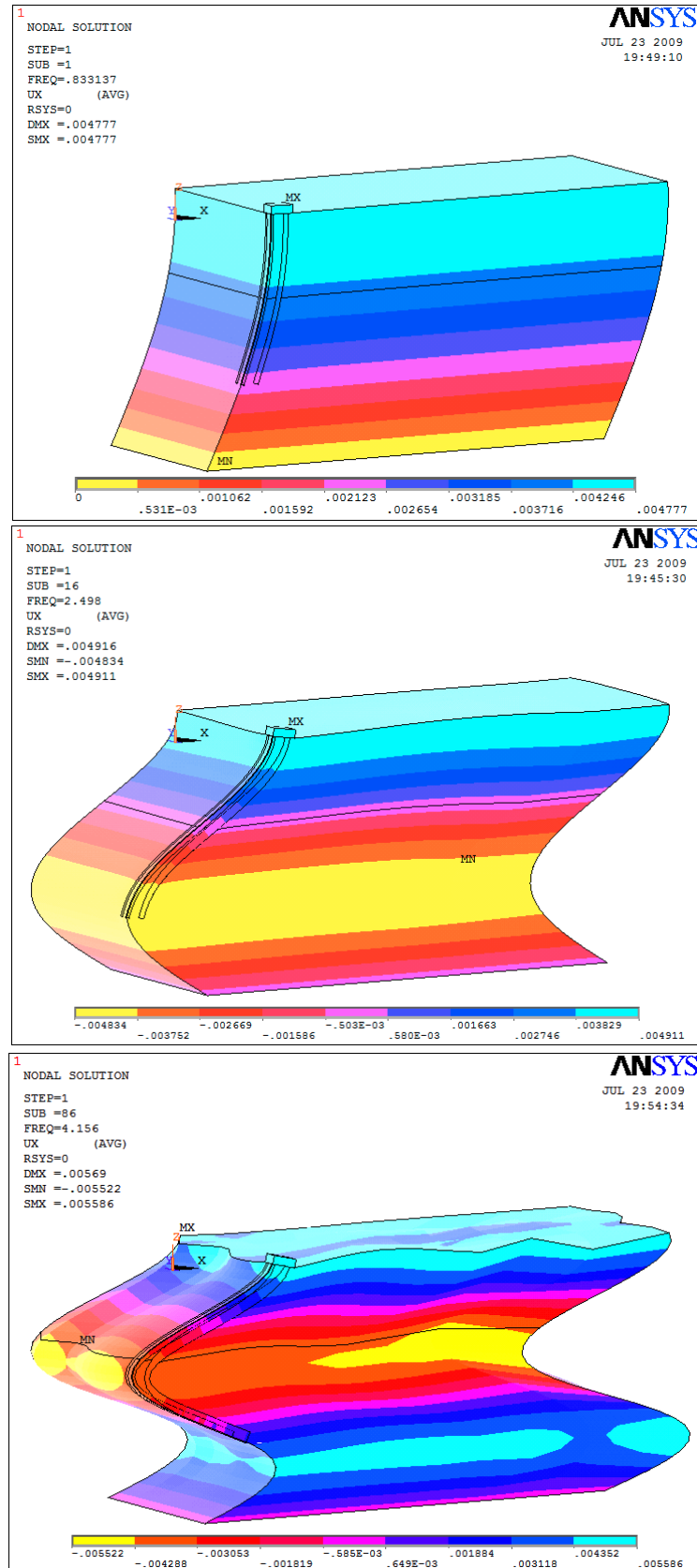


Figure 3.33: Displacement contours of the first three modes of vibration (homogeneous soil, $H=30\text{m}$, $V_s=100\text{m/s}$, $E_p=30\text{GPa}$; $D=10\%$, $\rho=1.7\text{t/m}^3$).

Table 3.1: Modes of vibrations

Mode n.	Freq. (Hz)	Period [s]	Participation factor	Ratio
1	0.83	1.20	269.0	1.000
16	2.50	0.40	-89.4	0.333
86	4.16	0.24	53.1	0.198

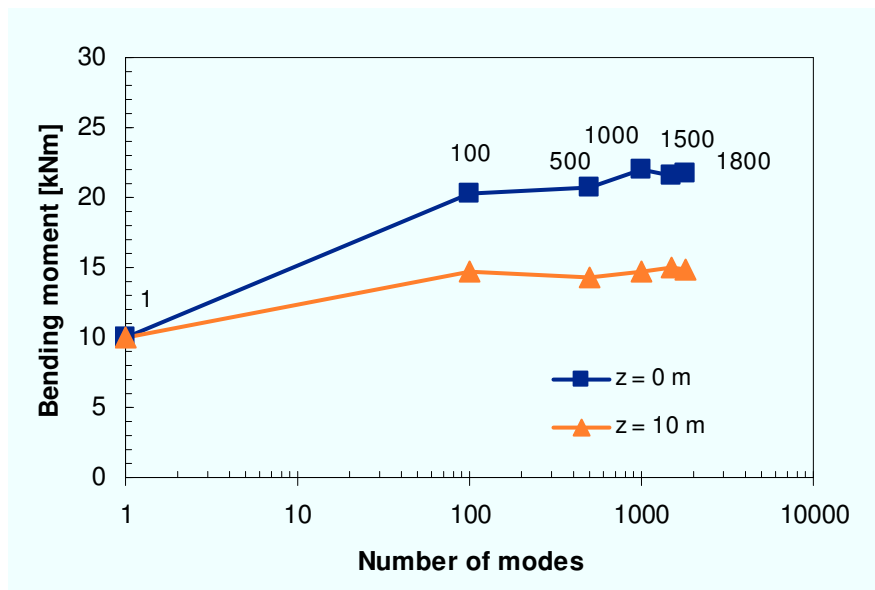


Figure 3.34: Effect of modes of vibration on the response of an homogeneous soil layer

Another interesting result is that the bending moment obtained from the free-field curvature (eq. 3.6) is practically the same of the actual maximum moment along the pile, except for the pile toe where different stress conditions exist as a consequence of soil restraint.

The same conclusions apply increasing the soil stiffness (Figure 3.37 and Figure 3.38).

Figure 3.39 shows the distribution of bending moments along the piles at a given time t , precisely at a time when the maximum bending moment at pile cap occurs (that is the same for pile group and single pile): once again, the previous results are confirmed.

As briefly mentioned before, all the analyses show a bending moment at pile toe. This result is in contrast with that from literature based on BDWF model. Although apparently wrong, it is believed that it is due to the choice of brick (solid) elements for modelling the piles, hence giving normal stresses into the pile to be equilibrated by soil stresses.

It is also interesting to note that this bending moment at pile toe increases for decreasing pile-soil relative stiffness (up to 1.5 times the pile cap moment for $V_s = 400$ m/s, $E_p = 30$ GPa, Figure 3.39).

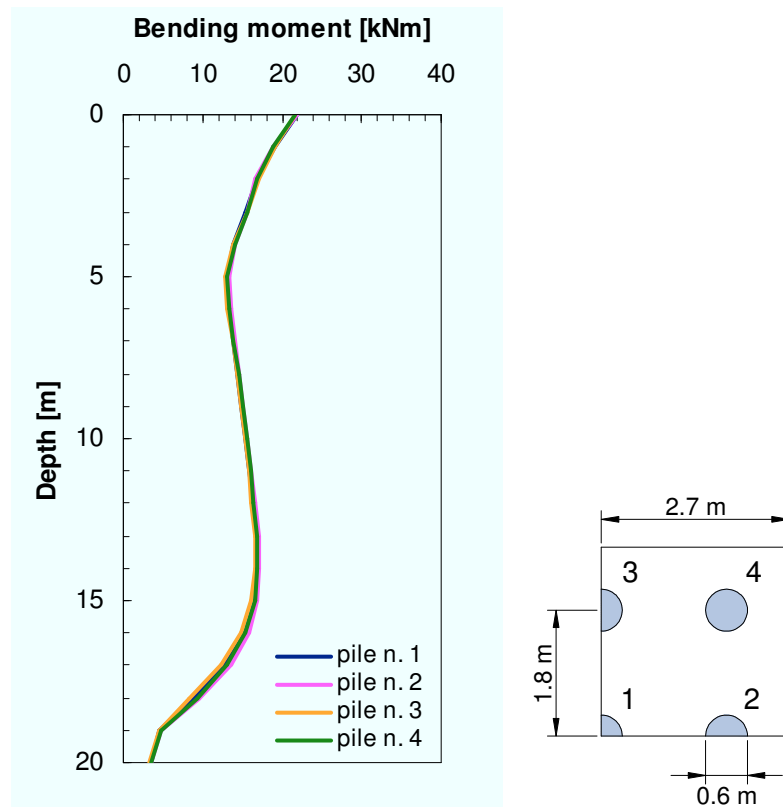


Figure 3.35: Distribution of maximum bending moments along the piles (homogeneous soil, $V_s=100$ m/s)

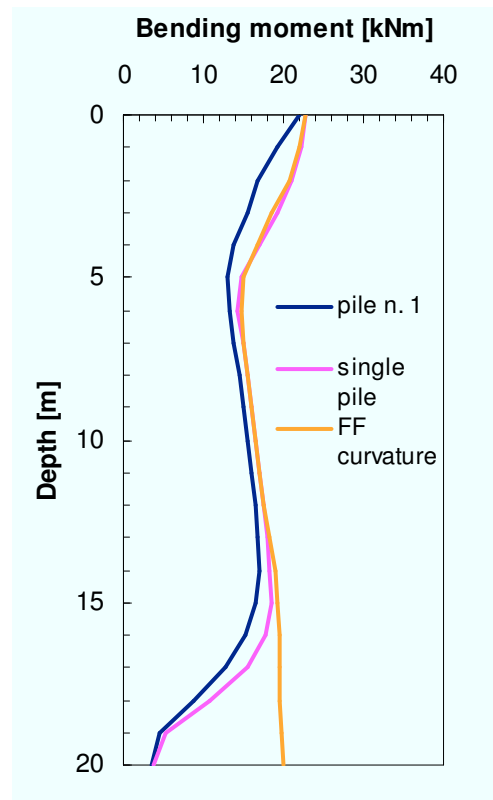


Figure 3.36: Differences between pile group and single pile

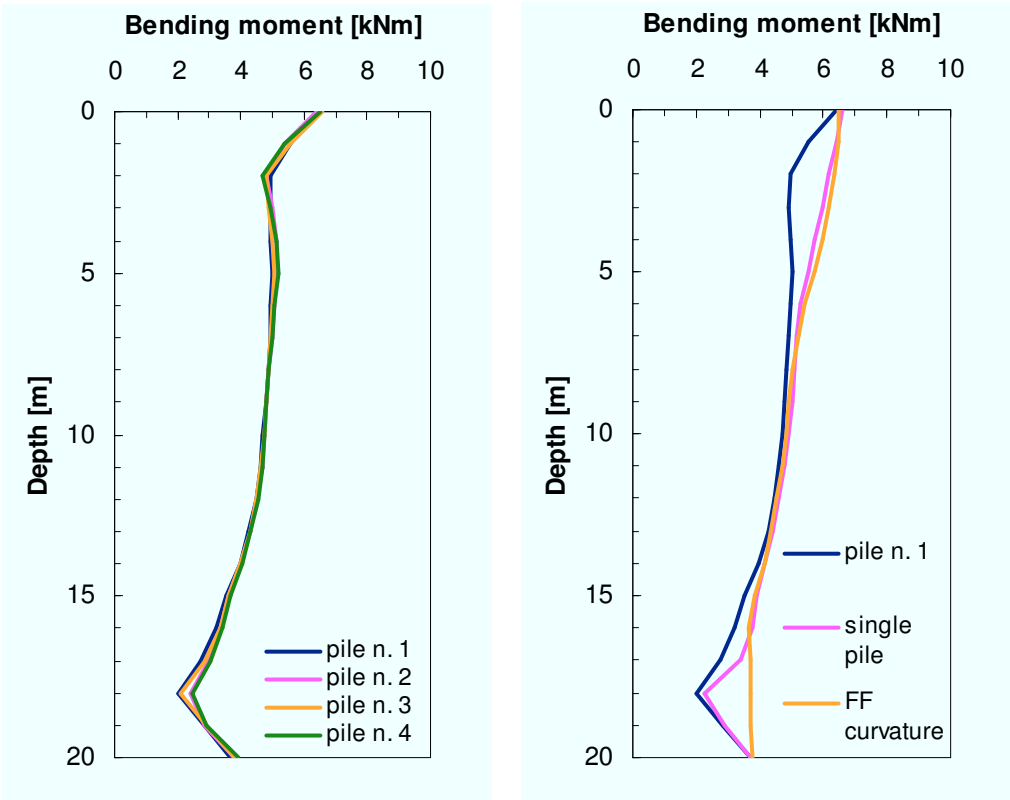


Figure 3.37: Group effects ($V_s=200$ m/s)

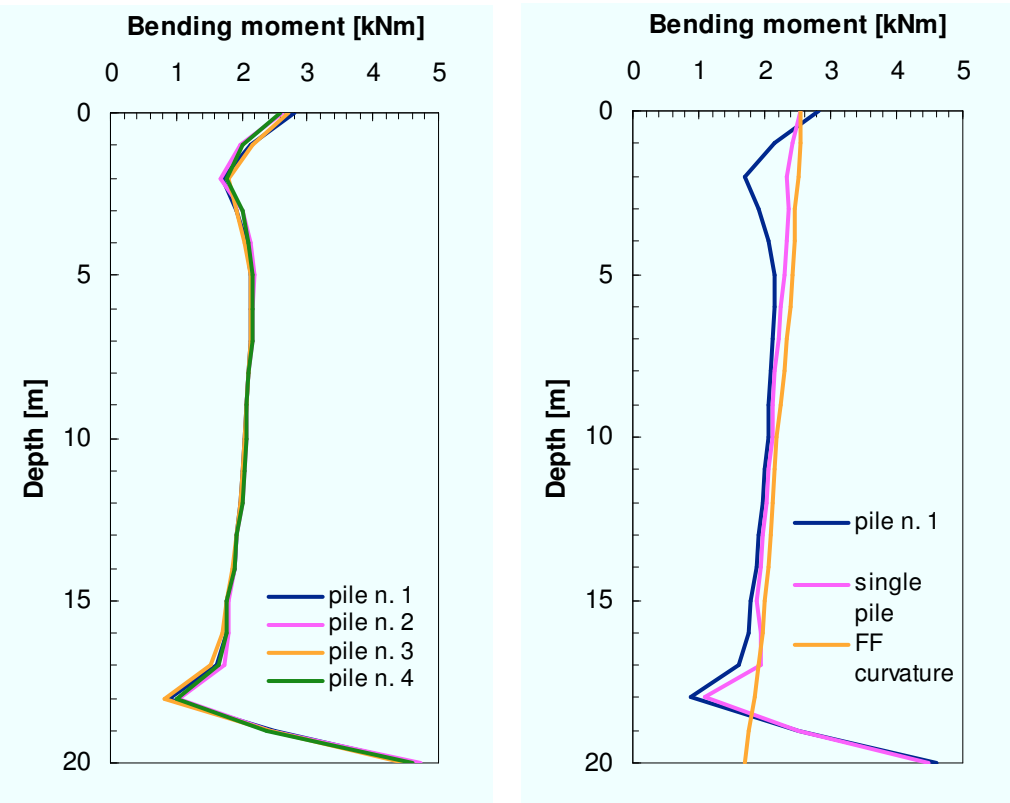


Figure 3.38: Group effects ($V_s=400$ m/s)

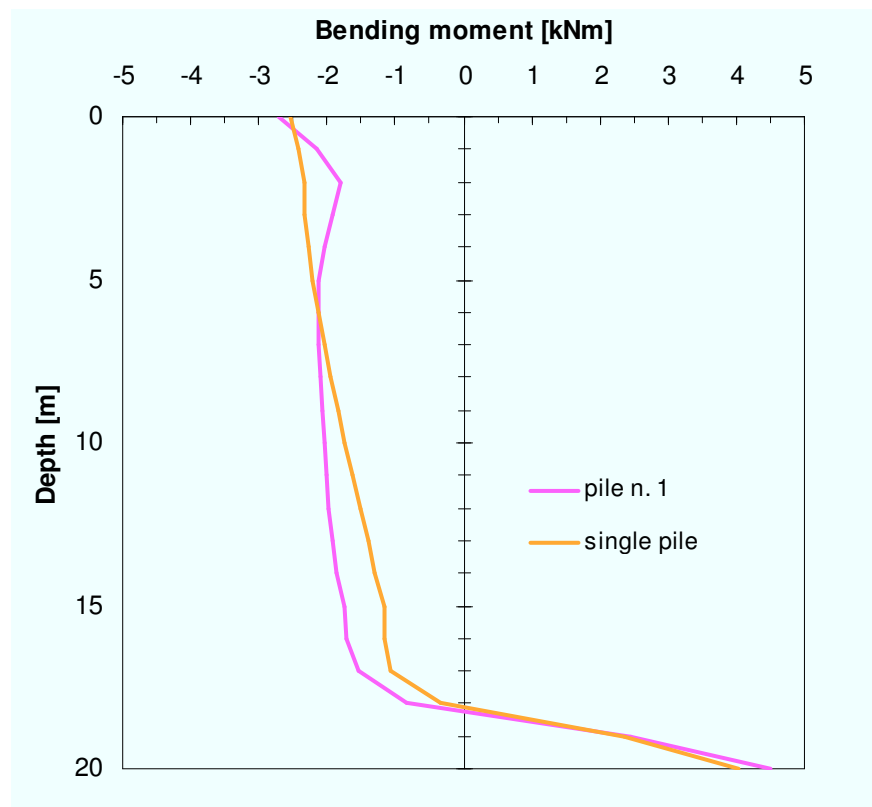


Figure 3.39: Distribution of bending moments along the pile in the instant in which the cap moment is maximum ($V_s=400$ m/s)

In order to investigate how the stiffness of the raft changes the response of the piles, the same analysis were carried out increasing by a factor 1000 the stiffness of the raft. Some results are shown in Figure 3.40: as it can be seen, for piles 1 and 2 there are no changes (and, hence, are not reported in the graph), while some effects are revealed for piles 3 and 4 even if very small.

3.2.3.3 Displacements and rotational component for pile groups

Due to the scattering of the waves from the piles, kinematic interaction generally causes an alteration of free-field signal; moreover, a rotational component of motion could rise up.

High frequency components of acceleration are more sensitive to be filtered with respect to lower ones. This clarifies that high-frequency signals are responsible of a larger difference between the two surface motions; on the contrary, low-frequency signals (such as TOLMEZZO, fig. 3.29) provoke a more similar motion of pile cap and soil (Figures 3.41 and 3.42). This matter will be discussed in detail later on.

From the theoretical point of view, the surface motion parameters (displacement, rotation) increase when the relevant frequencies of the seismic signal are close to the first frequency of the soil, hence depending on the signal and on the soil.

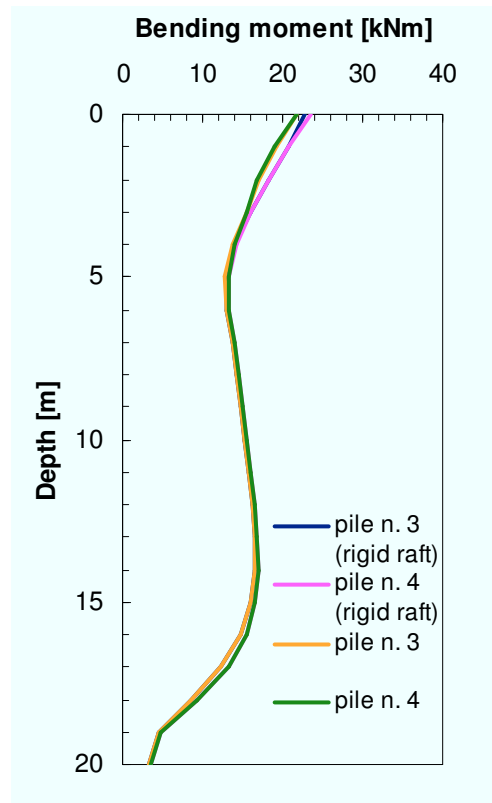


Figure 3.40: Effect of the stiffness of the raft on the maximum bending moments ($V_s=100$ m/s)

Despite that, the relevant frequencies of the signal are generally low, and its Fourier spectrum amplitude decrease with increasing frequency. It determines that, keeping fixed other influencing conditions like, for instance, the pile group layout, the softer is the soil layer (depending on its thickness and stiffness) the larger are surface motion parameters (Figures 3.43 and 3.44).

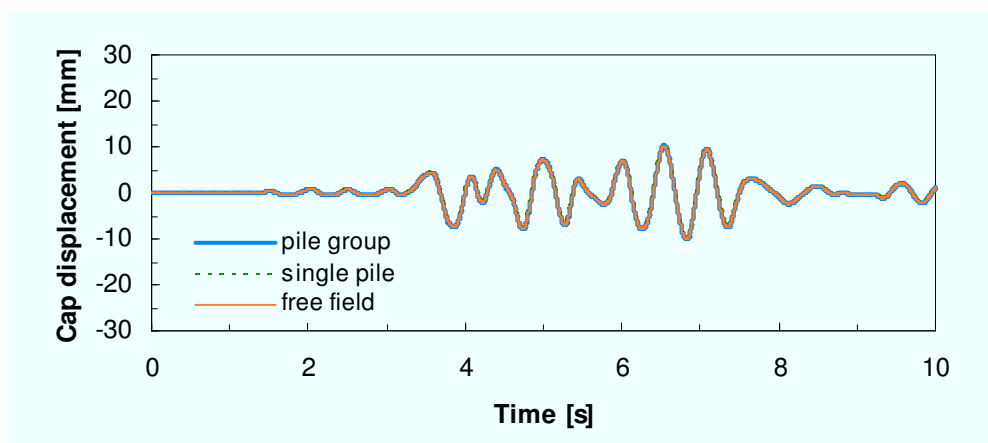


Figure 3.41: Cap horizontal displacement time history ($V_s=100$ m/s, $E_p=30$ GPa)

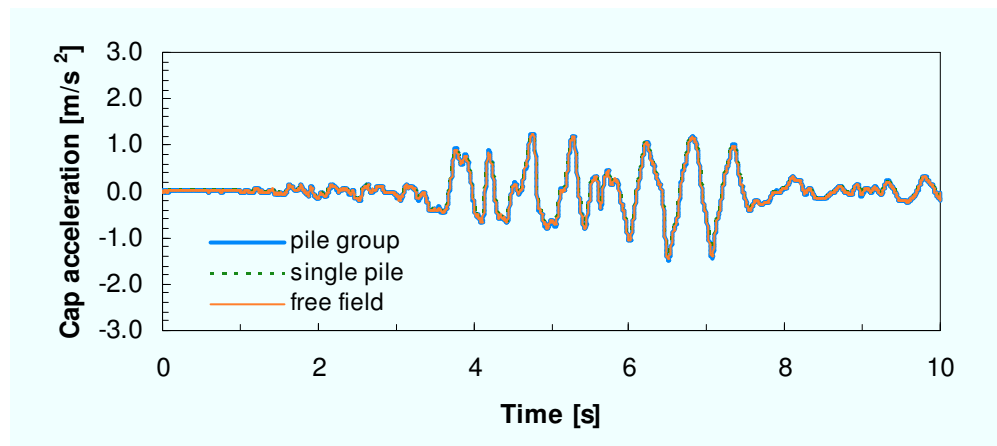


Figure 3.42: Cap acceleration time history ($V_s=100$ m/s, $E_p=30$ GPa)

Figure 3.45 shows the normalized amplitudes of the transfer functions from bedrock acceleration to rotation, acceleration and relative displacements of the cap. It is interesting to notice the different frequency distribution among the three different parameters of motion.

The acceleration is much more dependent on high frequencies with respect to displacements, because, for an harmonic input, the response in accelerations is ω^2 times the displacement. The rotation, despite being proportional to vertical displacement, is more sensitive to high frequencies with respect to the horizontal displacement, similarly to the horizontal acceleration. Such a similarity is confirmed by the phases of the transfer functions.

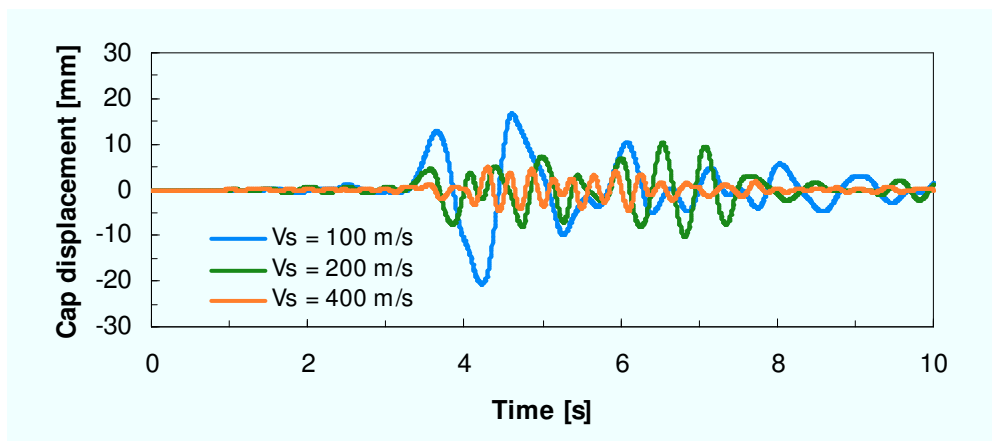


Figure 3.43: Cap displacement time histories for different soil stiffnesses.

The rotational component of motion generates axial forces in the piles (Figure 3.47), hence stressed not only by kinematic bending moments. Such axial (tensile or compressive) forces obviously increase with increasing rotational component of raft motion, even if generally negligible for design purposes.

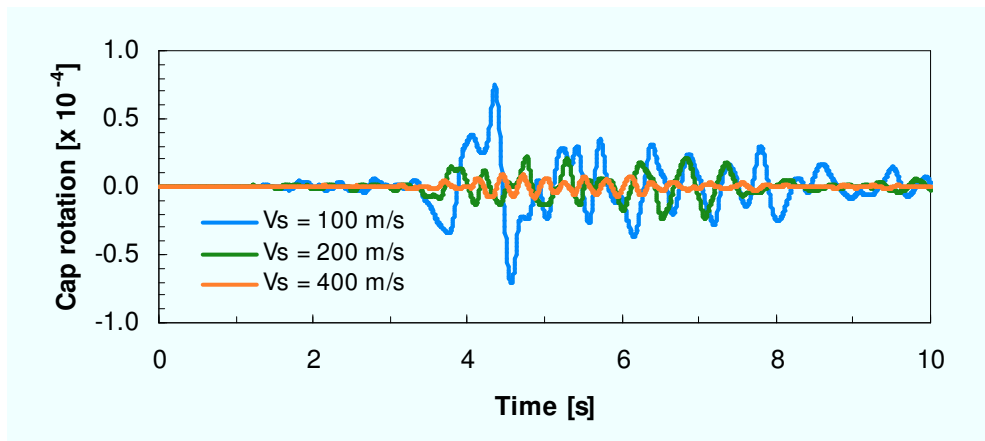


Figure 3.44: Cap rotation time histories for different soil stiffnesses.

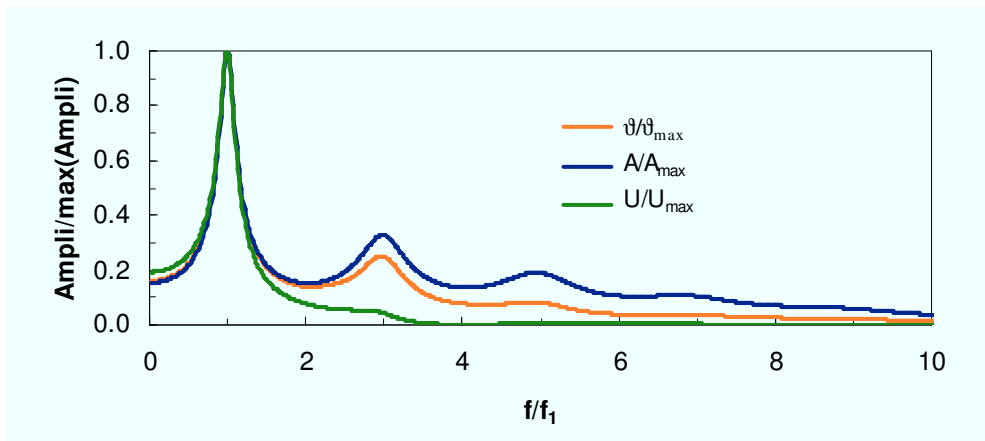


Figure 3.45: Normalized amplitudes of the transfer functions ($V_s=100$ m/s)

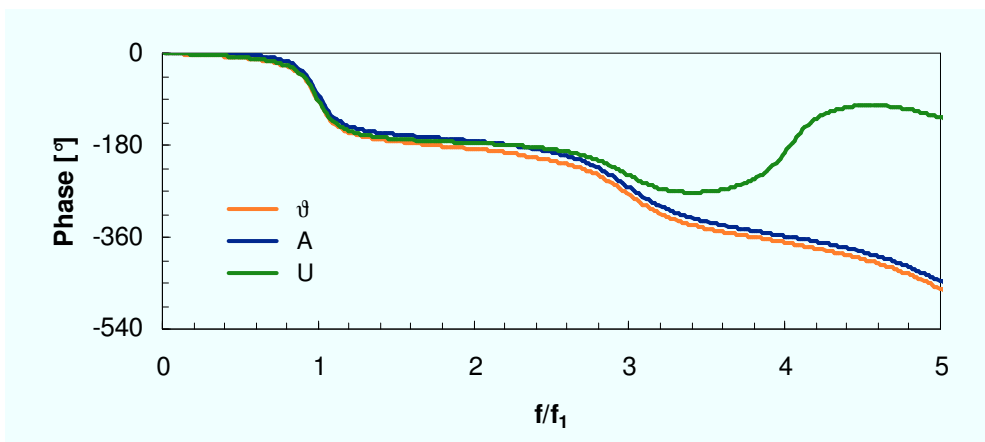


Figure 3.46: Phase of the transfer functions ($V_s=100$ m/s)

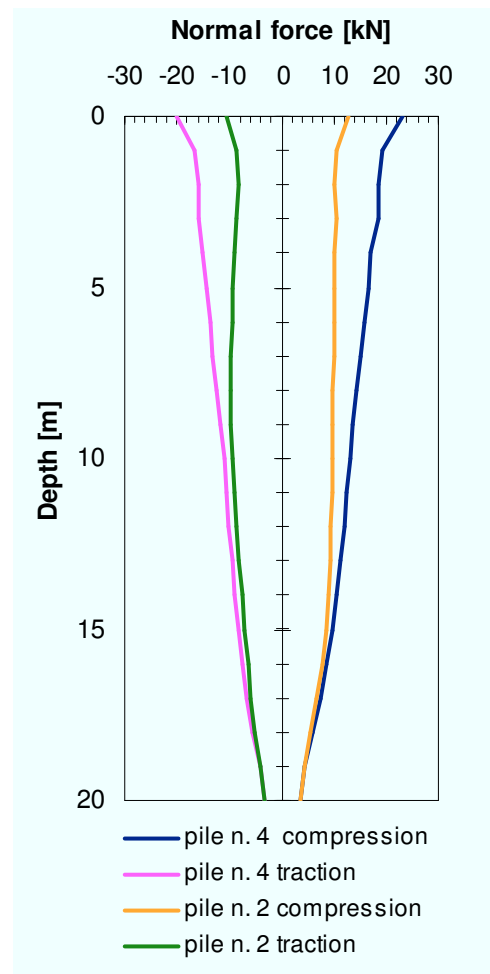


Figure 3.47: Tensile and compression maximum normal force ($V_s=100$ m/s, $E_p=30$ GPa)

3.2.4 Kinematic interaction analyses for piles embedded in 2-layers deposits

As well known from 1-D ground response analysis, the presence of an interface at a certain depth separating two layers generally increases the acceleration and the displacement at surface. As it can be seen from the Figure 3.48, the transfer function relative to the layered subsoil is generally above that derived for homogeneous subsoil.

The presence of an interface separating two layers with different stiffness causes the pile can't follow the soil deformations.

At the interface, the shear stress has to be the same for the equilibrium condition but, due to the different stiffness, different shear strain at interface are expected, hence the curvature becomes infinite. On the other hand, the pile will exhibit continuous shear strain.

Such different response at the soil interface provokes a concentration of strains and, hence, a peak in bending moment.

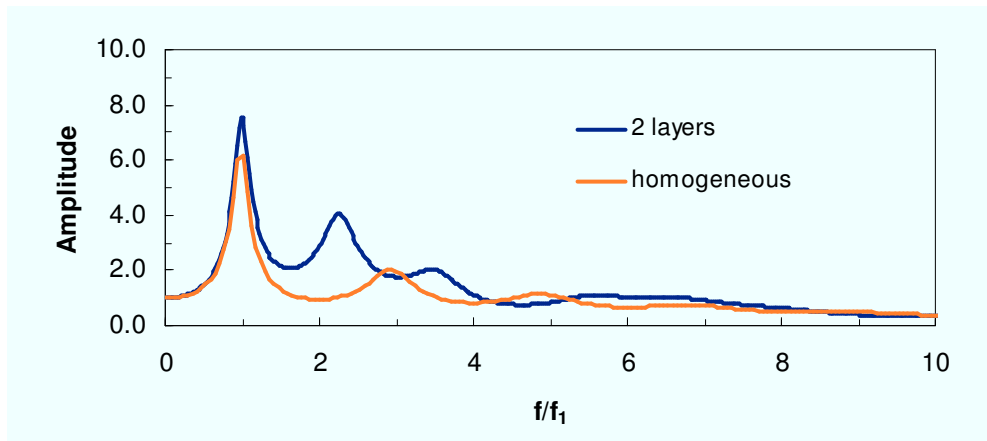


Figure 3.48: Acceleration transfer function from bedrock to surface for an homogeneous layer and for a 2-layered soil (interface at 10 m separating 100 and 400 m/s layers)

Figure 3.49 shows the profile of maximum bending moment for a case in which at the depth of 10 m an interface separates two layers having a shear wave velocity equal to 100 and 400 m/s.

As it can be seen, no group effects occur among the piles of a group; nevertheless, the single pile presents slightly larger moments.

Figure 3.49 also highlights another important result: apart from the neighbours of soil interface, the soil curvature is equal to the pile curvature. It means that the soil interface can be considered a singularity whose effect vanishes with distance, where the pile comes back to follow the soil deformations. As it will be shown later, it is true also for very high stiffness ratios between pile and soil.

In Figure 3.50 is shown the effect of modes of vibration on the kinematic pile response. As it can be seen, increasing the number of modes from 100 to 1800 does not change significantly pile response, hence suggesting that a smaller number of modes can be considered to adequately define the kinematic pile response.

As suggestion for practical purposes, particularly relevant is that the response of a single pile does not significantly differ from that of the piles belonging to a group; moreover, the single pile analysis gives larger kinematic bending moments, thus its use can be considered conservative.

3.2.5 Curvature and acceleration ratios vs. frequency

In Figure 3.51 a comparison between transfer functions from bedrock acceleration to pile and soil curvature is shown, as a function of dimensionless frequency.

Such results are in a good agreement with those given by Nikolaou et al 2001.

It is confirmed that even large pile-soil stiffness ratios allow pile and soil to exhibit the same curvature in an homogeneous deposit at least within the range of significant frequencies

($a_0 < 0.15$); for larger values of pile-soil relative stiffness (Figure 3.52, $E_p/E_s = 100000$), pile and soil curvatures start to be different, also for low frequencies.

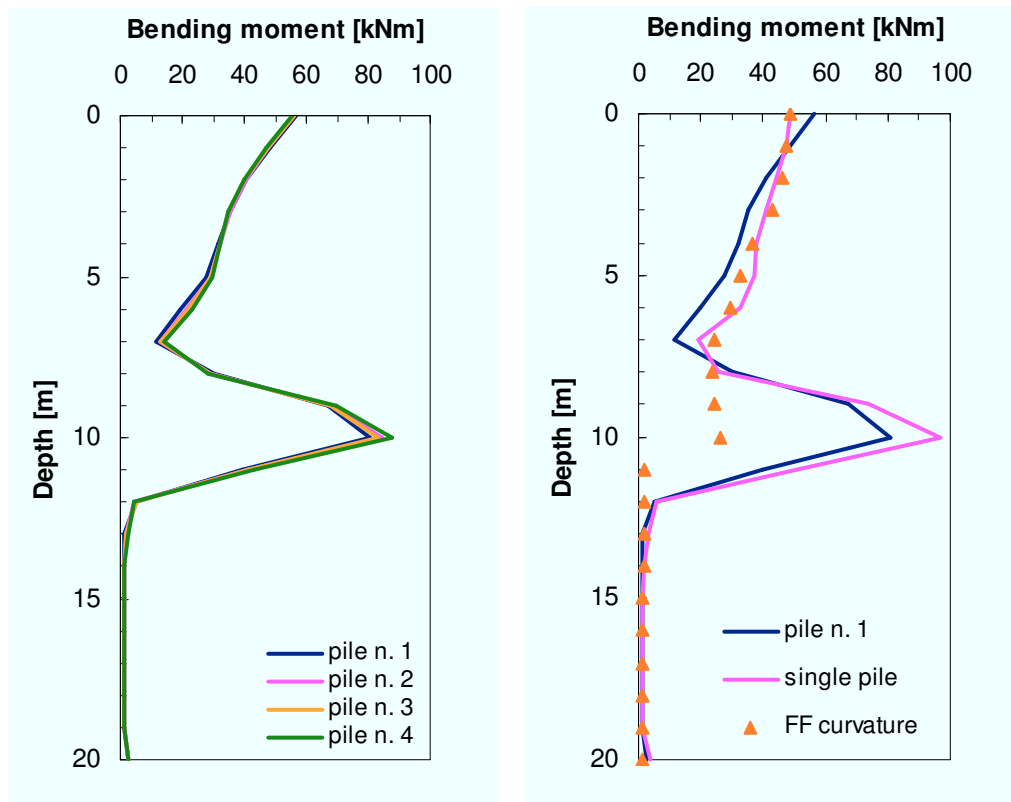


Figure 3.49: Profile of maximum bending moments along the depth for a group and for a single pile

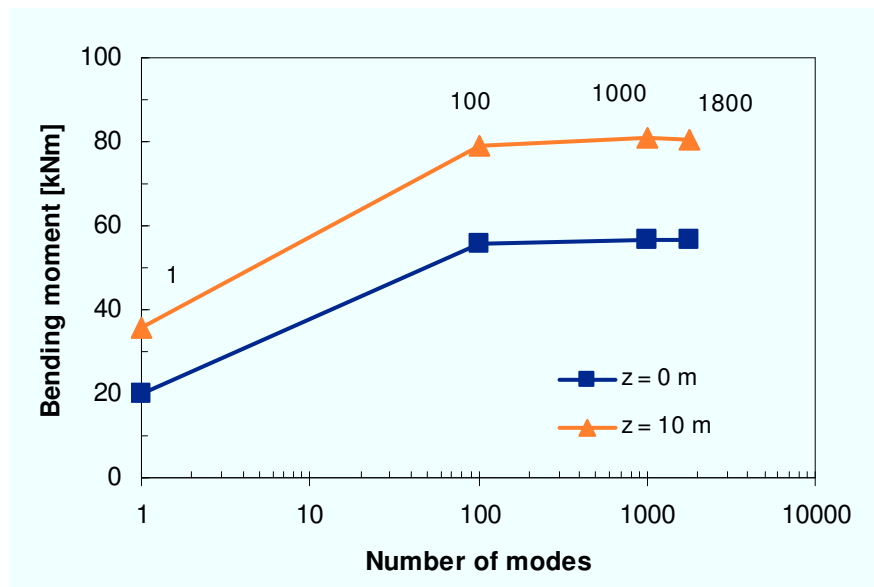


Figure 3.50: Effect of modes of vibration on the response of a 2-layers soil.

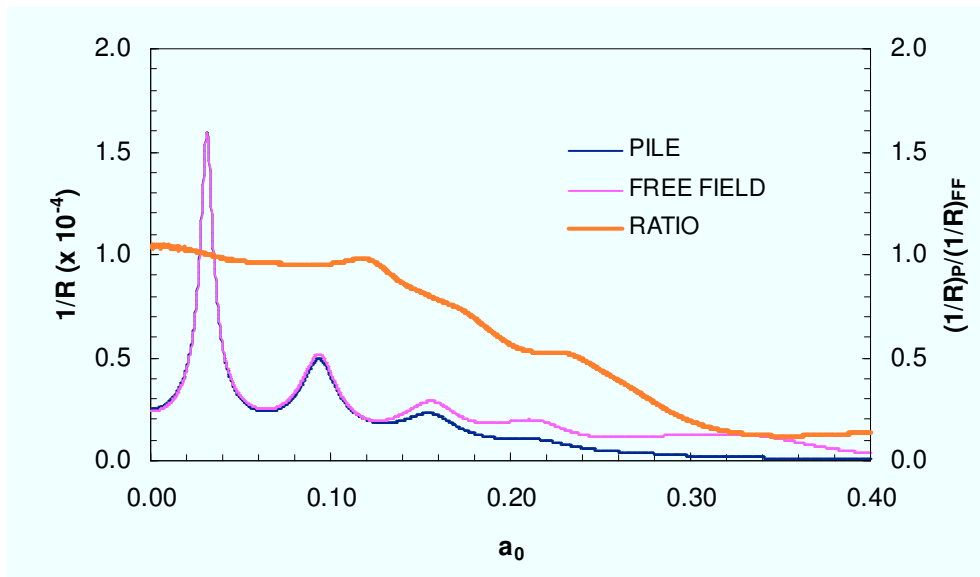


Figure 3.51: Transfer functions and curvature ratio against frequency ($V_s = 200$ m/s, $d = 0.6$ m, $L/d = 33$, $E_p/E_s = 10000$).

It has been seen that kinematic interaction affects both bending moments in the piles and their (filtered) acceleration; the two phenomena are not independent each other; Figure 3.53 shows that the acceleration ratio has the same trend of the curvature ratio with frequency.

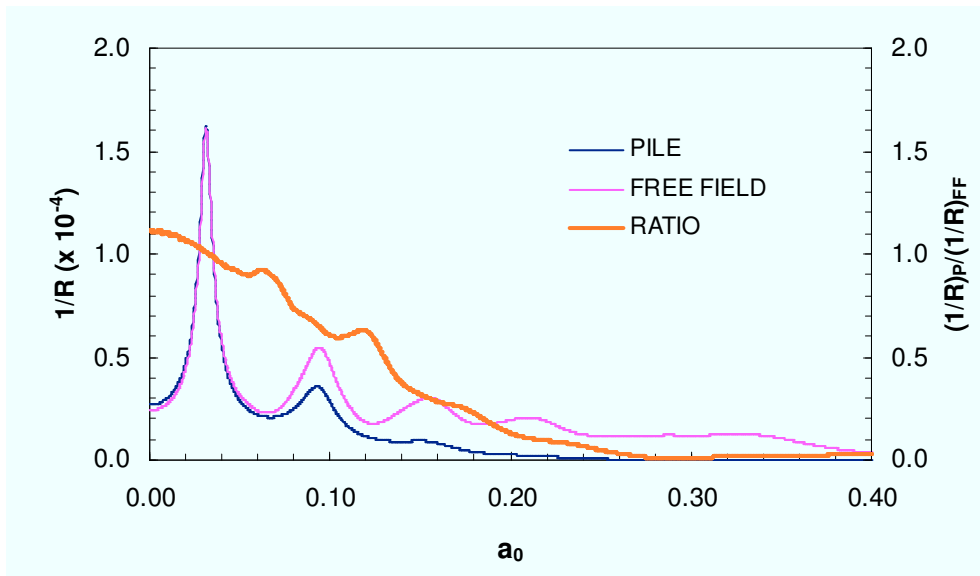


Figure 3.52: Transfer functions and curvature ratio against frequency ($V_s = 200$ m/s, $d = 0.6$ m, $L/d = 33$, $E_p/E_s = 100000$).

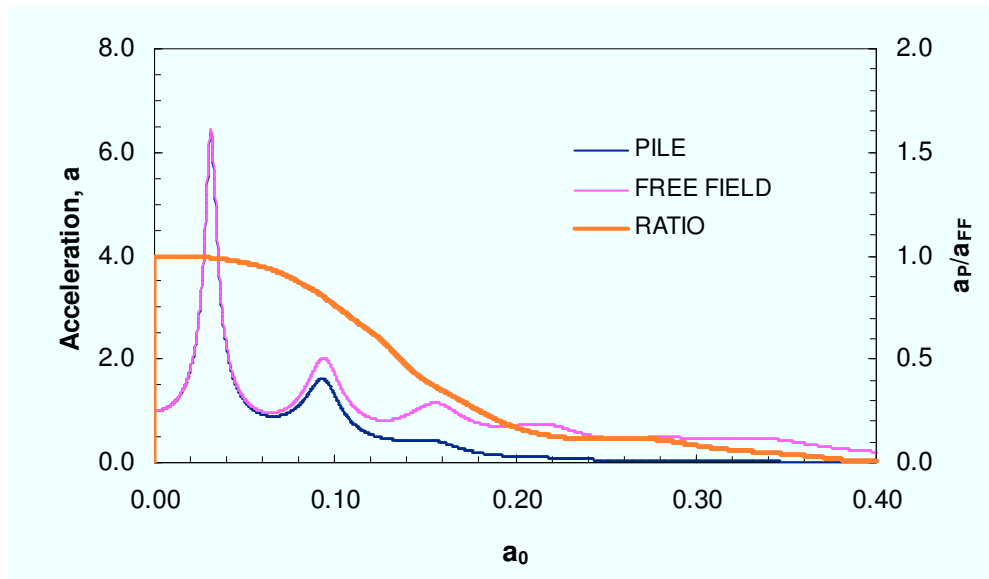


Figure 3.53: Transfer functions and acceleration ratio against frequency ($V_s = 200$ m/s, $d = 0.6$ m, $L/d = 33$, $E_p/E_s = 100000$).

3.2.6 Parametric studies

In order to understand the influence of the various parameters on kinematic response, two extensive parametric studies have been performed. They concern 2-layers deposits, and look for the effect exerted by input signal, depth of interface, stiffness contrast between the two layers and stiffness ratio between pile and first layer. The fixed parameters for the first one are:

$L =$	24 m
$d =$	1 m
$H =$	30 m
$E_I =$	50 MPa
$\rho_p =$	2.5 t/m ³
$\rho_{s1} =$	1.6 t/m ³
$\rho_{s2} =$	1.8 or 2.0 t/m ³
$\beta_p =$	0.1
$\beta_{s1} =$	0.1
$\beta_{s2} =$	0.1
$\nu_p =$	0.2
$\nu_{s1} =$	0.3
$\nu_{s2} =$	0.3

while its variable parameters are reported in Table 3.2.

Table 3.2: Variable parameters considered in parametric study n. 1

SIGNALS	E_p/E_1	V_{s2}/V_{s1}	h_1/d
BORGIO CERRETO	300	1.5	2
STURNO	1000	2	4
NOCERA UMBRA	10000	3	8
TOLMEZZO		6	16
SAN ROCCO			
TARCENTO			

In this study the variability of the stiffness ratio E_p/E_1 is taken into account fixing $E_1 = 50$ MPa; note that this results in pile Young moduli (for $E_p/E_1 = 10000$) out of typical civil engineering applications; nevertheless these cases can be useful to analyze the behaviour of rigid piles.

In the second parametric study the fixed parameters are the following:

$H =$	30 m
$d =$	0.5 m
$E_p =$	30 GPa
$\rho_p =$	2.5 t/m ³
$\rho_{s1} =$	1.6 t/m ³
$\rho_{s2} =$	1.8 or 2.0 t/m ³
$\beta_p =$	0.1
$\beta_{s1} =$	0.1
$\beta_{s2} =$	0.1
$\nu_p =$	0.2
$\nu_{s1} =$	0.3
$\nu_{s2} =$	0.3

The variable parameters are shown in the subsequent table.

Table 3.3: Variable parameters considered in parametric study n. 2

SIGNALS	E_p/E_1	V_{s2}/V_{s1}	h_1/d	L/d
BORGIO CERRETO	150	1.5	4	24
STURNO	666	2	8	40
NOCERA UMBRA	1500	3	16	
TOLMEZZO				
SAN ROCCO				
TARCENTO				

Further informations about the signals are available later on in the Figures 3.91 and 3.92.

The density of the second layer is equal to 1.6 t/m^3 when the stiffness contrast is 1.5 or 2, 1.8 t/m^3 when the latter is equal to 3 or 6.

In total 612 cases have been analyzed.

The FE model is shown in Figure 3.54; the numerical settings and procedures are the same of those described above, with the exception that the number of modes taken into account for the superposition is equal to 2000.

The results at free-field, as in the previous analyses, show an excellent agreement with the program EERA in terms of profile of maximum accelerations, response spectra at surface and acceleration time history.

The results for the pile, in terms of stresses, strains or internal forces have been processed to investigate the role of each parameter that rules in a significant way the dynamic phenomenon.

3.2.6.1 Effect of the depth of the interface

When $h_1 < L_a$ the bending moment at pile cap increases when increasing h_1 , as Figure 3.55 shows. This effect is not due to an increase in surface acceleration, as one could think; in fact, for the cases shown in Figure, for example, these accelerations decrease moving from $h_1/d = 2$ to $h_1/d = 16$. Strains and stresses decrease when the interface is approaching the surface because of the interference with the effect of the cap restraint; the constraint applied by stiffer layer limits deformations the more it is close to the pile head (that is restrained).

When $h_1 > L_a$ also in two-layer subsoils the pile follows the soil near the pile cap, so the ϵ_p (in correspondence of the outer fiber of the head section) depends only on the acceleration at surface, the shear wave velocity of the first layer, and the diameter of the pile, while, of course, stresses and bending moments depend also on the inertia and Young modulus of the pile. This fact doesn't mean that the second layer doesn't exert any effect on cap bending moment; indeed, it affects the acceleration at surface.

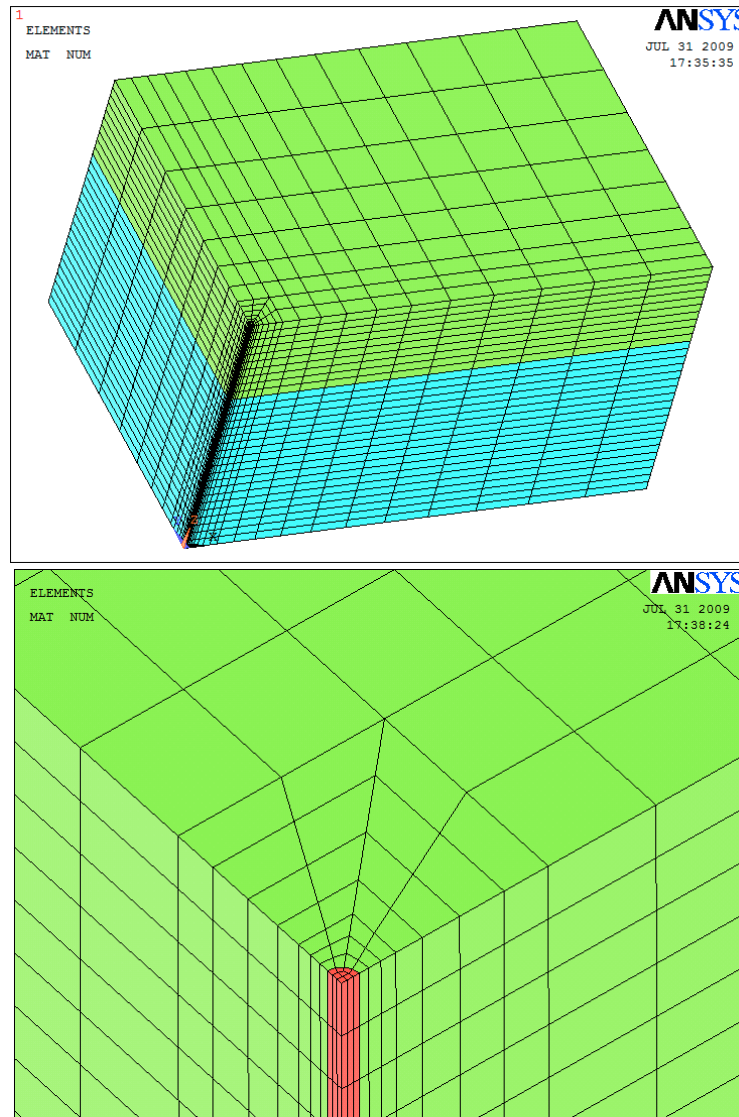


Figure 3.54: FE model for a single pile

Moments at interface can decrease (as shown in Figure 3.56) or increase (Figure 3.57) passing from $h_I/d = 2$ to $h_I/d = 4$ (that's to say inside the active length).

As a consequence of the interaction (at each time step) between the effects of the interface and the head restraint, moments can be higher or lower than the corresponding ones in the case of free head (in this case moments have to increase with increasing the depth of the interface even when $h_I < L_a$).

A reduction of bending moment is not due to the ground response; in fact, the free-field soil shear strain γ_I is increasing.

Inside L_a the response of the pile, because of the influence of the cap restraint, is not correlated only to free-field quantities.

As a result, it seems not possible to predict pile forces from simply one-dimensional ground response considerations.

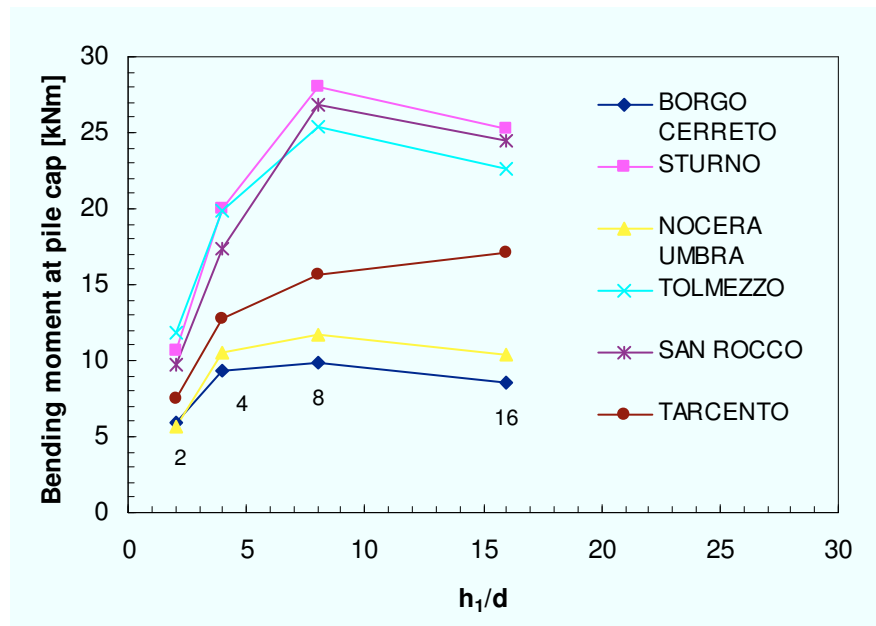


Figure 3.55: Bending moment at pile cap against depth of interface ($E_1 = 50$ MPa, $V_{s2}/V_{s1} = 1.5$, $E_p/E_1 = 300$, $d = 1$ m).

It's worth noting that in all these graphs the ratios between the moments at each depth are not constant varying the input signal. This is due to two distinct phenomena: firstly, changing the depth of the interface changes the dynamic characteristics of the ground which enters in resonance differently with the signals; the second reason is that also the transmissibility, as defined by Mylonakis (2001), is variable with frequency, and then with signal. This topic will be discussed later on.

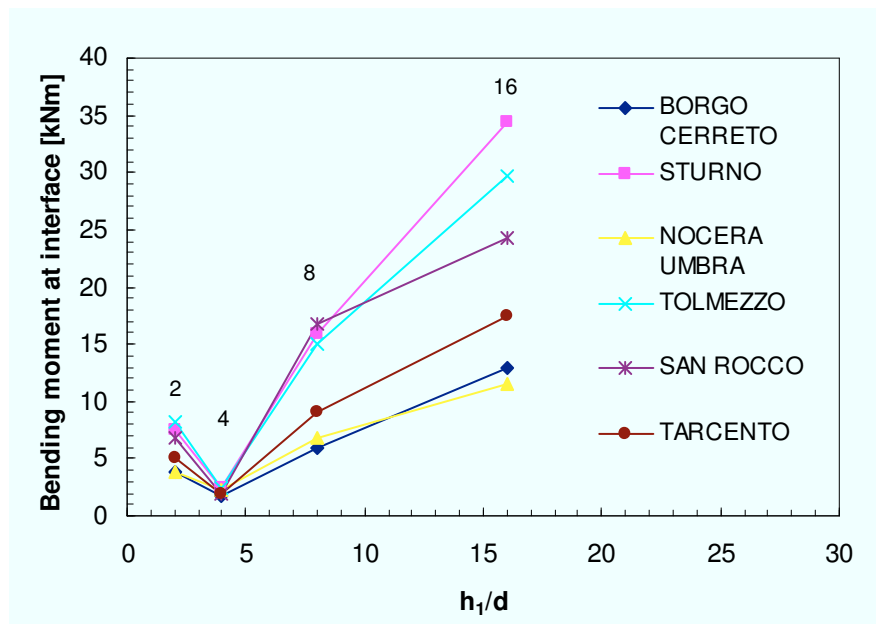


Figure 3.56: Bending moment at interface against its depth ($E_1 = 50$ MPa, $V_{s2}/V_{s1} = 1.5$, $E_p/E_1 = 300$, $d = 1$ m).

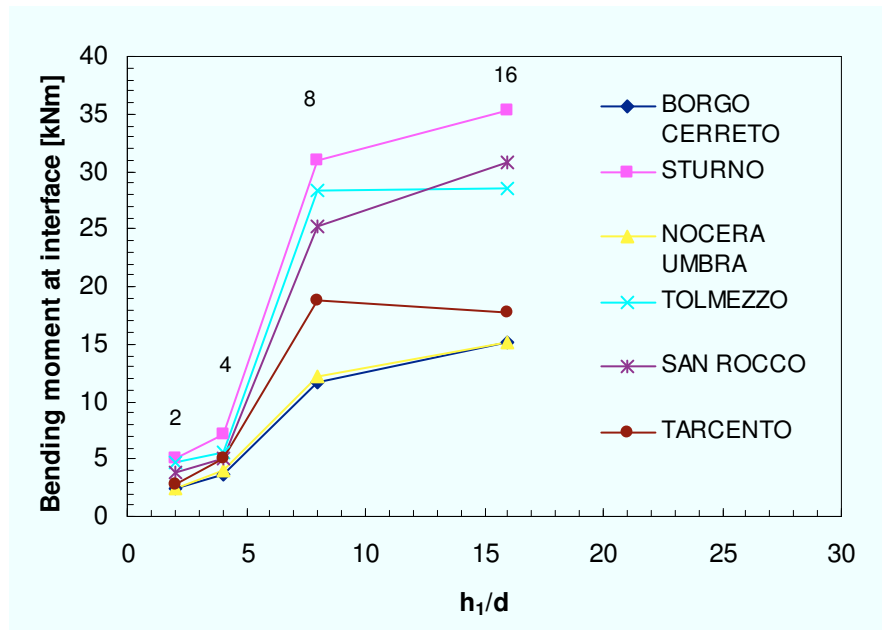


Figure 3.56: Bending moment at interface against its depth ($E_I = 50 \text{ MPa}$, $V_{s2}/V_{s1}=2$, $E_p/E_I = 300$, $d = 1 \text{ m}$).

3.2.6.2 Effect of the stiffness contrast

From a general point of view, increasing the stiffness contrast increases pile bending moments (Figure 3.57). Nevertheless, this sentence is not an axiom. There can be, for example, cases in which the ground response carries to higher shear strains decreasing the stiffness contrast because of a greater resonance with the signal. On the other hand the transmissibility can decrease a lot; this is frequent when the interface is inside the active length of the pile (Figures 3.58 and 3.59) because, analogously to what said before, the cap restraint prevent high deformations. In the Figures it can be noted that bending moments decrease with increasing stiffness contrast, while soil shear strains are increasing. The latter is true except from one case (TOLMEZZO) in which γ_1 decreases passing from $V_{s2}/V_{s1} = 3$ to $V_{s2}/V_{s1} = 6$, so the bending moment decreases because both free-field shear strain and transmissibility are decreasing.

About bending moment at pile cap, it depends (if $h_1 > L_a$) on the free-field acceleration at surface, that generally increases, but there are not few cases in which it happens the opposite.

3.2.6.3 Effect of the stiffness ratio

An increase in stiffness ratio always carries to an increase in bending moments both at pile head and interface.

About the latter, in fact, if E_I decreases (and E_p is constant, so E_p/E_I increases) remaining fixed the other parameters, the soil deformations at free-field have to increase and, as a consequence (with E_p constant) ε_p and then the bending moment increases (Figure 3.60).

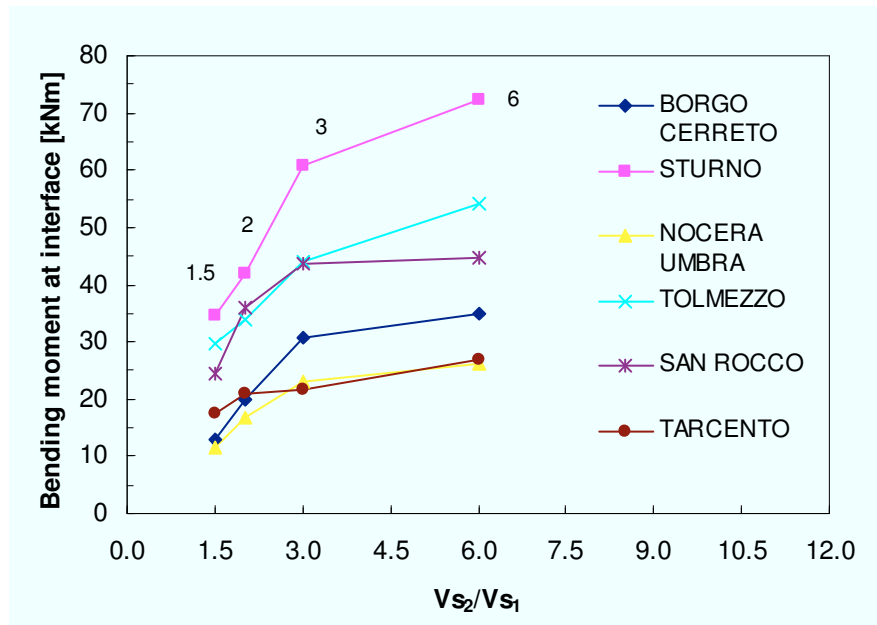


Figure 3.57: Bending moment at interface against stiffness contrast ($E_1 = 50$ MPa, $h_1/d = 16$, $E_p/E_1 = 300$, $d = 1$ m).

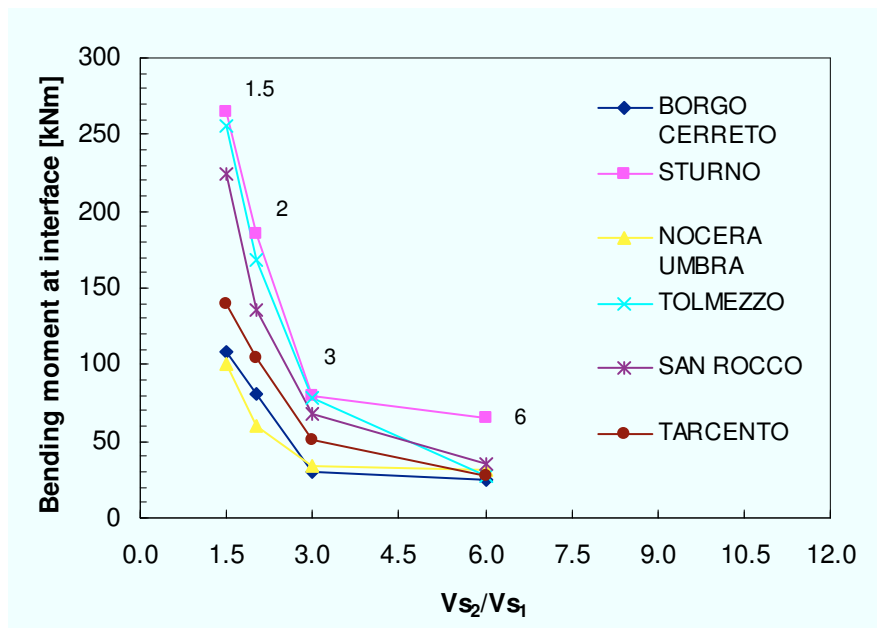


Figure 3.58: Bending moment at interface against stiffness contrast ($E_1 = 50$ MPa, $h_1/d = 4$, $E_p/E_1 = 10000$, $d = 1$ m).

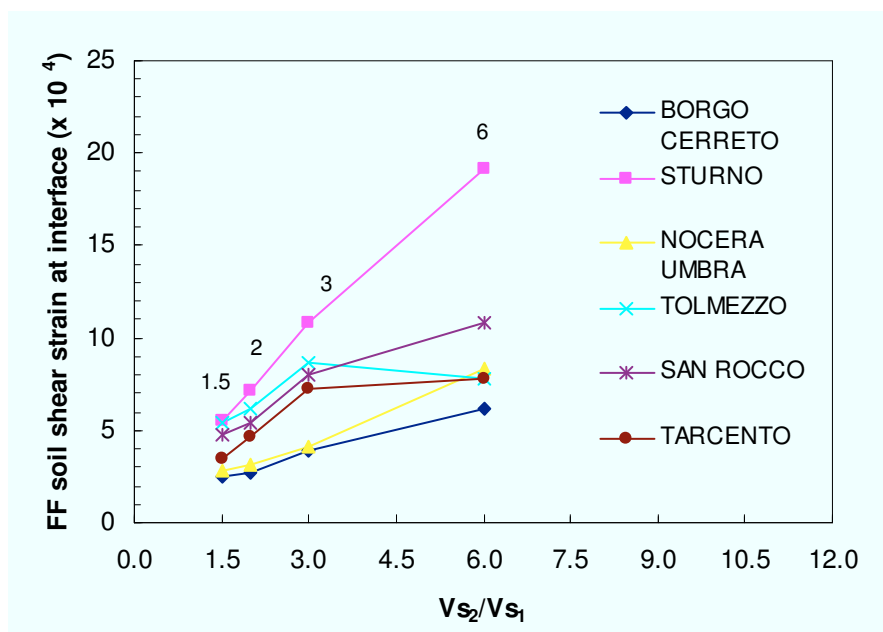


Figure 3.59: Free field soil shear strain (first layer) at interface against stiffness contrast ($E_1 = 50$ MPa, $h_1/d = 4$, $E_p/E_1 = 10000$, $d = 1$ m).

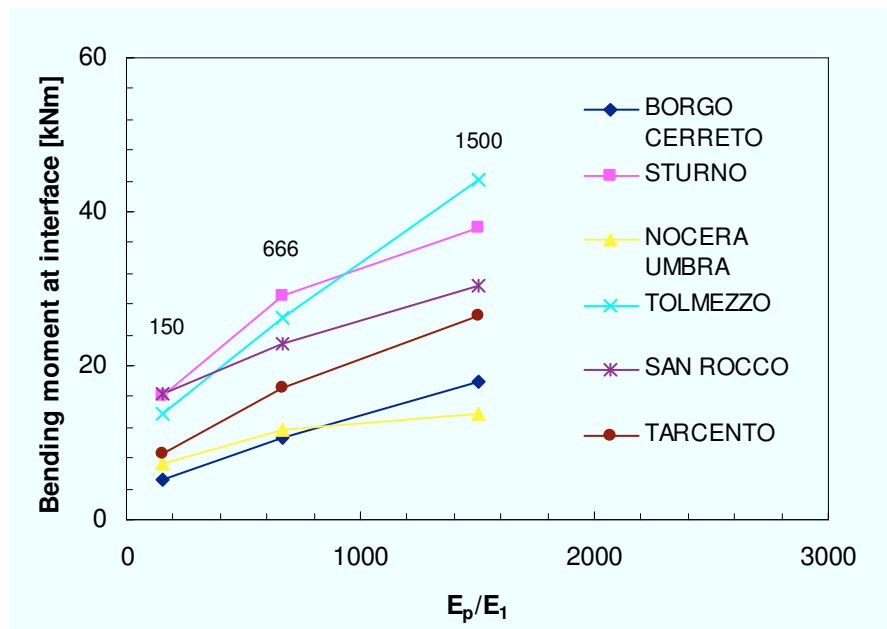


Figure 3.60: Bending moment at interface against stiffness ratio ($E_p = 30$ GPa, $h_1/d = 16$, $V_{s2}/V_{s1} = 2$, $d = 0.5$ m).

Moreover, about the interface moment, if E_p/E_l increases because of an increase in E_p with E_l constant, the free-field motion parameters, and then shear strains, remain constant resulting in smaller strains in the pile due to its greater stiffness (Figure 3.61).

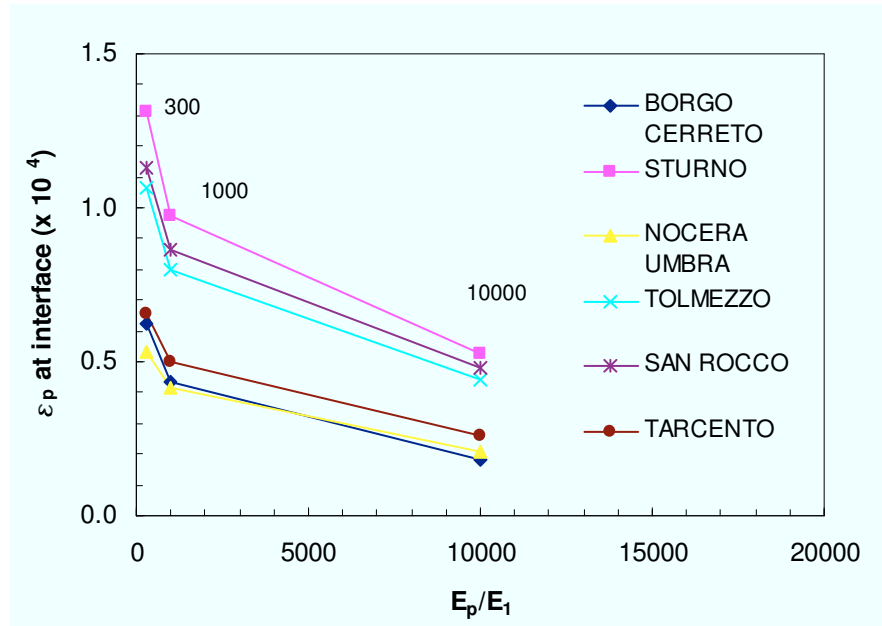


Figure 3.61: Pile bending strain (at outer fiber) at interface against stiffness ratio ($E_s = 50$ MPa, $h_l/d = 16$, $V_{s2}/V_{s1} = 2$, $d = 1$ m).

Nevertheless, it can be observed that the trend of the pile bending strain against the stiffness ratio is less than linear; as the bending moment is proportional to the Young modulus of the pile, it increases, as shown in Figure 3.62.

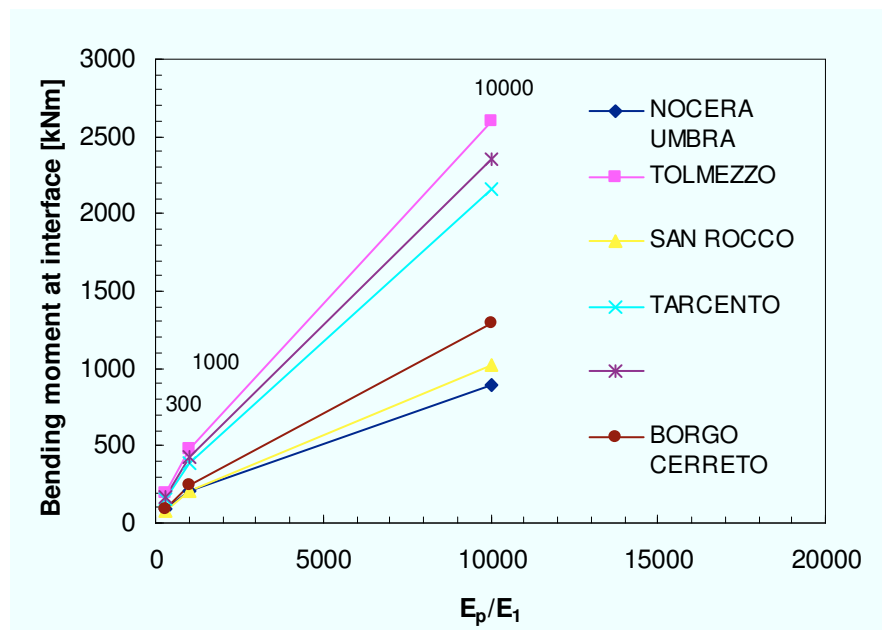


Figure 3.62: Bending moment at interface against stiffness ratio ($E_s = 50$ MPa, $h_l/d = 16$, $V_{s2}/V_{s1} = 2$, $d = 1$ m).

About the pile head, analogously to the interface, if E_p/E_1 increases because of an increase in E_p with E_1 constant, the free-field motion parameters remain constant resulting in greater moments; in this case, moreover, the reduction of pile bending strains is smaller than the previous case, because also for high values of the stiffness ratio the pile curvatures at its head tend to be very similar to the soil ones.

On the contrary, if E_1 decreases with E_p constant, accelerations decrease, as shown in Figure 3.63, but the soil curvature increases, as it is in inverse proportion to the soil Young modulus ($1/R = \alpha_{ff}/V_s^2$) and then bending strain at pile cap (Figure 3.64).

It's worth noting that very often, like in this case, an increase in soil stiffness, fixing other conditions, brings to larger surface accelerations, despite Code statements, according to which the amplification coefficient increases while soil stiffness decreases. Moreover, at least in linear elasticity hypotheses, the values of the surface maximum accelerations (the signals at bedrock are scaled to 1 m/s^2) lead to amplification factors larger than the values suggested by the Codes.

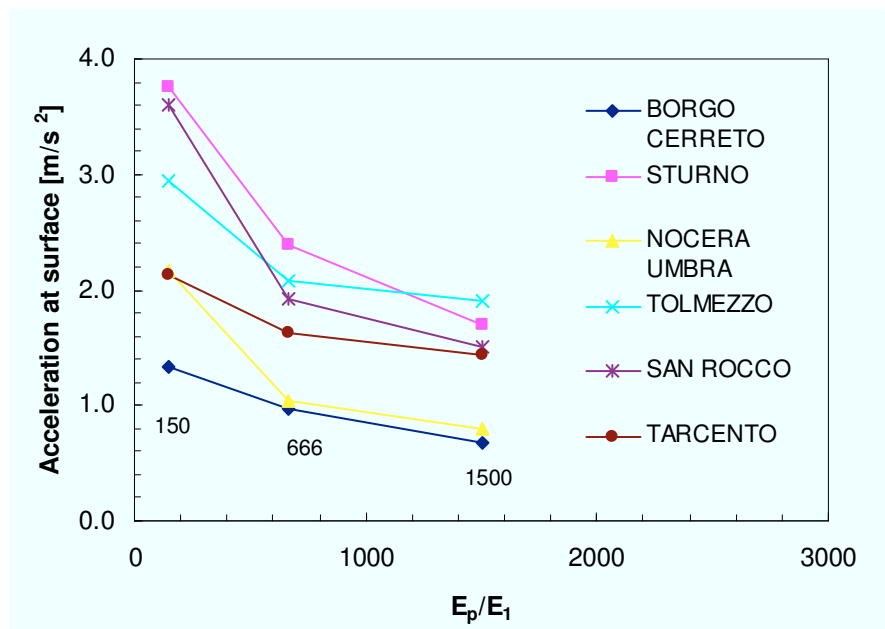


Figure 3.63: Acceleration at surface against stiffness ratio ($E_p = 30 \text{ GPa}$, $h_1/d = 16$, $V_{s2}/V_{s1} = 2$, $d = 0.5 \text{ m}$).

3.2.6.4 Effect of diameter and length

If the interface is located outside the active length of the pile, bending moments vary cubically against pile diameter. This is due to the fact that the pile bending strain at outer fiber is not dependent on pile diameter. Of course its increment increases the active length and the interface can locate inside that, so the ε_p can reduce.

The same happens for the pile length: if the interface remains outside the active length, the ε_p is not sensitive to it, but if the length decreases, the part of pile embedded in the second

layer can become too short and result to a lower pile bending strain due to a lower constraint of the stiffer layer.

Bending moments at pile cap are clearly proportional to r^4 and independent of pile length.

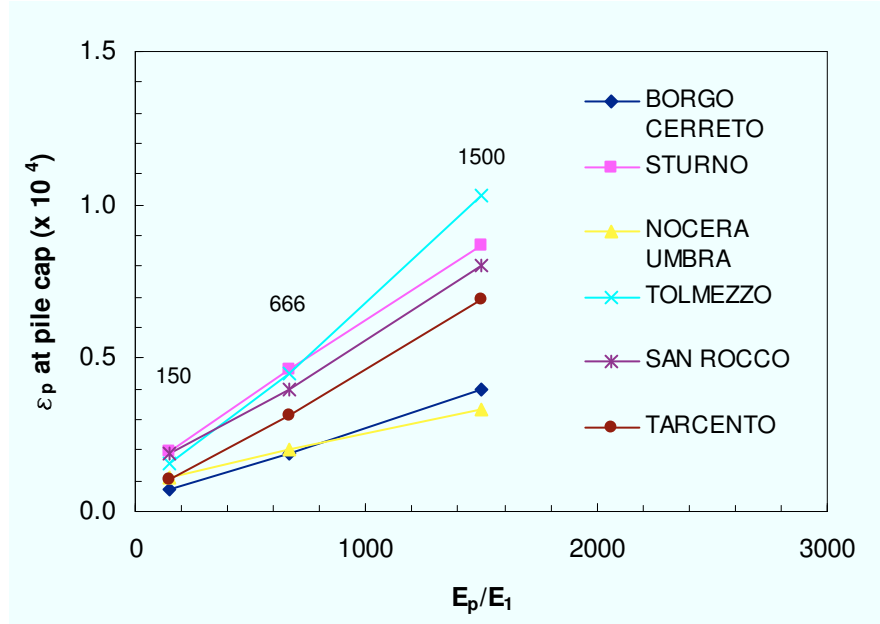


Figure 3.64: Pile bending strain (at outer fiber) at pile cap against stiffness ratio ($E_p = 30 \text{ GPa}$, $h_l/d = 16$, $V_{s2}/V_{s1} = 2$, $d = 0.5 \text{ m}$).

3.2.6.5 Simplified evaluation of interface and head bending moments

3.2.6.5.1 Interface bending moments

Similarly to the simplified formulas existing in literature, it has been tried to relate free-field parameters (simply to evaluate) to the bending moments at pile head and at the interface, needed in design. In particular, the regressions have been made with reference to ε_p , for the reasons explained above; of course it is simple to calculate bending moment once one has estimated it.

As in the formulas proposed by Nikolaou et al. (2001), stiffness contrast V_{s2}/V_{s1} and stiffness ratio E_p/E_1 have been used, even if with different exponents, while L/d (slenderness), as said, have no influence (if the interface is located outside the active length) and then it has been neglected.

Considering only the cases in which $h_l > L_a$, maintaining the same structure of the previous formulations, the results are shown in Figure 3.65.

There are also some cases in which the interface is located inside the active length, even if h_l is very close to L_a . They, of course, make worse the correlation, as can be noted in Figure 3.66.

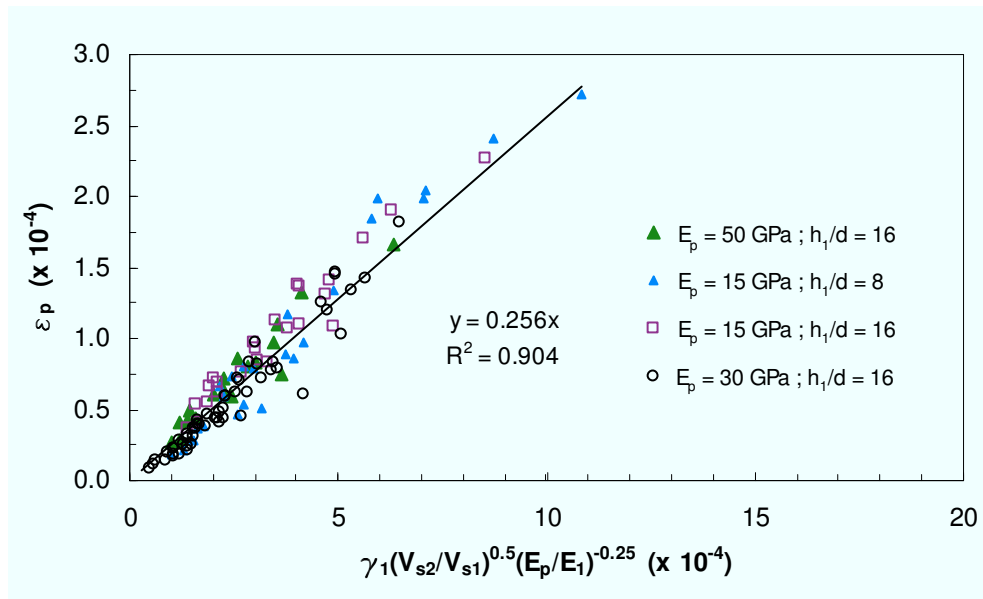


Figure 3.65: Pile bending strain (at outer fiber) at interface

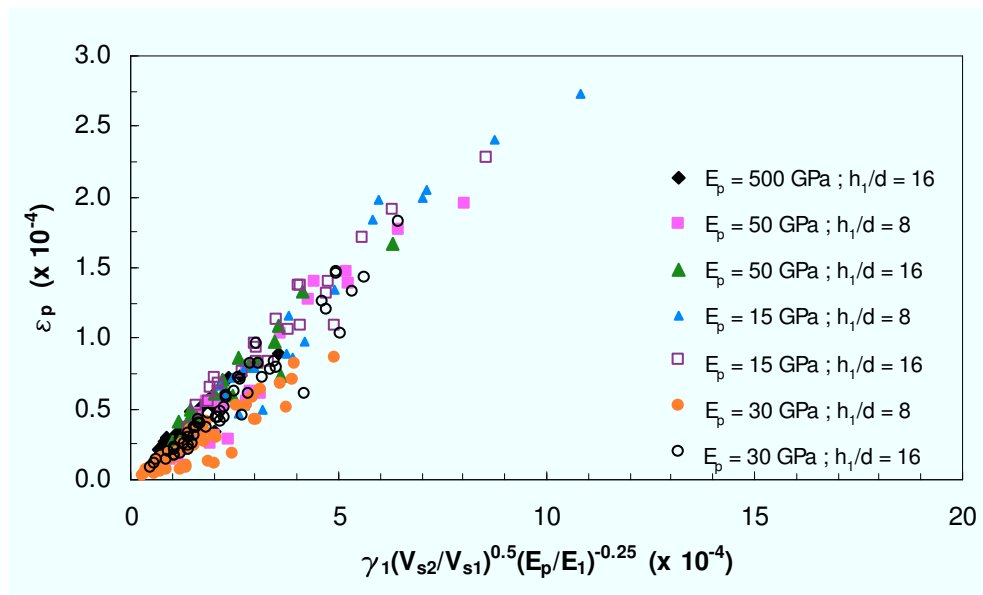


Figure 3.66: Pile bending strain (at outer fiber) at interface

Nevertheless, if the depth of the interface is close to the active length, the behaviour of the system is ruled by the same mechanisms, of course reducing ε_p ; for this reason it has tried to extend the rule also to these cases (in which the depth of interface is not more than 80% of the active length), multiplying the quantity on x -axis by a term taking into account the distance between h_l and L_a (Figure 3.67). The correlation, as it can be noted, improves.

Alternatively, instead of γ_l , it can be replaced the quantity $(\gamma_l - \gamma_2)$, obtaining the following graph in Figure 3.68.

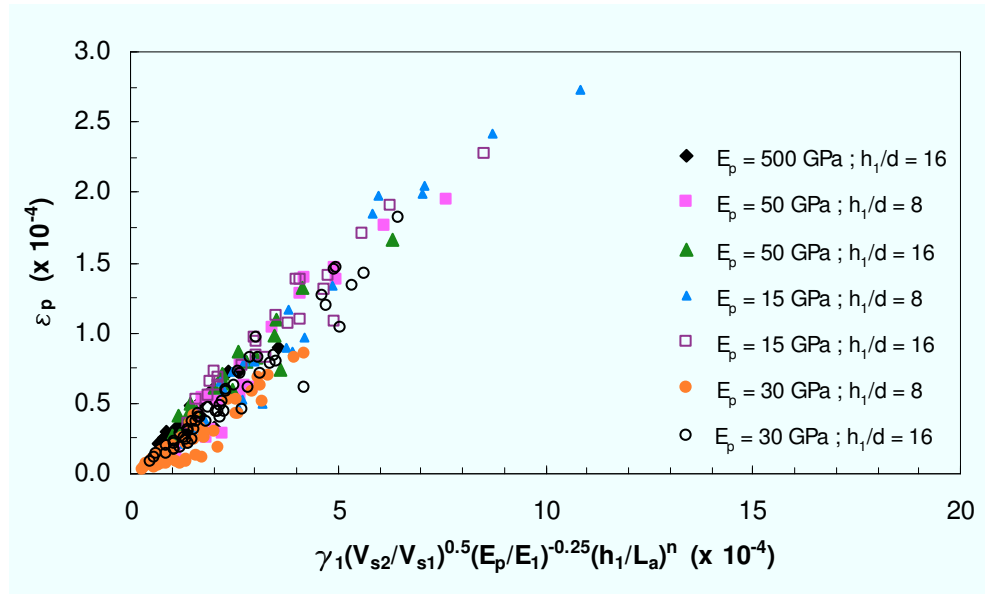


Figure 3.67: Pile bending strain (at outer fiber) at interface, also with $h_1 < L_a$. if $h_1 < L_a$, $n=1$; otherwise $n=0$

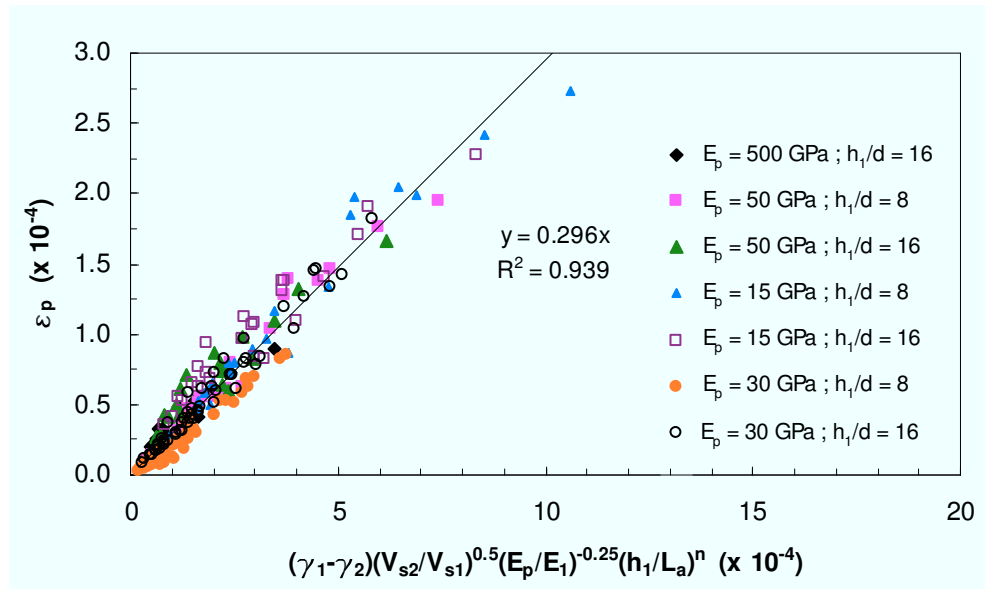


Figure 3.68: Pile bending strain (at outer fiber) at interface

Apparently, the last formulation has a drawback with respect to the previous one: with reference to an homogeneous soil, $(\gamma_1 - \gamma_2)$ tends to 0, and no bending moment is predicted along the pile, in contrast with the evidence. Actually, even if the previous formulation predicts a non-zero moment in this case, its numerical value is evidently wrong, because it becomes:

$$\varepsilon_p = \gamma \left(\frac{E_p}{E_s} \right)^{-0.25} \quad (3.42)$$

that is incorrect, as the ε_p is equal to the derivative of γ times the radius of the pile (in other words the soil curvature times the radius, as the pile follows the soil also for large stiffness ratios).

The interface acts as a further “source of bending moment”, ruled by other parameters, and this moment adds to the moment acting when the pile is embedded in an homogeneous soil; in the latter case, bending is ruled by different parameters (for example, the bending strain is proportional to the pile diameter).

It is evident that, when the stiffness contrast is sharp, the interface practically becomes the unique “source of bending moment”, and $(\gamma_1 - \gamma_2)$ tends to γ_1 .

According to writer’s judgement, due to its inertia, pile bending strain is also influenced by the distribution of shear strain in the vicinity of interface, so it has been tried to evaluate γ_1 and γ_2 a diameter far from it. The results are shown in Figure 3.69.

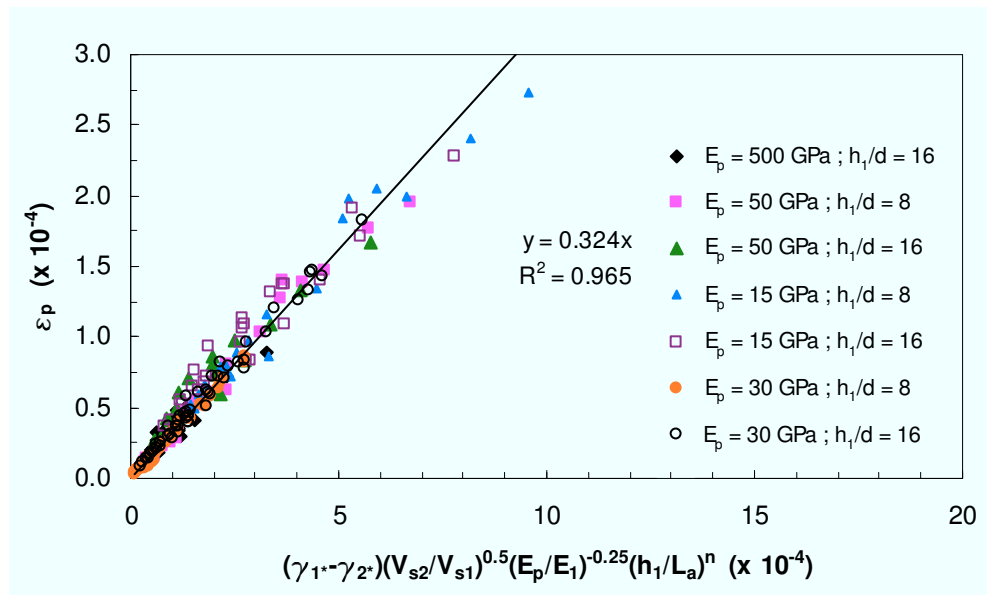


Figure 3.69: Pile bending strain (at outer fiber) at interface. γ_1^* and γ_2^* are evaluated at the depth h_1-d and h_2+d

The correlation improves appreciably, and the R^2 value is more than satisfactory, considering the large number of points (and then cases) in the graph.

This is valid if $h_1 > L_a$. When the interface is inside the active length, as said, the strains become much smaller, and it is not possible to relate them to free-field parameters, because of the effect of the restraint at the pile head. Analysing, for example, the cases in which $h_1/d = 2$ (only first parametric study), varying the stiffness of the pile (and then the stiffness ratio, as E_{s1} is constant), it can be immediately noticed that the points are scattered, confirming that no correlation exists with free-field shear strain (3.70a). Moreover, two issues can be derived.

Firstly, the strains (both free-field and pile) are very small and then kinematic interaction has a little influence on the seismic response of the pile. Secondly, the effect of the pile stiffness is limited. Indeed, the pile has no space to deform (only 2 diameters), because constrained, and then it is anyway rigid, regardless of its Young modulus (Figure 3.70b).

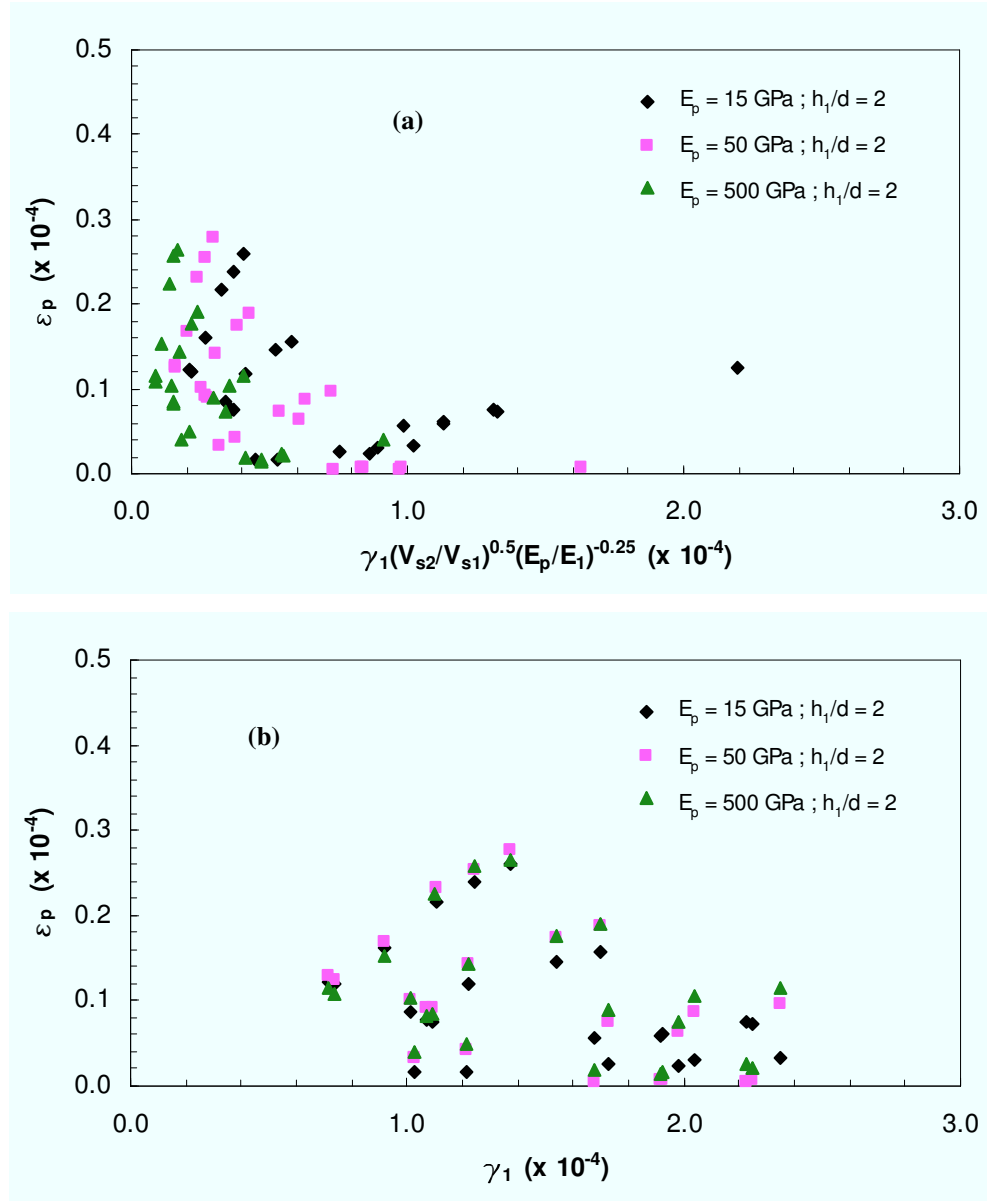


Figure 3.70: Pile bending strain (at outer fiber) at interface when $h_l/d = 2$

Putting in a graph all the cases with $h_l < L_a$ (Figure 3.71), it can be seen that for $h_l/d = 4$ there is a larger difference among the various stiffness ratios; as expected, ε_p decreases with increasing the pile Young modulus. This behaviour can be interpreted thinking that a stiffer pile, in the same free-field conditions, exhibits lower deformations; another explanation of the results is that increasing stiffness ratio also active length increases, and so h_l/L_a decreases

making the pile stiffer. In the light of the latter interpretation, it is reasonable that in the cases $h_I/d = 8$ the pile bending strains are larger than those $h_I/d = 4$ with the same stiffness ratio ($E_p/E_I = 10000$).

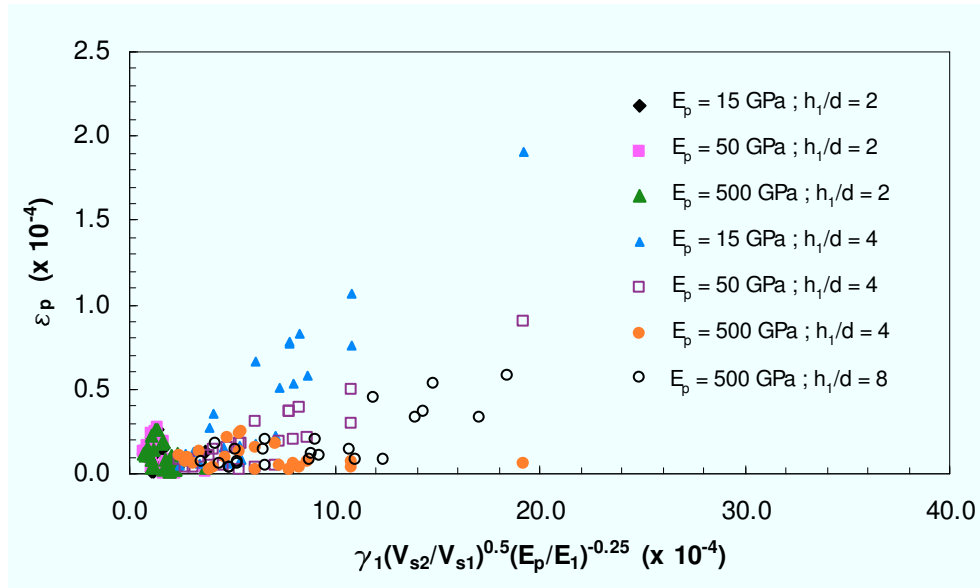


Figure 3.71: Pile bending strain (at outer fiber) at interface when $h_I < L_a$.

It has been seen that when $h_I < L_a$ it is impossible to estimate the pile bending moment to the free field shear strains. Nevertheless, when in design this situation occurs, it is possible to assume the bending moment correspondent to $h_I = L_a$ putting in the fitting formula the shear strain at the “fake” interface; it is possible to show, in fact, that it is conservative (see also *Effect of depth of interface*).

3.2.6.5.2 Head bending moments

About the pile bending strain at pile cap, in Figure 3.72 it is possible to see that pile curvature at its top is equal to free-field soil curvature at surface, as the slope of the trend line is about 1. There are shown only cases with $h_I > L_a$; it is clear that in this cases the constraint applied by second layer doesn't have any influence on the cap deformation, even if it has a sharp influence on the free-field surface curvature through a_{ff} .

It is well-known from soil dynamics that at free field:

$$\frac{a_{ff}}{V_s^2} = \gamma'_{ff} \quad (3.43)$$

As numerical evaluation of gamma is more accurate, it has been tried to make the same correlation substituting the left hand with the right hand of the eq. 3.43.

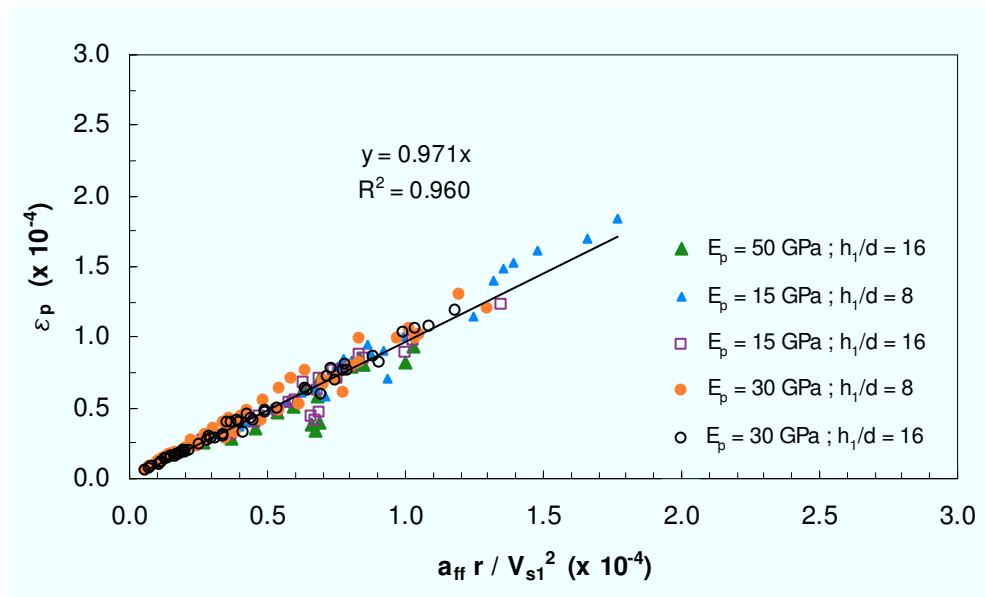


Figure 3.72: Pile bending strain (at outer fiber) at pile head when $h_l > L_a$.

The results are shown in Figure 3.73. Even if the difference with respect to the previous graph is not simple to catch, the correlation shows an improved (and very high) R^2 and the slope of the trend line gets closer to 1. The difference between the two graphs is only due to numerical approximations, but both indicates the same result. To graph the entity of the numerical difference between the two hands of the eq. 3.43, in Figure 3.74 are reported all the cases (including those in which $h_l < L_a$).

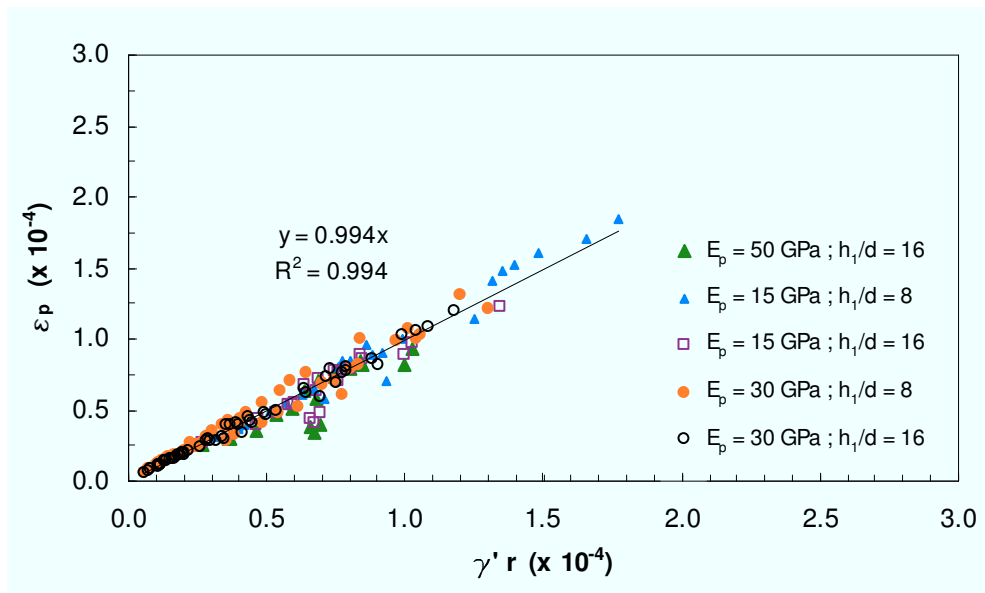


Figure 3.73: Pile bending strain (at outer fiber) at pile head when $h_l > L_a$.

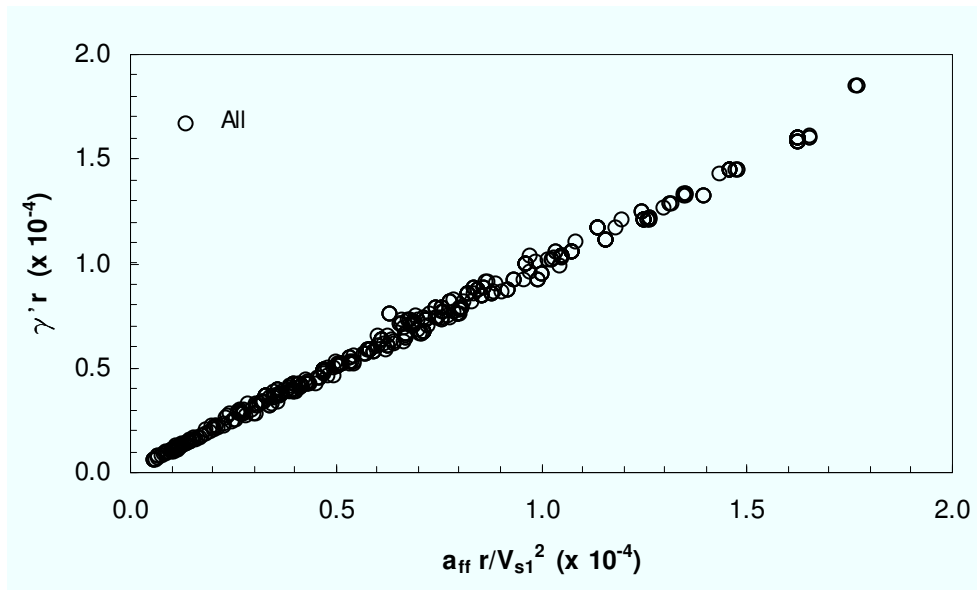


Figure 3.74: Comparison between the values of $a_{ff} r / V_{s1}^2$ and $\gamma' r$.

It is clear that part of the scatter of the points with respect to the trend line is due to the fact that the pile acceleration is lightly different from the free-field one; for this reason, substituting a_{ff} with a_p gives a better correlation (Figure 3.75).

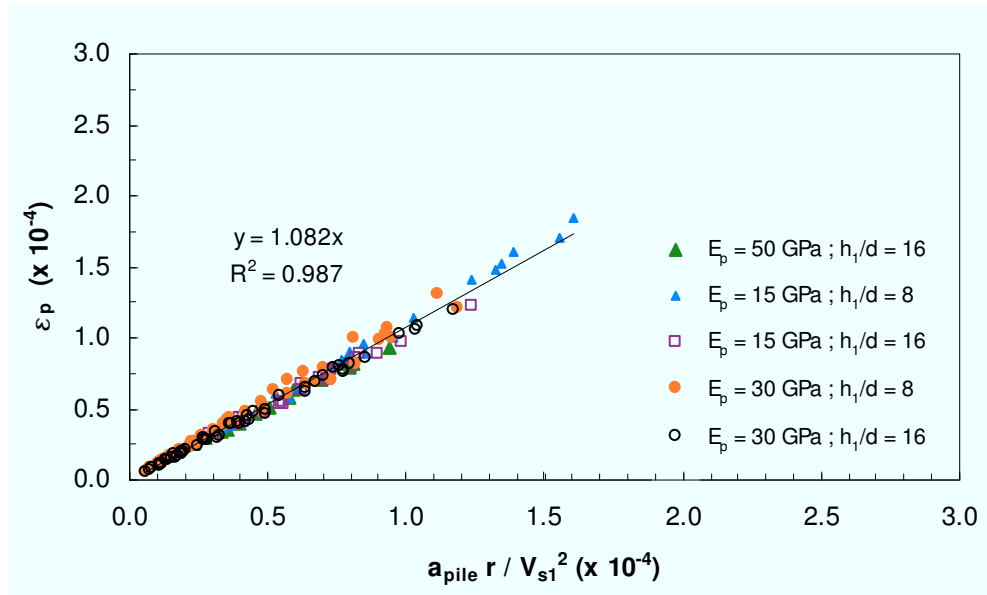


Figure 3.75: Pile bending strain (at outer fiber) at pile head when $h_l > L_a$.

Of course the trend line has a greater slope due to the fact that the average pile head acceleration is lightly smaller than the surface free-field one.

To better highlight this, in Figures 3.76 and 3.77 is shown the comparison between a_p and a_{ff} separately for the first and the second parametric study, with reference to all the cases (also those with $h_I < L_a$). In the first one, pile accelerations can be much smaller than the free-field ones, because of the presence of very large stiffness ratios (up to 10000) and also very low interface depths (very small h_I/L_a); of course these cases are very rare in practice. For usual stiffness ratios, as can be seen in Figure 3.77, the pile acceleration tends to get closer to free-field one. As it will be explain later, the scatter between the two accelerations depends also on the frequency content of the signal, and anyway can result not significant for design purposes as the response spectra of pile and soil signals coincide even for low structural periods.

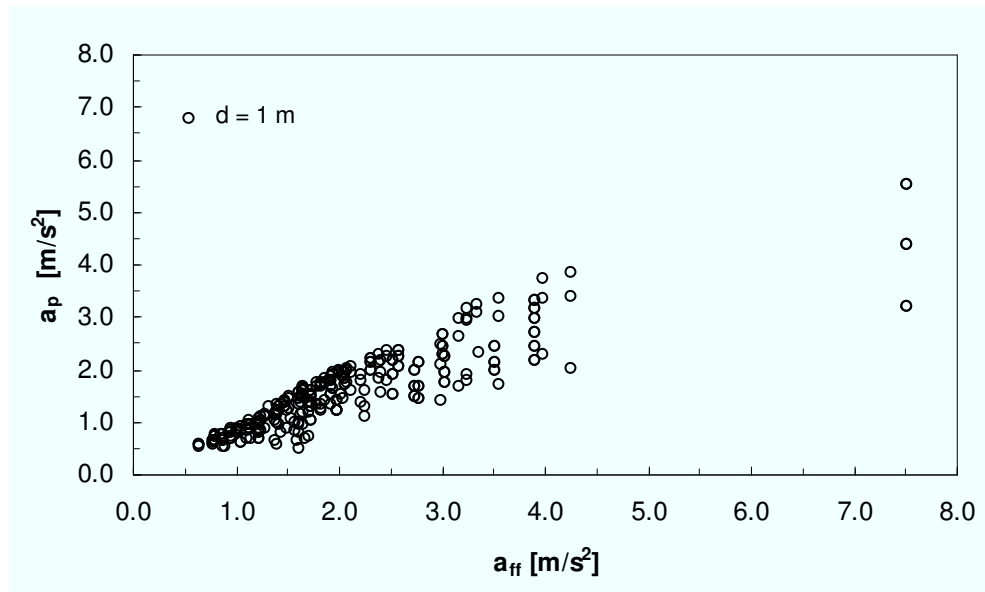


Figure 3.76: Comparison between free field and pile acceleration for parametric study n. 1.

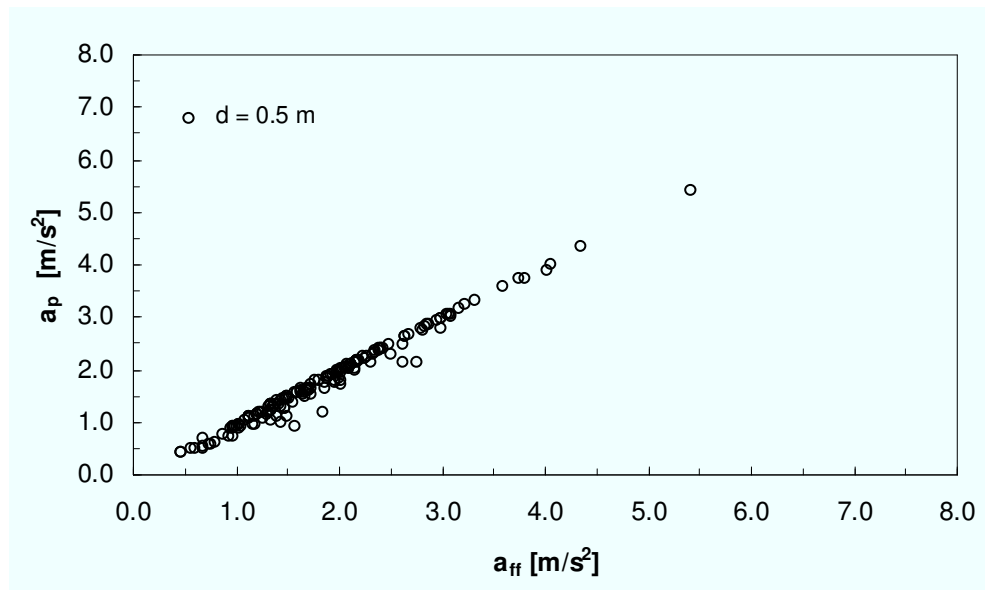


Figure 3.77: Comparison between free field and pile acceleration for parametric study n. 2.

About the prediction of bending moments at pile cap when $h_I < L_a$, in Figure 3.78 are reported all these points, maintaining the same quantities on x and y axes. For the case $h_I/d = 4$ - $E_p = 15$ GPa and the case $h_I/d = 8$ - $E_p = 500$ GPa, the slope is still about 1.

It's worth noting that the slope of the ideal trend line relative to the various cases decreases with decreasing h_I/L_a .

Anyway, ε_p at pile cap is always smaller than that obtained assuming pile curvature equal to soil curvature at surface (unit slope in the graph). For this reason, considering in design

$$\varepsilon_p = \frac{a_{ff}}{V_{s1}^2} r \quad (3.44)$$

is always conservative.

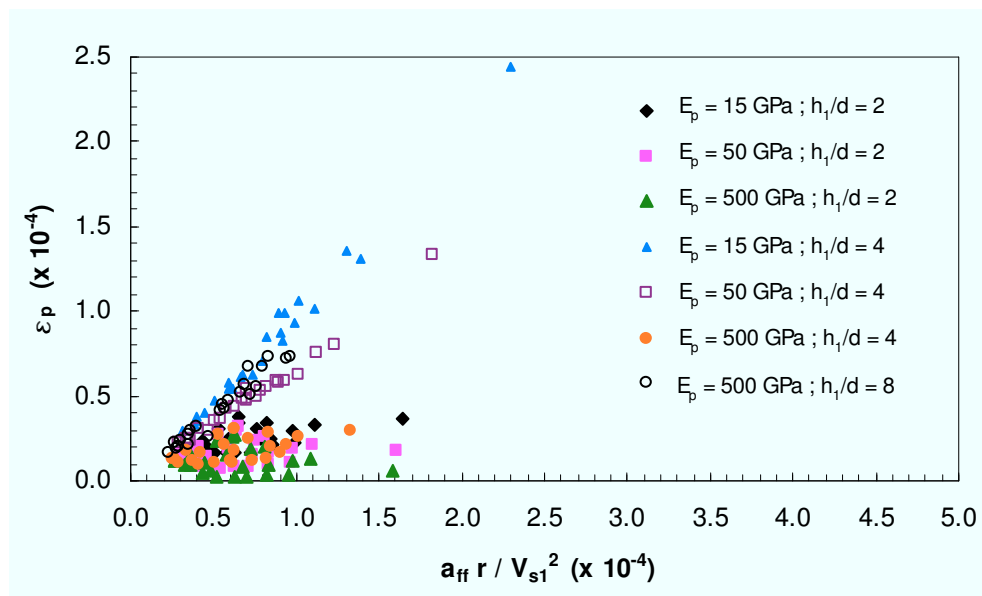


Figure 3.78: Pile bending strain (at outer fiber) at pile head when $h_I < L_a$.

3.2.6.6 Considerations about piles in multi-layer deposits

In the second parametric study two values of L/d have been used. As expected, the result is that the slenderness has no influence on pile bending strains at interface if the latter remains into the active length. Moreover it has been tried to divide the second layer into two sub-layers (with stiffness increasing with depth). The result (shown in Figure 3.79) is that, as expected, it has a little influence on pile bending; the values of ε_p are lightly larger than the two-layers case, as the deeper sub-layer has a small influence on them.

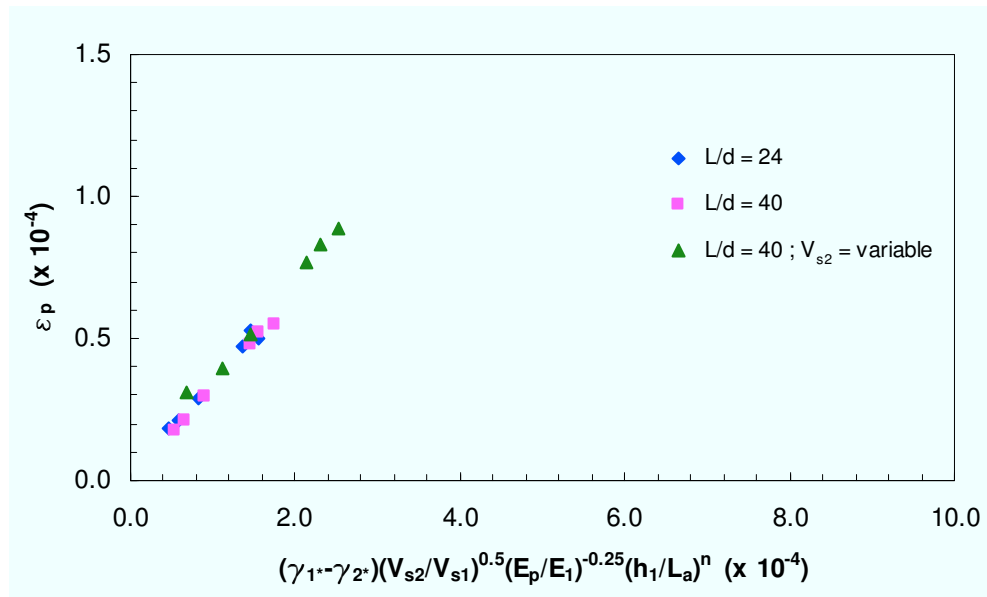


Figure 3.79: Pile bending strain (at outer fiber) at interface varying L/d and the second layer.

About the pile cap, a variation of the slenderness varying the length doesn't have any influence. Of course, if the diameter changes, pile bending strain varies proportionally to it. The subdivision of the second layer influences the surface acceleration but the relation 3.44 is still valid.

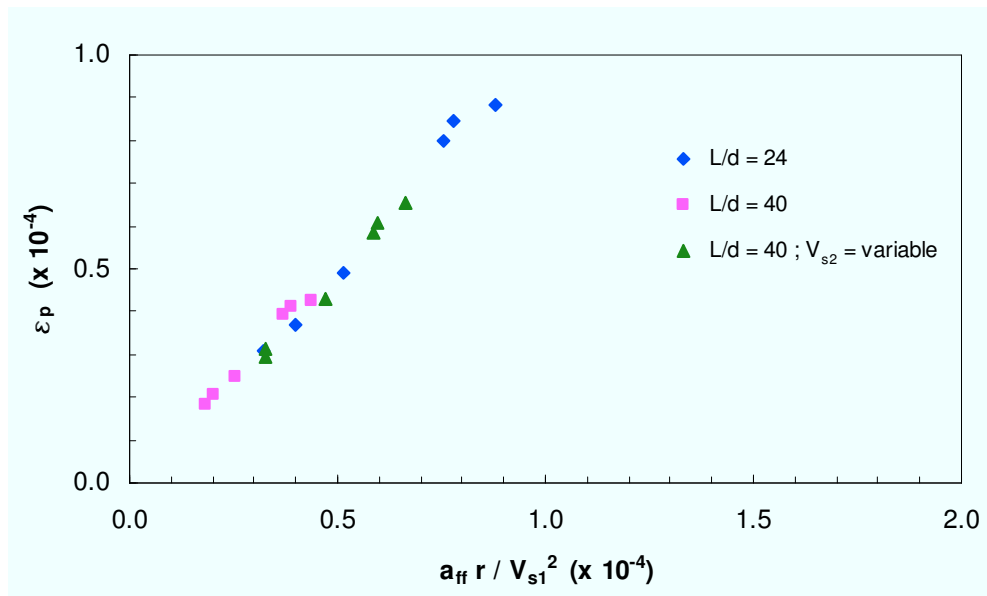


Figure 3.80: Pile bending strain (at outer fiber) at pile head varying L/d and the second layer.

3.2.6.7 Some considerations about transmissibility

Plotting in a graph the strain transmissibility, as defined by Mylonakis, ε_p/γ_1 against the term $(V_{s2}/V_{s1})^{0.5}(E_p/E_1)^{-0.25}$ it is more evident its dependence on the stiffness contrast and the stiffness ratio (Figure 3.81).

As on x and y axes there are the quantities used in graph 3.65 both divided for γ_1 , it is clear that the slope of the ideal trend lines of the two graphs is the same; it is also evident that the transmissibility increases with increasing the stiffness contrast and with decreasing the stiffness ratio. This kind of representation highlights the role played by the frequency of excitation (through the signal) and the depth of the interface (with reference to the cases in which $h_1 > L_a$); indeed, for a given x -value the y -axis point scattering is due to these two parameters. In agreement with Mylonakis (2001), the values of transmissibility varies in a range between 0.01 and 0.2, and has a weak dependence on h_1/d .

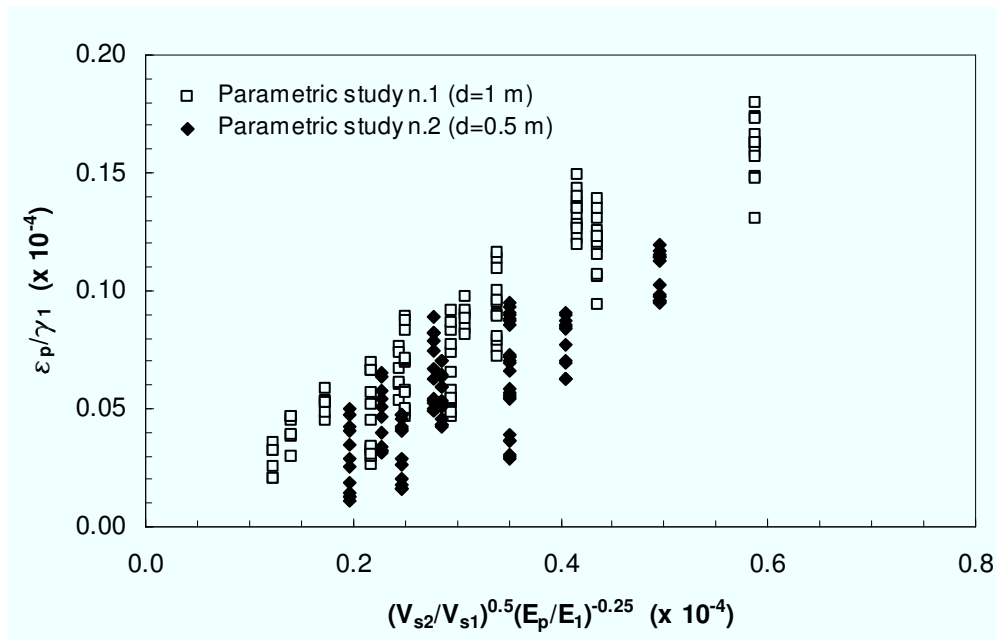


Figure 3.81: Strain transmissibility as defined by Mylonakis.

The results shown in the graph are apparently in contrast with a simple consideration: decreasing the stiffness of the pile until the stiffness of the soil, the pile (vertical) bending strain should tend to 0 (like the free-field), and this opposites to the trend of the transmissibility (that increases with decreasing pile Young modulus).

For this reason some analyses have been carried out to investigate the role of the stiffness ratio; this have been performed starting from a case ($d = 0.5$ m, $L = 12$ m, $V_{s1} = 110$ m/s, $V_{s2} = 439$ m/s, $h_1 = 8$ m) and decreasing the stiffness of the pile.

The result is that until the Young modulus of the pile reaches that of the second (stiffer) layer, the transmissibility increases (up to 0.25); when it decreases until E_1 it tends to zero as expected by physical considerations. For practical applications it can be concluded that transmissibility increases with decreasing stiffness ratio between pile and soil.

It is worthy noting that when the pile stiffness becomes comparable with the soil one, a distinction between the “actual” ε_z and the ε_p (the ratio between the vertical stress at outer fiber and the Young modulus of the pile) is needed due to the fact that the horizontal strains become comparable with the vertical ones, differently from the practical problems in which the values of ε_z and ε_p coincide, as the horizontal strains much smaller than the vertical ones.

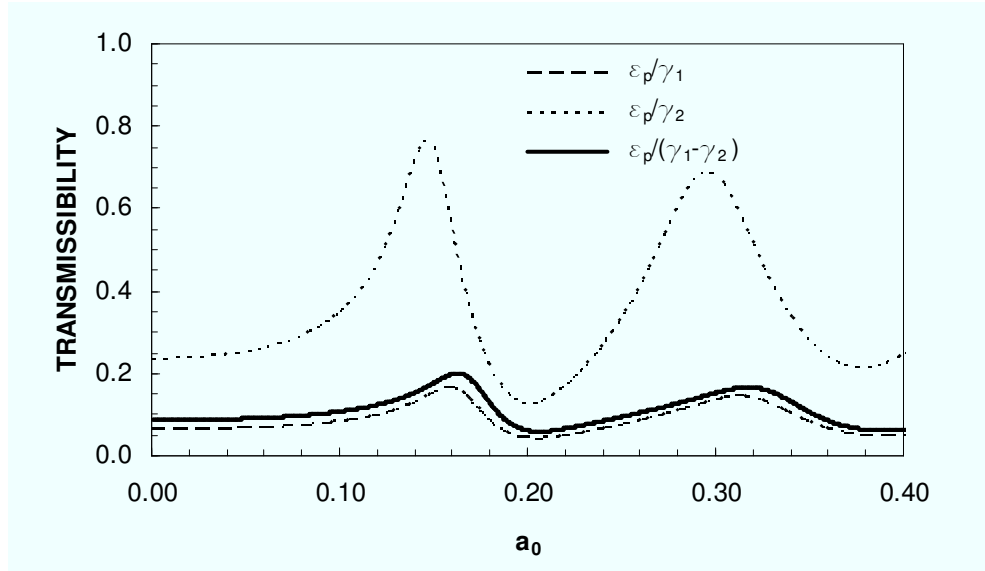


Figure 3.82: Variation of strain transmissibility with frequency ($E_p/E_1 = 1000$, $V_{s2}/V_{s1} = 3$, $h_p/d = 16$).

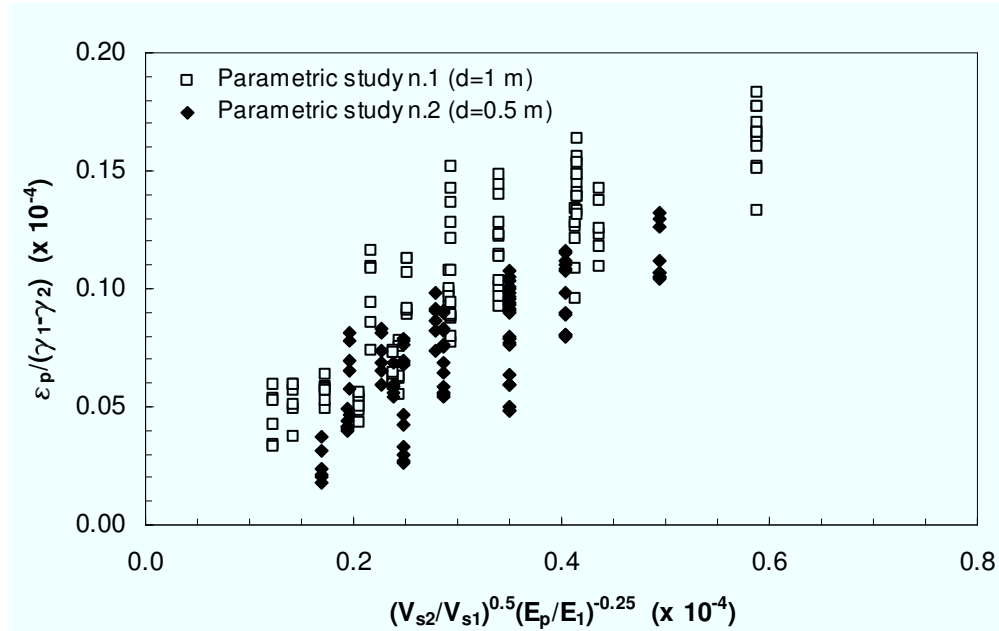


Figure 3.83: Strain transmissibility.

Another interesting issue is that assuming $E_p = E_{s1}$ the ratio ε_1/γ_1 (the ratio between the maximum principal strain and the free-field shear strain) can lightly overcome 0.5, the value occurring in the free-field conditions; once again, this is due to the horizontal strains that

become larger than the vertical ones, even if both much smaller than the pile (or soil, their values are identical) shear strains.

The effect of frequency on transmissibility is showed in Figure 3.82. As ε_p/γ_1 varies with frequency, it is not possible to find a very strict correlation (more than that is showed in the previous graphs) between the pile bending strain and the free field parameters; an improvement is possible only inserting a quantity taking into account the distribution of frequencies into the signal; in the writer's opinion, it is very difficult to synthesize in one parameter the complex composition of the Fourier spectrum. Moreover it can be noticed that the trend is similar to that showed (in Figure 3.22) by Mylonakis (2001), but for frequencies larger than $a_0 = 0.15$ (not showed in Figure 3.22) the strain transmissibility decreases.

Moreover, it is possible to express the strain transmissibility as $\varepsilon_p/(\gamma_2 - \gamma_1)$ or as $\varepsilon_p/(\gamma_2^* - \gamma_1^*)$; the results are shown in Figures 3.83 and 3.84. It seems that the last definition is more suitable for describing the dynamic phenomenon.

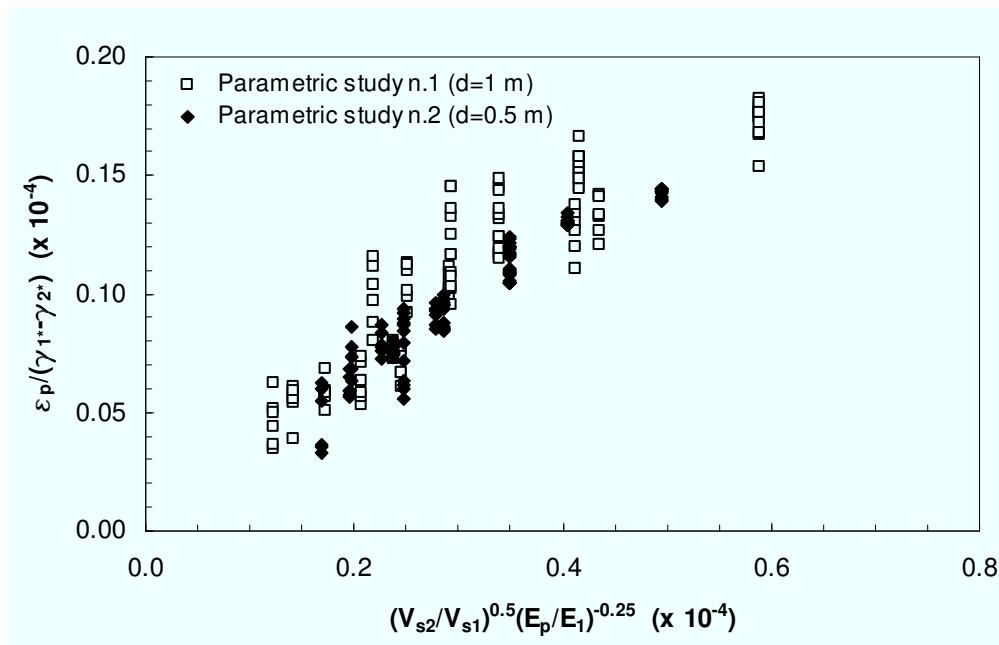


Figure 3.84: Strain transmissibility.

3.2.7 Alteration of the signal at the base of a structure due to the presence of piles

As already said, kinematic interaction between soil and piles results in two effects: the first is the increment of internal forces, while the second is the modify of the seismic signal at the base of the superstructure. This issue has a great importance in design when the kinematic effects are calculated only with reference to bending moments via simplified formulas, because no information is available to estimate the foundation input motion. It has tried, then, to find a simple criterion to establish when it is possible to neglect the presence the piles and

assume the superstructure being subjected to free-field motion at its base, without useless conservatism.

3.2.7.1 Parameters ruling the “filtering effect” for a two-layers soil deposit

The importance of the “filtering effect” exerted by the piles depends on various parameters; with reference to two-layers soil deposits, the primary variables influencing the phenomenon are, in analogy with bending moments, the stiffness contrast, the depth of the interface, the stiffness ratio between pile and soil and the frequency of excitation.

Figure 3.85 graphs the amplitude of the acceleration transfer function from bedrock to pile top and free-field surface for the case in which $d = 0.5$ m, $h_1/d = 16$, $V_{s2}/V_{s1} = 1.5$, $E_p/E_{s1} = 1500$, against the normalised frequency ω/ω_1 , where ω_1 is the first frequency of the ground.

It is evident that in this case no relevant filtering effect is exerted by the piles whatever is the signal (distribution of the relative importance of various frequencies).

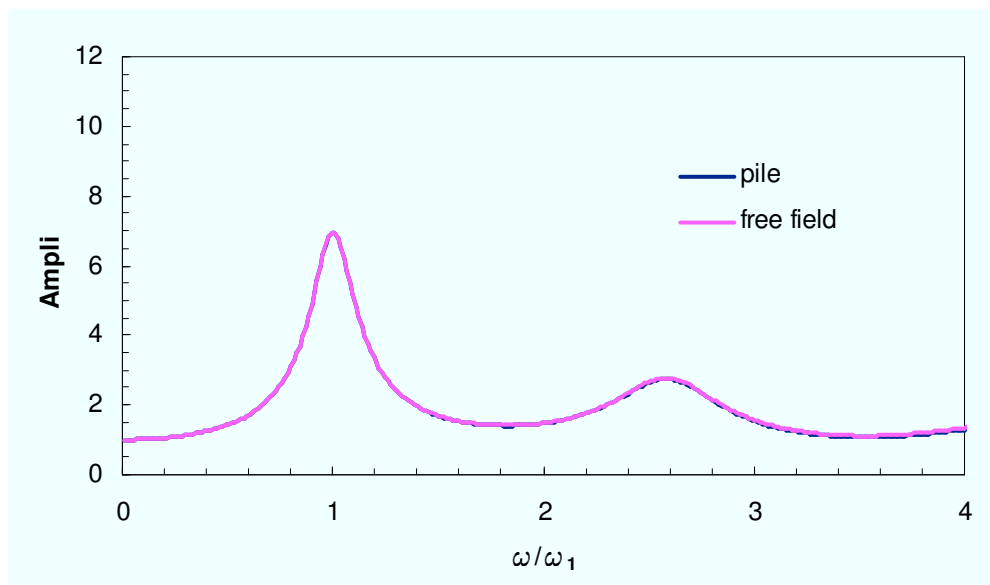


Figure 3.85: Acceleration transfer function amplitude ($d = 0.5$ m, $h_1/d = 16$, $V_{s2}/V_{s1} = 1.5$, $E_p/E_{s1} = 1500$).

It is also clear that increasing, for example, the stiffness contrast between the two soil layers, the pile tends to have a larger difference in motion with respect to the free-field conditions. Figure 3.86 shows the two transfer functions, moving the stiffness contrast of the previous case to 3.

As expected, a difference appears at high frequency, so in this case only high-frequency input signals can result in a significant difference between free-field and foundation motion.

For very high stiffness ratios this difference can exist also for low frequency; in Figure 3.87 it is shown a case in which $E_p/E_1 = 10000$. This is in contrast with Gazetas (1984), who stated that only frequencies larger than $1.5 \omega_1$ could produce differences in accelerations.

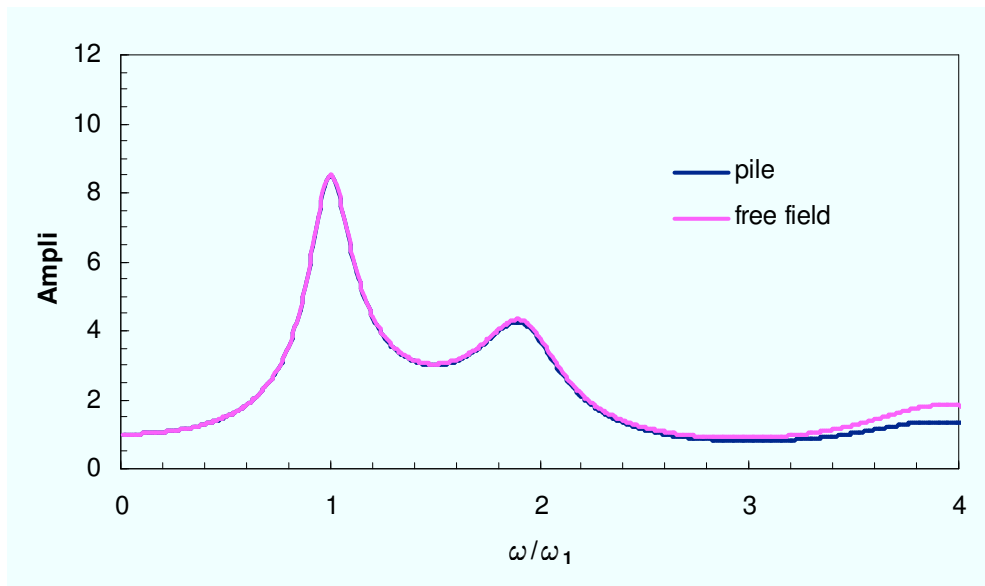


Figure 3.86: Acceleration transfer function amplitude ($d = 0.5$ m, $h_l/d = 16$, $V_{s2}/V_{s1} = 3$, $E_p/E_{s1} = 1500$).

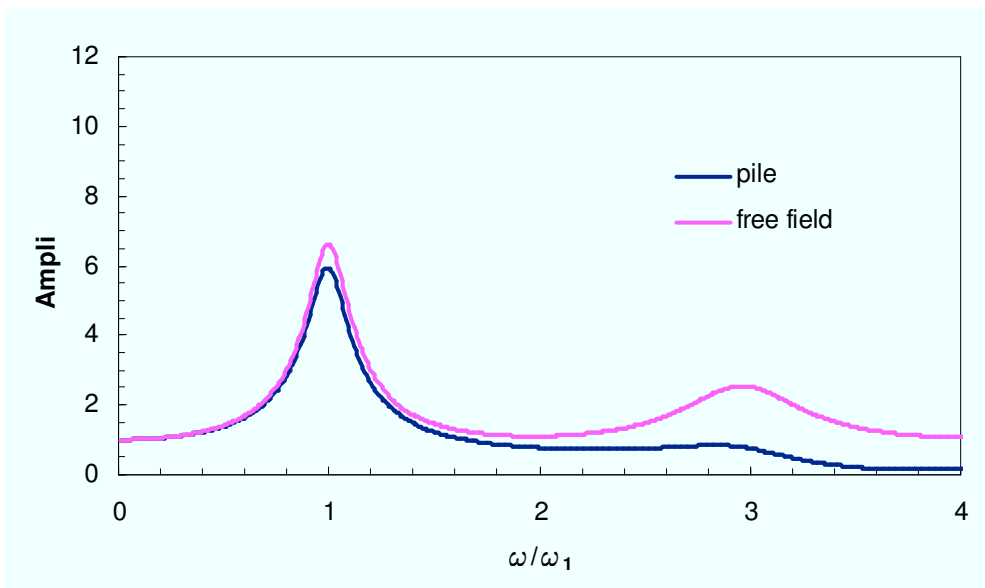


Figure 3.87: Acceleration transfer function amplitude ($d = 1$ m, $h_l/d = 16$, $V_{s2}/V_{s1} = 6$, $E_p/E_{s1} = 10000$).

To highlight the important role played by E_p/E_l , in Figure 3.88 is shown a case in which the only difference with respect to the previous one is the value of the stiffness ratio, set to 1000.

As it can be seen, also in presence of a sharp stiffness contrast, only high frequencies produce differences between the two acceleration motions.

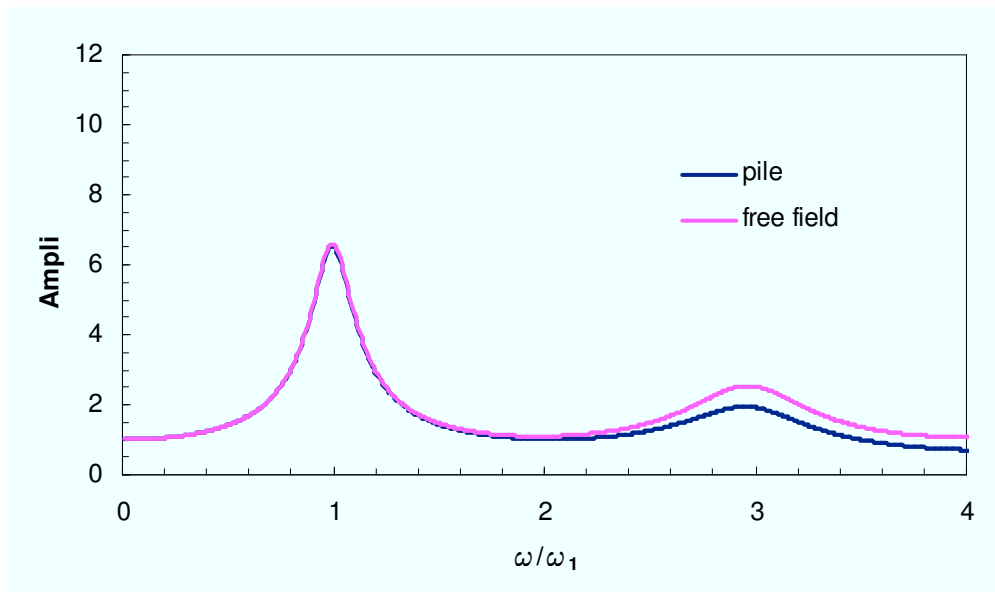


Figure 3.88: Acceleration transfer function amplitude ($d = 1$ m, $h_I/d = 16$, $V_{s2}/V_{s1} = 6$, $E_p/E_{s1} = 1000$).

The role of the depth of interface is showed with reference to the case in Figure 3.87, and reducing the value of h_I/d until reaching the values 8 and 2; the acceleration transfer functions are shown in Figures 3.89 and 3.90.

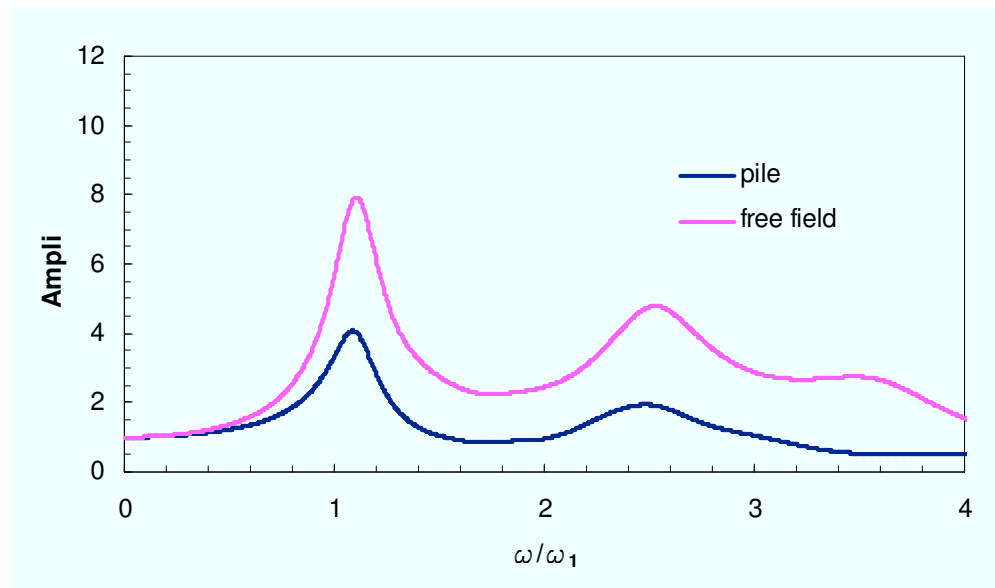


Figure 3.89: Acceleration transfer function amplitude ($d = 1$ m, $h_I/d = 8$, $V_{s2}/V_{s1} = 6$, $E_p/E_{s1} = 10000$).

It is evident that, in presence of high stiffness ratio and stiffness contrast, approaching the pile head (restrained) the difference in the two motions increases, because the pile is not able to follow the free-field.

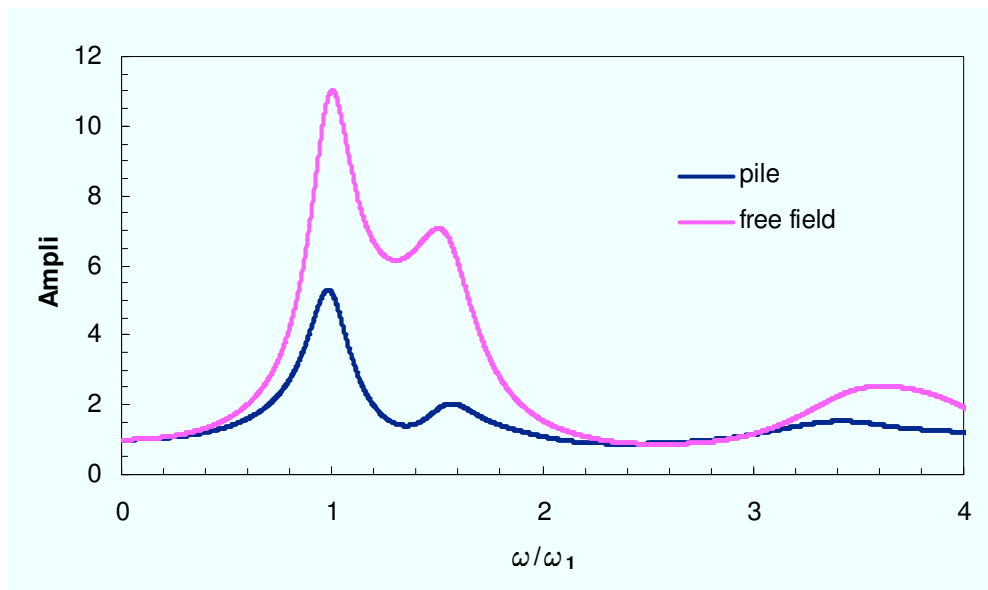


Figure 3.90: Acceleration transfer function amplitude ($d = 1$ m, $h_l/d = 2$, $V_{s2}/V_{s1} = 6$, $E_p/E_{s1} = 10000$).

Summarising, the foundation and free-field motion tend to be more and more different increasing the stiffness ratio, the stiffness contrast, the importance of high frequencies of the bedrock signal, and decreasing the value of h_l/L_a (inside the active length).

Table 3.4. Signals used in the analyses.

Station name	Earthquake	MI	Epicentral distance [km]	Component	PGA [g]	Arias Intensity [m/s]
TOLMEZZO - DIGA AMBIESTA	Friuli, 06/05/1976	6.4	20.23	NS	0.357	0.7865
STURNO	Irpinia 1st, 23/11/1980	6.5	30.37	WE	0.321	1.3935
BORGIO - CERRETO TORRE	Umbria-Marche (AS), 12/10/1997	5.1	10.25	WE	0.162	0.0648
SAN ROCCO	Friuli (AS), 11/09/1976	5.8	23.96	NS	0.090	0.0322
TARCENTO	Friuli (AS), 11/09/1976	5.5	8.38	NS	0.211	0.1079
NOCERA UMBRA - BISCONTINI	Umbria-Marche (AS), 03/10/1997	5.0	6.87	NS	0.186	0.1582

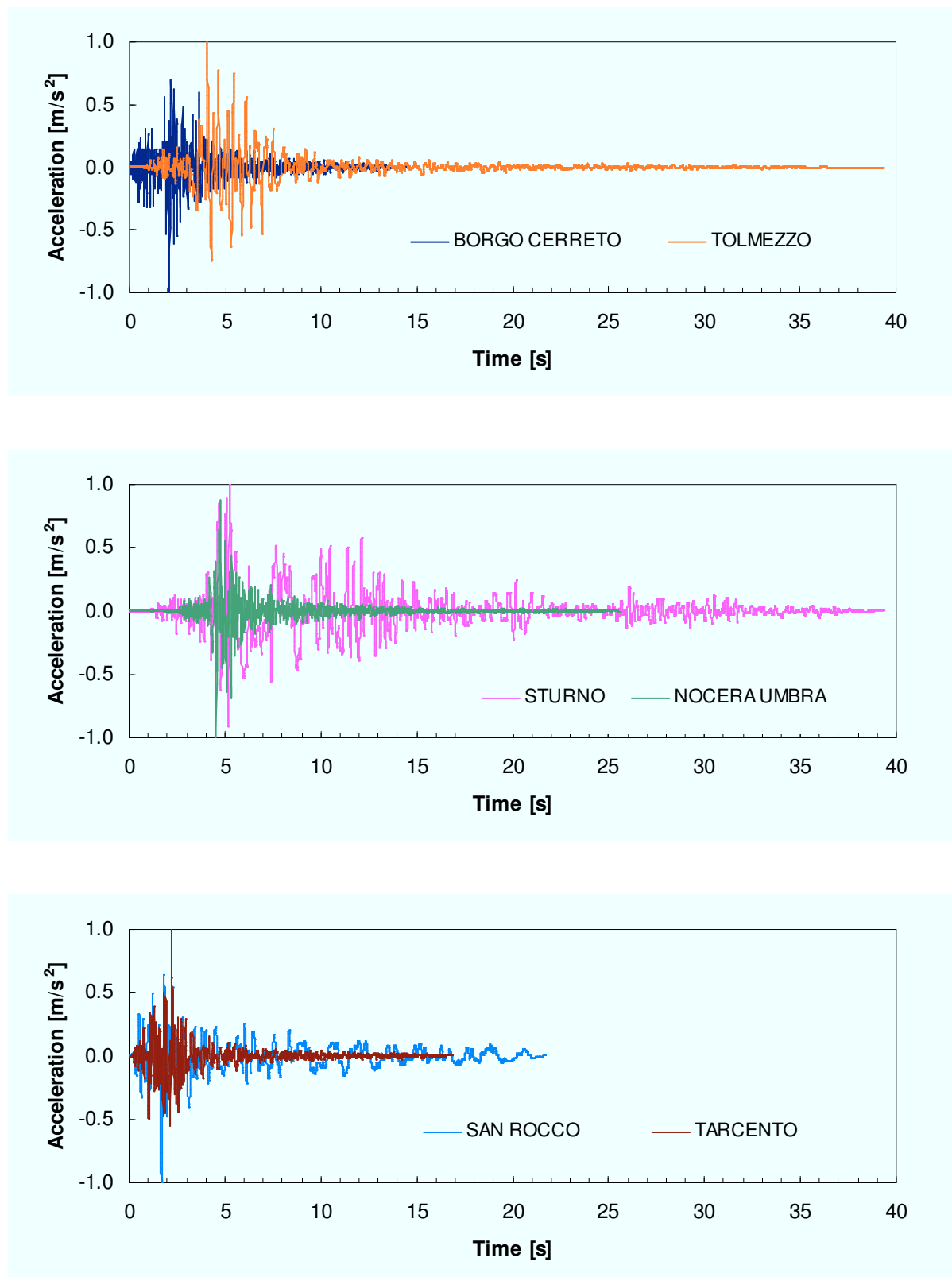


Figure 3.91. Signals used in the analyses: time histories

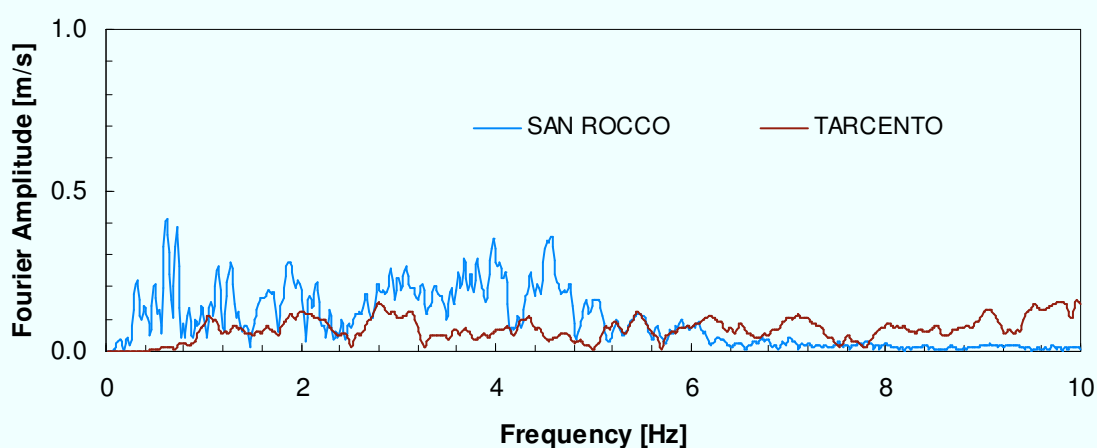
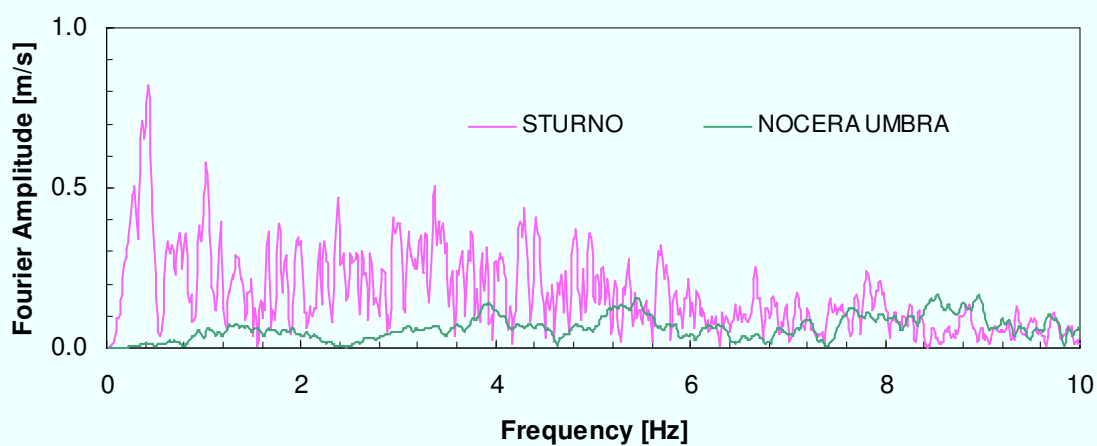
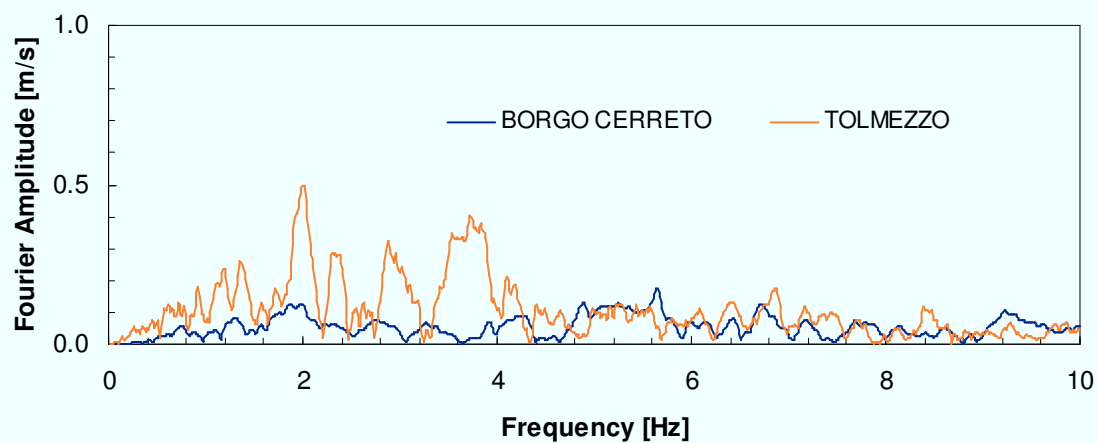


Figure 3.92. Signals used in the analyses: Fourier spectra

3.2.7.2 Response spectra

As high frequencies are more responsible for the difference in the motions, the response in acceleration of a structure is different (considering the two different signals) only for low structural periods. Long-period structure are prevalently influenced by low frequencies that have more similar amplitudes..

Then, to judge in which cases it is possible to neglect the filtering effect, all the acceleration response spectra (structural damping ratio equal to 5%) of the 612 cases of the two parametric studies have been analyzed, looking at free field and foundation signals ($612 \times 2 = 1224$ response spectra).

Further informations about the signals are available in Table 3.4; their time histories and Fourier spectra are shown in Figures 3.91 and 3.92.

The result is that in very rare cases, in which the following conditions:

- $h_1 < L_a$
- $V_{s2}/V_{s1} > 3$
- $E_p/E_{s1} \geq 10000$

are contemporary present, it is opportune to study the interaction case by case; it is possible to neglect the filtering effect (without a too large conservatism) only for structural periods $T_1 > 0.5$ s, as it is possible to check looking at the graphs in the Figures 3.93 and 3.94, with reference to two input signals, BORGO CERRETO and STURNO.

For the other (frequent) cases it is always possible to refer to free-field motion with reference to low-frequency bedrock signals (i.e. STURNO). In the case of high-frequencies signals (i.e. BORGO CERRETO) it is possible to neglect the filtering effect exerted by the piles only when the structural period is larger than 0.3 s (Figures 3.95 and 3.96).

It's important to clarify that the analyses have been undertaken considering the superstructure as a SDOF system.

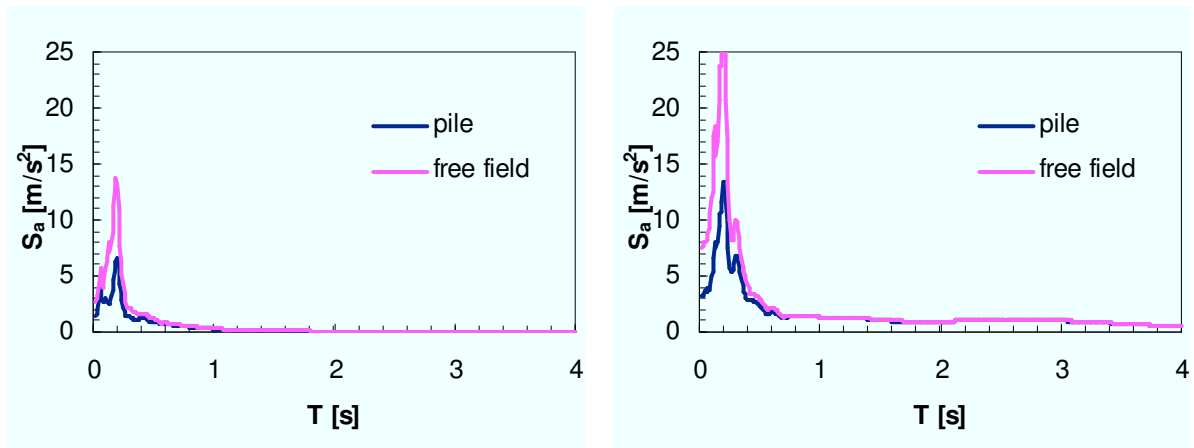


Figure 3.93: Acceleration response spectra at surface ($d = 1$ m, $h_1/d = 2$, $V_{s2}/V_{s1} = 6$, $E_p/E_{s1} = 10000$). On the left side the bedrock signal is BORGO CERRETO, while on the right one it is STURNO.

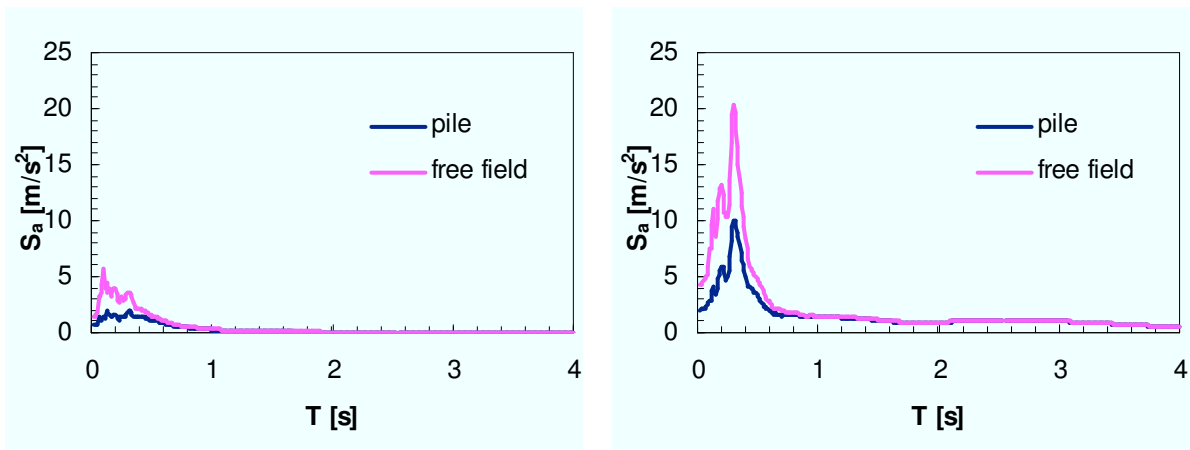


Figure 3.94: Acceleration response spectra at surface ($d = 1$ m, $h_l/d = 8$, $V_{s2}/V_{s1} = 6$, $E_p/E_{s1} = 10000$). On the left side the bedrock signal is BORGIO CERRETO, while on the right one it is STURNO.

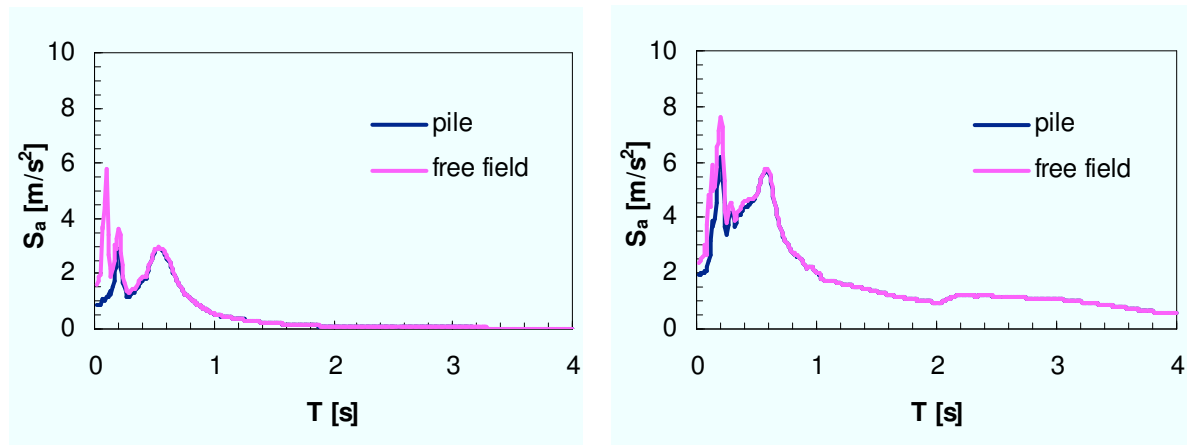


Figure 3.95: Acceleration response spectra at surface ($d = 1$ m, $h_l/d = 16$, $V_{s2}/V_{s1} = 6$, $E_p/E_{s1} = 1000$). On the left side the bedrock signal is BORGIO CERRETO, while on the right one it is STURNO.

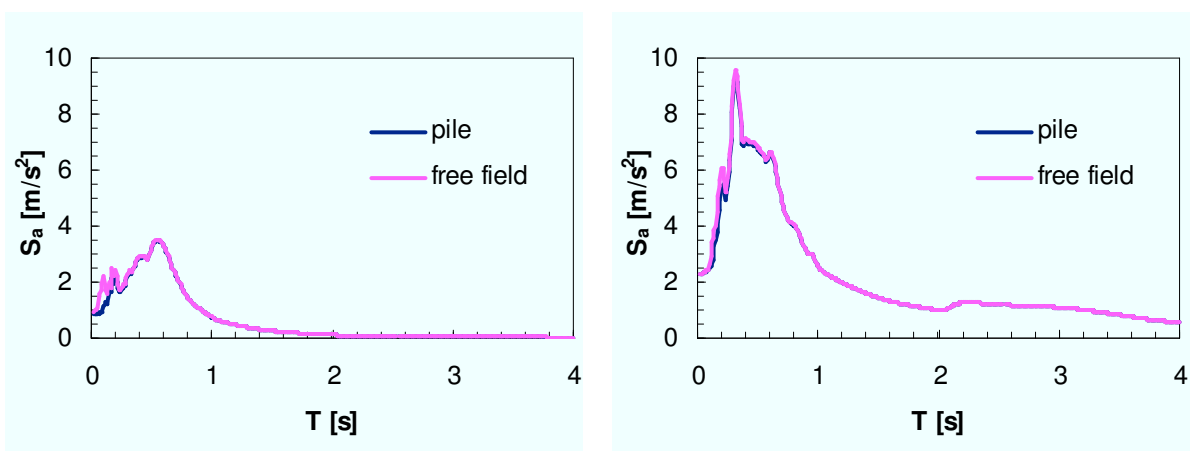


Figure 3.96: Acceleration response spectra at surface ($d = 0.5$ m, $h_l/d = 16$, $V_{s2}/V_{s1} = 3$, $E_p/E_{s1} = 1500$). On the left side the bedrock signal is BORGIO CERRETO, while on the right one it is STURNO.

These conclusions can be considered still valid if the structure (the real MDOF system) is regular, so the contribution of the other modes is not significant; these, indeed, are characterised by higher frequency (with respect to the first one) and then can suffer the difference between the two motions.

Moreover, the analyses are linear elastic; it is evident that non linearity can increase this difference, for example, increasing the stiffness ratio.

It's anyway important to keep in mind that referring to free-field motion for inertial interaction analyses is always conservative.

4 Inertial interaction

4.1 LITERATURE REVIEW

4.1.1 *Dynamic impedance of a single pile*

It has been said that during earthquakes, soil deforms under the influence of seismic waves and “carries” dynamically with it the foundation and the superstructure; the motion of the superstructure generates inertial forces which result in dynamic stresses and strains at the foundation that are transmitted into the surrounding soil. Thus, superstructure-induced deformations develop in the soil while additional waves emanate from the soil–foundation interface. Then, foundation and superstructure exhibit further displacements, which generate further inertial forces and so on. Despite these phenomena occur simultaneously, it appears convenient (both conceptually and computationally) to separate them into two successive phenomena referred to as *kinematic interaction* and *inertial interaction* and obtain the response of the soil–foundation–structure system as a superposition of these two interaction effects.

Inertial interaction refers to the response of the complete soil–foundation–structure system to the excitation by D’Alembert forces associated with the acceleration of the superstructure due to the kinematic interaction.

Inertial interaction analysis is also conveniently performed in two steps: firstly computing the foundation dynamic impedance (“springs” and “dashpots”) associated with each mode of vibration, and then calculating the seismic response of the structure and foundation supported on these springs and dashpots, and subjected to the kinematic accelerations $a_k(t)$ of the base.

As a result, a key step is to estimate, using analytical or numerical methods, the (dynamic) impedance functions associated with a rigid foundation. A number of techniques have been developed in the past for computing and using foundation impedances, including analytical solutions based on integral transform techniques, semianalytical and boundary-element formulations requiring discretisation of only the top surface, dynamic finite-element methods using special “wave-transmitting” lateral boundaries and hybrid methods combining analytical and finite-element approaches.

In practical applications the selection of an appropriate method depends to a large extent on the size and economics of the project, as well as the availability of pertinent computer

codes. Moreover, the method to be selected should adequately reflect the following key characteristics of the foundation-soil system and the excitation:

- the shape of the foundation
- the amount of embedment
- the nature of the soil profile
- the mode of vibration and the predominant frequencies of excitation.

Gazetas (1991), collecting the work of several previous authors, presented a complete set of simple formulas and graphs covering surface and embedded foundations in an homogeneous halfspace; this choice has been made because this soil model is the only idealization for which a complete set of results could be found or easily obtained, and that keeps the number of problem parameters to a minimum; actually, however, the deposit need not be very deep for the half-space idealization to be applicable.

For the usual case of a rigid foundation, there are six modes of vibration: three translational (dynamic displacements along the axes x , y and z) and three rotational (dynamic rotations around the same axes). For each mode, soil can be replaced for the dynamic analysis by a dynamic spring of stiffness \bar{K} and by a dashpot of modulus C . Their values will be discussed later on. Figure 4.1 illustrates the vertical spring and dashpot of an embedded foundation.

Subjected to harmonic vertical force $P_z(t) = P_z \cos(\omega t + a)$, with amplitude P_z and frequency ω , this foundation experiences a harmonic steady-state displacement $u_z(t)$ which has the same frequency but is out-of-phase with $P_z(t)$.

Expressing the above quantities as complex numbers, the dynamic vertical impedance (force–displacement ratio) becomes:

$$\mathbb{k}_z = \frac{\bar{P}_z}{\bar{u}_z} = \bar{K}_z + i\omega C_z \quad (4.1)$$

in which both \bar{K}_z and C_z are, in general, functions of frequency. The spring constant \bar{K}_z , termed dynamic stiffness, reflects the stiffness and inertia of the supporting soil; its dependence on frequency relates solely to the influence that frequency exerts on inertia, since soil material properties are frequency independent. The dashpot coefficient C_z reflects the two types of damping (radiation and material) generated in the system; the former due to energy carried by the waves spreading away from the foundation, and the latter due to energy dissipated in the soil through hysteretic action. As evident from eq. (4.1), damping is responsible for the phase lag between the excitation \bar{K}_z and the displacement \bar{u}_z .

Similarly, eq. (4.1) is also applicable to each of the other five modes of vibration, obtaining the values of $\mathbb{k}_x, \mathbb{k}_y, \mathbb{k}_{rx}, \mathbb{k}_{ry}, \mathbb{k}_t$.

Moreover, in embedded foundations and piles, horizontal forces along principal axes induce rotational in addition to translational oscillations; hence, a cross-coupling horizontal-rocking impedance also exists: $\mathbb{k}_{x-ry}, \mathbb{k}_{y-rx}$. These coupling impedances are usually negligible in shallow foundations.

The evaluation of the impedance of pile groups starts from the impedance of a single pile, and then takes into account group effects through (dynamic) interaction coefficients.

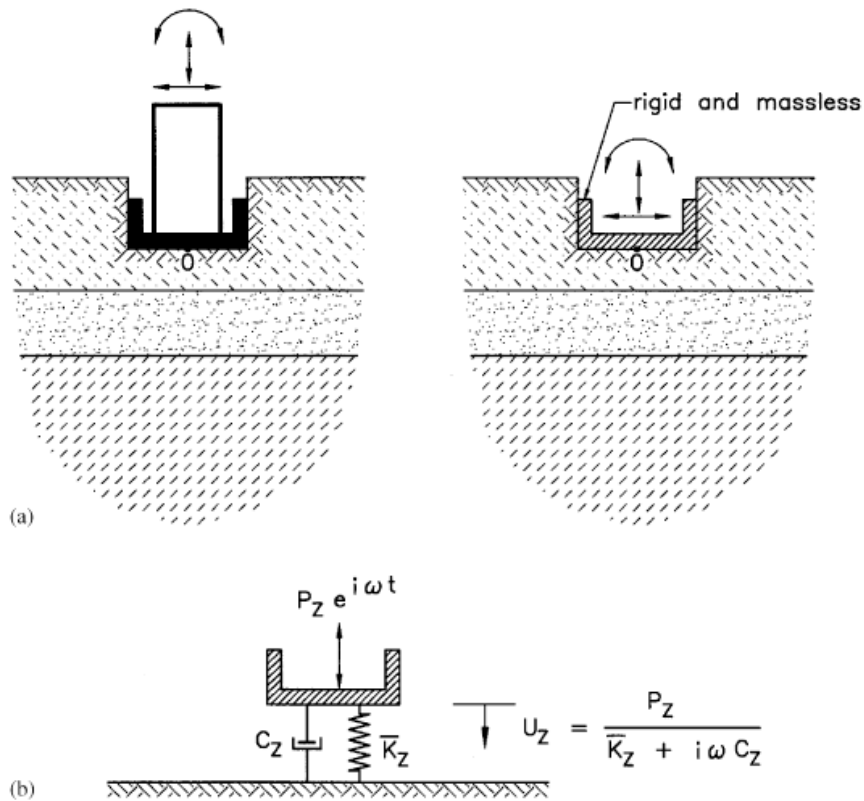


Figure 4.1: Physical interpretation of dynamic impedance in vertical mode of vibration (Mylonakis et al., 2006).

Gazetas (1991) presented a very useful table containing simply formulas for the dynamic impedance of a single pile; to use that, it's important to keep in mind that the response of piles laterally loaded (by horizontal forces and moments) is independent of their length is the latter is larger than the active length, defined in the previous chapter.

For the three lateral impedances ("springs" and "dashpots") defined in Figure 4.2, the table presents formulas, which, however, are valid only for piles with length greater than the active length. These piles are described as "flexible" piles in the literature, but a good majority of piles, even some with large diameters, fall into this category.

It's worth precisising that the dynamic stiffness ("springs"), is expressed as the product of the static stiffness, K , times the dynamic stiffness coefficient k , function of frequency:

$$\bar{K} = K \cdot k(\omega) \quad (4.2)$$

The damping coefficient C , as it is made of two parts, taking into account material and radiation damping, is expressed as:

$$total\ C = radiation\ C + \frac{2\bar{K}\beta}{\omega} \quad (4.3)$$

Where the symbol β , used in the tables, stands for the hysteretic damping coefficient.

The formulas in the table, shown in Figure 4.3, take into account both parts and then provide the total value of C .

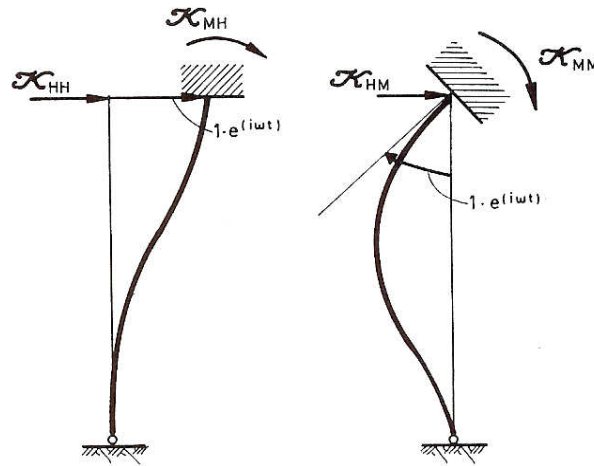


Figure 4.2: Dynamic impedance of a single pile (Gazetas, 1991).

Gazetas (1991) advises that from a theoretical point of view most of the formulas in the table are reasonably accurate, as they are basically curve fits to rigorous numerical results. The real difficulty, however, is to select the proper profile and modulus for the supporting soil. Even with a uniform top layer, the secant soil modulus will change with the magnitude of induced strains, which decreases with depth. Other nonlinear phenomena, such as development of a gap between pile and soil near the ground surface, further complicate the problem.

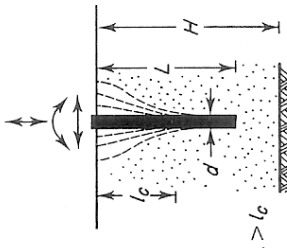
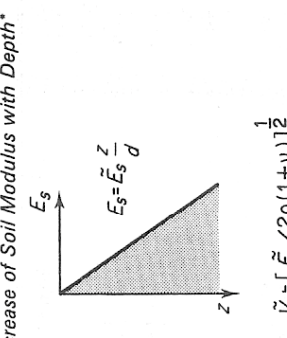
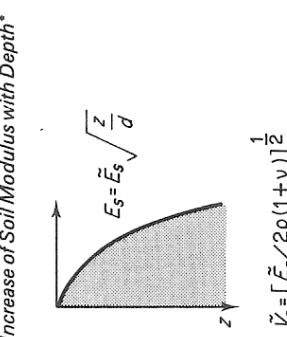
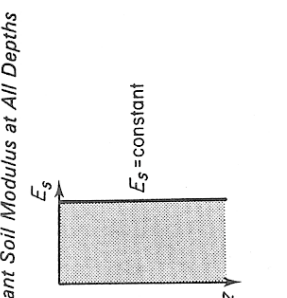
Another complication is the prediction of the impedances of pile groups, accounting for pile-to-pile interaction. Also at static working loads, in fact, the displacement of a pile increases if this pile is located within the deformation field of a neighbouring pile, and then the overall displacement of the group of piles is larger than the individual displacement which each pile would experience when alone to carry the average load.

4.1.2 Dynamic impedance of a pile group

Rational analyses of pile group displacements were pioneered by Poulos (1968, 1971), who introduced the concept of *interaction factors* and showed that pile group effects can be assessed by superimposing the effects of only two piles.

Static interaction factors do not provide useful information on the steady-state dynamic response of pile groups, except perhaps at very low frequencies of vibration. Dobry & Gazetas (1988) provided a very simple analytical solution to the problem of dynamic pile-soil-pile interaction in uniform soil and presented interesting parametric results for the stiffness and damping of groups of floating piles.

Figure 4.4 shows the two soil profiles for which parametric results are presented.

 <p>$L > l_c$</p>	<p>Linear Increase of Soil Modulus with Depth*</p>  $\tilde{E}_s = [\tilde{E}_s / 2\rho(1+\nu)]^{\frac{1}{2}}$	<p>Parabolic Increase of Soil Modulus with Depth*</p>  $\tilde{E}_s = [\tilde{E}_s / 2\rho(1+\nu)]^{\frac{1}{2}}$	<p>Constant Soil Modulus at All Depths</p>  $E_s = \text{constant}$
<p>"Active length"</p>	$l_c \approx 2d(E_p/\tilde{E}_s)^{0.20}$	$l_c \approx 2d(E_p/\tilde{E}_s)^{0.22}$	$l_c \approx 2d(E_p/E_s)^{0.25}$
<p>Natural shear frequency of deposit</p>	$f_s = 0.19V_{sH}/H$ where V_{sH} = the S-wave velocity at depth $z = H$ (bottom of stratum)	$f_s = 0.223V_{sH}/H$ where V_{sH} = the S-wave velocity at depth $z = H$ (bottom of stratum)	$f_s = 0.25V_s/H$
<p>Static lateral (swaying) stiffness</p> <p>Lateral (swaying) stiffness coefficient</p> <p>Lateral (swaying) coefficient:</p> $C_{HH} = 2K_{HH}D_{HH}/\omega$	$K_{HH} = 0.6d\tilde{E}_s(E_p/\tilde{E}_s)^{0.35}$ $k_{HH} \approx 1$ $\begin{cases} D_{HH} \approx 0.60\beta + 1.80fd\tilde{V}_s^{-1}, & \text{for } f > f_s \\ D_{HH} \approx 0.60\beta, & \text{for } f \leq f_s \end{cases}$	$K_{HH} = 0.8d\tilde{E}_s(E_p/\tilde{E}_s)^{0.28}$ $k_{HH} \approx 1$ $\begin{cases} D_{HH} \approx 0.70\beta + 1.20fd(E_p/\tilde{E}_s)^{0.08}\tilde{V}_s^{-1}, & \text{for } f > f_s \\ D_{HH} \approx 0.70\beta, & \text{for } f \leq f_s \end{cases}$	$K_{HH} = dE_s(E_p/E_s)^{0.21}$ $k_{HH} \approx 1$ $\begin{cases} D_{HH} \approx 0.80\beta + 1.10fd(E_p/E_s)^{0.17}\tilde{V}_s^{-1}, & \text{for } f > f_s \\ D_{HH} \approx 0.80\beta, & \text{for } f \leq f_s \end{cases}$
<p>Static rocking stiffness</p> <p>Rocking stiffness coefficient</p> <p>Rocking dashpot coefficient:</p> $C_{MM} = 2K_{MM}D_{MM}/\omega$	$K_{MM} = 0.15d^3\tilde{E}_s(E_p/\tilde{E}_s)^{0.80}$ $k_{MM} \approx 1$ $\begin{cases} D_{MM} \approx 0.20\beta + 0.40fd\tilde{V}_s^{-1}, & \text{for } f > f_s \\ D_{MM} \approx 0.20\beta, & \text{for } f \leq f_s \end{cases}$	$K_{MM} = 0.15d^3\tilde{E}_s(E_p/\tilde{E}_s)^{0.77}$ $k_{MM} \approx 1$ $\begin{cases} D_{MM} \approx 0.22\beta + 0.35fd(E_p/\tilde{E}_s)^{0.10}\tilde{V}_s^{-1}, & \text{for } f > f_s \\ D_{MM} \approx 0.22\beta, & \text{for } f \leq f_s \end{cases}$	$K_{MM} = 0.15d^3E_s(E_p/E_s)^{0.75}$ $k_{MM} \approx 1$ $\begin{cases} D_{MM} \approx 0.35\beta + 0.35fd(E_p/E_s)^{0.20}\tilde{V}_s^{-1}, & \text{for } f > f_s \\ D_{MM} \approx 0.25\beta, & \text{for } f \leq f_s \end{cases}$
<p>Static swaying-rocking cross-stiffness</p> <p>Swaying-rocking cross-stiffness coefficient</p> <p>Swaying-rocking dashpot coefficient:</p> $C_{HM} = 2K_{HM}D_{HM}/\omega$	$K_{HM} = K_{MH} = -0.17d^2\tilde{E}_s(E_p/\tilde{E}_s)^{0.80}$ $k_{HM} = k_{MH} \approx 1$ $\begin{cases} D_{HM} \approx 0.30\beta + fd\tilde{V}_s^{-1}, & \text{for } f > f_s \\ D_{HM} \approx 0.30\beta, & \text{for } f \leq f_s \end{cases}$	$K_{HM} = K_{MH} = -0.24d^2\tilde{E}_s(E_p/\tilde{E}_s)^{0.53}$ $k_{HM} = k_{MH} \approx 1$ $\begin{cases} D_{HM} \approx 0.60\beta + 0.70fd(E_p/\tilde{E}_s)^{0.05}\tilde{V}_s^{-1}, & \text{for } f > f_s \\ D_{HM} \approx 0.35\beta, & \text{for } f \leq f_s \end{cases}$	$K_{HM} = K_{MH} = -0.22d^2E_s(E_p/E_s)^{0.50}$ $k_{HM} = k_{MH} \approx 1$ $\begin{cases} D_{HM} \approx 0.80\beta + 0.85fd(E_p/E_s)^{0.18}\tilde{V}_s^{-1}, & \text{for } f > f_s \\ D_{HM} \approx 0.50\beta, & \text{for } f \leq f_s \end{cases}$

Static axial stiffness	The axial stiffness of a pile depends not only on its relative compressibility (E_p/E_s) but also on the slenderness ratio L/d and the tip support conditions (end-bearing versus floating). See the pertinent geotechnical literature for a proper estimation of the static stiffness. The expressions given herein are <i>only</i> for estimates of the axial stiffness of floating piles in a homogeneous stratum of total thickness $H \approx 2L$.		
	$K_z \approx 1.8 E_{sL} d \left(\frac{L}{d} \right)^{0.55} \left(\frac{E_p}{E_{sL}} \right)^{-(L/d)(E_p/E_{sL})}$ $E_{sL} = \bar{E}_s \cdot (L/d)$	$K_z \approx 1.9 E_{sL} d \left(\frac{L}{d} \right)^{0.6} \left(\frac{E_p}{E_{sL}} \right)^{-(L/d)(E_p/E_{sL})}$ $E_{sL} = \bar{E}_s \cdot \sqrt{(L/d)}$	$K_z \approx 1.9 E_s d \left(\frac{L}{d} \right)^{2/3} \left(\frac{E_p}{E_s} \right)^{-(L/d)(E_p/E_s)}$
Axial dynamic stiffness coefficient	$k_z \approx 1$ (for $a_0 = \omega d / V_{sL} < 0.5$, where V_{sL} is the S-wave velocity at depth L)	$L/d < 20: k_z \approx 1$ $L/d \geq 50: k_z \approx 1 + \frac{1}{3} \sqrt{a_0}$ interpolate in between (for $a_0 = \omega d / V_{sL} < 0.5$)	$L/d < 15: k_z \approx 1$ $L/d \geq 50: k_z \approx 1 + \sqrt{a_0}$ interpolate in between (for $a_0 = \omega d / V_s < 1$)
	In all cases, k_z shows a narrow valley at the resonant frequency f_r of the soil stratum; as a first approximation, $f_r \approx f_c \approx \bar{V}_{La} / 4H$ and $k_z(f_r) \approx 0.8$ for material soil damping $\beta = 0.05$. \bar{V}_{La} is the average V_{La} over the whole stratum depth.		
Axial radiation dashpot coefficient	$C_z \approx \frac{2}{3} a_0^{-1/3} \rho V_{sL} \pi d L r_d$ for $f > 1.5 f_r$, where: $r_d \approx 1 - e^{-2(E_p/E_{sL})(L/d)^{-2}}$ $C_z \approx 0$ for $f \leq f_r$ linearly interpolate for $f_r < f < 1.5 f_r$	$C_z \approx \frac{2}{3} a_0^{-1/4} \rho V_{sL} \pi d L r_d$ for $f > 1.5 f_r$, where: $r_d \approx 1 - e^{-1.5(E_p/E_{sL})(L/d)^{-2}}$ $C_z \approx 0$ for $f \leq f_r$ linearly interpolate for $f_r < f < 1.5 f_r$	$C_z \approx a_0^{-1/5} \rho V_s \pi d L r_d$ for $f > 1.5 f_r$, where: $r_d \approx 1 - e^{-(E_p/E_s)(L/d)^{-2}}$ $C_z \approx 0$ for $f \leq f_r$ linearly interpolate for $f_r < f < 1.5 f_r$
<i>Pile-to-Pile Interaction Factors for Assessing the Response of Floating Pile Groups</i>			
Interaction factor α_z for axial in-phase oscillations of the two piles	$\alpha_z \approx \sqrt{2} \left(\frac{S}{d} \right)^{-3/4} \cdot e^{-0.5\beta\omega S / V_{sL}} \cdot e^{-i\omega\sqrt{2}S / V_{sL}}$	$\alpha_z \approx \sqrt{2} \left(\frac{S}{d} \right)^{-2/3} \cdot e^{-(2/3)\beta\omega S / V_{sL}} \cdot e^{-i\omega\sqrt{2}S / V_{sL}}$	$\alpha_z \approx \sqrt{2} \left(\frac{S}{d} \right)^{-1/2} \cdot e^{-\beta\omega S / V_s} \cdot e^{-i\omega S / V_s}$
	V_{sL} = the S-wave velocity at depth $z = L$; $\bar{V}_s = V_s$ at pile mid-length; S = axis-to-axis pile separation; β = soil hysteretic damping. Note: although α_z are complex numbers their use is identical to the familiar use of static interaction factors introduced by Poulos.		
Interaction factor α_{HH} for lateral in-phase oscillation	Very little information presently available	Very little information presently available	$\alpha_{HH}(90^\circ) \approx (3/4) \alpha_z$ $\alpha_{HH}(0^\circ) \approx 0.5 \left(\frac{S}{d} \right)^{-1/2} \cdot e^{-\beta\omega S / V_{La}} \cdot e^{-i\omega S / V_{La}}$ $\alpha_{HH}(\theta^\circ) \approx \alpha_{HH}(0^\circ) \cos^2 \theta + \alpha_{HH}(90^\circ) \sin^2 \theta$ $\alpha_{MM} \approx \alpha_{MH} \approx 0$
Interaction factors: α_{MM} for in-phase rocking, and α_{HM} for swaying-rocking	$\alpha_{MM} \approx \alpha_{MH} \approx 0$	$\alpha_{MM} \approx \alpha_{MH} \approx 0$	$\alpha_{MM} \approx \alpha_{MH} \approx 0$

* \bar{E}_s and \bar{V}_s (for the two inhomogeneous deposits) denote Young's modulus and S-wave velocity, respectively, at depth.

Figure 4.3: Table for dynamic impedance, interaction factors and active length of a single pile (Gazetas, 1991).

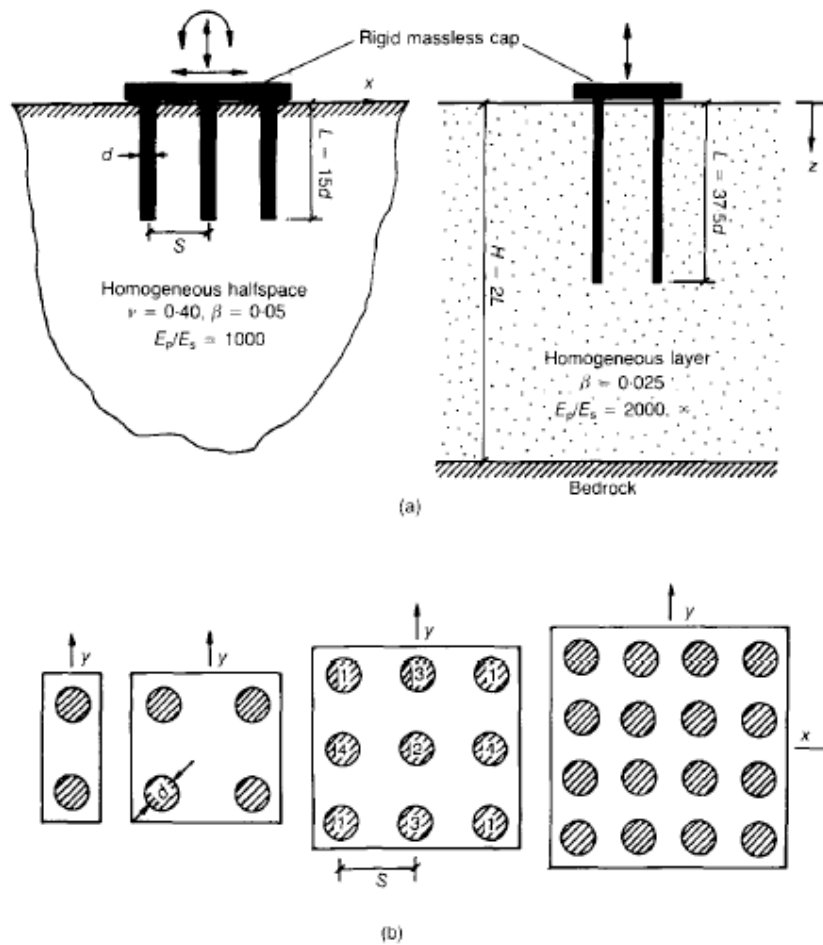


Figure 4.4: Parametric study by Dobry & Gazetas (Dobry & Gazetas, 1988)

Poulos' (1968, 1971) superposition procedure, originally developed for statically loaded pile groups, is also valid for the dynamic problem (but with different coefficients taking into account the dynamic nature of the excitation), as various authors have demonstrated that the results of this approximation are in very good agreement with more rigorous dynamic solutions. Therefore, the response of the pile group can be obtained from interaction factors derived from the study of only two piles at a time. In other words, it is assumed that the other piles do not appreciably affect the interplay between the two piles being considered. This means that, when computing the influence of pile p on pile q the intermediate piles are considered to be transparent; this assumption is not far from reality, as the wavelengths of practical interest ($\lambda > 6d$) are too large for the waves propagating in the soil to “see” the cylindrical pile. Nevertheless, when the number of piles in a group is very large and the pile spacing relatively short, the interaction between two distant piles in the group will unavoidably be reduced due to ‘scattering’ of waves and the corresponding ‘shadows’ formed by the piles in-between.

To derive the influence of the motion of pile p (active) on pile q (passive), pile q can be replaced by its axis, neglecting its dimensions. The simple method presented by Dobry &

Gazetas assumes that the cylindrical waves emanate simultaneously from all points along the pile (p) length and hence, for a homogeneous deposit, to spread out in-phase and form a cylindrical wavefront having a common axis with that of the generating pile (see figure 4.5).

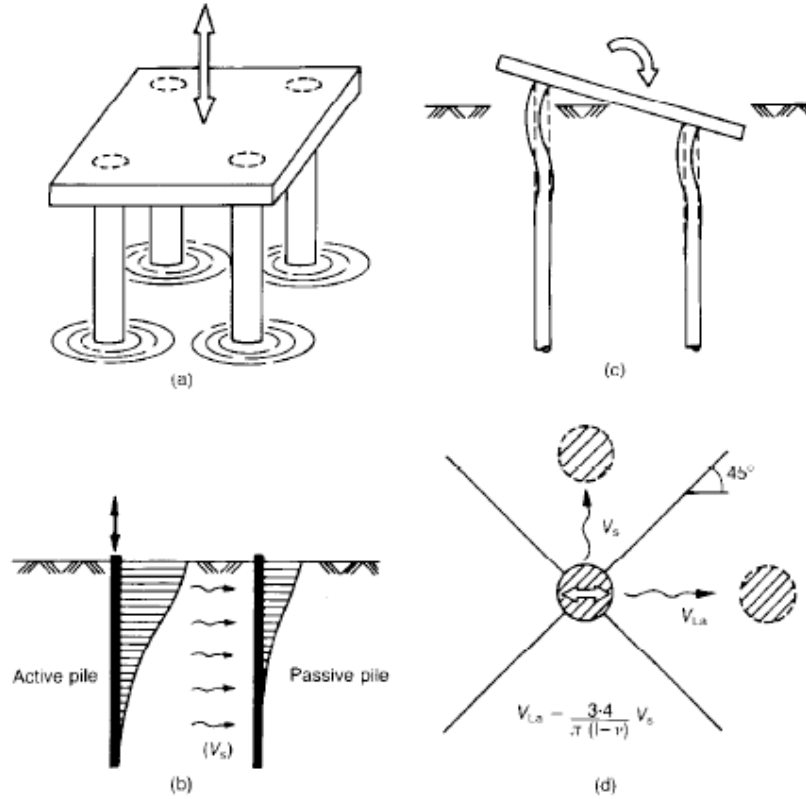


Figure 4.5: (a) analogy between with the cylindrical water waves; (b) distribution of displacement amplitudes along the shaft of an active and a passive pile; (c) pile head deformation and reactions during rocking; (d) waves emanating from a laterally oscillating pile (Dobry & Gazetas, 1988)

The variation of wave amplitude with depth along the cylindrical front arriving to the passive pile is assumed to be analogous with the amplitude variation of the active single pile, as depicted in Figure 4.5(b).

Another hypothesis is, in order to simplify, to substitute Hankel functions in the exact cylindrical wave solution with simple exponentials; the error is negligible.

In addition to these, some other assumptions are made when studying the horizontal and rocking modes of vibration.

The dynamic displacement field around the vibrating pile p (in an homogeneous soil) is described by the following asymptotic cylindrical wave expression:

$$w(r) \simeq A \frac{1}{\sqrt{r}} e^{-\beta \omega r / V_s} e^{i \omega (t - r / V_s)} \quad (4.4)$$

where r = horizontal distance from the axis of pile p and $A = A(z)$ = an amplitude constant. The other three factors in equation (4.4) imply that:

- the amplitude of motion decays in proportion to $r^{-1/2}$ times the hysteretic damping dependent factor β ;

- the phase lag of the motion at a particular location within the soil is only a function of the radial distance r .

At the axis of the pile q , located at a distance $r = s$,

$$w_{qp} \equiv w(r = s) = A \frac{I}{\sqrt{s}} e^{-\beta \omega s / V_s} e^{i \omega (t - s / V_s)} \quad (4.5)$$

Assuming that eq. (4.4) is still valid in the periphery of pile q , the displacement w_{qq} of pile q under its own dynamic load,

$$w_{qq} \simeq A \frac{I}{\sqrt{r_0}} e^{i \omega t} \quad (4.6)$$

Eq. (4.7) means also that there is no time lag between the axis and perimeter of the pile vibrating under its own load. Dividing eq. (4.5) by eq. (4.6), it can be obtained the expression for the vertical interaction factor:

$$\alpha_v \simeq \left(\frac{s}{r_0} \right)^{-1/2} e^{-\beta \omega s / V_s} e^{-i \omega s / V_s} \quad (4.7)$$

Rocking of piles fixed to a rigid cap induces both axial and rotational deformations (figure 4.5(c)). Based on the evidence available from the static solutions (Poulos & Davis, 1980) and on indirect evidence for the dynamic problem, it is assumed that no interaction takes place due to the rotational deformation of each pile. This kind of deformation (under zero lateral head displacement) is felt only a few diameters down from the pile head and so neighbouring piles fall outside each other's zone of influence for this effect.

For laterally oscillating piles the interaction factor α_h depends, for a given frequency ω , not only on the distance S but also on the angle between the line of the two piles and the direction of the horizontal applied force. However, it is sufficient to compute α_h only for 0° and 90° angles, and then use:

$$\alpha_h(\theta) \simeq \alpha_h(0) \cos^2 \theta + \alpha_h(90) \sin^2 \theta \quad (4.8)$$

Based on evidence provided by Gazetas & Dobry (1984) the 90° -pile q is affected essentially only by S-waves which emanate from active pile p and which have a phase velocity V_s , while the 0° -pile q is affected by compression-extension waves coming from p and propagating with an apparent phase velocity which is approximately equal to the so-called Lysmer's analog velocity, $V_{La} = 3.4 V_s [\pi(1 - \nu)]$. Hence,

$$\begin{aligned} \alpha_h(90^\circ) &\simeq \alpha_v \\ \alpha_h(0) &\simeq \left(\frac{s}{r_0} \right)^{-1/2} e^{-\beta \omega s / V_{La}} e^{-i \omega s / V_{La}} \end{aligned} \quad (4.9)$$

Dobry & Gazetas (1988) showed the result of a parametric study; some of these results will be presented here, as they may help to understand the dynamic behaviour of pile groups.

Figures 4.6 and 4.7 plot as a function of the dimensionless frequency factor $\omega d/V_s$ the dynamic stiffness and damping group factors, defined as the ratios of the dynamic stiffness or the dashpot coefficient to the sum of the static stiffnesses of the individual single piles. At zero frequency the foregoing stiffness group factor reduces to the static group efficiency factor (Fleming et al., 1985). If there had been no interaction the group factor curves would have coincided with those of the single pile. Figure 4.7 plots the distribution of forces among the piles of a 3 x 3 group as a function of frequency.

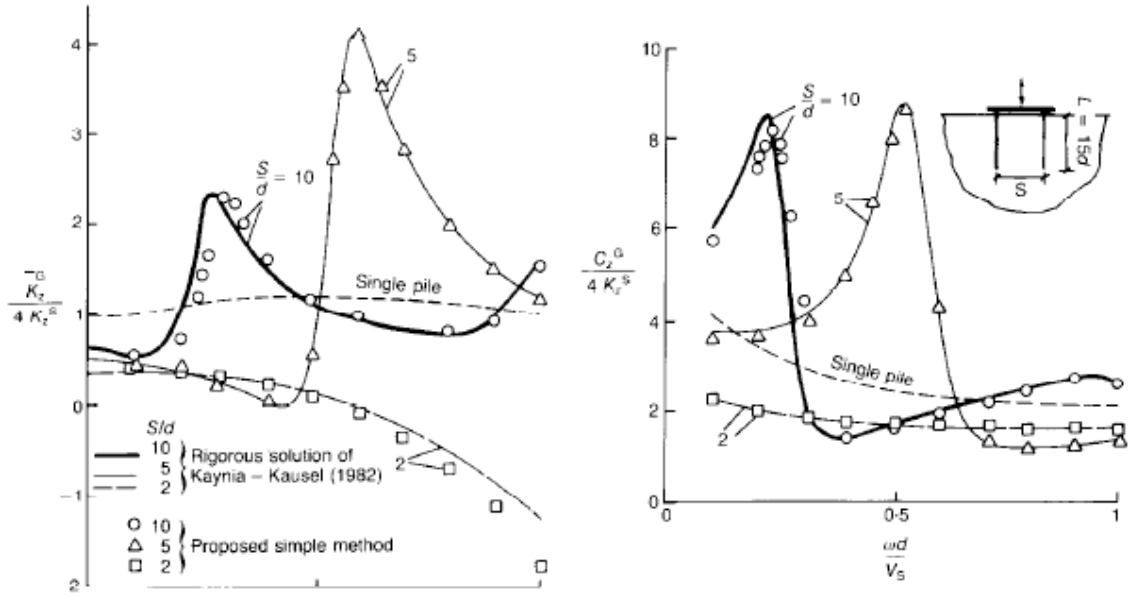


Fig. 4.6: Vertical dynamic stiffness and damping group factors as a function of frequency - comparison of proposed simple method with rigorous solution of Kaynia & Kausel (1982) for a group of 2 x 2 fixed-head piles in a homogeneous halfspace ($E_p/E_s = 1000$, $L/d = 15$) (Dobry & Gazetas, 1988)

For very close pile spacings ($s/d = 2$) the stiffness and damping group factors exhibit a smooth variation with frequency, with the pile group behaving very much like an isolated embedded foundation (Gazetas, Dobry & Tassoulas, 1985). Indeed, while the damping coefficients remain essentially constant in the frequency range studied, the dynamic group stiffnesses decrease with increasing frequency, achieving negative values at higher frequency factors. Such a behaviour is reminiscent of the simple SDOF system having mass M , spring constant K and dashpot coefficient C (see Chapter 1), the effective dynamic stiffness of which,

$$\bar{K} = K - M \omega^2 \quad (4.10)$$

decreases parabolically with frequency while C is constant. The causes of the similarity is that at such close spacings (the important wavelengths are larger than 3 spacings) the soil mass between piles tends to vibrate in phase with the piles and so the pile group-soil system responds as a block.

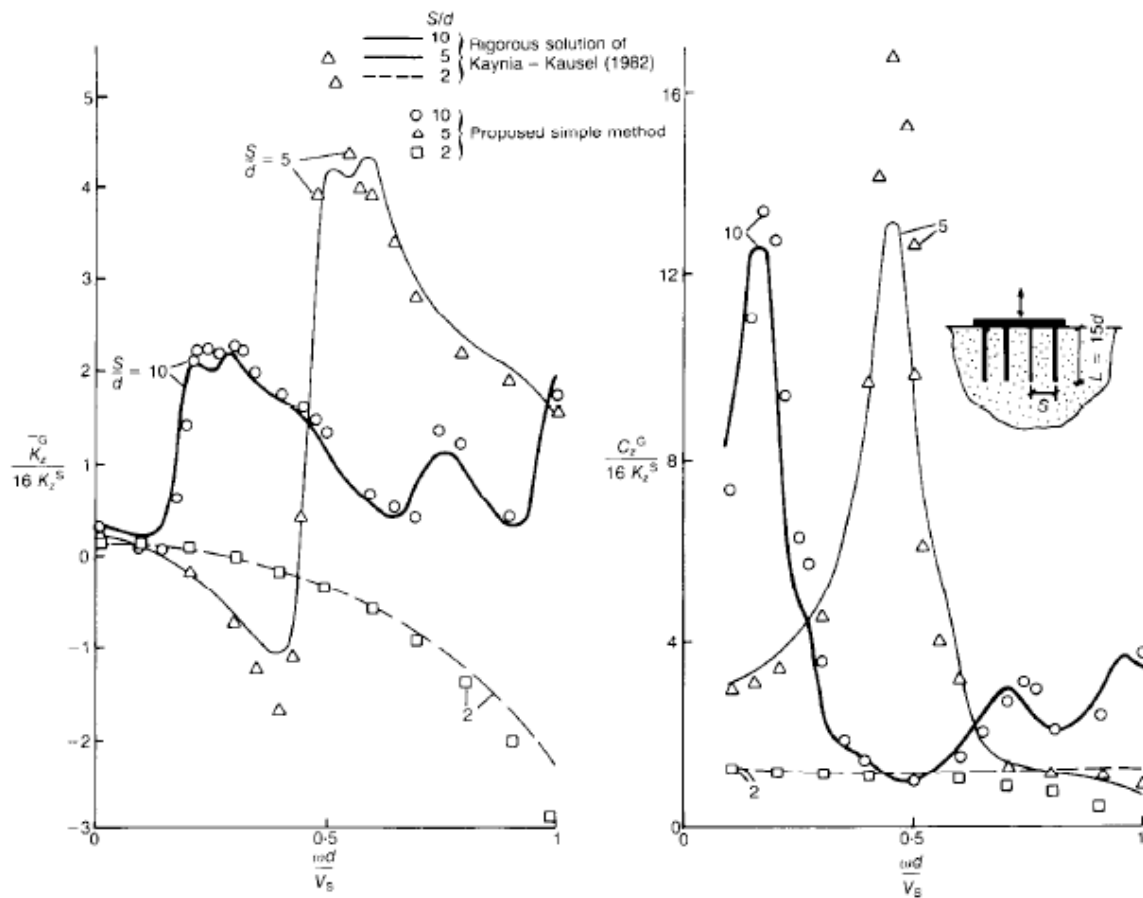


Fig. 4.7: Vertical dynamic stiffness and damping group factors as a function of frequency - comparison of proposed simple method with rigorous solution of Kaynia & Kausel (1982) for a group of 4 x 4 fixed-head piles in a homogeneous halfspace ($E_p/E_s = 1000$, $L/d = 15$) (Dobry & Gazetas, 1988).

Groups with more amply spaced piles ($s/d = 5$ or 10) exhibit a more complicated behaviour. Initially, at low enough frequencies, the group stiffnesses invariably decrease with frequency, as the relevant wavelengths are again large enough compared to pile spacing and the soil between the piles moves in phase with the piles (response as a block). However, beyond a certain limiting value of the frequency, wave interference phenomena start dominating the response of the soil-pile group system. This limiting frequency is essentially independent of group size but decreases with increasing pile spacing.

When the frequency exceeds that limiting value, pile-to-pile interaction leads to stiffness group factors that may far exceed both unity and the single-pile factor. The predominant peaks occur in each case at the frequency at which the corresponding wavelength is about two times the pile spacing s . The explanation is that in this case cylindrical waves originating with a certain phase from a pile p arrive at the neighbouring pile q in exactly opposite phase, thereby inducing a displacement which is negative compared to the displacement due to this pile's own load. Hence, the dynamic interaction factor is negative and a larger force must be applied onto pile q to enforce a certain displacement amplitude. The distribution of forces among the piles of the 3 x 3 group, shown in Figure 4.8, is very sensitive to variations in frequency and pile spacing.

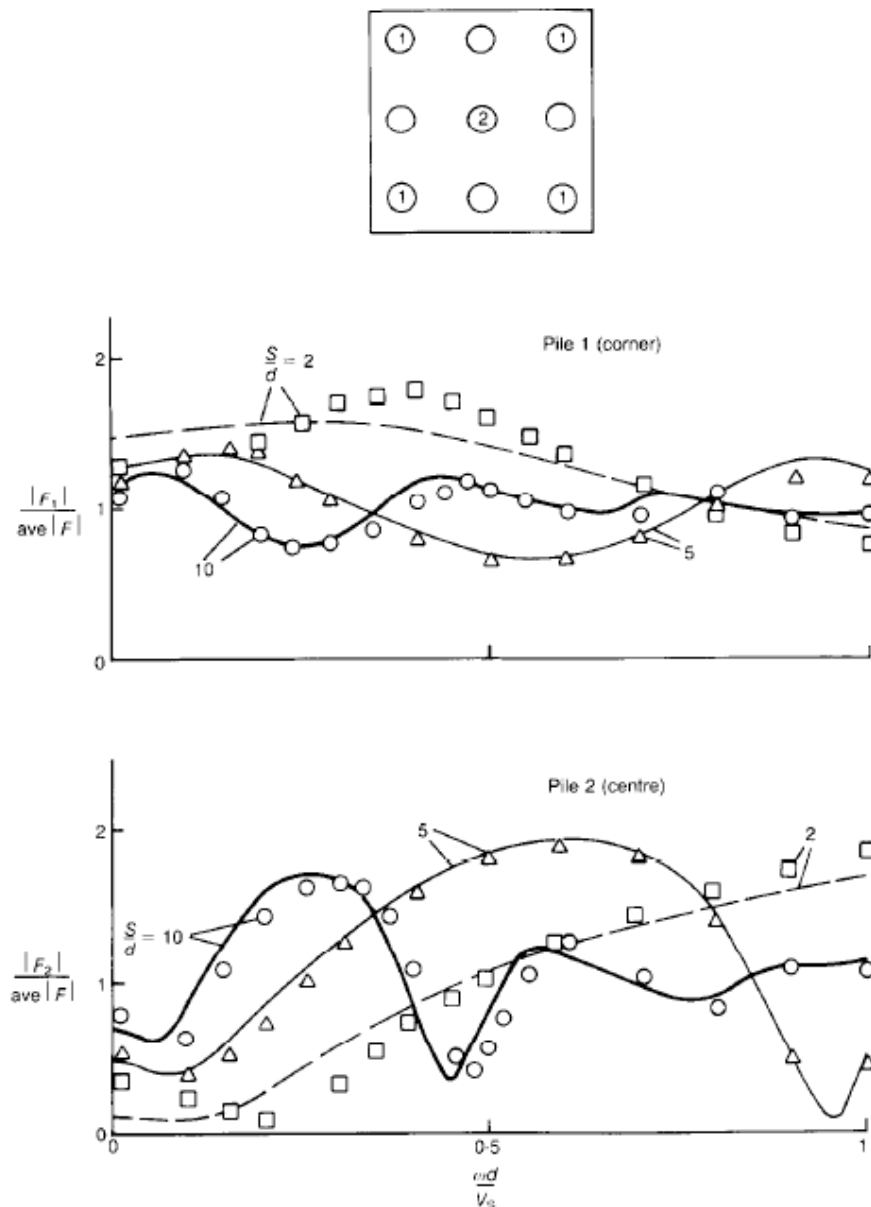


Fig. 4.8: Variation of the distribution of axial force amplitudes carried by the corner and centre piles in a 3 x 3 fixed-head pile group, as a function of vibration frequency and pile spacing $E_p/E_s = 1000$, $L/d = 15$, vertical loading: comparison of proposed simple method with rigorous solution of Kaynia & Kausel (1982) (Dobry & Gazetas, 1988).

For static and low-frequency excitation the corner piles carry the largest portion of the applied load, but in some frequency ranges the centre pile carries 2 times the average load (regardless of pile spacing) while the share of the corner piles drops down to nearly 60% of the average load, in opposition to the static situation.

For rocking around the x -axis Figure 4.9 plots the dynamic stiffness and damping, divided by the sum of the contributions of the single pile axial static stiffnesses to the rocking static stiffness of the group. The dynamic stiffness and damping group factors for fixed-head horizontal oscillation (without rotation) are portrayed in Figures 4.10 and 4.11. The trends

observed in these figures can be explained by recourse to arguments similar to those advanced for vertical oscillations.

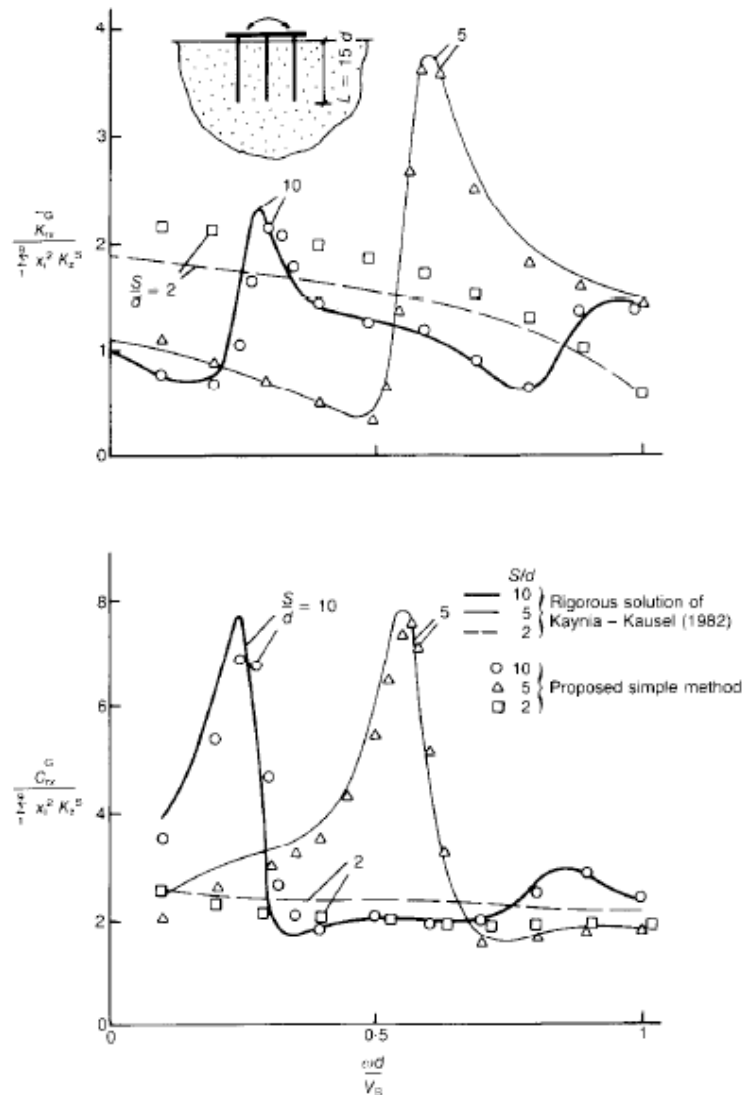


Fig. 4.9. Rocking stiffness and damping group factors as a function of frequency: comparison of proposed simple method with the rigorous solution of Kaynia & Kausel (1982) for a group of 3 x 3 fixed-head piles in a homogeneous halfspace, $E_p/E_s = 1000$, $L/d = 15$ (Dobry & Gazetas, 1988).

4.1.3 The role of SSI

Mylonakis & Gazetas (2000) elucidated the role of seismic soil-structure interaction.

The soil supporting a structure, in fact, being deformable, modifies its seismic response for different reasons. Firstly, the structure has a longer fundamental period (with respect to the case in which the structure is fully restrained at its base), and, secondly, part of the energy of the vibrating flexibly-supported structure is dissipated into the soil through wave radiation and hysteretic action, resulting in a larger effective damping (Figure 4.12).

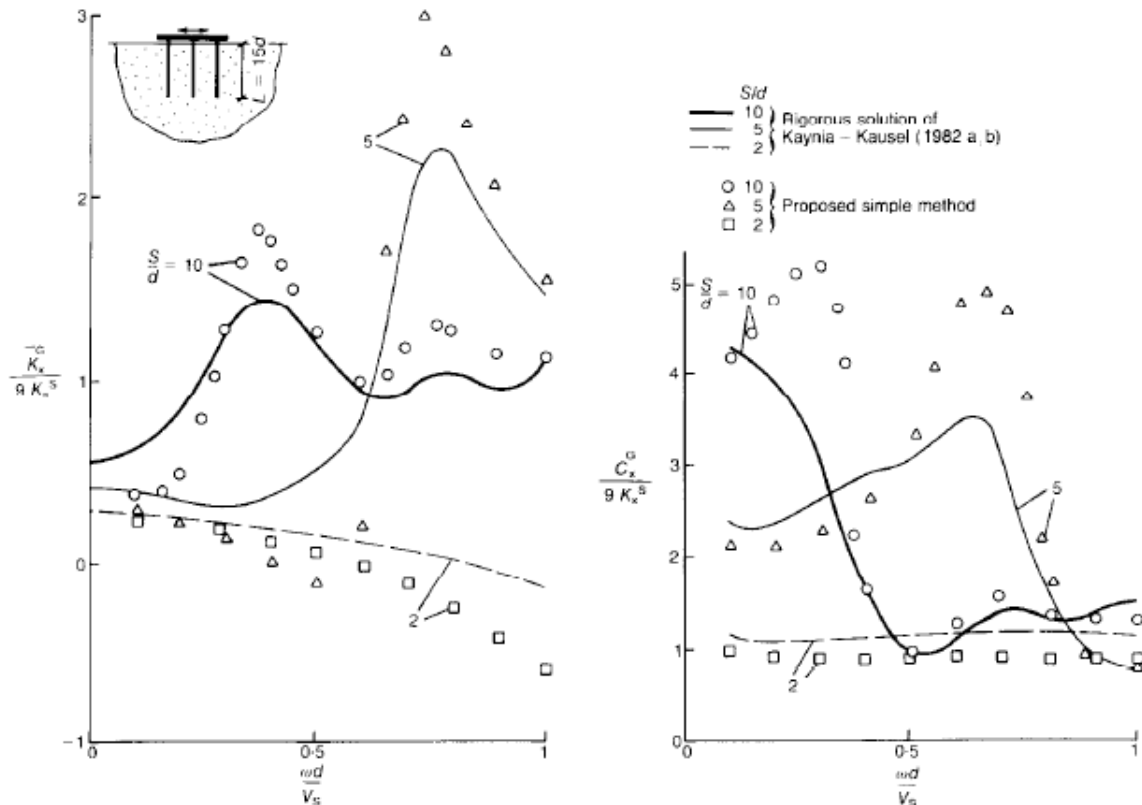


Fig. 4.10. Lateral (swaying) stiffness and damping group factors as a function of frequency: comparison of proposed simple method with rigorous solution of Kaynia & Kausel (1982) for a group of 3 x 3 fixed-head piles in a homogeneous halfspace, $E_p/E_s = 1000$, $L/d = 15$ (Dobry & Gazetas, 1988).

The seismic codes generally refer to design spectra reaching constant acceleration up to a certain period, then decreasing monotonically with period; as a consequence, SSI has to lead to smaller accelerations (and then stresses in the structure and its foundation). The assessment of a beneficial role of SSI is not always true.

There is evidence, documented in numerous case histories, that assuming a beneficial role of SSI may lead to unsafe design for both the superstructure and the foundation. To elucidate this, the ordinates of a conventional design spectrum for soft deep soil, are compared graphically in Figure 4.13 against four selected response spectra; as it can be noticed, all the recorded spectra reach their maxima at periods exceeding 1.0 s, some of these are a result of resonance of the soil deposit with the seismic waves (as in the case with the Mexico City SCT record). It is evident that an increase in the fundamental period due to SSI may lead to increased response (but also a possible increase in damping), which is in contrast with conventional design spectrum. It is important to note that all three earthquakes induced damage associated with SSI effects.

Mexico earthquake was particularly destructive to 10- to 12-storey buildings founded on soft clay, whose period increased from about 1.0 s (under the hypothesis of fixed base) to about 2.0 s in reality due to SSI.

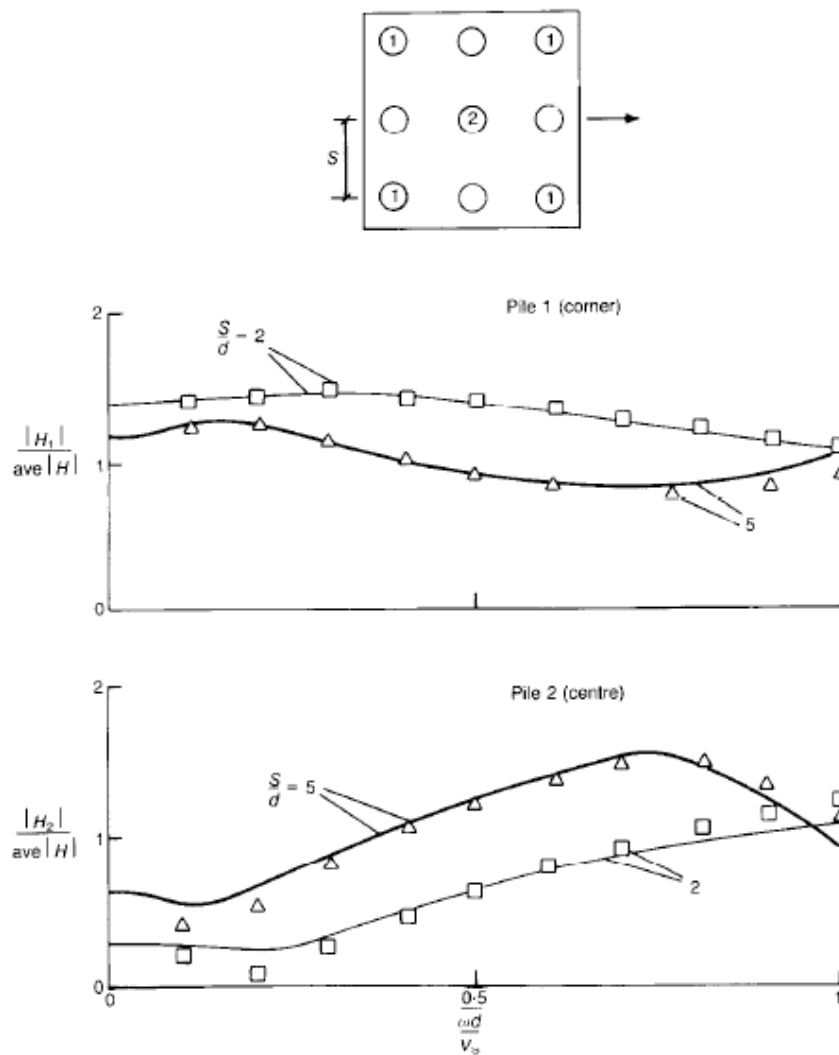


Fig. 4.11. Variation of the distribution of shear force amplitudes carried by the corner and centre piles in a 3 x 3 fixed-head pile group, as a function of lateral vibration frequency and pile spacing: comparison of proposed simple method with rigorous solution of Kaynia & Kausel (1982) for a group of 3 x 3 fixed-head piles in a homogeneous halfspace, $E_p/E_s = 1000$, $L/d = 15$ (Dobry & Gazetas, 1988).

The role of SSI on the failure of the 630 m elevated highway section of Hanshin Expressway's Route 3 in Kobe (Fukae section) has also been detrimental and is discussed in Gazetas and Mylonakis (1998) and (Mylonakis et al., 2000).

Hence, using the conventional design spectra and simplified soil profiles in may not reveal the danger of increased seismic demand on the structure. To elucidate this, the Authors analysed a set of 24 actual records. The average acceleration spectrum obtained from these motions is presented in Figure 4.14, in terms of spectral amplification. The structural period is presented in three different ways:

- actual period T
- normalised period $T = T_g$ (T_g = “effective” ground period, defined as the period where the 5% velocity spectrum attains its maximum (Miranda and Bertero, 1994))

- normalised period $T = T_a$ (T_a = period where acceleration spectrum attains its maximum).

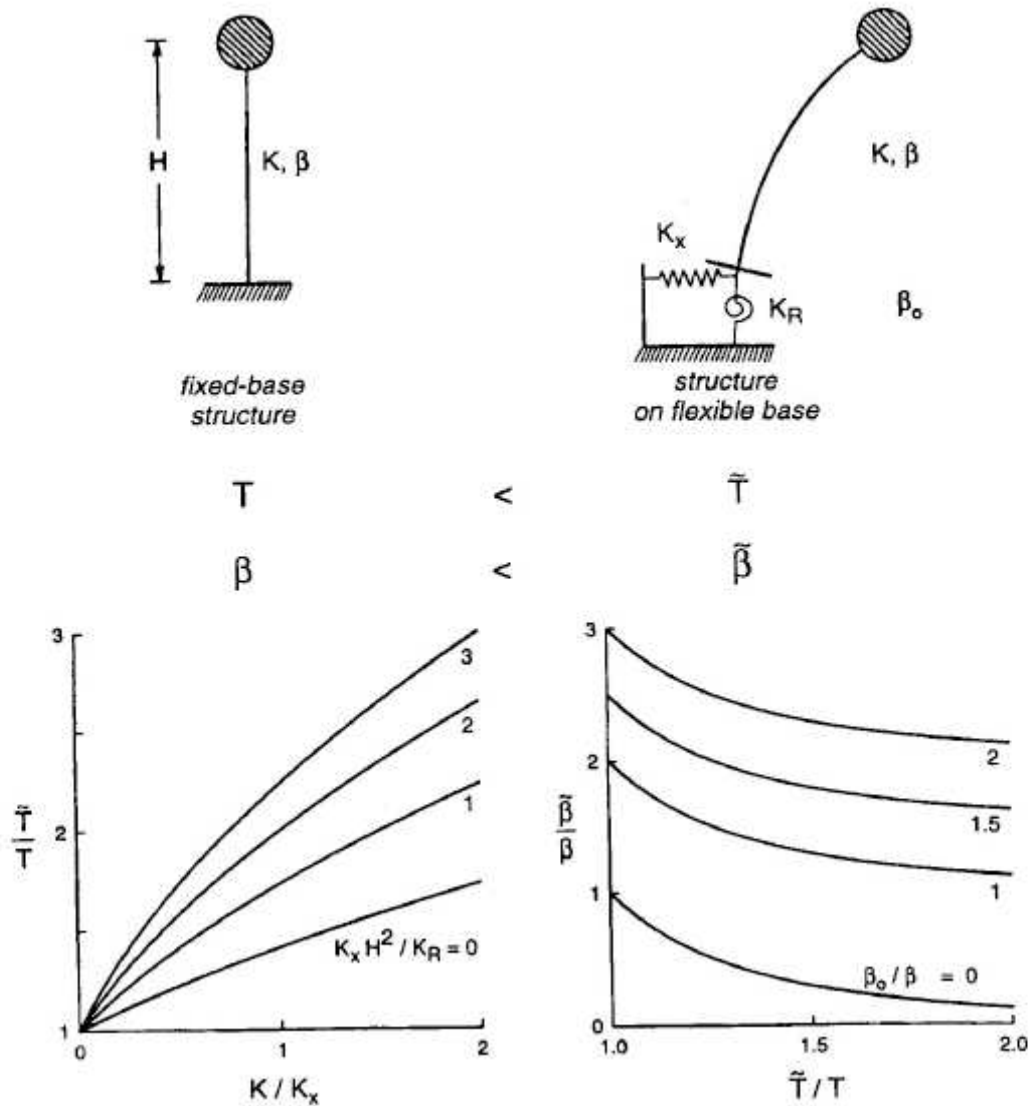


Figure 4.12: Fixed base vs. flexible base structure (Mylonakis & Gazetas, 2000).

It is seen that with the actual period is similar to that used in current seismic codes, because the spectra of motions recorded on soft soil attain their maxima at well separated periods and, hence, averaging them eliminates the peaks. In contrast, with the normalised periods the average spectrum exhibits a characteristic peak close to 1, which reproduces the trends observed in actual spectra.

Recently developed procedures for displacement-based design utilise displacement (instead of acceleration) spectra that, differently to acceleration spectra, show increasing trends over large ranges of periods and, hence, SSI effects will not be always beneficial for seismic response.

Gazetas & Mylonakis (2000) also found that, analysing the response of inelastic system, SSI can increase the ductility demand, and, hence, neglecting SSI may be unsafe.

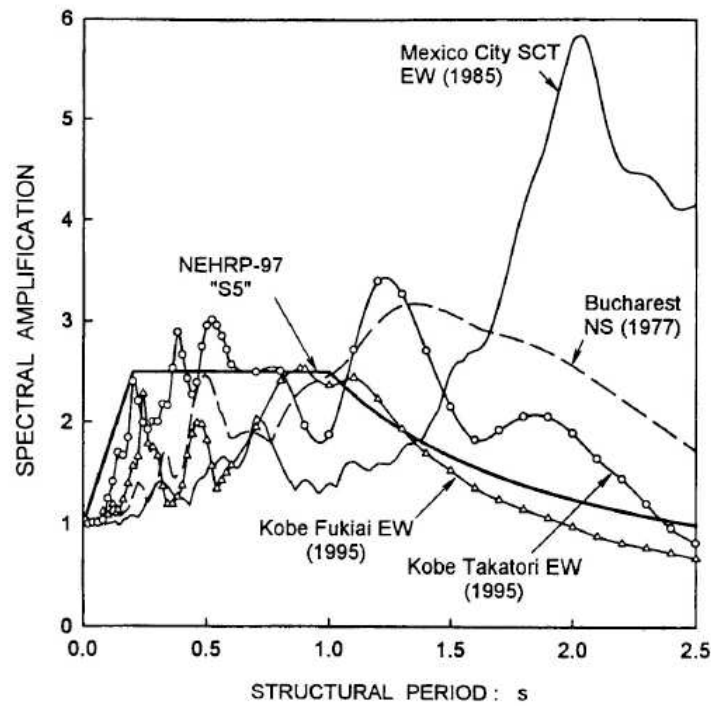


Figure 4.13: Comparison of a typical seismic code design spectrum to actual spectra from catastrophic earthquakes with strong long-period components; $\beta = 5\%$ (Mylonakis & Gazetas, 2000).

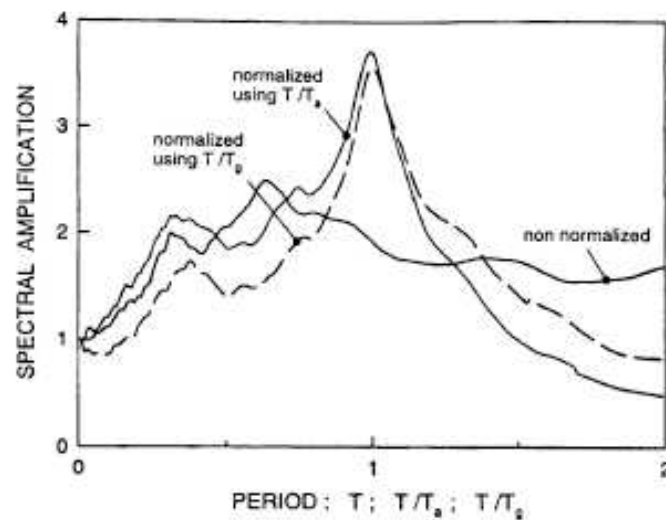


Figure 4.14: Average acceleration spectra based on 24 actual motions recorded on soft soil. The periods are either normalised before averaging with: (a) period of peak spectral acceleration (T_a); (b) period of peak spectral velocity (T_g); or (c) average without any normalisation; $\beta = 5\%$ (Mylonakis & Gazetas, 2000).

4.2 KINEMATIC VS. INERTIAL INTERACTION

4.2.1 *Relative importance of kinematic vs. inertial interaction*

Several recent seismic Codes impose to evaluate the effects of kinematic interaction only under certain conditions, but regardless of the amount and the distribution of masses of the structure.

It is evident that it should be allowable to neglect kinematic interaction when its effects are negligible with respect to inertial ones; for this reason the Codes indications appears to be incomplete, as the inertial effects are proportional to the structure mass, while kinematic ones are evidently not dependent on it.

To investigate the relative importance of inertial vs. kinematic interaction (and then to verify the veracity of the indications of the Codes), once it has been estimated the effects of the latter through the formulas proposed in the Chapter 3, it has been built a simple tool for evaluating the foundation impedance and the resulting inertial effects at piles top.

To account for the dynamic nature of the excitation, it has been said that the foundation impedance is function of frequency ω ; therefore, the evaluation of both the compliances of a single pile and the interaction coefficients should be carried out taking into account the soil damping and the frequency of excitation.

Nevertheless, for low frequencies, it is possible to refer to the static case; if the aim is to highlight the relative importance of kinematic vs. inertial interaction this simplification appears even more allowable.

The kinematic moment at pile top can be well estimated through the formula presented in the previous Chapter, leading to:

$$M_{kin} = \frac{a_s r^4 \pi E_p}{4V_{s,l}^2} \quad (4.11)$$

with a_s the maximum acceleration at free-field ground surface.

About the soil-foundation stiffness, the expressions for evaluating the compliances of a single pile by Randolph (1981) have been chosen. They are:

$$C_{uu} = \frac{0.54 \left(\frac{E_p}{G^*} \right)^{\frac{1}{7}}}{G^* L_c} \quad (4.12)$$

$$C_{u\theta} = C_{\theta u} = \frac{1.2 \left(\frac{E_p}{G^*} \right)^{\frac{1}{7}}}{G^* L_c^2} \quad (4.13)$$

$$C_{\vartheta\vartheta} = \frac{6.4 \left(\frac{E_p}{G^*} \right)^{\frac{1}{7}}}{G^* L_c^3} \quad (4.14)$$

where:

$$L_c = 2r \left(\frac{E_p}{G^*} \right)^{\frac{2}{7}} \quad (4.15)$$

$$G^* = G \left(1 + 3 \frac{\nu}{4} \right) \quad (4.16)$$

Setting the Poisson coefficient to 0.3, the vertical stiffness given by Randolph and Wroth (1979) becomes:

$$k_{zz,s} = r G_s \frac{5.71 + \frac{2\pi L \tanh(\mu L)}{\zeta L} \frac{\mu L}{\pi r \lambda}}{1 + 5.71 \frac{L}{\pi r \lambda} \frac{\tanh(\mu L)}{\mu L}} \quad (4.17)$$

where:

$$\lambda = \frac{E_p}{G_s}, \zeta = \ln \left(1.75 \frac{L}{r} \right), \mu L = \frac{L}{r} \left(\frac{2}{\zeta \lambda} \right)^{0.5} \quad (4.18)$$

The interaction coefficient for vertical loads is:

$$\alpha_v^{ij} = 1 - \frac{\ln \frac{s_{ij}}{r}}{\ln \frac{r_m}{r}} \quad (4.19)$$

As evident, it has been neglected the interaction among the bases of the piles, taking into account only the interaction among the lateral shafts.

About the swaying/rocking coefficients, it has been adopted the expression:

$$\alpha_{uu}^{ij} = 0.4 \left(\frac{E_p}{G^*} \right)^{\frac{1}{7}} (1 + \cos^2 \beta) \frac{r}{s_{ij}} \quad (4.20)$$

At very close spacings ($\alpha > 0.333$) the previous expression is substituted by:

$$\alpha_{uu}^{ij} = 1 - \frac{2}{\sqrt{27}\alpha} \quad (4.21)$$

to allow to tend to unity as s_{ij} tends to zero.

The coupled interaction coefficient are:

$$\alpha_{u\vartheta}^{ij} = \alpha_{\vartheta u}^{ij} = (\alpha_{uu}^{ij})^2 \quad (4.22)$$

$$\alpha_{\vartheta\vartheta}^{ij} = (\alpha_{uu}^{ij})^3 \quad (4.23)$$

This set of compliances and interaction coefficient allows to build an equation system whose unknowns are the lateral force, the bending moment and the axial force of each pile of a group, considering the raft as rigid. The equation system is shown in eq. (4.24); $d_{i,G}$ is the abscissa of pile i taking the centre of the group as origin. This system allow to consider both horizontal forces and moments. Therefore, to evaluate the (seismic) generalized forces acting on the raft, one can use both Code response spectra and real signals acceleration spectra; it has also been said in the previous chapter that, apart from particular cases, considering free-field spectra is accurate enough.

The structural period must take into account the compliance of the soil-foundation system; of course if the reference spectra is taken by Codes, considering the fixed-base period would be surely conservative.

4.2.1.1 Parametric study

The role played by various parameters on inertial (and relative importance of kinematic vs. inertial) interaction has been investigated with reference to pile cap. Considering a square group $n \times n$ embedded in an homogeneous soil, the following parameters have been fixed:

$r =$	0.3 m
$L =$	20 m
$s =$	1.8 m
$n =$	3
$E_p =$	30 GPa
$E_s =$	30 MPa
$\rho =$	1.6 t/m ³
$a_{ff} =$	1.1 m/s ²
$m =$	500 t
$T =$	0.5 s
$H_{str} (M / H) =$	0 m

$$\begin{bmatrix}
C_{uu} & C_{u\vartheta} & 0 & \alpha_{uu}^{2,1} C_{uu} & \alpha_{u\vartheta}^{2,1} C_{u\vartheta} & 0 & \dots\dots & \alpha_{uu}^{n-n,1} C_{uu} & \alpha_{u\vartheta}^{n-n,1} C_{u\vartheta} & 0 & -1 & 0 \\
C_{\vartheta u} & C_{\vartheta\vartheta} & 0 & \alpha_{\vartheta u}^{2,1} C_{\vartheta u} & \alpha_{\vartheta\vartheta}^{2,1} C_{\vartheta\vartheta} & 0 & \dots\dots & \alpha_{\vartheta u}^{n-n,1} C_{\vartheta u} & \alpha_{\vartheta\vartheta}^{n-n,1} C_{\vartheta\vartheta} & 0 & 0 & -1 \\
0 & 0 & C_{vv} & 0 & 0 & \alpha_{vv}^{2,1} C_{vv} & \dots\dots & 0 & 0 & \alpha_{vv}^{n-n,1} C_{vv} & 0 & -d_{1,G} \\
\alpha_{uu}^{1,2} C_{uu} & \alpha_{u\vartheta}^{1,2} C_{u\vartheta} & 0 & C_{uu} & C_{u\vartheta} & 0 & \dots\dots & \alpha_{uu}^{n-n,2} C_{uu} & \alpha_{u\vartheta}^{n-n,2} C_{u\vartheta} & 0 & -1 & 0 \\
\alpha_{\vartheta u}^{1,2} C_{\vartheta u} & \alpha_{\vartheta\vartheta}^{1,2} C_{\vartheta\vartheta} & 0 & C_{\vartheta u} & C_{\vartheta\vartheta} & 0 & \dots\dots & \alpha_{\vartheta u}^{n-n,2} C_{\vartheta u} & \alpha_{\vartheta\vartheta}^{n-n,2} C_{\vartheta\vartheta} & 0 & 0 & -1 \\
0 & 0 & \alpha_{vv}^{1,2} C_{vv} & 0 & 0 & C_{vv} & \dots\dots & 0 & 0 & \alpha_{vv}^{n-n,2} C_{vv} & 0 & -d_{2,G} \\
\dots\dots & \dots\dots & \dots\dots & \dots\dots & \dots\dots & \dots\dots & \dots\dots & \dots\dots & \dots\dots & \dots\dots & \dots\dots & \dots\dots \\
\dots\dots & \dots\dots & \dots\dots & \dots\dots & \dots\dots & \dots\dots & \dots\dots & \dots\dots & \dots\dots & \dots\dots & \dots\dots & \dots\dots \\
\dots\dots & \dots\dots & \dots\dots & \dots\dots & \dots\dots & \dots\dots & \dots\dots & \dots\dots & \dots\dots & \dots\dots & \dots\dots & \dots\dots \\
\dots\dots & \dots\dots & \dots\dots & \dots\dots & \dots\dots & \dots\dots & \dots\dots & \dots\dots & \dots\dots & \dots\dots & \dots\dots & \dots\dots \\
1 & 0 & 0 & 1 & 0 & 0 & \dots\dots & 1 & 0 & 0 & 0 & 0 \\
0 & 1 & d_{1,G} & 0 & 1 & d_{2,G} & \dots\dots & 0 & 1 & d_{n-n,G} & 0 & 0
\end{bmatrix}
\begin{bmatrix}
T_l \\
M_l \\
N_l \\
\cdot \\
\cdot \\
\cdot \\
\cdot \\
\cdot \\
\cdot \\
u_G \\
\vartheta_G
\end{bmatrix}
=
\begin{bmatrix}
0 \\
0 \\
0 \\
\cdot \\
\cdot \\
\cdot \\
\cdot \\
\cdot \\
\cdot \\
H_{PG} \\
M_{PG}
\end{bmatrix}$$

(4.24)

Hence, maintaining fixed the others, some of these parameters have been taken as variable (one by one).

The effect of the pile stiffness E_p is shown in Figure 4.14. It is evident that the kinematic bending moment is proportional to E_p , because (as shown in the previous Chapter) the pile curvature is equal to the soil curvature (except for very high stiffness ratios). On the contrary, inertial moments depend mainly on the structure mass, while pile Young modulus can only slightly change the internal forces among the piles; in particular, if E_p increases, the pile wave length increases leading to larger bending moments at pile top. Hence, increasing E_p leads to an increase in relative importance of kinematic with respect to inertial interaction. Of course, a difference among piles can be noticed, due to pile-soil-pile interaction for inertial loading; hence, the central pile, that evidently suffers a larger interaction, carries a smaller bending moment.

The effect of soil stiffness is depicted in Figure 4.15. Kinematic interaction drops very quickly increasing soil stiffness. This results in an increase in relative importance of inertial interaction.

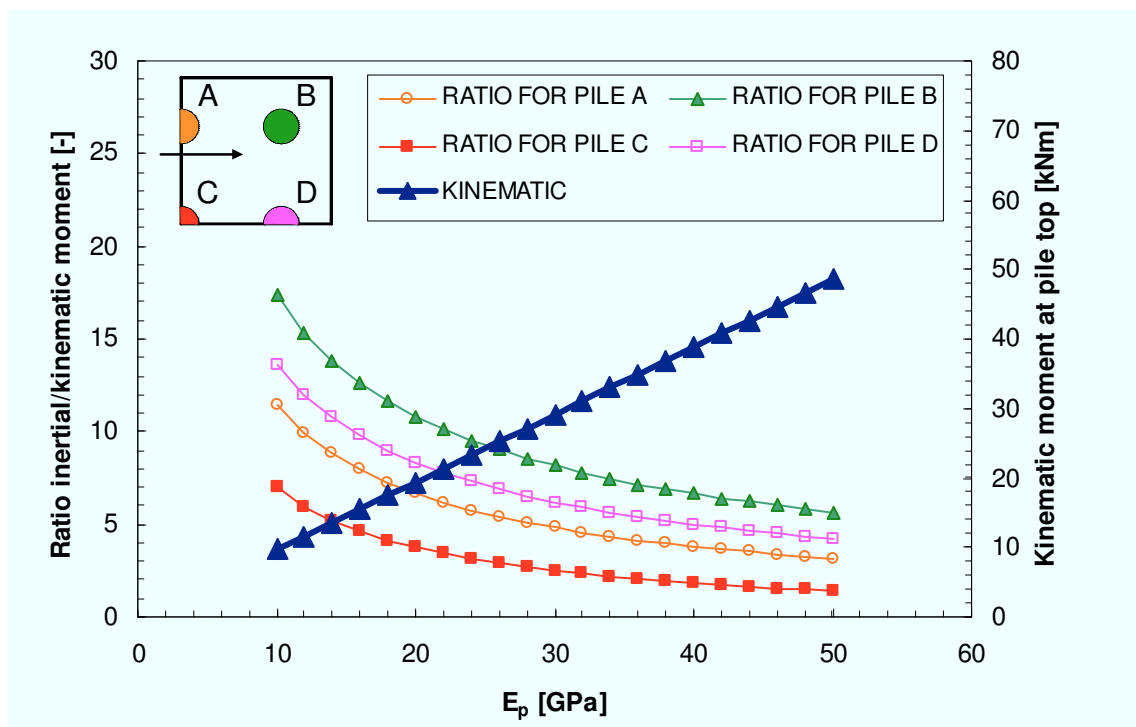


Figure 4.14: Influence of pile Young modulus.

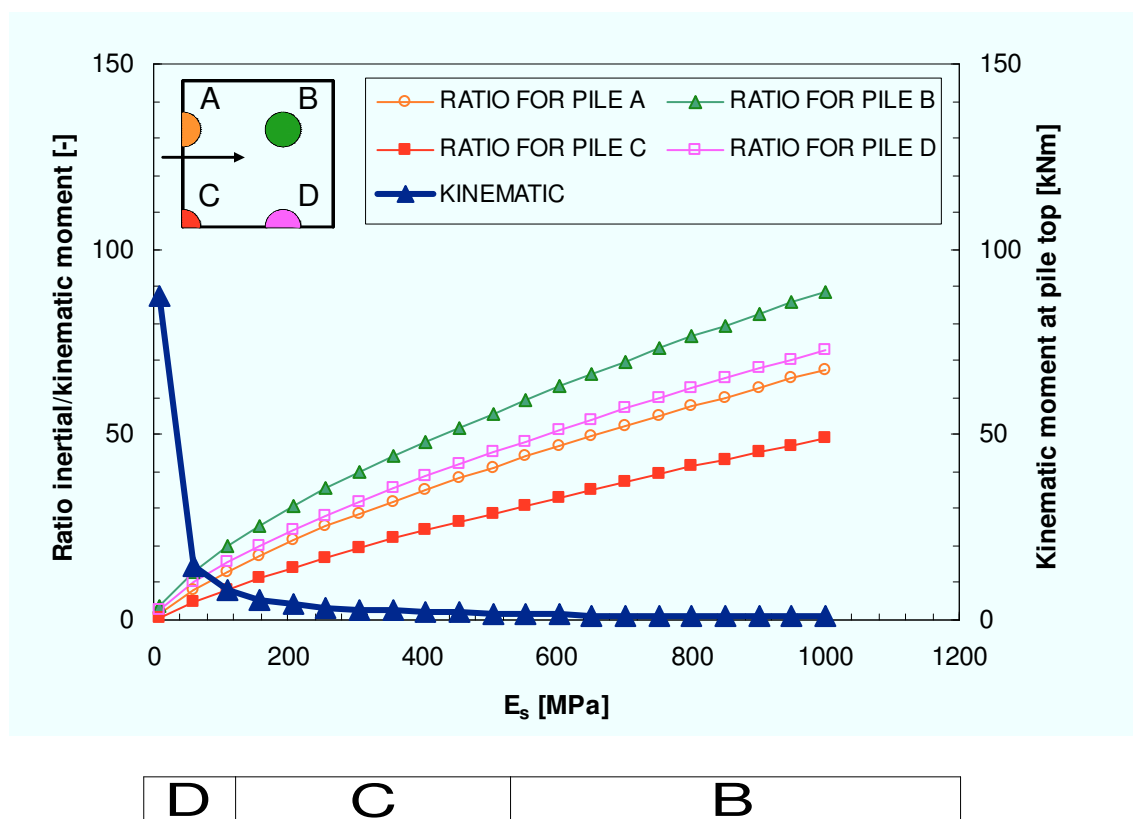


Figure 4.15: Influence of soil Young modulus. B, C, D refers to Italian Code subsoil classification.

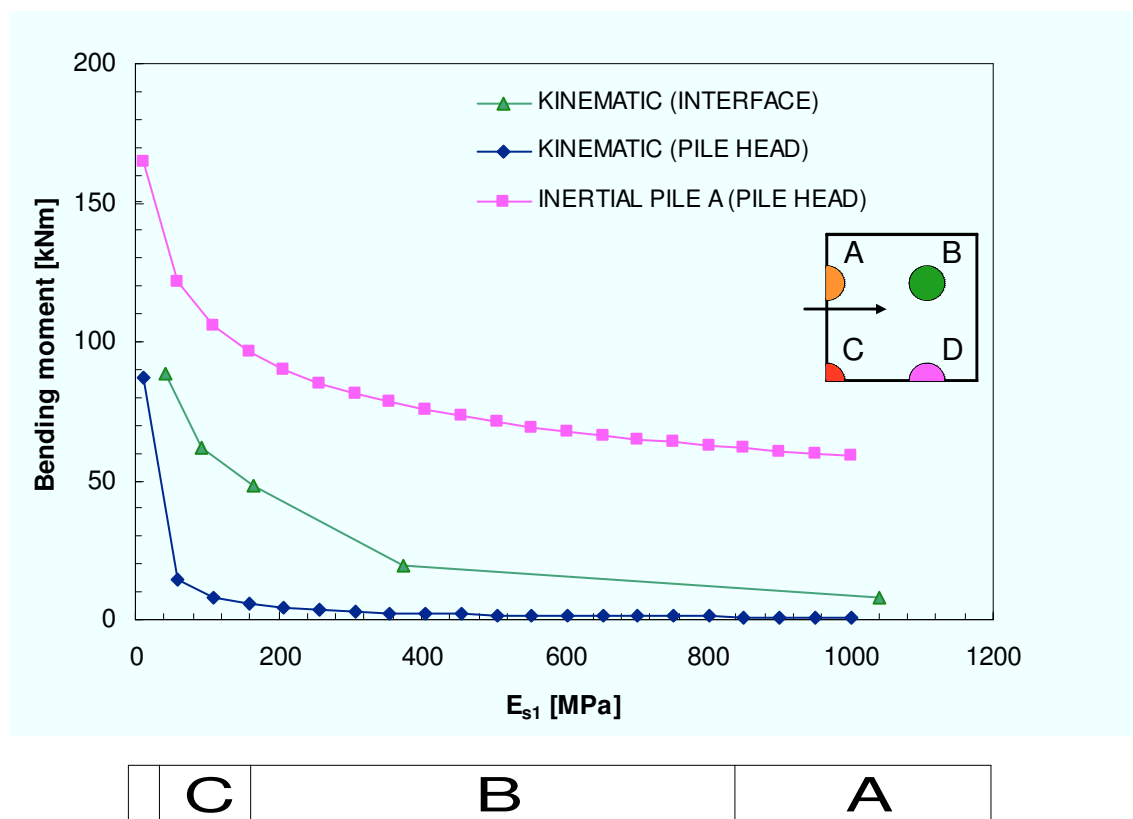


Figure 4.16: Influence of E_{s1} for a two-layer soil body. C, B, A refers to Italian Code subsoil classification.

$$V_{s2}/V_{s1} = 3.$$

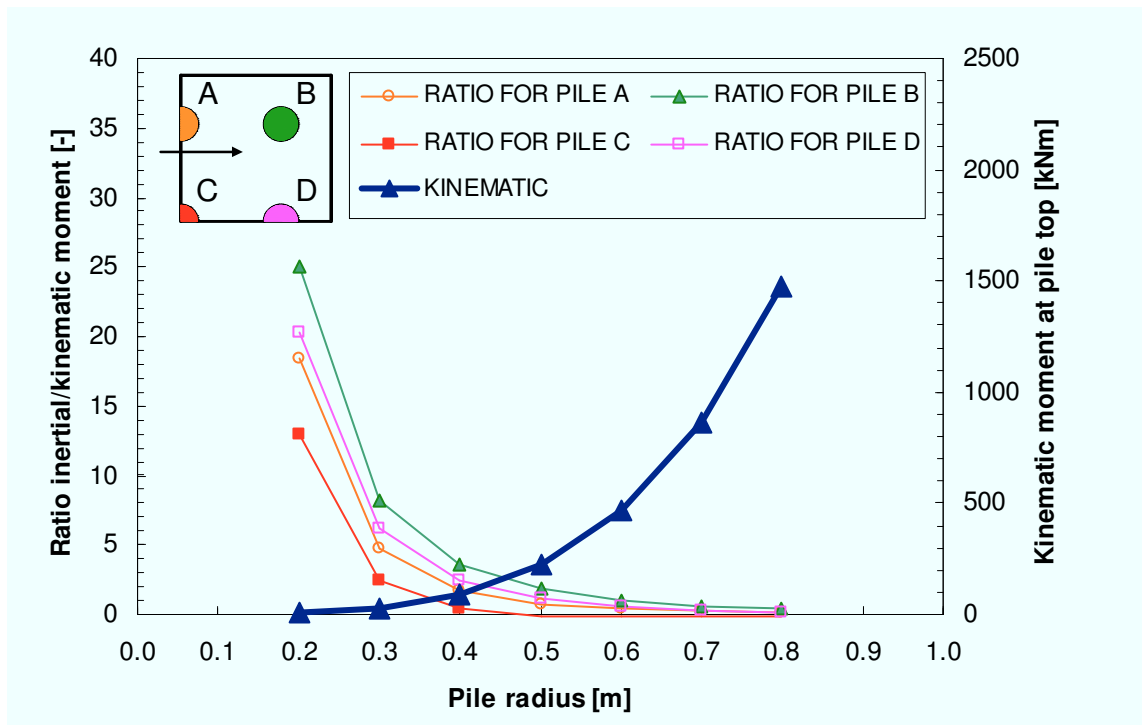


Figure 4.17: Influence of pile radius.

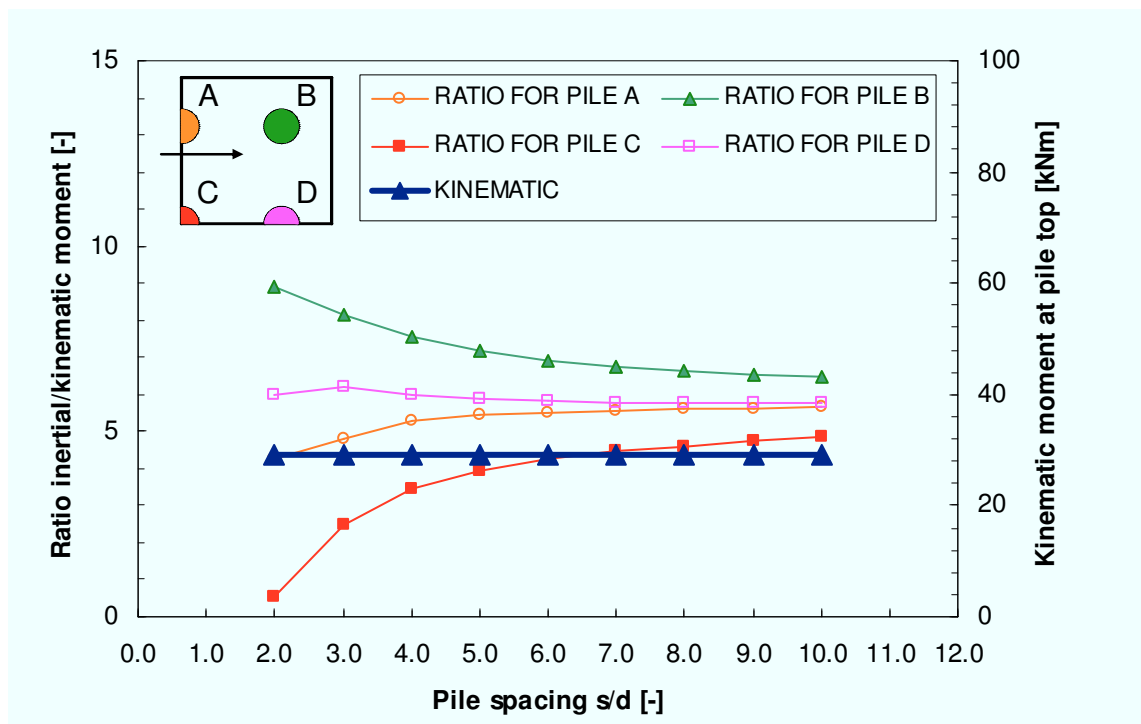


Figure 4.18: Influence of pile spacing.

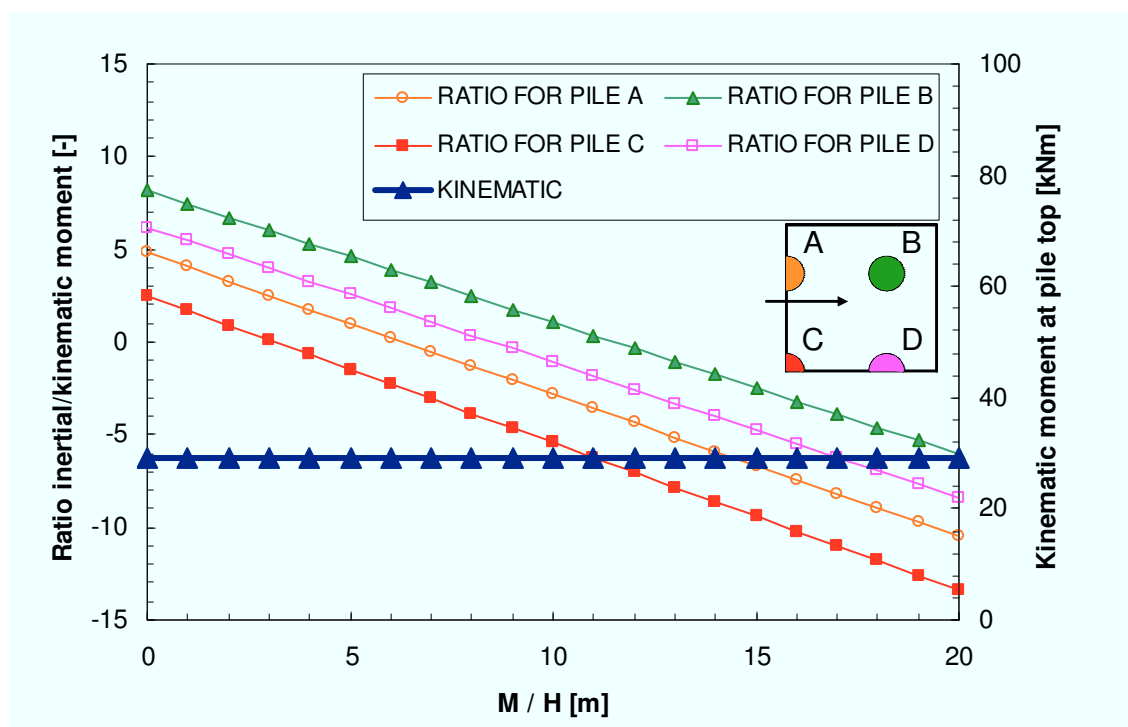


Figure 4.19: Influence of ratio between moment and lateral force.

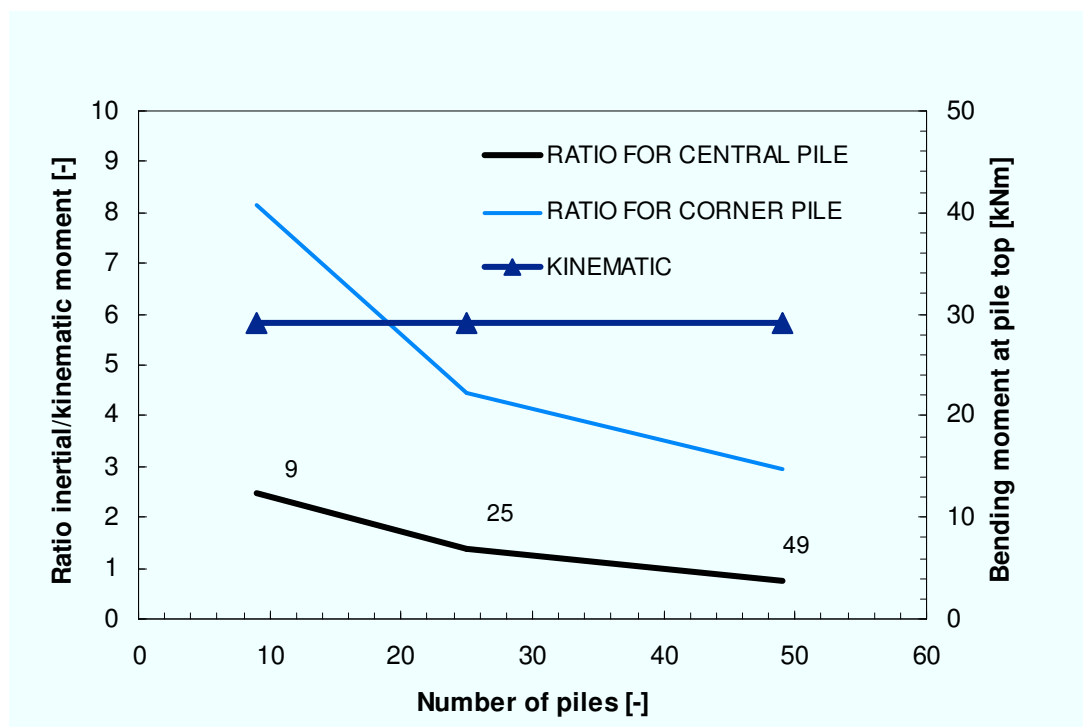


Figure 4.20: Influence of number of piles.

In this graph, it seems that kinematic interaction is always negligible with respect to inertial one; nevertheless, this is only the consequence of the hypothesis, and, above all,

kinematic effects at pile top in an homogeneous soil are much more smaller than those at interface in a two-layers soil body. For this reason, to elucidate quantitatively the relative importance of kinematic vs. inertial interaction, the Figure 4.16 shows a comparison between the two interactions with reference to an inhomogeneous soil with stiffness contrast equal to 3. The interface moments have been evaluated performing a free-field analysis and using the fitting formula in the Figure 3.65. Actually, the data in the graph is not perfectly congruent, as both inertial and kinematic interaction at pile top have been evaluated fixing free-field acceleration equal to 1 m/s^2 , while the free-field shear strain depends also on the surface acceleration, that is variable. Nevertheless, this carries to small differences. .

It is evident that Code fails, as it attributes an important influence of kinematic interaction only for subsoils classified as D, while in the graph also subsoils “B” lead to a kinematic moment that is about 50% of the inertial one, and, hence, not negligible. It is also evident that, decreasing the structural mass, kinematic interaction becomes even more important (because the inertial one has smaller effects).

Pile radius also has a large influence on relative importance of the two interactions (Figure 4.17).

It has an influence similar to that exerted by pile Young modulus, as kinematic moment is proportional to r^4 , while radius only re-distribute inertial effects among piles.

It’s worthy noting the trends shown in figure 4.18 with reference to the influence of pile spacing s/d . Inertial moments relative to different piles tend to converge to the same value if pile spacing increases. In fact an increase in pile spacing leads to a smaller interaction, and then each pile tends to assume the behaviour of a single pile. This means that, increasing s/d , the ratio inertial/kinematic interaction, as the denominator is constant, increases for centre piles and decreases for piles at the corners.

It’s interesting to note the influence of the ratio between the moment M and the lateral force H acting on the rigid raft; for a SDOF system, this ratio is evidently the structure height.

Conventionally, in figure 4.19 positive moments are due to the translation of the raft

Increasing M/H , it is clear that negative moments (essentially due to the moment acting on the raft) tend to prevail over the positive ones (due to the lateral force). Once the resulting moment acting at pile cap becomes negative, it will grow up indefinitely with increasing this ratio. Of course, it means that also relative importance of inertial vs. kinematic interaction increases.

A clear influence is exerted by the number of piles (at constant spacing and total lateral force), as shown in figure 4.20. Inertial moments, in fact, tend to decrease with increasing piles number, as H is distributed among a larger amount of piles.

Structural period has an obvious influence and, hence, is not reported in a graph. In fact, maintaining the kinematic moment constant, the ratio is function of inertial moments, proportional to the spectral acceleration.

It’s worthy reminding that the kinematic moments subject of discussion here are referred to pile cap (apart from the considerations about the influence of soil Young modulus), and so its relative importance with respect to the inertial one doesn’t regard the kinematic moments which can develop at the interface between layers with different stiffnesses, that are generally much more severe and, hence, rule the design.

4.2.2 Phase lag between kinematic and inertial interaction

The ideal separation of total strains and stresses acting on piles during earthquakes appears convenient, as is possible to estimate in a simple way the maxima of the two contributions. Nevertheless, once one has estimated the moments at pile cap due to both interactions, summing them may lead to a great overestimation of the actual stresses existing in the piles, as the superstructure can generate a stress time history that is in opposition to kinematic one.

It appears useful, hence, to find a simple criterion to estimate the phase lag between kinematic and inertial interaction and then combine their maximum effects.

It is opportune to remind that inertial bending moments can be divided (as said above) in two different parts: the first one is due to the rotation of the raft, while the other is the restraint reaction (of the raft) against swaying.

This distinction is necessary, as it is evident that the two different contributions in inertial interaction have a phase lag equal to 180° .

4.2.2.1 Theoretical considerations

It is possible to express, in the frequency domain, the kinematic stress acting on pile cap as follows:

$$KS(\omega) = H_{I-KS}(\omega)I(\omega) \quad (4.25)$$

where $I(\omega)$ is the input motion, $KS(\omega)$ is the kinematic stress and $H_{I-KS}(\omega)$ the transfer function which relates them, all complex functions of frequency ω .

Similarly, the free field surface acceleration is given by:

$$A(\omega) = H_{I-A}(\omega)I(\omega) \quad (4.26)$$

with the same meaning specified above.

As the acceleration of piles, neglecting high frequencies, is the same of the free field one, it is possible to express the inertial stress as:

$$IS(\omega) = H_{AP-IS}(\omega)AP(\omega) \cong H_{AP-IS}(\omega)A(\omega) = H_{AP-IS}(\omega)H_{I-A}(\omega)I(\omega) \quad (4.27)$$

where $AP(\omega)$ is the pile acceleration, $IS(\omega)$ is the inertial normal stress generated at pile head, $H_{AP-IS}(\omega)$ is the transfer function relating them.

It can be seen, by numerical analyses, that kinematic acceleration (H_{I-A}) and stress (H_{I-KS}) transfer functions are in-phase, as Figure 4.21 shows.

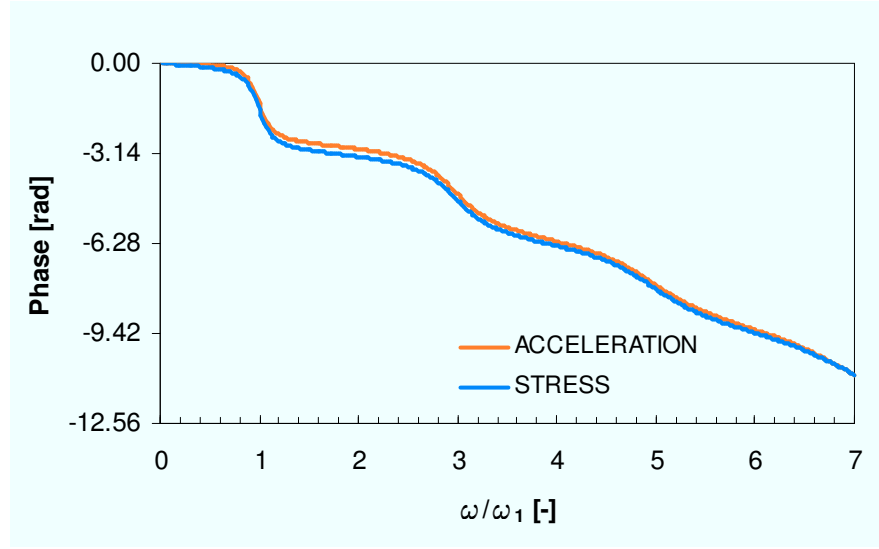


Figure 4.21: Acceleration and stress transfer function phase comparison. ω_1 is the fundamental frequency of soil.

So, since $Phase[H_{I-A}(\omega)] \cong Phase[H_{I-KS}(\omega)]$, is possible to write that:

$$Phase[IS(\omega)] \cong Phase[H_{AP-IS}(\omega)] + Phase[H_{I-A}(\omega)] + Phase[I(\omega)] \quad (4.28)$$

$$Phase[KS(\omega)] = Phase[H_{I-KS}(\omega)] + Phase[I(\omega)] \quad (4.29)$$

$$Phase[IS(\omega)] - Phase[KS(\omega)] \cong Phase[H_{AP-IS}(\omega)] \quad (4.30)$$

In the hypothesis, for instance, that the bending moment due to raft rotation prevails, structure accelerations and inertial stress on the pile cap have a phase lag approximately equal to π radians (see Figure 4.22).

Then the phase lag between the inertial and kinematic stress is:

$$Phase[IS(\omega)] - Phase[KS(\omega)] \cong \pi - Phase[H_{I-AS}(\omega)] \quad (4.31)$$

where H_{I-AS} is the transfer function of a SDOF system with a period T equal to the fundamental period of the structure.

This means that the phase lag between inertial and kinematic stresses can be easily evaluated looking at the phase diagram of a SDOF system, shown in Figure 4.23. Harmonics that have a frequency smaller than the fundamental frequency of the structure will produce approximately out-of-phase kinematic and inertial responses, while harmonics whose frequency is larger than the frequency of the structure will produce in-phase responses.

Is important to notice that the phase lag of each harmonic is independent of kinematic interaction; it depends only on the inertial one, through the structural period (taking into account period elongation due to soil-structure interaction).

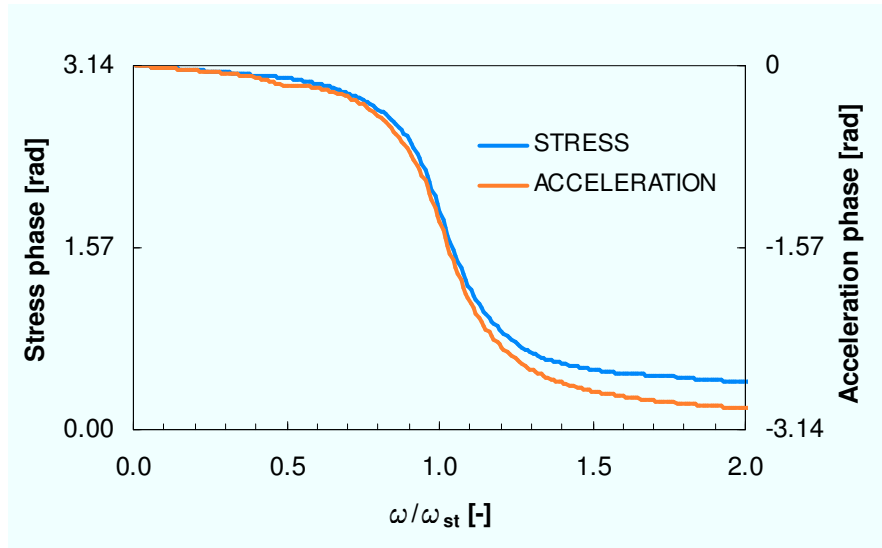


Figure 4.22: Structure acceleration and pile cap stress phase comparison. ω_{st} is the fundamental frequency of the structure.

This does not mean that inertial interaction, by itself, rules if kinematic and inertial stress time histories are in-phase or out-of-phase; indeed, the approximate phase lag between the entire time histories has to depend on the frequency of prevalent harmonics in the surface free-field signal (rigorously foundation motion). The consequent phase lag between the two interactions is prevalently ruled by the phase lag of such relevant harmonics.

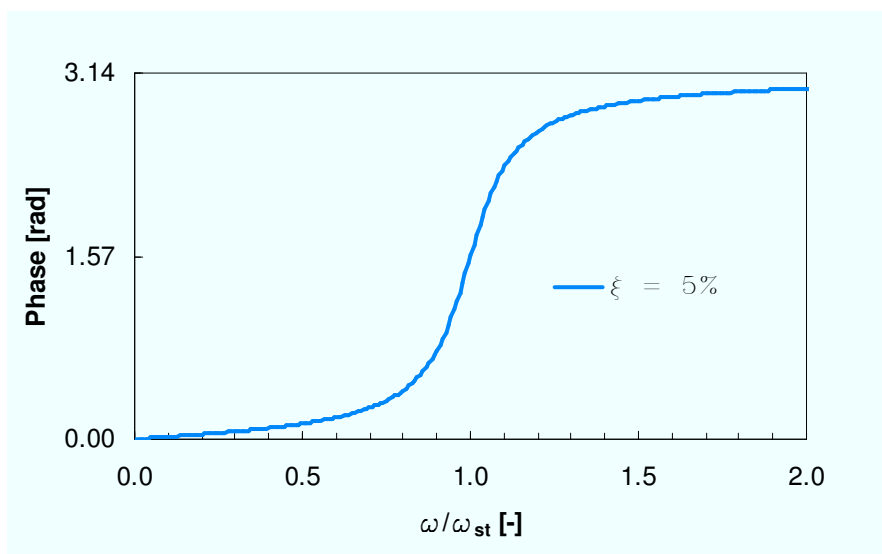


Figure 4.23: SDOF phase.

Operatively one can judge if is the case (or not) of summing maximum kinematic and inertial effects performing firstly a seismic local response analysis (EERA), and then verifying if the frequency content of the surface signal is prevalently larger (or not) than the fundamental frequency of the structure (evaluated taking into account SSI interaction).

4.2.2.2 Numerical analyses

In order to verify the reliability of this simple method, some FEM numerical analyses have been performed. In Table 4.1 the analysed cases are summarised.

Table 4.1. Analysed cases

	$E_{\text{soil}}[\text{MPa}]$	$w_{\text{soil}} [\text{Hz}]$	$w_{\text{str}} (\text{with SSI}) [\text{Hz}]$
A	30	0.71	1.45
B	120	1.42	1.45
C	120	1.42	1.02
D	120	1.42	0.72

The foundation is a 3x3 piled raft (rigid), with $d=0.6$ m and $s=3d=1.8$ m. Young modulus of piles is 30 GPa, while the height of the structure is 10 m; damping ratio is set to 10% for all modes. With this layout bending moments (and then stresses) due to raft rotation prevail.

The FE model is shown in Figure 4.24.

The signals are those used for kinematic interaction analyses; their main characteristics are reported in Chapter 3.

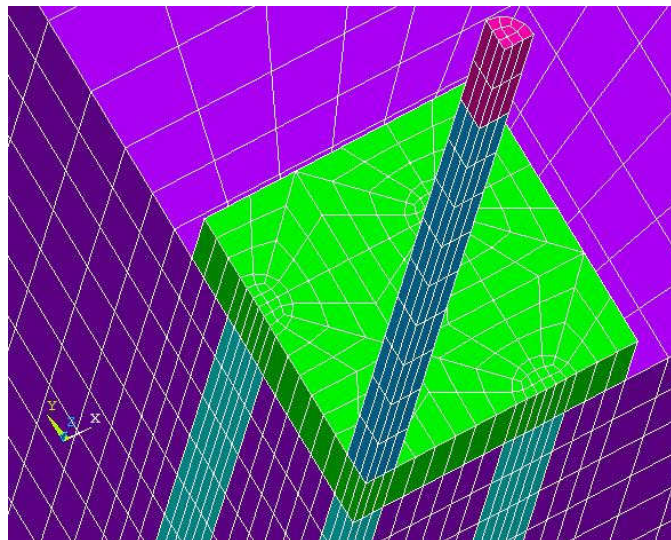


Figure 4.24: FE model.

Looking at the results, in figures 4.25 and 4.26 the surface free field acceleration transfer function is showed. It is valid for homogeneous soil (damping ratio $\xi = 10\%$, soil layer height $H = 30$ m) on rigid rock.

It can be seen that in correspondence of natural frequencies $\omega_n = \omega_1(1+2n)$, with $n = 0, 1, 2, \dots$ and $\omega_1 = V_s/4H$, amplitude and imaginary part reach their absolute maxima, phase is $\pi/2$, and real part is 0.

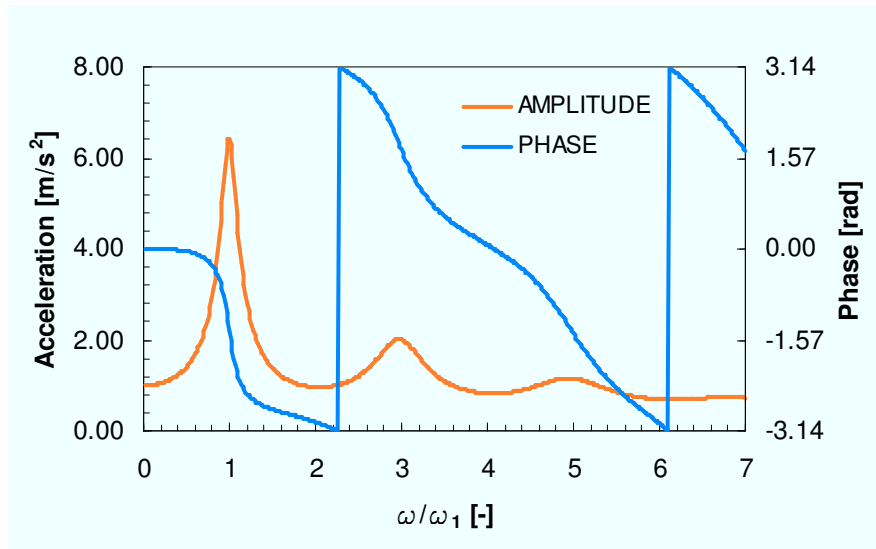


Figure 4.25: Surface free field acceleration transfer function. Amplitude and phase.

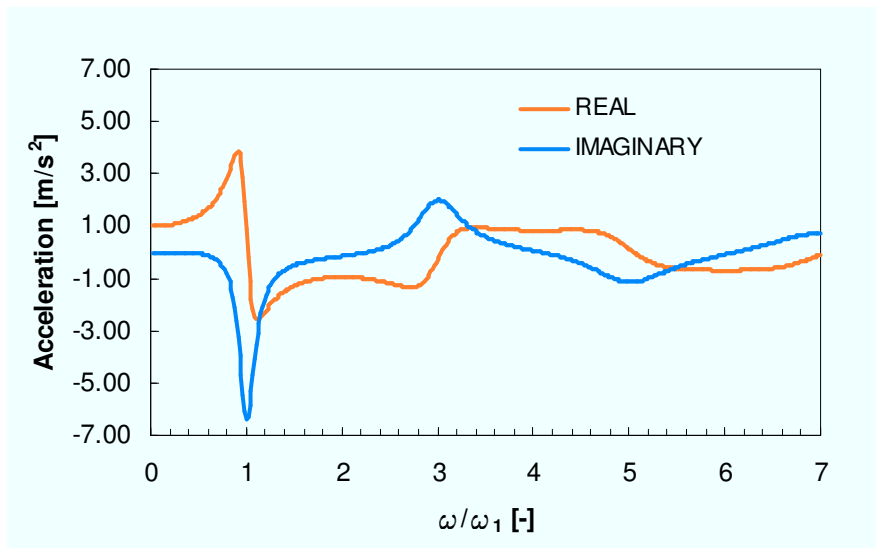


Figure 4.26: Surface free field acceleration transfer function. Real and imaginary part.

This transfer function leads to the graphs in Figures 4.27 and 4.28. In Figure 4.27 the case of STURNO signal is shown with reference to both different subsoil. As can be seen the softer subsoil amplifies frequencies around 0.7, 2.1 and 3.5 Hz, while the stiffer soil amplifies 1.4, 4.2 and 7 Hz. Since the structure has a fundamental frequency equal to 1.45 Hz,

according to the above method in the case A inertial and kinematic stresses should be mostly in opposition, as the greatest part of the frequency content is above 1.45 Hz.

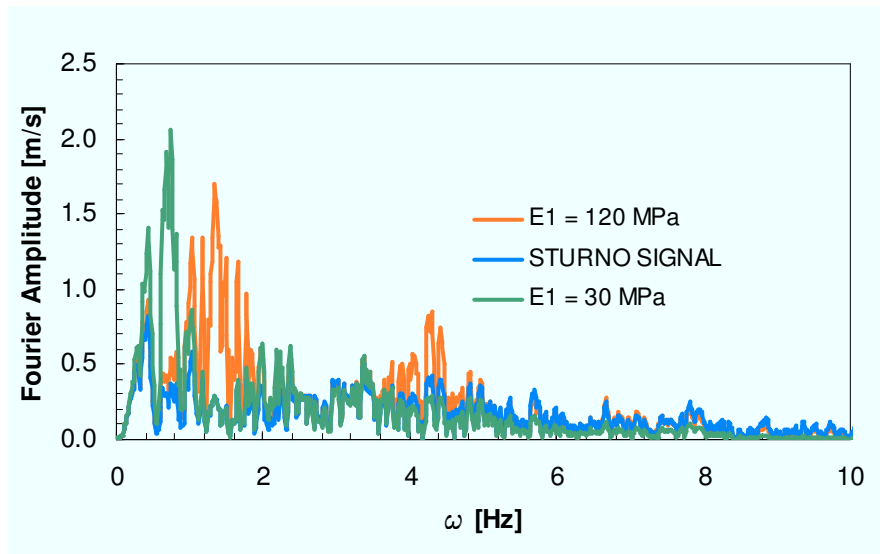


Figure 4.27: Acceleration Fourier spectra for STURNO signal.

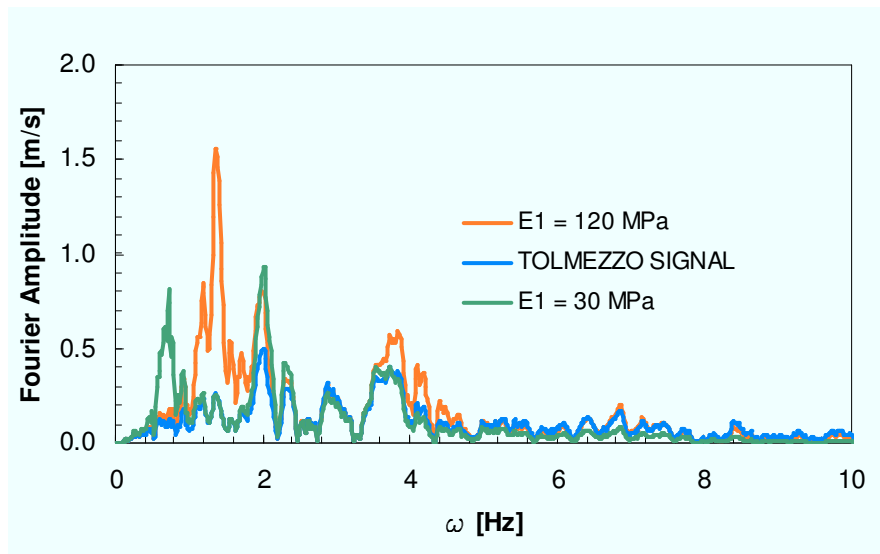


Figure 4.28: Acceleration Fourier spectra for TOLMEZZO signal.

Looking at the acceleration Fourier spectra for TOLMEZZO signal (Figure 4.28), it is noted that the case B ($E_1 = 120$ MPa) is very particular, because there is resonance between soil and structure, and for this reason inertial stresses are important. The important frequency content is then concentrated around the structure frequency and then the phase lag between inertial and kinematic stress should be approximately equal to $\pi/2$.

In the Figure 4.29 and 4.30 the time histories relative to these cases (with reference to centre pile) are shown.

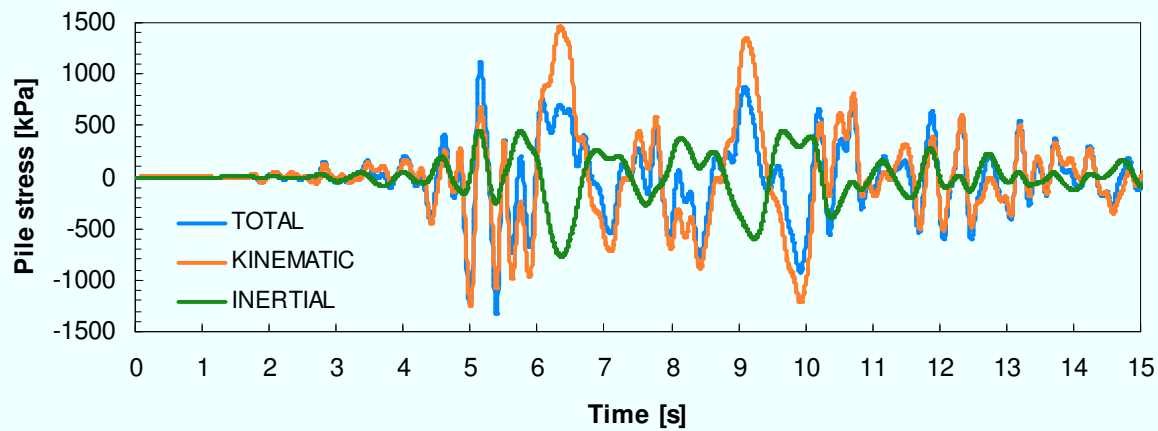


Figure 4.29: Stress time histories (STURNO, case A).

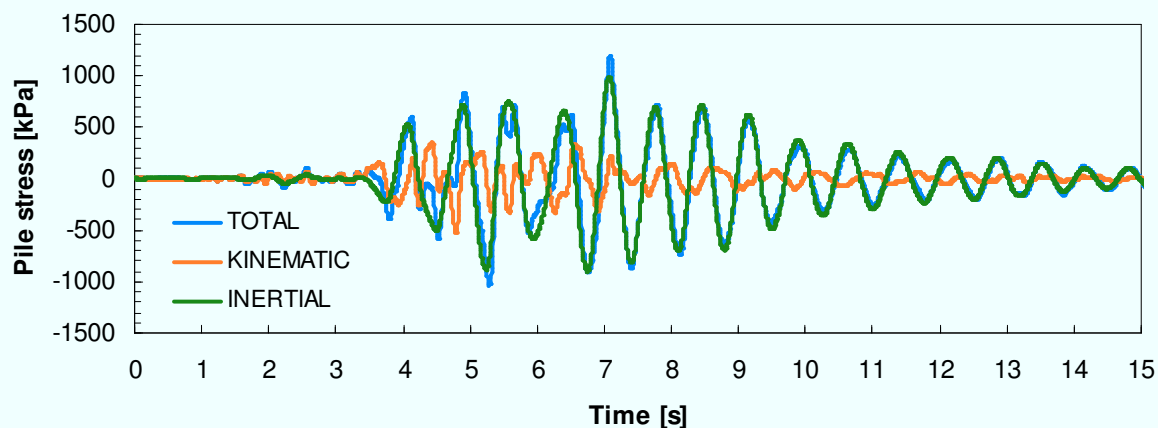


Figure 4.30: Stress time histories (TOLMEZZO, case B).

The time histories shown above confirm the predictions. It is noted that for STURNO signal, case A, summing the maxima may be very dangerous, as the kinematic maximum moment is larger than the total one.

For the resonance case shown in Figure 4.30 the phase lag is about $\pi/2$, as predicted; summing maxima leads then to a small error.

Starting from this case (TOLMEZZO, case B), decreasing the frequency of the structure (cases C and D) should lead to in-phase kinematic and inertial stresses, as can be seen in Figure 4.28, because the relevant frequencies (in surface acceleration spectra) would be larger than the structure frequency.

In Figures 4.31 and 4.32 time histories for the cases C and D are shown with reference to TOLMEZZO signal.

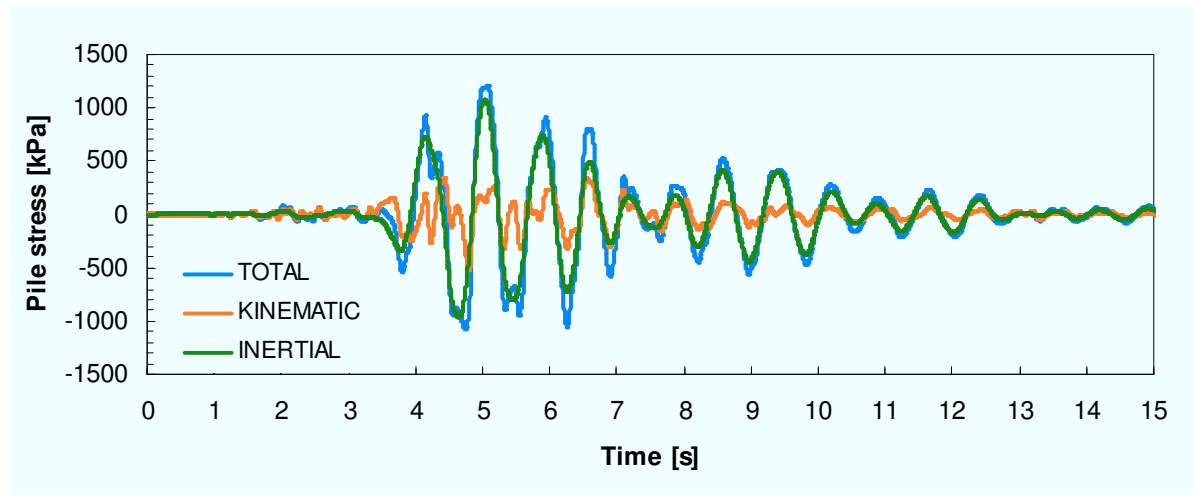


Figure 4.31: Stress time histories (TOLMEZZO, case C).

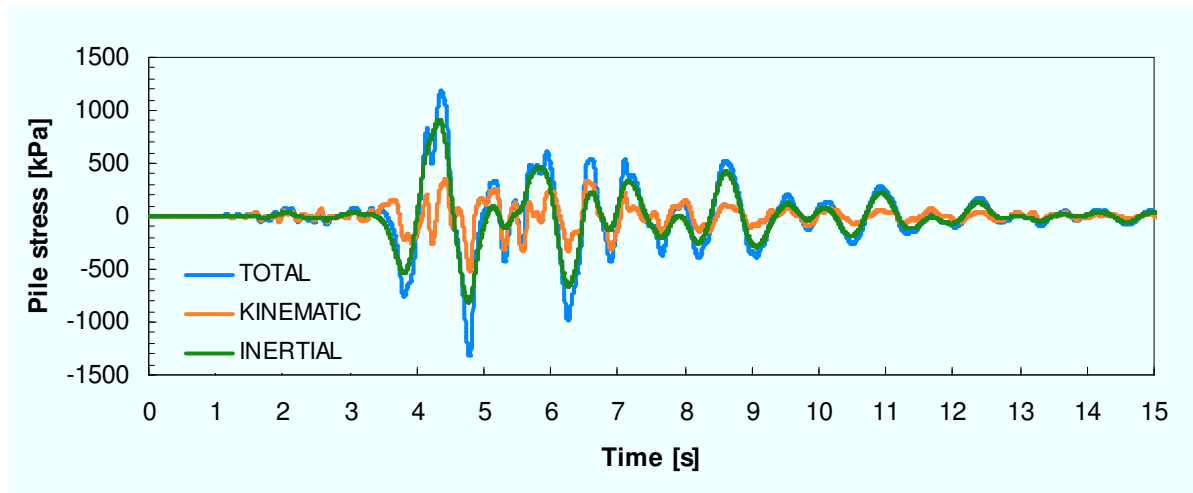


Figure 4.32: Stress time histories (TOLMEZZO, case D).

As predicted, for these cases there is no phase lag between inertial and kinematic stress time histories, and then summing maxima is a correct operation that can lead only to unappreciable errors.

In the hypothesis in which the bending moment due to the raft rotation prevails, the phase lag decreases (fixing other conditions):

- decreasing the frequency of the structure;
- increasing the frequency of the soil;
- moving the frequency content of input signal to higher frequencies.

If the bending moment due to raft translation prevails, opposite conclusions have to be derived; in this case, the three conditions above have to increase the phase lag.

To prove that, it has been analysed a case in which, starting from the case A, the structure height reduces to 4 m (let's say case A2).

As it can be noted from Figure 4.33, inertial and kinematic moments are in-phase; as evident, in fact, decreasing the structure height leads to a decrease in the negative moment contribution due to raft rotation, changing the sign of the bending moment.

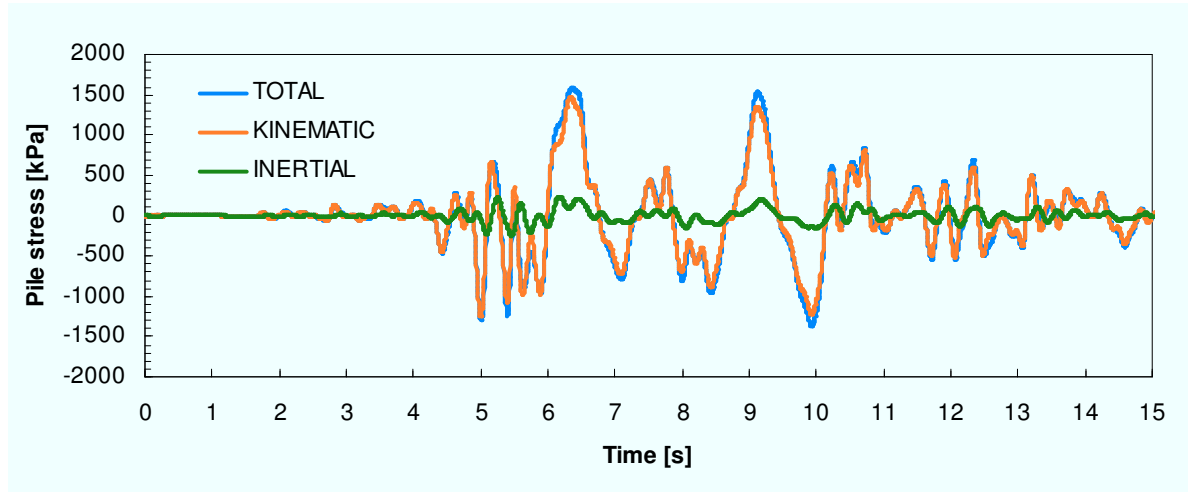


Figure 4.33: Stress time histories (TOLMEZZO, case A2).

4.2.2.3 Combination of kinematic and inertial maxima at pile cap

Summarizing, a simple method to estimate the phase lag between kinematic and inertial stresses has been found. This can be useful when the design of a piled foundation is made calculating only the maximum effect of kinematic and/or inertial interaction.

Basing on the described method, in design it is possible to combine the two effects in the following way:

- in the case they are in-phase, sum the maxima;
- if the phase lag is approximately 180° , take the maximum between the kinematic and the inertial contribution;
- in the rare case in which the phase lag is about 90° , it is still licit to sum maximum effects without committing large errors; it is worthy noting that in this case inertial interaction is particularly important because of the resonance between foundation input motion and structure.

Concluding remarks

The research effort has been aimed to the analysis of the seismic soil-structure interaction for pile supported structures.

Once highlighted the role played by the several parameters governing the kinematic interaction, some simplified formulas have been proposed for a straightforward evaluation of kinematic bending moment at the interface between soils with different stiffness and at pile head.

In order to make analyses as simple as possible, some effort was dedicated to select cases for which is possible to neglect the filtering effect exerted by piles, hence allowing for analyses based only on the analysis of the wave propagation into the subsoil.

Furthermore, the relative importance of kinematic vs. inertial interaction has been investigated. Even if under linear elastic hypothesis, it has been highlighted that some cases could exist in which some Codes suggest to not carry out kinematic interaction analysis but its effects in terms of bending moment along piles are not negligible if compared with that coming from inertial interaction.

Finally, some results have been derived in terms of phase lag between kinematic and inertial effects. A criterion has been proposed to combine their maxima.

All the results have been obtained assuming a linear elastic behavior of the materials involved (soil, pile, structure), being the only case in which kinematic and inertial interaction effects can be separately evaluated and then superposed.

Further research in this field could be aimed to define the range in which the results are still valid. This could be obtained by including non linearity of the behavior and plasticity.

References

- Bardet J.P., Ichii K., Lin C.H., *EERA: a computer program for equivalent-linear earthquake site response analyses of layered soil deposits*, Department of Civil Engineering, University of Southern California, Los Angeles, Calif. Available from geoinfo.usc.edu/gees.
- CNEL-ENEL (1976), *Contribution to the study of the Friuli earthquake of May 1976*, Rome.
- Chopra, A. (1995), *Dynamics of Structures: Theory and Application to Earthquake Engineering*, Ed. Prentice Hall.
- Dobry, R. & O'Rourke, M. J. (1983), Discussion on 'Seismic response of end-bearing piles' by Flores-Berrones, R. & Whitman, R. V. J. Geotech. Engng Div., ASCE p. 109.
- EEFIT (1986), *The Mexican earthquake of 19 September 1985*, London: Institution of Civil Engineers.
- Fan, K., Gazetas, G., Kaynia, A., Kausel, E. and Ahmad, S. (1991), *Kinematic seismic response of single piles and pile groups*, J. Geotech. Engng Div., ASCE 117, No. 12, 1860-1879.
- Fleming, W. G. K., Weltman, A. J., Randolph, M. F. and Elson, W. K. (1985), *Piling engineering*, pp. 188-198. Glasgow: Surrey University Press.
- Gazetas, G. & Dobry, R. (1984), *Simple radiation damping model for piles and footings*, J. Geotech. Engng Div., ASCE 110, No. 6, 937-956.
- Flores-Berrones, R. & Whitman, R. V. (1982), *Seismic response of end-bearing piles*, J. Geotech. Engng Div., ASCE, 108, No. 4, pp. 554-569.
- Gazetas, G. (1984), *Seismic Response of End-Bearing Single Piles*, Soil Dyn. Earthq. Engng 3, No. 2, pp. 82-93.
- Gazetas, G. (1991), *Foundation Vibrations in Foundation Engineering Handbook* (H.Y. Fang Ed.), Kluwer Academic Pub., Boston
- Gazetas, G. & Dobry, R. (1984), *Simple radiation damping model for piles and footings*, J. Geotech. Engng Div., ASCE 110, No. 6, 937-956.
- Gazetas, G., Dobry, R. and Tassoulas, J. (1985), *Vertical Response of Arbitrarily-Shaped Embedded Foundations*, Foundation Analysis and Design (J. Bowles Ed.), McGraw-Hill, 1988, 4th Edition.
- Gazetas, G., Fan, K., Tazoh, T., Shimizu, K., Kava and Makris, N. (1992), *Seismic pile-group-structure interaction*, In: S. Prakash (ed.), *Piles Under Dynamic Loads*, Geotech. Engng. Div., Geotechnical Special Publication No. 34, ASCE, pp. 56-94.
- Gazetas, G. & Mylonakis, G. (1998), *Seismic soil-structure interaction: new evidence and emerging issues*, Geotech Earthq. Engng & Soil Dynamics III, vol. 2, pp. 1119-1174,

ASCE.

- Kavvadas, M. & Gazetas, G. (1993), *Kinematic seismic response and bending of free-head piles in layered soil*, Geotechnique, Vol. 43, No. 2, pp. 207-222.
- Kaynia, A. M. & Kausel, E. (1982), *Dynamic stiffness and seismic response of pile groups*, Research Report R82-03. Massachusetts Institute of Technology.
- Kaynia, A. & Kausel, E. (1991), *Dynamics of piles and pile groups in layered soil media*, Soil Dyn. Earthquake Eng 10, pp. 386–401.
- Kramer, Steven L. (1996), *Geotechnical Earthquake Engineering*, Publ. Prentice Hall Upper Saddle River, N.J.
- Makris, N. & Gazetas, G. (1992), *Dynamic Pile-Soil-Pile Interaction. Part II: Lateral and Seismic Response*, Earthq. Engng. & Struct. Dynamics, Vol. 21, No. 2.
- Margason, E. (1975), *Pile bending during earthquakes*. Lecture, 6 March 1975, ASCE-UC/Berkeley Seminar on Design Construction and Performance of Deep Foundations (unpublished).
- Margason E. and Holloway, D. M. (1977), *Pile Bending during Earthquakes*, Proc., Sixth World Conference on Earthquake Engineering, Sarita Prakashan, Meerut, India, 1977, pages 1690-1696, Vol. II.
- Mineiro, A.J.C. (1990), *Simplified Procedure for Evaluating Earthquake Loading on Piles*, De Mello Volume, Lisbon.
- Miranda, E. & Bertero, V. (1994), *Evaluation of strength reduction factors of earthquake-resistant design*, Earthq. Spectra 10(2), 357-379.
- Mizuno, H. (1987), *Pile damage during earthquakes in Japan*, In *Dynamic response of pile foundations* (ed. T. Nogami), ASCE Special Publication, pp. 53-78.
- Mylonakis, G. (1999), *Seismic Pile Bending at Deep Interfaces*, Report GEL-99-01, Geotechnical Laboratory, City College of New York.
- Mylonakis, G. (2001), *Simplified model for seismic pile bending at soil layer interfaces*, Soils and Foundations, 41(4), 47–58.
- Mylonakis G. & Gazetas G. (2000), *Seismic Soil-Structure Interaction: Beneficial or Detrimental ?*, Journal of Earthquake Engineering, Vol. 4, p.p. 277-301.
- Mylonakis, G., Gazetas, G., and Nikolaou, S. (2006), *Footings under Dynamics Loads: Analysis and Design Issues with Emphasis on Bridge Foundations*, Soil Dynamics and Earthquake Engineering, Vol. 26, No. 9, pp 824-853.
- Mylonakis, G., Gazetas, G., Nikolaou, A. and Michaelides, O. (2000), *The role of soil on the collapse of 18 piers of the elevated Hanshin Expressway in the Kobe earthquake*, Proc. 12th World Conference on Earthquake Engineering, New Zealand, 7 pp.
- Nikolaou, A. & Gazetas, G. (1997), *Seismic Design Procedure for Kinematically Loaded Piles*, XIV ICSMFE, Special Volume, ISSMFE TC4 Earthquake Geotechnical Engineering, Hamburg, Germany, Sept. 6-12, pp. 253-260.
- Nikolaou, A., Mylonakis, G. and Gazetas, G. (1995), *Kinematic Bending Moments in Seismically Stressed Piles*, Report. NCEER-95-0022, National Center for Earthquake Engineering Research, State University of New York, Buffalo.
- Nikolaou, A.S., Mylonakis, G., Gazetas, G., and Tazoh, T. (2001), *Kinematic pile bending during earthquakes analysis and field measurements*. Géotechnique, 51(5), 425–440.
- Nishizawa, T., Tajiri, S. & Kawamura, S. (1984), *Excavation and response analysis of a*

- damaged rc pile by liquefaction*, Proc. 8th World Conf. Earthquake Engng 3, 593-600.
- Okamoto, S. (1983), *An introduction to earthquake engineering*, 2nd edn. University of Tokyo Press.
- Pender, M. (1993). *Aseismic pile foundation design analysis*, Bulletin of the New Zealand National Society for Earthquake Engineering, 26(1), 49–160
- Potts, D. M. & Zdravkovic, L. (1999), *Finite element analysis in geotechnical engineering*, Thomas Telford Ltd, London.
- Poulos, H. G. (1968), *Analysis of the settlement of pile groups*, Geotechnique 18, No. 4, 449-471.
- Poulos, H. G. (1971), *Behavior of laterally-loaded piles II: pile groups*, J. Soil Mech. Fdns Div. Am. Soc. Civ. Engrs 97, SM5,733-751.
- Poulos, H.G. & Davis, E.H. (1980), *Pile foundation analysis and design*, John Wiley & Sons.
- Randolph, M.F. (1981), *Response of flexible piles to lateral loading*, Géotechnique, 31(2), 247–259.
- Randolph, M. F. & Wroth, C. P. (1979), *An analysis of the vertical deformation of pile groups*, Géotechnique 29, No. 4, 423-439.
- Ross, G. A., Seed, H. B. and Migliaccio, R. (1969), *Bridge foundations in the Alaska earthquake*, J. Soil Mech. Found. Engng, ASCE, 95.
- Scasserra G., Lanzo G., Mollaioli F., Stewart J.P., Bazzurro P., Decanini L.D. (2006), *Preliminary comparison of ground motions from earthquakes in Italy with ground motion prediction equations for active tectonic regions*, in Proceedings of the 8th U.S. National Conference on Earthquake Engineering, San Francisco, CD rom, Paper No. 1824.
- Tazoh, T., Shimizu, K. & Wakahara, T. (1987), *Seismic observations and analysis of grouped piles*. In *Dynamic response of pile foundations: experiment, analysis and observation*, Geotechnical Special Publication No. 11. ASCE.
- Wang, E. & Nelson, T. (2002), *Structural Dynamic Capabilities of ANSYS*, Proceedings of 2002 International Ansys Conference.